

Dissertation zur Erlangung des Doktorgrades
der Fakultät für Chemie und Pharmazie
der Ludwig-Maximilians-Universität München

Synthesis, Structure and Optoelectronic Properties of New Hybrid Perovskites

Claudia Lermer

aus

Ludwigshafen am Rhein

2018

Erklärung

Diese Dissertation wurde im Sinne von § 7 der Promotionsordnung vom 28. November 2011 von Frau Prof. Dr. Bettina Lotsch betreut.

Eidesstattliche Versicherung

Diese Dissertation wurde eigenständig und ohne unerlaubte Hilfe erarbeitet.

München, 15.05.2018

Claudia Lermer

Dissertation eingereicht am	25.05.2018
1. Gutachterin:	Prof. Dr. Bettina Lotsch
2. Gutachter:	Prof. Dr. Lukas Schmidt-Mende
Mündliche Prüfung am	25.06.2018

To my family

Acknowledgments

First of all, I would like to thank Prof. Bettina Lotsch for her motivation, ongoing support, academic freedom and concomitant guidance.

In addition, I would like to thank Prof. Lukas Schmidt-Mende for his considerate acceptance of giving a second opinion on my thesis.

Sincere thanks to Prof. Konstantin Karaghiosoff, Prof. Wolfgang Schnick, Prof. Hans-Christian Böttcher and Prof. Dirk Johrendt for being part of my examination committee.

I am very thankful to all of my collaborators without whom the accomplishment of my PhD projects wouldn't have been possible: Susanne Birkhold accompanied me during my first two projects and provided photoluminescence and absorption data. Thank you for your reliable work, fruitful discussions and your commitment even late at night and at weekends when deadlines were urging. Tobias Seewald followed up the great work during the last project and contributed the optical characterization. Dr. Igor Moudrakovski shed light on phase transitions and mobile carriers with skilled solid-state NMR spectroscopy measurements and was always ready to explain and discuss the evaluation of the data. Alessandro Senocrate carried out many elaborated conductivity experiments. Thank you for your comments and ideas when proofreading the manuscript! Dr. Peter Mayer elucidated the structure of innumerable hybrid perovskites and hybrid compounds.

Many thanks to the whole Lotsch group for the great working atmosphere, a good team spirit and many group lunch breaks with scientific and most importantly non-scientific conversations. I want to particular acknowledge Sascha Harm for his advice concerning all upcoming crystallographic issues and his active cooperation in the invited paper, Anna Hatz for persistent attempts to measure the conductivity of my samples until we finally succeeded, Dr. Leslie Schoop and Dr. Florian Pielhofer for carrying out DFT calculations and Dr. Sophia Betzler for performing EDX experiments.

Further, I would like to give thanks to Christine Stefani, Armin Sorg, Christian Minke, Willi Hölle, Peter Mayer, Brigitte Breitenstein, Robert Eicher, Susanne Ebert and Thomas Miller for numerous measurements, Wolfgang Wünschheim for technical support and Olga Lorenz for advice regarding administrative questions.

I'm very grateful to my interns Jannik Schwab, Fabian Huck, Christopher Kutz and Julian Jaser who did a great part of the practical work. Fabian Huck and Julian Jaser continued their commitment as "HiWis". Thank you for your reliable, passionate and creative work!

Claudia Kamella, Viola Duppel, Roland Eger and all the other members of the Lotsch group in Stuttgart always gave me a very warm welcome when I visited the MPI.

Michi, Angie and Adri lightened up many lunch breaks and I'm grateful for their friendship and support during the whole course of our studies.

I would also like to thank the Center for NanoScience for providing funding for my conference visit at the ACS spring meeting in San Francisco, the Deutsche Telekom Stiftung for financial support, many interesting workshops and the wonderful "Jahrestreffen" and the German National Academic Foundation for a fantastic "Sommerakademie" and many insightful workshops.

Finally, I would like to especially thank my parents, my brother Fabian, my sister Nina and Simon for their endless support, patience, encouragement and advice during the whole course of my PhD.

»Das Rätsel gibt es nicht.

Wenn sich eine Frage überhaupt stellen läßt, so kann sie auch beantwortet werden.«

Ludwig Wittgenstein

Contents

1. Introduction.....	1
1.1 Broader context.....	1
1.2 The development of MAPI as a promising solar cell material.....	2
1.2.1 Challenges on the way to commercialization	3
1.3 Structural remarks	4
1.3.1 3D hybrid perovskites.....	4
1.3.2 2D and quasi-2D hybrid perovskites	5
1.3.3 1D and 0D hybrid perovskites.....	6
1.4 Optoelectronic properties in 2D hybrid perovskites.....	6
1.4.1 Excitons in 3D and 2D hybrid perovskites.....	6
1.4.2 Photoluminescence from 2D hybrid perovskites.....	7
1.5 Applications of layered hybrid perovskites.....	9
1.5.1 Phosphors for WLED (White light-emitting diodes)	9
1.5.2 Solar cells.....	13
1.6 Objectives.....	19
1.7 References	20
2. Toward Fluorinated Spacers for MAPI-Derived Hybrid Perovskites: Synthesis, Characterization, and Phase Transitions of $(\text{FC}_2\text{H}_4\text{NH}_3)_2\text{PbCl}_4$	29
2.1 Introduction	30
2.2 Experimental Section	31
2.3 Results and Discussion	34
2.4 Conclusions	41
2.5 References	42
3. Benzimidazolium Lead Halide Perovskites: Effects of Anion Substitution and Dimensionality on the Bandgap.....	45
3.1 Introduction	46
3.2 Results and Discussion	47
3.3 Conclusions	54
3.4 Experimental Section	55
3.5 References	58
4. Completing the picture of 2-(aminomethylpyridinium) lead hybrid perovskites – Insights into structure, conductivity behavior and optical properties.....	62
4.1 Introduction.....	62
4.2 Experimental Section	64
4.3 Results and Discussion	68
4.4 Conclusions	75

4.5	References	75
5.	Summary	81
6.	Conclusions & Outlook.....	83
6.1	References	85
7.	Appendix.....	87
A	Supporting Information for Chapter 2.....	88
A.1	Crystallographic data for $(\text{FC}_2\text{H}_4\text{NH}_3)_2\text{PbCl}_4$	88
A.2	Rietveld refinement results for $(\text{FC}_2\text{H}_4\text{NH}_3)_2\text{PbCl}_4$	92
A.3	Partial density of states (PDOS) plot for $(\text{FC}_2\text{H}_4\text{NH}_3)_2\text{PbCl}_4$ and band structure of $(\text{FC}_2\text{H}_4\text{NH}_3)_2\text{PbCl}_4$	93
A.4	DSC measurements of $(\text{FC}_2\text{H}_4\text{NH}_3)_2\text{PbCl}_4$	93
A.5	Temperature-dependent PXRD investigation of $(\text{FC}_2\text{H}_4\text{NH}_3)_2\text{PbCl}_4$ illustrating the reversibility of the first phase transition	94
A.6	Photoluminescence spectra of $(\text{FC}_2\text{H}_4\text{NH}_3)_2\text{PbCl}_4$	95
A.7	Photoluminescence excitation spectra of $(\text{FC}_2\text{H}_4\text{NH}_3)_2\text{PbCl}_4$	95
A.8	Discussion of the crystal structure of $(\text{FC}_2\text{H}_4\text{NH}_3)\text{PbBr}_3 \cdot \text{DMF}$	96
A.9	Crystal structure of $(\text{FC}_2\text{H}_4\text{NH}_3)\text{PbBr}_3 \cdot \text{DMF}$	96
A.10	Crystallographic data for $(\text{FC}_2\text{H}_4\text{NH}_3)\text{PbBr}_3 \cdot \text{DMF}$	97
A.11	Rietveld analysis for $(\text{FC}_2\text{H}_4\text{NH}_3)\text{PbBr}_3 \cdot \text{DMF}$	101
A.12	Characterization of $(\text{FC}_2\text{H}_4\text{NH}_3)\text{PbBr}_3 \cdot \text{DMF}$	102
A.13	References.....	102
B	Supporting Information for Chapter 3.....	103
B.1	Crystallographic data for $(\text{C}_7\text{H}_7\text{N}_2)_2\text{PbCl}_4$, $(\text{C}_7\text{H}_7\text{N}_2)_2\text{PbBr}_4$ and $(\text{C}_7\text{H}_7\text{N}_2)_2\text{PbI}_4$	103
B.2	Crystallographic data for $(\text{C}_7\text{H}_7\text{N}_2)\text{PbI}_3$	115
B.3	Rietveld refinement results	119
B.4	Photograph of $\text{BzImPbI}_4/3$	125
B.5	EDX analysis.....	126
B.6	Solid-state NMR spectroscopy – Assignment of chemical shifts	128
B.7	Absorption measurements.....	129
B.8	Thermal analysis	130
B.9	References.....	130
C	Supporting Information for Chapter 4.....	131
C.1	Crystallographic data for $(\text{C}_6\text{H}_{10}\text{N}_2)_6\text{IPb}_5\text{I}_{21} \cdot 3 \text{H}_2\text{O}$ at 296 K and 100 K.....	131
C.2	Crystallographic data for $(\text{C}_6\text{H}_{10}\text{N}_2)\text{PbCl}_4$, $(\text{C}_6\text{H}_{10}\text{N}_2)\text{PbBr}_4$ and $(\text{C}_6\text{H}_{10}\text{N}_2)\text{PbI}_4$ at 296 K.....	147
C.3	Crystallographic data for $(\text{C}_6\text{H}_{10}\text{N}_2)\text{PbCl}_4$, $(\text{C}_6\text{H}_{10}\text{N}_2)\text{PbBr}_4$ and $(\text{C}_6\text{H}_{10}\text{N}_2)\text{PbI}_4$ at 100 K and 153 K, respectively.....	157
C.4	Hydrogen bonds in $(\text{C}_6\text{H}_{10}\text{N}_2)_6\text{IPb}_5\text{I}_{21} \cdot 3 \text{H}_2\text{O}$ and $(\text{C}_6\text{H}_{10}\text{N}_2)\text{PbI}_4$ at 296 K.....	174
C.5	Disorder in $(\text{C}_6\text{H}_{10}\text{N}_2)\text{PbBr}_4$ at 100 K.....	175

C.6	Temperature-dependent phase transition in $(\text{C}_6\text{H}_{10}\text{N}_2)\text{PbCl}_4$	176
C.7	Octahedral distortion in $(\text{C}_6\text{H}_{10}\text{N}_2)\text{PbX}_4$ ($X = \text{Cl}, \text{Br}$ and I) and $(\text{C}_6\text{H}_{10}\text{N}_2)_6\text{IPb}_5\text{I}_{21} \cdot 3 \text{H}_2\text{O}$	177
C.8	Rietveld refinement results	177
C.9	Thermal analysis.....	183
C.10	Solid-state NMR spectroscopy.....	183
C.11	Optical measurements	189
C.12	Band structure calculations.....	191
C.13	References.....	192
D	List of publications within this thesis and author contributions.....	193
E	CCDC deposition numbers	195
F	List of presentations.....	196
	Oral presentations.....	196
	Poster presentations	196
G	Abbreviations.....	197

1. Introduction

1.1 Broader context

In light of the world's increasing energy consumption and the limited resources of fossil fuels, new clean and low-cost solutions for the production of renewable energy are high in demand. The sun is the largest energy resource at disposal for humankind and only a small percentage of its potential is being exploited nowadays. According to the "Global Energy Assessment" conducted by the International Institute for Applied Systems Analysis in 2012, the technical potential of solar energy exceeds the current and future worldwide energy needs.¹ A direct conversion of solar energy to electrical energy is achieved by the use of photovoltaic systems. Several kinds of solar cells have been developed so far among which crystalline silicon solar cells ($\eta = 26.7\%$) and several thin-film solar cells consisting of amorphous silicon ($\eta = 10.5\%$), GaAs ($\eta = 28.8\%$), CdTe ($\eta = 21.0\%$) and copper indium gallium selenide (CIGS) ($\eta = 21.7\%$), respectively, are commercially available nowadays.² Certified record efficiencies for the respective single-junction terrestrial cells and submodules are given in brackets.² While the largest market shares, still, by far are held by silicon solar cells,³ the thin-film technologies are on the rise by increasing the efficiencies and keeping the manufacturing costs low.² In addition, research is focusing on several other approaches including organic cells and dye-sensitized solar cells (DSSC), which are still in a developmental stage.⁴⁻⁵

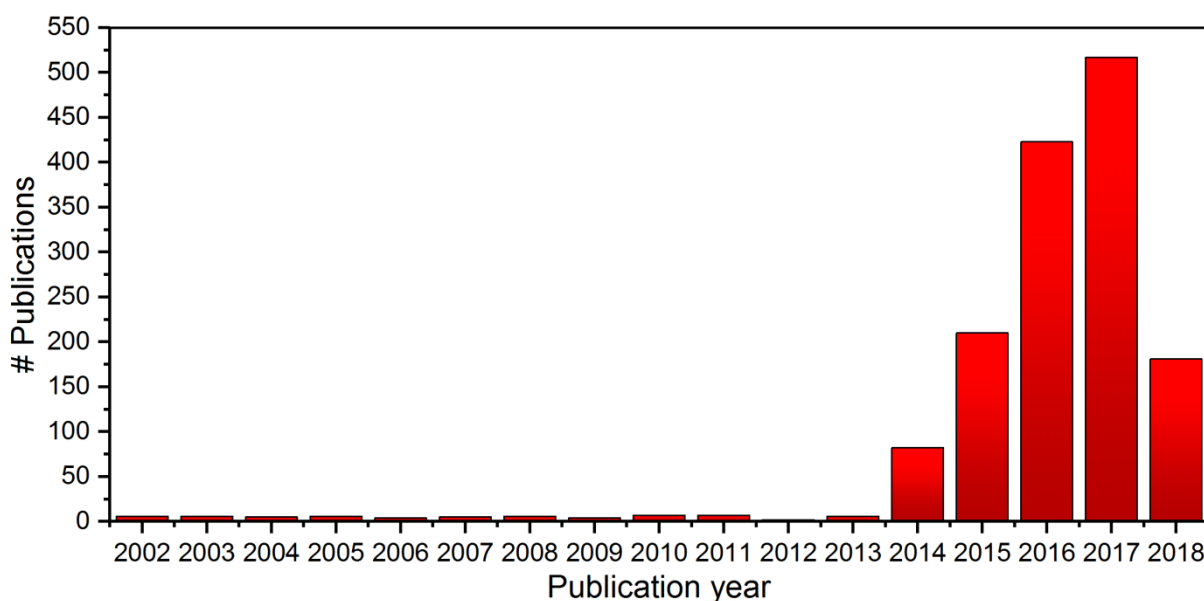


Figure 1.1. The number of publications on hybrid perovskites per year. Analysis is based on a search on the topic "hybrid perovskite" in the database SciFinder on 12/04/2018.

In 2009 a new contender came into the spotlight.⁶ Methylammonium lead iodide, $(\text{CH}_3\text{NH}_3)\text{PbI}_3$, (hereafter MAPI) belongs to the compound class of hybrid perovskites (see section 1.3.1). Its intriguing optoelectronic properties including ambipolar charge transport,⁷ long diffusion lengths,⁸⁻⁹ a high absorption coefficient¹⁰ and a medium bandgap of 1.6 eV¹¹ combined with a low-cost solution-based synthesis makes this semiconductor an excellent candidate for solar cell materials.¹²

1.2 The development of MAPI as a promising solar cell material

The synthesis of $(\text{CH}_3\text{NH}_3)\text{PbX}_3$ ($X = \text{Cl}, \text{Br}$ and I) was reported by D. Weber in 1978 for the first time. He also discovered the miscibility of methylammonium lead halides featuring adjacent halides in the periodic table,¹³ which became important later on when fine-tuning the bandgap. Research by Mitzi et al. paved the way for the rediscovery of this material. They investigated a tin based family of hybrid perovskites, namely $(\text{C}_4\text{H}_9\text{NH}_3)_2(\text{CH}_3\text{NH}_3)_{n-1}\text{Sn}_n\text{I}_{3n+1}$, where n is the number of perovskite sheets in the inorganic layer. The compound exhibits a structure related to the inorganic Ruddlesden-Popper phases where two butylammonium ions separate the blocks of $(\text{CH}_3\text{NH}_3)_{n-1}\text{Sn}_n\text{I}_{3n+1}$ perovskite layers (see section 1.3.2). When n is increased and with it the thickness of the perovskite blocks, a transition from a semiconducting to a metallic behavior is observed. Hence, variation of n opens up the possibility to tune the electronic properties.¹⁴

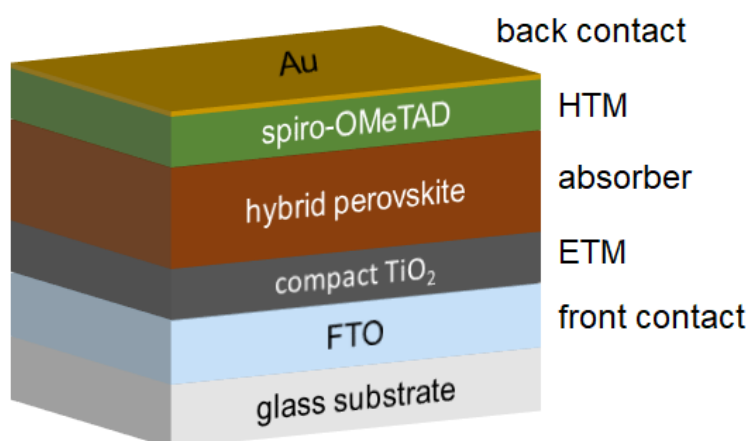


Figure 1.2. Schematic representation of a planar hybrid perovskite solar cell (HTM = hole transporting material, ETM = electron transporting material).

In 2009 Kojima and coworkers employed $(\text{CH}_3\text{NH}_3)\text{PbI}_3$ and $(\text{CH}_3\text{NH}_3)\text{PbBr}_3$ instead of the otherwise applied dye as an absorber material in a DSSC structure: The $(\text{CH}_3\text{NH}_3)\text{PbX}_3$ ($X = \text{Br}, \text{I}$) nanoparticles were deposited on a mesoporous TiO_2 film to form the anode. The solar cell was completed by a Pt-coated FTO (fluorine doped tin oxide) glass serving as the cathode and a liquid organic electrolyte. Although the power conversion efficiencies (PCE, η) were still rather low

showing values of 3.81% and 3.13%, high open-circuit voltages of 0.61 V and 0.96 V could be measured for the iodide and the bromide, respectively.⁶ However, the largest pitfall of this system is its poor stability attributable to the dissolution of the hybrid perovskite nanocrystals by the liquid electrolyte.¹⁵ A decisive change in the solar cell architecture to overcome this issue was implemented by Kim et al. and Lee et al. simultaneously in 2012. They replaced the liquid electrolyte by a solid hole-transporting material, namely spiro-OMeTAD, and reached efficiencies of 9.7% and 7.6%, respectively, besides promising long-term stability (Figure 1.2).¹⁶⁻¹⁷ Moreover, the ambipolar character of MAPI was demonstrated by two experiments: The Snaith group replaced the electron-conductor TiO₂ by the insulator Al₂O₃ and still measured an efficiency of 10.9 %, which proves that MAPI itself is able to act as an electron conductor.¹⁷ The Grätzel group designed a hole-conductor free solar cell only containing TiO₂ and MAPI as the active components and reached an efficiency of 5.5 %. From this it follows that MAPI also assumes the role as a hole conductor.¹⁸ The picture of a highly promising solar cell material is completed by panchromatic light absorption¹⁹ with an absorption onset at 800 nm,²⁰ large absorption coefficients in the order of 10⁵ cm⁻¹²¹ and long charge carrier diffusion lengths of at least 100 nm in the triiodide.⁸ A steep rise in efficiency within less than a decade came along with an enormous boost of the field of hybrid perovskites (Figure 1.1.). Improvements in device architecture and deposition techniques led to record efficiencies above 22%.²²⁻²³

1.2.1 Challenges on the way to commercialization

Besides consistently raising the PCE of hybrid perovskite solar cells to new levels, research still has to tackle a few challenges on the way to commercialize hybrid perovskite solar cells: These include (1) MAPI's inherent instability toward humidity, light, heat and oxygen²⁴⁻²⁵ and (2) the toxicity of lead.²⁶⁻²⁸ The hazards of lead exposure can be reduced to a minimum by a thorough and effective encapsulation of perovskite solar cells following the protocol for commercial solar panels.²⁹ In addition, recycling strategies have been developed to regain all major components in a step-by-step dismantling process. Subsequently, it was shown that the expensive FTO substrates which serve as front electrodes and the toxic PbI₂ can be reused for the production of new efficient solar cells. Hence, these protocols help to conserve resources, to lower material cost and to reduce health hazards by avoiding the production of Pb-containing waste.³⁰⁻³² Life cycle assessments (LCA) are currently performed to capture all relevant environmental impacts connected to the use of perovskite solar cells.³³⁻³⁶

Many studies are conducted to understand the mechanisms underlying the degradation of MAPI and to find approaches to solve this problem. The most relevant threat is thought to be the exposure to moisture.²⁵ In a first step, the compound is hydrated which is still partially reversible.³⁷ In a subsequent step, a complete degradation to PbI₂, methylamine and hydroiodic acid can be observed.³⁸ A leakproof encapsulation of the whole device is a first handle to prevent

the contact with humidity.³⁹ In addition, advancements in the device setup including the insertion of protecting layers^{38, 40}, the use of more stable charge transport layers⁴¹⁻⁴² and the modification of the device architecture⁴³⁻⁴⁴ are explored. Another important tool is perovskite material engineering by complete or partial substitution of the methylammonium cation by formamidinium and Cs⁺ and of the iodide anion by Br⁻ and I⁻, respectively.^{24, 45} This process does not only affect the stability of the resulting compound but also the optoelectronic properties including the size of the bandgap.⁴⁶ Finally, quasi two-dimensional systems along the lines of Mitzi's (C₄H₉NH₃)₂(CH₃NH₃)_{n-1}Sn_nI_{3n+1} hybrid perovskite series and 2D hybrid perovskites are under investigation, since they show an intrinsic higher stability than their 3D relatives.⁴⁷ Another factor promoting the degradation of MAPI to PbI₂ is the diffusion of ions during illumination.⁴⁸⁻⁴⁹ A study by Lin et al. showing that ion migration was suppressed in the layered hybrid perovskite (C₄H₉NH₃)₂(CH₃NH₃)₃Pb₄I₁₃ awakened hope that low-dimensional systems might hold great promise as stable active constituents in optoelectronics⁵⁰ which is drawing additional attention to these compounds (see section 4). Besides, ion migration is assumed to be the main cause of the anomalous hysteresis in current-voltage curves recorded for solar cells based on MAPI and related systems.⁵¹⁻⁵² Further possible explanations include MAPI's ferroelectric properties⁵³ and charge trapping and detrapping processes.⁵⁴

1.3 Structural remarks

1.3.1 3D hybrid perovskites

Three-dimensional (3D) hybrid perovskites feature the ABX₃ perovskite structure, whereby the A site is occupied by a small organic cation which is mostly methylammonium (CH₃NH₃⁺) or formamidinium (CH(NH₂)₂⁺). The metal cations located at the B site, typically Sn²⁺ or Pb²⁺, and the halides at the X site, usually Cl⁻, Br⁻ or I⁻, form a corner-sharing metal-halide-octahedra network, whose voids enclose the organic molecules (Figure 1.3). It is crucial that the size of the organic cations does not exceed the space offered by the network. Otherwise, the formation of low-dimensional hybrid perovskites is triggered. Goldschmidt's tolerance factor t provides a good indication if a 3D structure can be expected. The equation to determine t relates the radii r of the constituents A, B, and X:⁵⁵

$$t = (r_A + r_X) / \sqrt{2}(r_B + r_X) \quad (1)$$

It was empirically found that cubic perovskite structures most likely form when t is in the range of 0.9–1.0, whereas values from 0.80 to 0.89 can be found for distorted perovskites.⁵⁶ The tolerance factor t is an important guideline when choosing combinations of metals, halides and organic cations to design new 3D hybrid perovskites. Kieslich et al. have predicted the existence of several undiscovered 3D hybrid perovskites on the basis of equation (1) and the calculation of the effective radii of a variety of relevant ions including all halides, Sn²⁺, Pb²⁺ and a collection of

small protonated amines.⁵⁶⁻⁵⁷ These studies are helpful to initiate and to guide experimental work. The introduction of Chapter 3 revisits this topic in regard to the synthesis and structure of 2-fluoroethylammonium lead chloride.

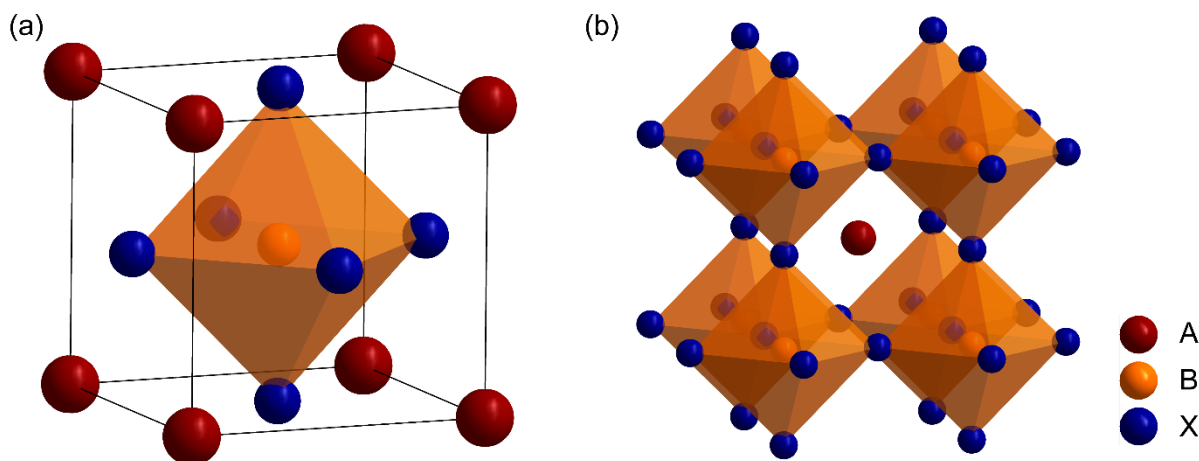


Figure 1.3. (a) Unit cell of the basic ABX_3 perovskite structure and (b) representation of the extended corner connected network of metal-halide octahedra.

1.3.2 2D and quasi-2D hybrid perovskites

If the organic cation is too large to fit inside the cavities of the metal halide octahedra network, low-dimensional structures form. When selecting organic cations for the synthesis of hybrid perovskites, the interactions prevailing in this compound class have to be considered: They comprise, arranged in descending order of strength, ionic interactions between the negatively charged inorganic lattice and the positively charged organic lattice, hydrogen bonds between the protonated terminal organic cation groups and halides of the MX_6^{4-} octahedra and also van der Waals interactions among the organic molecules. Hence, the organic molecules need to exhibit one or more terminal groups which can be protonated and act as proton donors. Typically, the cations are doubly protonated at maximum. Therefore, the general formulas $A^{2+}M^{2+}X_4$ and $A_2^+M^{2+}X_4$ (A = organic cation, M = metal cation, X = halide) are found for 2D hybrid perovskites.⁵⁸ Their structure is derived by slicing the cubic lattice of their 3D congeners along specific crystallographic planes and separating these single metal halide octahedra layers by the organic entities. Increasing the number n of (001) inorganic layers leads to so-called quasi-2D dimensional perovskites, namely $A'_2A_{(n-1)}M_nX_{(3n+1)}$ (Figure 1.4).⁵⁹ Their synthesis requires small organic cations (*perovskitizer*, A) which fit in the cavities of the metal halide octahedra network to form the 3D perovskite structure besides large aliphatic or aromatic cations (*spacer*, A') sitting between the quasi-3D perovskite blocks.⁶⁰ (001) hybrid perovskites are most common in literature and are structurally related to the inorganic Ruddlesden-Popper phases, $A'_2A_{(n-1)}M_nO_{(3n+1)}$. Here, A' and the excess O atom are arranged in a rock-salt type structure between blocks of n perovskite layers.⁶¹

In addition, (110) hybrid perovskites are investigated which feature corrugated inorganic layers instead of flat sheets being found for (001) perovskites (Figure 1.7).^{59, 62}

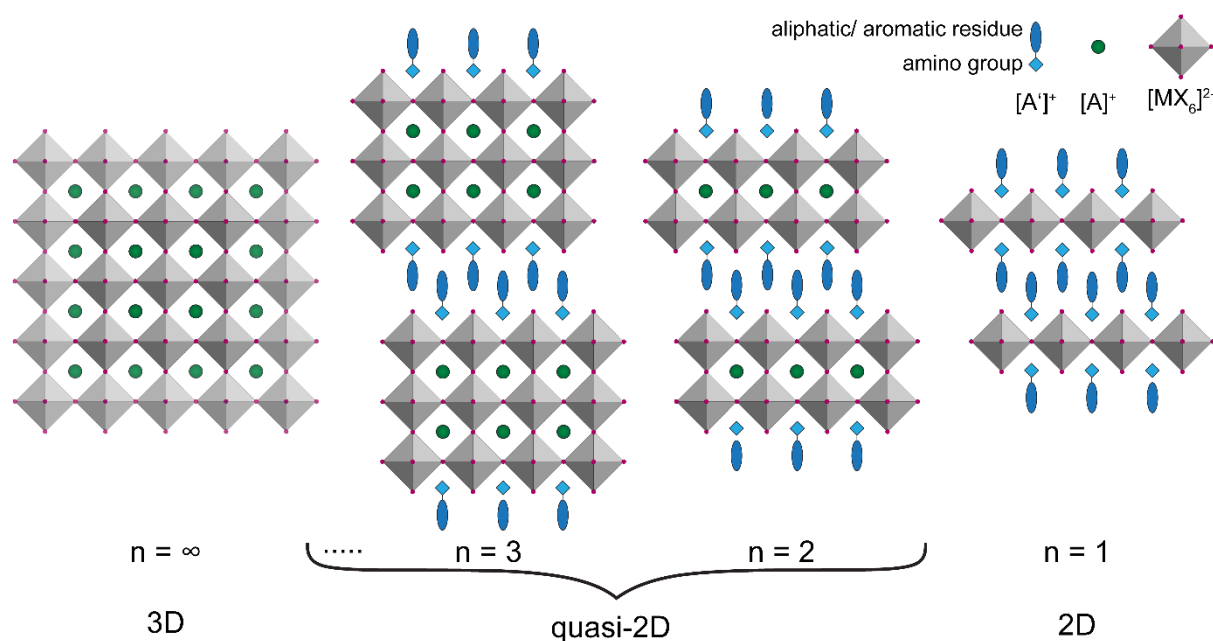


Figure 1.4. Schematic representation of the (100) oriented layered hybrid perovskite series $A'_2A_{(n-1)}M_nX_{(3n+1)}$ ($n = \text{integer}$) showing the connection between 3D ($n = \infty$), quasi-2D ($n > 1$) and 2D ($n = 1$) hybrid perovskites.

1.3.3 1D and 0D hybrid perovskites

For completeness, it is mentioned that the family of hybrid perovskites also contains 1D and 0D systems which can be derived by further dissecting the 3D cubic lattice. 1D hybrid perovskites feature chains of corner-sharing metal halide octahedra which are surrounded by organic cations,⁶³ while 0D systems exhibit isolated metal halide octahedra.^{59, 64}

1.4 Optoelectronic properties in 2D hybrid perovskites

1.4.1 Excitons in 3D and 2D hybrid perovskites

The term exciton refers to strongly bound electron-hole pairs which can form upon excitation of an electron in the ground-state (GS). Due to the Coulombic interaction between the excited electron and the hole which is generated at the same time in the valence band, these charge carriers can be bound to each other.⁶⁵⁻⁶⁶ The magnitude of attraction between electron and hole is reflected in the exciton binding energy, E_b , which energetically stabilizes excitons compared to free carriers as shown in Figure 1.5a.⁶⁷ Consequently, free carriers are only generated when the thermal energy k_bT which is 25.7 meV at 298 K, exceeds E_b .⁶⁷ While 3D hybrid perovskites stand out due to their small exciton binding energies in the range of 2 – 20 meV, leading to a dissociation

of excitons into free carriers at room temperature,^{11, 68} 2D hybrid perovskites exhibit exciton binding energies in the order of a few hundred meV.⁶⁹⁻⁷² This pronounced difference in electronic properties can be ascribed to the incorporation of organic layers dissecting the inorganic lattice when moving from 3D to 2D. As a result, a multiple-quantum-well structure emerges in which the insulating organic sheets can be considered as potential “barriers” and the semiconducting metal-halide-sheets as potential “wells”.⁷³ Consequently, excitons are confined to the two-dimensional inorganic layers leading to a 4-fold increase in E_b .⁷⁴ However, the very large E_b can only be explained as a synergetic effect of quantum and dielectric confinement - the organic layer exhibiting a low dielectric constant does not provide sufficient shielding to prevent the attraction of holes and electrons giving rise to a further enhancement of E_b .⁷⁵⁻⁷⁶ These distinct difference in E_b for 3D and 2D hybrid perovskites gives rise to their suitability for diverging fields, i.e. photovoltaics and solid-state lighting, respectively.

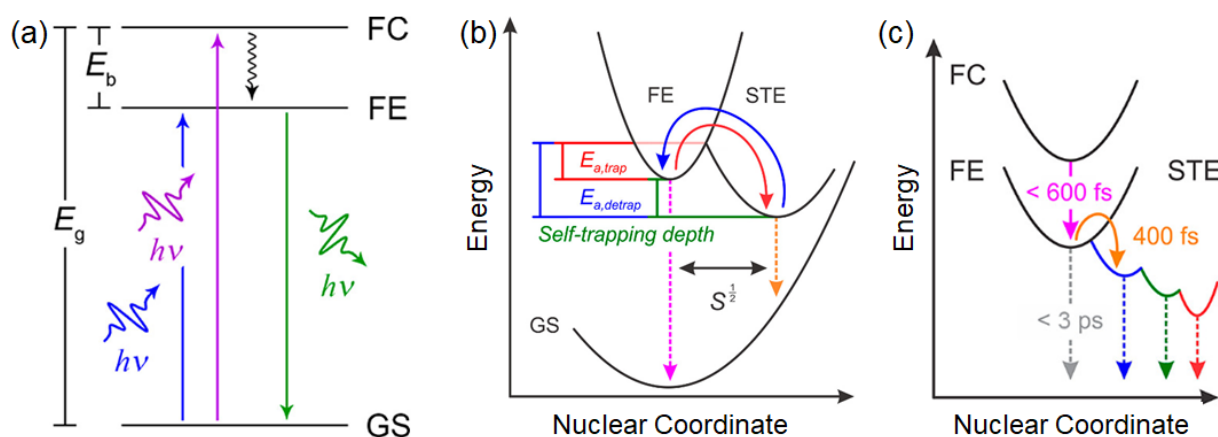


Figure 1.5. (a) Energy level diagram (b,c) and nuclear coordinate diagrams demonstrating the charge carrier dynamics and the corresponding radiative decay channels in 2D hybrid perovskites. (a) Free carrier and free exciton formation upon absorption (blue, purple arrows). The nonradiative relaxation is depicted with a black arrow and FE photoluminescence is indicated with a green arrow. (b) Transition between STE and FE states. STE and FE photoluminescence are indicated by dashed orange and purple arrows, respectively. (c) Carrier dynamics leading to self-trapping in a distribution of self-trapped excitonic states. Abbreviations: FC = free carriers, FE = free exciton state, GS = ground state, E_b = exciton binding energy, E_g = bandgap energy, STE = self-trapped exciton state, $E_{a,trap}$ = activation energy for self-trapping, $E_{a,detrap}$ = activation energy for detrapping, S = Huang-Rhys parameter.⁷⁷ (a) was reprinted with permission from ref 77. Copyright 2018 American Chemical Society. (b) was adapted from ref 78 with permission of The Royal Chemical Society. (c) was adapted with permission from ref 79. Copyright 2016 American Chemical Society.

1.4.2 Photoluminescence from 2D hybrid perovskites

The majority of (001) hybrid perovskites shows a sharp PL emission peak with small Stokes shift upon UV excitation at room temperature, which is attributed to the radiative decay of free excitons.^{59, 80-81} Yet, broadband white-light emission together with a large Stokes shift has also

been observed for a to date small group of layered hybrid perovskites.⁶⁷ On the way to unveil the origin of the observed broad emission, PL spectra of white-light emitting hybrid perovskites in various forms of appearance including ball-milled powders, single crystals and pellets were recorded. The negligible differences between the individual spectra were indicative of an intrinsic nature of the broad emission feature.^{62, 82-84} In addition, permanent defects were excluded by demonstrating a linear correlation between PL intensity and excitation power density⁸² - if permanent trap states were the major source of the broad emission feature, PL saturation would be expected upon populating the limited number of defects at high excitation powers, which is in contrast to the observed behavior.⁸⁵⁻⁸⁶

The mechanism inducing the emission of broadband white-light was finally elucidated using ultrafast spectroscopic measurements,⁷⁹ which confirmed the initial hypothesis by the Karunadasa group conjecturing that the emission was due to exciton self-trapping.⁶² The term self-trapped excitons (STEs) describes strictly transient excited-state defects arising from strong exciton-lattice coupling.^{67, 77, 87} STEs only form when the elastic lattice deformations which emerge upon trapping energetically stabilize the excitons. The broad emission is finally a result of an energetic distribution of these trap states⁷⁹ and the distortion of the self-trapped state with respect to the ground state which is defined by the Huang-Rhys parameter S .⁶⁷ The large Stokes shift observed for white-light emitting hybrid perovskites is the result of the self-trapping depth describing the energetic stabilization of STEs compared to FEs and S (Figure 1.5b).⁶⁷

Hu et al. gained insights into charge carrier dynamics directly following photoexcitation in the white-light emitting hybrid perovskite (N -MEDA) $PbBr_4$ (N -MEDA = N^1 -methylethane-1,2-diammonium) by a combination of ultrafast excited-state spectroscopies. Terahertz spectroscopy ($\lambda_{\text{excitation}} = 266$ nm) revealed the generation of free carriers within ~ 600 fs which leave the conduction band immediately. These measurements also testified the high exciton binding energies found for (N -MEDA) $PbBr_4$, since free carrier formation did not occur at the higher excitation wavelength 387 nm. To further elucidate the dynamics following the removal of free carriers from the conduction band, transient absorption (TA) spectroscopy was applied. Instead of permanent defects causing the broadband emission, new transient states were detected within 400 fs after the first photoexcitation, speaking of a negligible potential barrier between FE and STE states. The comparison of TA traces from a free excitonic emitter to the TA spectra of the broadband emitter (N -MEDA) $PbBr_4$ substantiated that the transient states emerging upon photoexcitation are STE states (Figure 1.5c).⁷⁹

Temperature-dependent photoluminescence measurements strongly suggest that self-trapped and free excitonic states are connected by a thermal equilibrium including the coexistence of STEs and FEs.⁸⁸ The transformation between these states is linked to the activation energies $E_{a,\text{trap}}$ and $E_{a,\text{detrap}}$ for the trapping and the detrapping process, respectively (Figure 1.5b). Thus, it has been

observed that broad emission features appear or gain in intensity at the expense of narrow PL emission upon cooling 2D hybrid perovskites to low temperatures^{71, 88-89} - Upon decreasing the thermal energy the number of self-trapped excitons which can overcome the potential barrier to the free excitonic states diminishes. However, if the thermal energy drops below $E_{a,trap}$, excitons are not able to transition to the self-trapped excitonic states anymore and the narrow PL intensity will increase again.⁷⁸

1.5 Applications of layered hybrid perovskites

1.5.1 Phosphors for WLED (White light-emitting diodes)

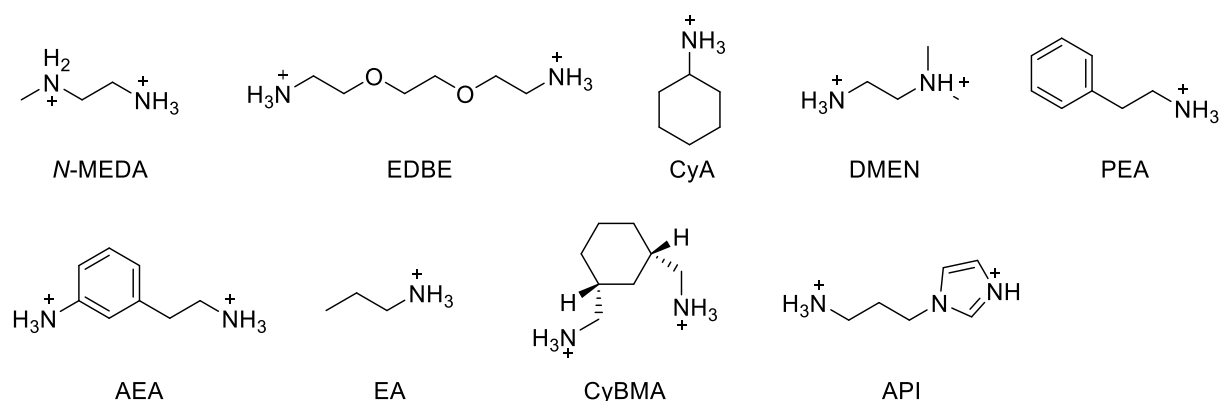


Figure 1.6. Structures of aliphatic and aromatic cations which are part of the white-light emitting layered hybrid perovskites presented in this section. The abbreviations used in this thesis are included.

The generation of white light using light-emitting diodes (LEDs) is currently achieved by two major strategies. Firstly, green, red and blue LEDs are assembled to obtain a white color impression in total. However, these red-green-blue (RGB) LEDs suffer from a poor color rendering index (CRI), which quantifies the light source's ability to accurately reproduce illuminated colors with respect to a blackbody light source serving as a reference. In addition, color changes were observed due to different ageing times of the single LEDs. Secondly, a single yellow phosphor or multiple phosphors are combined with blue or ultraviolet (UV) LEDs to convert their radiation to white light. The number of phosphors used for these phosphor-converted LEDs (pc-LEDs) is a trade-off between high efficiency and high CRI values. The white-color rendition is improved for multiple-phosphor approaches at the cost of a decreased efficiency due to self-absorption effects.⁹⁰⁻⁹³ Therefore, a single-source phosphor emitting continuously through the whole visible spectrum is highly desirable.⁶²

White light emission from layered hybrid perovskites is at the center of attention since Dohner et al. reported the 2D hybrid perovskites (N-MEDA)PbBr₄ (N-MEDA = N¹-methylethane-1,2-diammonium) and (EDBE)PbX₄ (EDBE = 2,2'-(ethylenedioxy)bis(ethylammonium)) (X = Br, Cl) (Figure 1.7a,b) featuring broadband emission in the visible spectrum upon near-UV excitation.

They also demonstrated that the chromaticity of the emitted light can be easily tuned from “warm” white light for $(N\text{-MEDA})\text{PbBr}_4$ and $(\text{EDBE})\text{PbBr}_4$ to “cold” white light for $((N\text{-MEDA})\text{PbBr}_{3.5}\text{Cl}_{0.5})$ and $(\text{EDBE})\text{PbCl}_4$ by halide substitution.^{62,82} The influence of the halide composition is also clearly shown with the layered hybrid perovskite series $(\text{EA})_2(\text{EA})_2\text{Pb}_3\text{Br}_{10-x}\text{Cl}_x$ ($x = 0, 2, 4, 6, 8, 9.5, 10$) (EA = ethylammonium) which covers a broad range of various white-light color impressions. In contrast to the other layered white-light emitting hybrid perovskites which feature single inorganic perovskite layers ($n = 1$), this series is a multi-layered system with $n = 3$ where the ethylammonium cation has the role of the *spacer* and the *perovskitizer*.⁹⁴

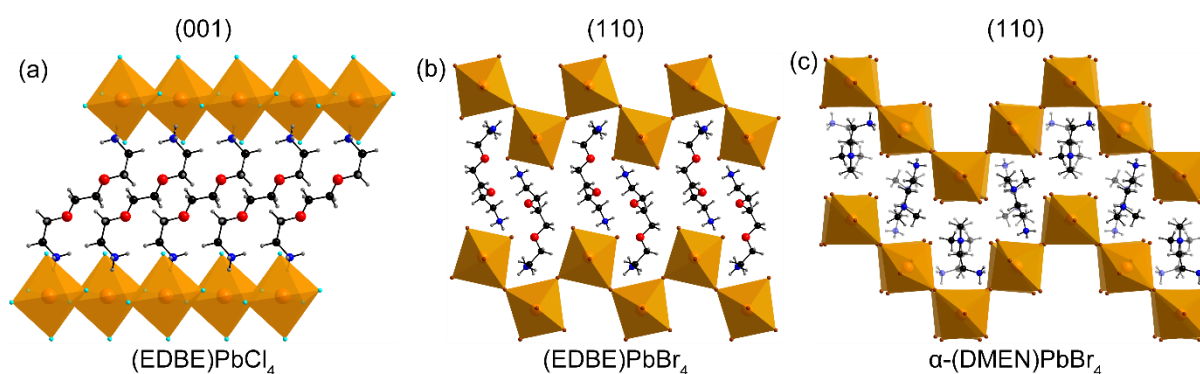


Figure 1.7. Crystal structures of the (001) hybrid perovskite $(\text{EDBE})\text{PbCl}_4$ ⁸² and the (110) hybrid perovskites $(\text{EDBE})\text{PbBr}_4$ ⁸² and $\alpha\text{-(DMEN)PbBr}_4$ ⁹⁵ showing the diversity of white-light emitting compounds. C is displayed in black, N is blue, O is red, H is grey, Pb is orange, Cl is turquoise and Br is brown.

The overview of all organic cations (Figure 1.6) used for white-light emitting layered hybrid perovskites so far shows clearly that this compound class has the potential to reproduce all shades of white light. The advantages of hybrid perovskites do not only comprise their versatility which manifests in the tunability of their structural and optical properties by changing the organic *spacer* cation, the metal cation, the halide anion and the inorganic layer thickness n . They also include easy and low-cost processing enclosing uniform film formation, which is highly desirable for commercial phosphors, since they need to be coated on LEDs. The satisfying quality of the white-light emitted by layered hybrid perovskites is reflected by CRI values above 80 for the vast majority of the reported compounds which is required for general lighting (Figure 1.8).⁹¹ Recently, Wu et al. reported a record CRI value of 93 for $(\text{API})\text{PbCl}_4$ (API = $N\text{-(3-aminopropyl)imidazolium}$).⁸⁴ However, photoluminescence quantum efficiencies (PLQE) at room temperature are still far from competitive. The highest PLQE was measured for $(\text{EDBE})\text{PbBr}_4$ to be 9%,⁸² whereby this is rather exceptional considering that the other reported white-light emitting hybrid perovskites feature efficiencies below 2%.⁷⁷ Several groups showed that the PLQE increases with decreasing temperature^{71, 89} reaching efficiencies as high as 85% at 105 K in the case of $(\text{EDBE})\text{PbBr}_4$.⁸² Thirumal et al. investigated this phenomenon using the example of

(PEA)₂PbCl₄ and traced it back to two processes by determining their activation energies (E_a): (1) a bound exciton detrapping process ($E_a = 12 \pm 1 \text{ meV} \cong 140 \text{ K}$) and (2) a decreased level of nonradiative recombination due to less phonon absorption ($E_a = 120 \pm 10 \text{ meV}$). (1) At temperatures below 140 K the thermal energy is not sufficient anymore to enable the conversion process from bound to free excitons which increases the broad PL stemming from bound excitons (Figure 1.5b). (2) At lower temperatures radiative channels gain in importance leading to higher PL intensity.⁸³ For phosphors to be commercially relevant, a long lifetime is also crucial. (EDBE)PbBr₄ showed no signs of degradation after 3 months of constant illumination under vacuum which indicates that layered hybrid perovskites may fulfill the requirement of photostability.⁸²

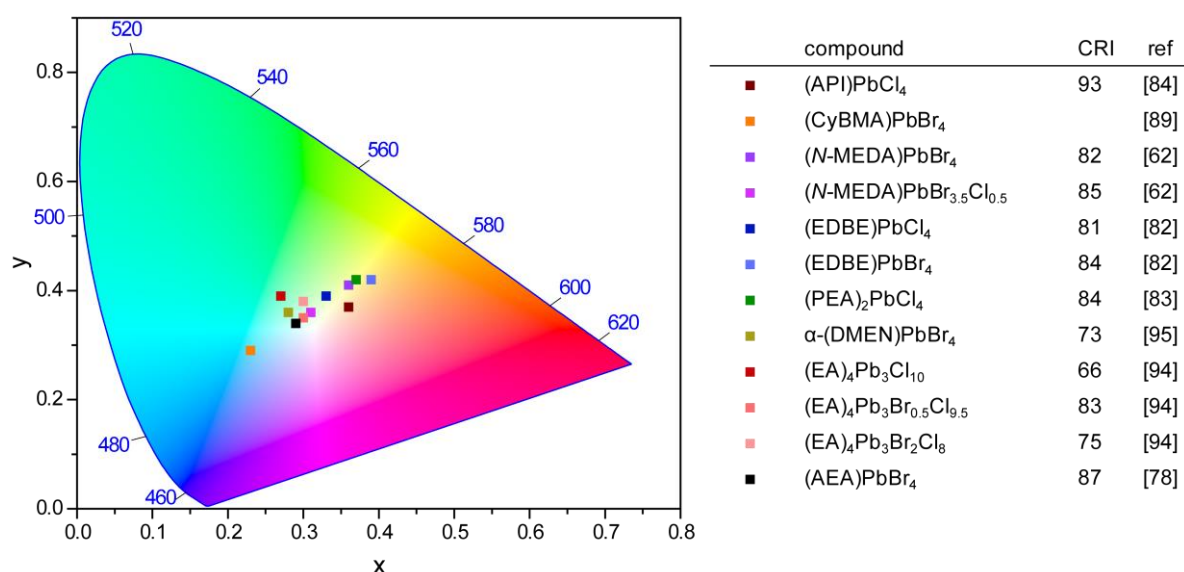


Figure 1.8. Chromaticity coordinates and CRI values of the reported 2D white-light emitting hybrid perovskites in a CIE 1931 color space chromaticity diagram. (CyA)₂PbBr₄ is not displayed in this overview, since Yangui et al.⁸⁹ provided neither CIE coordinates nor a CRI value. The chromaticity diagram template was acquired from OriginLab Technical Support.

1.5.1.1 Design Principles

After discovering the first examples of broadband white-light emitting hybrid perovskites, attempts were made to derive design principles to systematically search for new representatives with improved optical properties. In this regard, Mao et al. investigated a series of Pb-Br hybrid perovskites based on *N*¹,*N*¹-dimethylethane-1,2-diaminium (DMEN), *N*¹,*N*¹-dimethylpropane-1,3-diaminium (DMAPA) and *N*¹,*N*¹-dimethylbutane-1,4-diaminium (DMABA), which vary in the length of the ammoniumalkyl chain. While the thermodynamically stable α -(DMEN)PbBr₄ exhibits corrugated (110)-oriented layers, (DMAPA)PbBr₄ and (DMABA)PbBr₄ are (001) hybrid perovskites. To quantify the relative octahedral distortion Δd present in these compounds, the

following equation was used, which considers the individual Pb-halide distances d_n and the arithmetic mean of these individual distances d :⁹⁶

$$\Delta d = \frac{1}{6} \sum \left[\frac{d_n - d}{d} \right]^2 \quad (2)$$

As a result, a correlation between the experimentally observed width of the PL emission together with the length of PL lifetime and the extent of distortion could be derived. Consequently, α -(DMEN)PbBr₄, which has the largest octahedral distortion, shows the broadest PL emission and the longest PL lifetimes in this series.⁹⁵

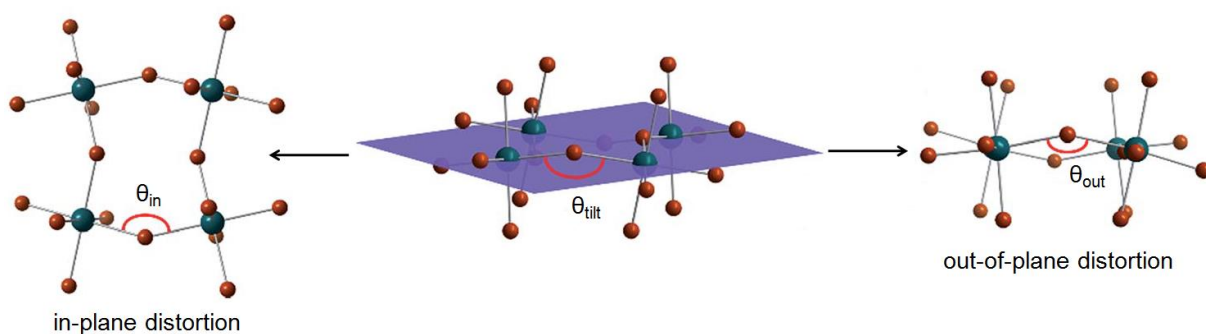


Figure 1.9. Illustration of the in-plane projection θ_{in} and out-of-plane projection θ_{out} of the Pb-(μ -Br)-Pb angle θ_{tilt} in a single corner-sharing lead bromide octahedra layer. On the basis of this separation the in-plane distortion D_{in} is defined as $D_{in} = 180^\circ - \theta_{in}$ and the out of-plane distortion D_{out} as $D_{out} = 180^\circ - \theta_{out}$. Adapted from ref 78 with permission from The Royal Society of Chemistry.

Smith et al. focused on a selection of nine (001) Pb-Br hybrid perovskites and searched for correlations between structural parameters of the inorganic lattice and the breadth of PL emission. The only unambiguous relationship was found for the out-of-plane distortion D_{out} in respect to the inorganic plane which is defined by the out-of-plane projection (θ_{out}) of the average Pb-(μ -Br)-Pb angle θ_{tilt} (Figure 1.9):

$$D_{out} = 180^\circ - \theta_{out} \quad (3)$$

Since the PL emission of (001) hybrid perovskites consists of narrow emission (NE) and broadband emission (BE) features in most cases, Smith et al. chose the ratio of their integrated intensities ($I_{BE} \cdot I_{NE}^{-1}$) as a measure for the presence of broad emission. They demonstrated a linear correlation between D_{out} and $\ln(I_{BE} \cdot I_{NE}^{-1})$. The hybrid perovskite exhibiting the largest out-of-plane distortion in their investigation, namely (AEA)PbBr₄ (AEA = 3-(2-ammonioethyl)anilinium)), finally shows white light emission. However, it is also noted that the (001) hybrid perovskite (CyA)PbBr₄ (CyA = cyclohexylammonium), which does not feature any out-of-plane distortion, was reported to emit white-light anyhow.⁸⁹ While Smith et al. only chose compounds with

centrosymmetric space groups, (CyA)PbBr₄ is a polar material which can show enhanced electron-phonon coupling influencing broad emission. It is speculated that this might be the reason for the deviating behavior of (CyA)PbBr₄.⁷⁸

The approaches by Mao et al. and Smith et al. provide helpful strategies for the targeted synthesis of future broadband white-light emitting hybrid perovskites.

1.5.2 Solar cells

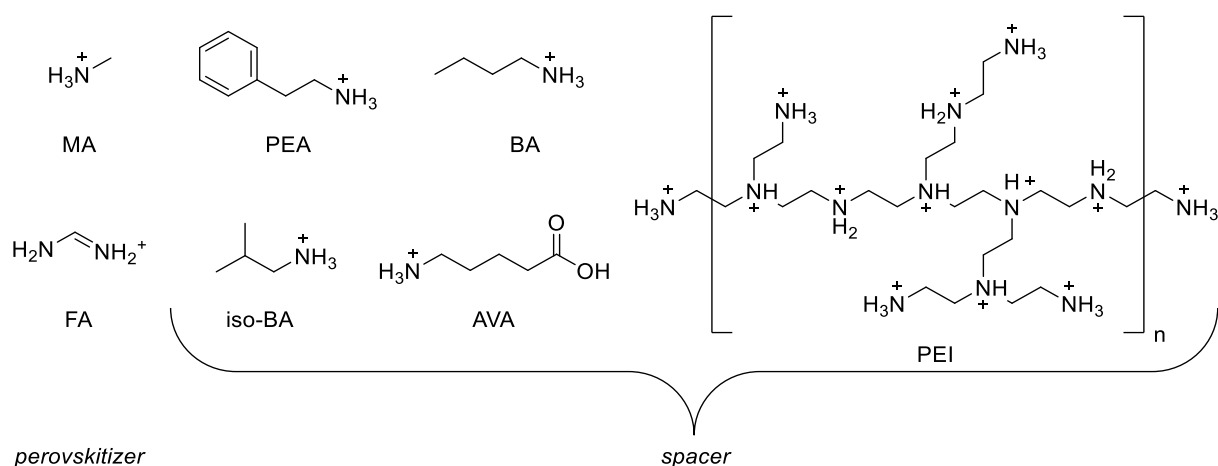


Figure 1.10. Structures of *perovskitizer* and *spacer* cations to form 3D, quasi-2D and 2D hybrid perovskites which are applied in solar cells as absorber and protective layers, respectively. The abbreviations used in this thesis are included.

The largest obstacle for the practical usage of MAPI in solar cell modules is its instability towards humidity. Exploring 2D and quasi-2D hybrid perovskites for solar cell applications showing a higher stability than their 3D counterparts might be an approach to overcome this hindrance. The higher resistance towards moisture is most likely due to the incorporation of large aliphatic and thereby hydrophobic cations.⁴⁷ Smith et al. introduced a solar-cell device based on the quasi-2D hybrid perovskite (PEA)₂(MA)₂[Pb₃I₁₀] (PEA = phenethylammonium, MA = methylammonium) (Figure 1.11a) which featured a maximum high-open circuit voltage of 1.18 V, superior stability towards moisture but a rather low efficiency of 4.73%. Comparative humidity studies were performed with (PEA)₂(MA)₂[Pb₃I₁₀] and MAPI films deposited on quartz slides and stored at a relative humidity level of 52%. (PEA)₂(MA)₂[Pb₃I₁₀] showed no change in composition after 46 days in contrast to MAPI where first signs of degradation could be observed after only 4-5 days (Figure 1.11b). Another advantage of this quasi-2D system entails the ease of high-quality film fabrication which can be performed under humid conditions.⁴⁷ Cao et al. followed up with a study on a series of layered hybrid perovskites containing butylammonium as a spacer cation, namely (BA)₂(MA)_{n-1}Pb_nI_{3n+1} (BA = butylammonium) with $n = 1 - 4$. Varying the thickness of the perovskite blocks from $n = 1$, which corresponds to (BA)₂PbI₄, a regular 2D hybrid perovskite, to $n = 3$ and 4 changed the growth direction of the perovskite layers from parallel to perpendicular with respect

to the substrate plane. Thus, an improvement in charge carrier transport can be expected, as the perpendicular arrangement of the inorganic layers allows a direct diffusion of the charge carriers to the contacts without having to pass the insulating organic layers. $(\text{BA})_2(\text{MA})_2\text{Pb}_3\text{I}_{10}$, which was applied in the best performing solar cell device showing a PCE of 4.02%, proved to be stable for 2 months in an atmosphere with a relative humidity of 40%. In addition, Cao et al. confirmed that uniform films of high quality can easily be synthesized in a one-step process.⁶⁰

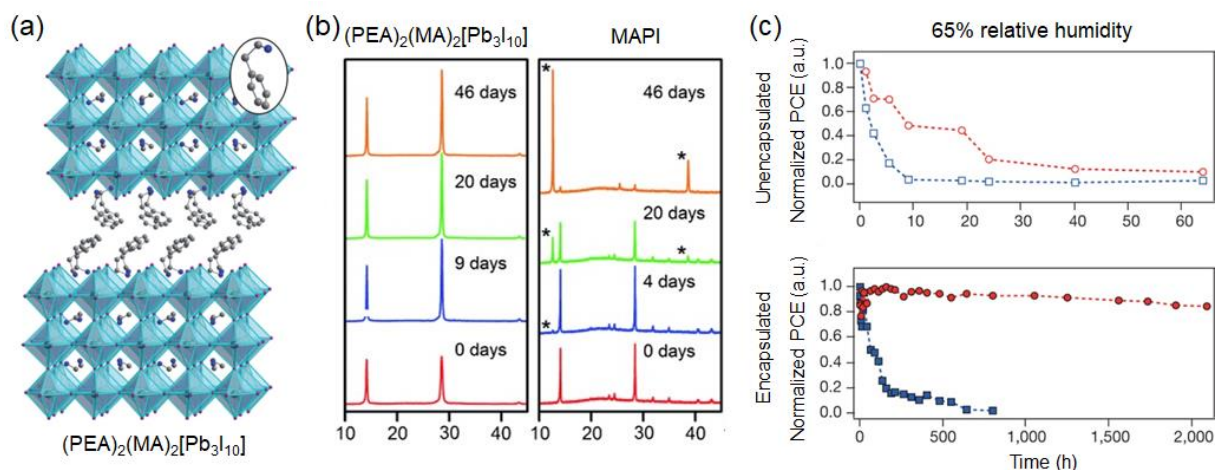


Figure 1.11. (a) Crystal structure of the quasi-2D hybrid perovskite $(\text{PEA})_2(\text{MA})_2[\text{Pb}_3\text{I}_{10}]$. (b) PXRD patterns of $(\text{PEA})_2(\text{MA})_2[\text{Pb}_3\text{I}_{10}]$ (left) and MAPI films (right) exposed to a relative humidity level of 52%. Signals assigned to PbI_2 are marked with asterisks. (c) Stability study at 65% relative humidity for solar cells based on the quasi-2D hybrid perovskite $(\text{BA})_2(\text{MA})_3\text{Pb}_4\text{I}_{13}$ (red) and the 3D hybrid perovskite MAPI (blue). The tests were performed without encapsulation (top) and with an encapsulation consisting of glass and epoxy (bottom). Device architecture: aluminium, PCBM ([6,6]-phenyl- C_{61} -butyric acid methyl ester), PEDOT:PSS (poly(3,4-ethylenedioxythiophene) polystyrene sulfonate), FTO. (a) and (b) were adapted with permission from ref 47. Copyright 2014 Wiley-VCH Verlag GmbH & Co. KGaA. (c) was adapted with permission from ref 97. Copyright 2016 Springer Nature.

A rise in efficiency to 15.3% could be reached by increasing n in $(\text{PEA})_2(\text{MA})_{n-1}\text{Pb}_n\text{I}_{3n+1}$ to values as high as 60. However, the better performance came at the price of a reduced stability towards humidity which can be ranked between the good long-term stability of compounds with low n and the poor stability of MAPI.⁹⁸ A breakthrough regarding the power conversion efficiencies for quasi-2D hybrid perovskite solar cells with small n was achieved by Tsai et al. who introduced a new deposition protocol, the so-called hot-casting technique. The perovskite film, in this case $(\text{BA})_2(\text{MA})_{n-1}\text{Pb}_n\text{I}_{3n+1}$ ($n = 3$ and 4), is spin-coated on a preheated substrate, which resulted in films with almost single-crystalline quality and a strict alignment of the inorganic layers perpendicular to the substrate plane.⁹⁷ In comparison, investigations on room temperature cast films showed that this arrangement was not as consistent as assumed by Cao et al. in the first place,⁶⁰ but the crystal domains were rather orientated randomly.⁹⁷ These insights make the difference in PCEs

comprehensible: For high charge mobility the charge carriers need to diffuse along continuous conductive pathways ($(\text{MA})_{n-1}\text{Pb}_n\text{I}_{3n+1})^{2-}$) to the contacts without encountering insulating barriers formed by the large organic cations. This can only be realized when the orientation of all crystal domains coincide. The champion device, which was produced with the hot-casting technique and contained $(\text{BA})_2(\text{MA})_3\text{Pb}_4\text{I}_{13}$ as the absorber layer, reached an efficiency of 12.52%. Stability tests demonstrated the superior resistance towards light, heat and humidity in comparison to MAPI but long-term stability could only be reached by encapsulation of the device (Figure 1.11c).⁹⁷ Also, the shape of the spacer cation has a strong influence on crystallization behavior, optoelectronic properties and stability as demonstrated by a study from Chen et al. on $(\text{A})_2(\text{MA})_3\text{Pb}_4\text{I}_{13}$ ($\text{A} = n$ -butylammonium or iso-butylammonium). The incorporation of the branched organic cation iso-butylammonium led to an improvement in all mentioned areas resulting in a PCE of 8.82%.⁹⁹ A further rise to 10.63% was achieved by applying the hot-casting technique which confirmed the results by Tsai et al.^{97, 99} Not only small molecules but also polymers can be introduced for confining the inorganic perovskite slabs as shown by Yao et al. They investigated the series $(\text{PEI})_2(\text{MA})_{n-1}\text{Pb}_n\text{I}_{3n+1}$ ($n = 3, 5, 7$) based on the polycation polyethylenimine (PEI), which links adjacent inorganic layers tightly. The resulting compaction of the perovskite films is assumed to improve the charge transfer between the $(\text{MA})_{n-1}\text{Pb}_n\text{I}_{3n+1})^{2-}$ layers, which explains the superior power conversion efficiencies compared to $(\text{BA})_2(\text{MA})_{n-1}\text{Pb}_n\text{I}_{3n+1}$ based devices which were produced for comparison. The excellent uniform and pin-hole free film formation observed for the whole series was manifested when Yao et al. took steps towards up-scaling: An efficiency of up to 8.77% was measured for $(\text{PEI})_2(\text{MA})_6\text{Pb}_7\text{I}_{22}$ solar cells spanning an area of 2.32 cm², which is only a small decrease compared to the small area solar cells (0.04 cm²) which exhibited a PCE of over 10%. Finally, no signs of degradation were observed after exposing $(\text{PEI})_2(\text{MA})_6\text{Pb}_7\text{I}_{22}$ films to air with 50% relative humidity for 30 days. This is reflected in the almost unchanged PCE of solar cells using $(\text{PEI})_2(\text{MA})_{n-1}\text{Pb}_n\text{I}_{3n+1}$ ($n = 5, 7$) as an absorber layer after 500 h of light-soaking at short-circuit condition, whereas the MAPI-based devices suffered a loss in efficiency of over 50 % after only 5 days. The moisture-stability of these quasi-2D hybrid perovskites results most likely from the hydrophobicity of the organic polymer combined with a stronger steric hindrance preventing water molecules interacting with the inorganic layer.¹⁰⁰ As a preliminary conclusion several aspects are summarized, which show how quasi-2D hybrid perovskites combine the virtues of their 2D and 3D congeners: (1) The improved moisture stability of 2D-quasi hybrid perovskites results from the hydrophobic nature of the large alkylammonium spacer cations.¹⁰¹ (2) High-quality films can be fabricated in a single step. (3) Higher open-circuit voltages are reached due to the larger bandgaps compared to MAPI. (4) Quasi-2D hybrid perovskites provide a versatile platform to tailor their optoelectronic properties by not only adjusting the number of inorganic layers n , but also by choosing from the wide variety of possible *spacer* cations. (5) In order to

benefit from the good charge mobilities within the inorganic layers, a strict out-of-plane alignment of these layers is absolutely crucial.

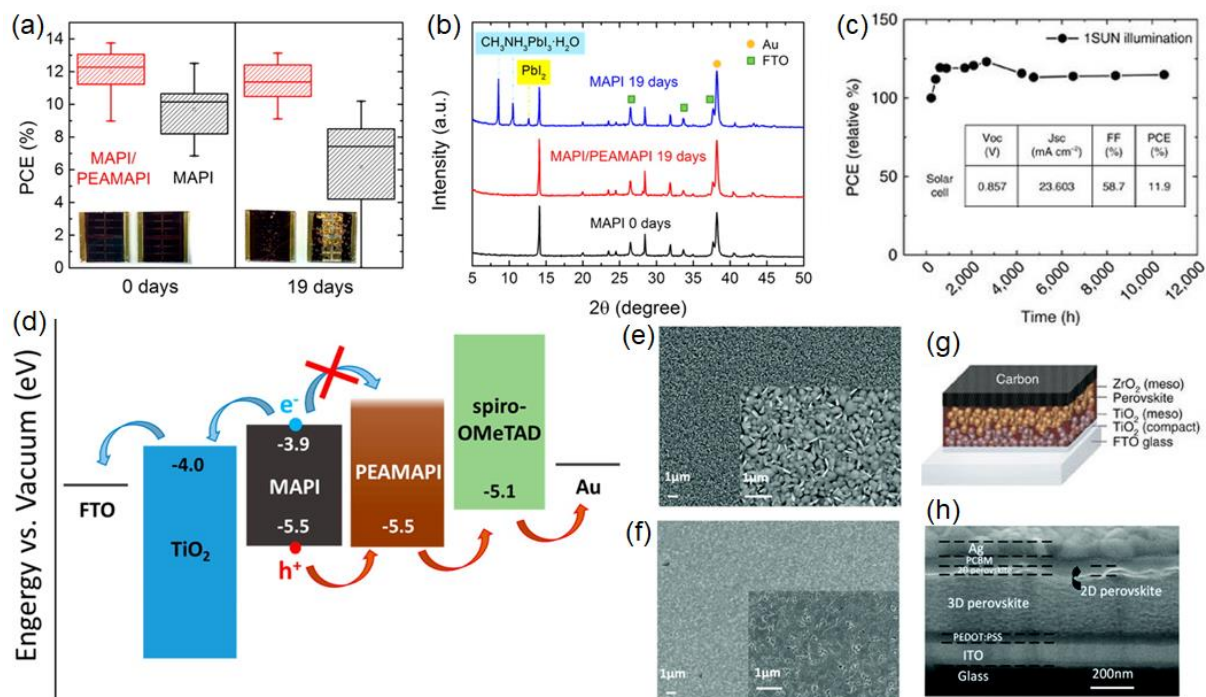


Figure 1.12. (a,b) Stability tests on the 2D/3D heterojunction solar cell devices whose architecture is indicated in (d) and on MAPI based devices. (a) The PCE was determined for 20 devices each before starting the stability test and after exposure to a relative humidity level of 75% in air at room temperature for 19 days. The visible change upon exposure to humidity is demonstrated with corresponding photographs of a MAPI/(PEA)₂(MA)₄Pb₅I₁₆ (PEAMAPI) cell (left) and a MAPI cell (right) displayed in the inset. (b) PXRD pattern of a pristine MAPI cell in comparison to PXRD patterns of a MAPI/PEAMAPI cell and a MAPI cell after exposure to humidity for 19 days. (c) Stability tests on the solar cell device depicted in (g), which was sealed with a glass cover. The device was exposed at 55°C under ambient conditions to 1sun illumination for 24 h per day. The inset displays the initial device parameters. (d) Energy band diagram of a MAPI/PEAMAPI heterojunction solar cell. (e,f) Top view SEM images of (e) a pristine MAPbI_xCl_{3-x} film and (f) a MAPbI_xCl_{3-x} film treated with cyclopropylammonium iodide (CAI). (g) Device architecture of HTM-free solar cell. The perovskite layer is MAPI with a thin capping layer of (AVA)₂PbI₄. (h) Cross-sectional SEM image of a perovskite solar cell based on a CA₂PbI₄/MAPbI_xCl_{3-x} heterojunction. (a), (b) and (d) were reprinted with permission from ref 102. Copyright 2016 American Chemical Society. (c) was adapted and (g) was reprinted with permission from ref 103. (e), (f) and (h) were reprinted from ref 101 with permission of The Royal Society of Chemistry.

A second pathway to solar cells with enhanced stability and possibly higher performance is the insertion of a 2D or quasi-2D hybrid perovskite capping layer next to its 3D congener which acts as a barrier against moisture (Figure12.1h). Hu et al. fabricated a perovskite/perovskite heterojunction solar cell by infiltrating the top layer of MAPI with phenethylammonium (PEA)

cations resulting in the formation of a thin coating of $(\text{PEA})_2(\text{MA})_4\text{Pb}_5\text{I}_{16}$ and a reorganization of the MAPI surface. The organic layers of the quasi-2D perovskite are aligned parallel to the substrate plane forming an insulating barrier, which becomes apparent in a drop in short-circuit current density (J_{sc}). However, this deleterious effect is compensated by an increase in open-circuit voltage (V_{oc}) and fill factor (FF).¹⁰² A study by Juarez-Perez et al. investigating incomplete perovskite cells missing either the electron-selective contact, the hole-selective contact, or both in comparison to full devices illustrated clearly that a high V_{oc} is mainly attributable to the hole-selective contact. In addition, they found that recombination rates drop while the FF and V_{oc} increase with the use of carrier-selective contacts.¹⁰⁴ In turn, the observed enhancement in V_{oc} and FF for the MAPI/ $(\text{PEA})_2(\text{MA})_4\text{Pb}_5\text{I}_{16}$ heterojunction solar cell may be attributed to $(\text{PEA})_2(\text{MA})_4\text{Pb}_5\text{I}_{16}$ acting as a more efficient hole-selective material than spiro-OMeTAD and thereby reducing interface recombination. Hu et al. substantiated their hypothesis by analyzing the energy level alignment of MAPI and $(\text{PEA})_2(\text{MA})_4\text{Pb}_5\text{I}_{16}$, which allows the transfer of holes and inhibits the diffusion of electrons from the 3D perovskite to the quasi-2D perovskite (Figure 1.12d). In addition to optimizing the device performance, $(\text{PEA})_2(\text{MA})_4\text{Pb}_5\text{I}_{16}$ proved to protect MAPI from degradation when exposing a non-encapsulated device to air at a relative humidity level of 75% for 19 days (Figure 1.12b). However, a slight decline in average efficiency from around 13% to 11.4% was observed (Figure 1.12a).¹⁰² Phenethylammonium cations have also been incorporated into the more complex mixed perovskite system $(\text{FAPbI}_3)_{0.85}(\text{MAPbBr}_3)_{0.15}$ (FA = formamidinium) leading to enhanced crystallinity and a passivation of the perovskite grains in glass/fluorine doped tin oxide (FTO)/compact TiO_2 /mesoporous TiO_2 test devices, since the PEA cations are located preferentially at the perovskite/mesoporous TiO_2 interface. Although charge recombination is assumed to be reduced by this process, the insulating nature of the quasi-2D layer has a detrimental effect on the J_{sc} , which results in a slightly decreased PCE compared to the pristine 3D hybrid perovskite. On the other hand, the hydrophobic low-dimensional perovskite retards the degradation process in humid atmosphere.¹⁰⁵ Several 2D hybrid perovskites have been integrated into perovskite solar cells including $(\text{PEI})_2\text{PbI}_4$ (PEI = polyethylenimine),¹⁰⁶ $(\text{CA})_2\text{PbI}_4$ (CA = cyclopropylammonium),¹⁰¹ $(\text{AVA})_2\text{PbI}_4$ (AVA = 5-ammoniumvaleric acid),¹⁰³ $(\text{BA})_2\text{PbI}_4$ ¹⁰⁷ and $(\text{PEA})_2\text{PbI}_4$.¹⁰⁸ Two different synthesis methods were applied. On the one hand, stacked structures were obtained by spin-coating a solution containing the spacer cation^{101, 108} or amine¹⁰⁷ on top of the beforehand synthesized 3D absorber layer. In all cases, the surface of the perovskite film became smoother and more uniform (Figure 1.12e,f). On the other hand, Grancini et al. introduced a one-pot-synthesis where all constituents for the 2D and 3D perovskite layer were deposited in solution at the same time.¹⁰³ The 2D layer assembled next to the TiO_2 layer of the solar cell device since the protonated carboxylic acid groups of the 5-aminovaleric acid bind

to the oxide network.¹⁰⁹ Interestingly, the formation of the 2D layer also influences the orientation of the 3D perovskite at their interface.¹⁰³

Comparing the stability against environmental stresses in different studies is quite challenging, as the test conditions including encapsulation, humidity level and device architecture vary. In general, an enhanced stability against moisture^{101, 103, 108} or heat¹⁰⁷ is observed in all cases. Nevertheless, the record device concerning long-term stability featuring a (AVA)₂PbI₄/MAPI heterojunction is presented: The hole transporting material (HTM) free solar cell is built up on a FTO glass substrate containing TiO₂ as the electron transporting material (ETM) and a carbon electrode (Figure 1.12g). Sealed under ambient atmosphere with a glass slide, the solar cell maintained its performance ($\eta = 11.9\%$) for > 10000 h (Figure 12.c).¹⁰³ At this point it may be noted that some studies reported no degradation for 2D/3D films under humid conditions, whereas the respective solar cell devices suffered losses in efficiency. This observation indicates that the device stability is not only dependent on the perovskite, but that also factors like the degradation of other solar cell components like the ETM [6,6]-phenyl-C₆₁-butyric acid methyl ester (PCBM)^{101, 110} and the migration of gold used as a contact material into the perovskite have to be considered.¹¹¹ Another interesting aspect is the influence of the inserted 2D perovskite layer on the electronic properties of the device and its components. Lin et al. reported increased carrier life-times for MAPI capped with a thin (BA)₂PbI₄ film compared to untreated MAPI. This improvement was attributed to healing of defects, present at pristine MAPI's surface, during the top layer conversion process to (BA)₂PbI₄. Average efficiencies of $18.89 \pm 0.34\%$ were measured for these devices, exceeding the values recorded for pure-MAPI based devices ($\eta = 17.05 \pm 0.20\%$).¹⁰⁷ Cho et al. probed the recombination resistance, which is inversely proportional to the recombination rate,¹⁰⁴ by impedance spectroscopy. They found that the insertion of a thin layer of (PEA)₂PbI₄ on top of Cs_{0.1}FA_{0.74}MA_{0.13}PbI_{2.48}Br_{0.39} (CFMPIB) doubled the recombination resistance for the respective devices, hinting towards an improved charge transfer at the perovskite interface. This is in line with the evaluation of the energy level alignment of ETM, 3D perovskite, 2D perovskite and HTM following up on the study by Hu et al. (see above).¹⁰² The 2D perovskite serves as electron blocking layer, since its conduction band (CB) is energetically higher than the CB of the 3D perovskite. At the same time holes can diffuse freely to the HTM as the perovskites' valence bands (VB) are well aligned. This would explain the observed reduced charge carrier recombination and the enhancement in average PCE from 18.7% for the CFMPIB based device to 20.08% for the (PEA)₂PbI₄/CFMPIB based solar cells.¹⁰⁸

2D and quasi-2D perovskites have not only the ability to protect its 3D congener against moisture, they can also improve the electronic properties of the device including a reduction of charge recombination. Optimizing the thickness of the capping layer is crucial to find the sweet spot between the just mentioned benefits and a reduction in J_{SC} due to the insulating nature of the

organic layers.^{101, 105} Sealing of perovskite based solar cells is still necessary to keep the initial efficiency, as the degradation was only slowed down in the stacked 2D/3D architectures. In addition, encapsulation is an important measure to protect the device against mechanical damage and to keep the Pb-comprising compounds contained.

1.6 Objectives

The versatility of hybrid perovskites results from the plethora of possible combinations of metal cations and halides with the vast number of organic molecules including ammonium and sulfonium cations.¹¹² One objective of this thesis is to expand this compound class by probing new low-dimensional hybrid perovskites and hybrid compounds for their unique properties including strong photoluminescence at room temperature.⁵⁹ But it is also necessary to explore further characteristics including ion diffusion, which is one of the reasons for degradation processes in MAPI-based solar cells.⁴⁸⁻⁴⁹ The only study on ion migration in layered hybrid perovskite, to our knowledge, stated that ion mobility is suppressed, which may be highly advantageous in regard to optoelectronic applications.⁵⁰ We aim to provide additional insights into the conductive behavior, considering both electrons and ions, of layered hybrid compounds.

In addition, we systematically investigate series of hybrid perovskites which only differ by the choice of the halide. These comparative studies together with detailed analyses of their characteristics are fundamental to find structure-property-relations being crucial to tailor hybrid perovskites with optimized properties according to the desired application.

Although the rapid rise of efficiency for MAPI-based solar cells has raised high expectations concerning its application in the photovoltaic field, its intrinsic moisture instability is still a concern. A highly promising approach to circumvent this issue is the concept of quasi-2D hybrid perovskites which combine MAPI's superior optoelectronic properties with the higher stability of 2D hybrid perovskites. Layered hybrid perovskites' moisture resistance is associated with the hydrophobic nature of the applied organic cations comprising long alkyl chains or aromatic residues. The consistent further development is the application of fluorinated cations which exhibit a much higher hydrophobicity compared to analogous hydrocarbons.¹¹³ In addition, Frost et al. made a connection between a strong polarization of the lattice which is determined by the organic cation's dipole moment and enhanced charge separation and carrier lifetimes. Fluorination of the organic cation will increase its dipole moment and with it may manipulate the lattice polarization.¹¹⁴ Therefore, we attempt to comprehensively investigate fluorinated hybrid perovskites and hybrid compounds.

1.7 References

1. Turkenburg, W. C.; Arent, D. J.; Bertani, R.; Faaij, A.; Hand, M.; Krewitt, W.; Larson, E. D.; Lund, J.; Mehos, M.; Merrigan, T.; Mitchell, C.; Moreira, J. R.; Sinke, W.; Sonntag-O'Brien, V.; Thresher, B.; van Sark, W.; Usher, E.; Usher, E., Chapter 11 - Renewable Energy. In *Global Energy Assessment - Toward a Sustainable Future*, Cambridge University Press, Cambridge, UK and New York, NY, USA and the International Institute for Applied Systems Analysis, Laxenburg, Austria, 2012; pp 761-900.
2. Green, M. A.; Hishikawa, Y.; Dunlop, E. D.; Levi, D. H.; Hohl-Ebinger, J.; Ho-Baillie, A. W. Y., Solar cell efficiency tables (version 51). *Prog. Photovolt., Res. Appl.* **2018**, *26* (1), 3-12.
3. Fraunhofer ISE: Photovoltaics Report, updated: 26 February 2018.
4. Cao, Y.; Saygili, Y.; Ummadisingu, A.; Teuscher, J.; Luo, J.; Pellet, N.; Giordano, F.; Zakeeruddin, S. M.; Moser, J. E.; Freitag, M.; Hagfeldt, A.; Grätzel, M., 11% efficiency solid-state dye-sensitized solar cells with copper(II/I) hole transport materials. *Nat. Commun.* **2017**, *8*, 15390.
5. Mitchell, V. D.; Jones, D. J., Advances toward the effective use of block copolymers as organic photovoltaic active layers. *Polym. Chem.* **2018**, *9* (7), 795-814.
6. Kojima, A.; Teshima, K.; Shirai, Y.; Miyasaka, T., Organometal Halide Perovskites as Visible-Light Sensitizers for Photovoltaic Cells. *J. Am. Chem. Soc.* **2009**, *131* (17), 6050-6051.
7. Ball, J. M.; Lee, M. M.; Hey, A.; Snaith, H. J., Low-temperature processed meso-superstructured to thin-film perovskite solar cells. *Energy Environ. Sci.* **2013**, *6* (6), 1739-1743.
8. Xing, G.; Mathews, N.; Sun, S.; Lim, S. S.; Lam, Y. M.; Grätzel, M.; Mhaisalkar, S.; Sum, T. C., Long-Range Balanced Electron- and Hole-Transport Lengths in Organic-Inorganic CH₃NH₃PbI₃. *Science* **2013**, *342* (6156), 344-347.
9. Dong, Q.; Fang, Y.; Shao, Y.; Mulligan, P.; Qiu, J.; Cao, L.; Huang, J., Electron-hole diffusion lengths > 175 μm in solution-grown CH₃NH₃PbI₃ single crystals. *Science* **2015**, *347* (6225), 967-970.
10. De Wolf, S.; Holovsky, J.; Moon, S.-J.; Löper, P.; Niesen, B.; Ledinsky, M.; Haug, F.-J.; Yum, J.-H.; Ballif, C., Organometallic Halide Perovskites: Sharp Optical Absorption Edge and Its Relation to Photovoltaic Performance. *J. Phys. Chem. Lett.* **2014**, *5* (6), 1035-1039.
11. Herz, L. M., Charge-Carrier Dynamics in Organic-Inorganic Metal Halide Perovskites. *Annu. Rev. Phys. Chem.* **2016**, *67* (1), 65-89.
12. Green, M. A.; Ho-Baillie, A., Perovskite Solar Cells: The Birth of a New Era in Photovoltaics. *ACS Energy Lett.* **2017**, *2* (4), 822-830.
13. Weber, D., CH₃NH₃PbX₃, ein Pb(II)-System mit kubischer Perowskitstruktur. *Z. Naturforsch. B* **1978**, *33*, 1443-1445.
14. Mitzi, D. B.; Feild, C. A.; Harrison, W. T. A.; Guloy, A. M., Conducting tin halides with a layered organic-based perovskite structure. *Nature* **1994**, *369* (6480), 467-469.

15. Im, J.-H.; Lee, C.-R.; Lee, J.-W.; Park, S.-W.; Park, N.-G., 6.5% efficient perovskite quantum-dot-sensitized solar cell. *Nanoscale* **2011**, *3* (10), 4088-4093.
16. Kim, H.-S.; Lee, C.-R.; Im, J.-H.; Lee, K.-B.; Moehl, T.; Marchioro, A.; Moon, S.-J.; Humphry-Baker, R.; Yum, J.-H.; Moser, J. E.; Grätzel, M.; Park, N.-G., Lead Iodide Perovskite Sensitized All-Solid-State Submicron Thin Film Mesoscopic Solar Cell with Efficiency Exceeding 9%. *Sci. Rep.* **2012**, *2*.
17. Lee, M. M.; Teuscher, J.; Miyasaka, T.; Murakami, T. N.; Snaith, H. J., Efficient Hybrid Solar Cells Based on Meso-Superstructured Organometal Halide Perovskites. *Science* **2012**, *338* (6107), 643-647.
18. Etgar, L.; Gao, P.; Xue, Z.; Peng, Q.; Chandiran, A. K.; Liu, B.; Nazeeruddin, M. K.; Grätzel, M., Mesoscopic CH₃NH₃PbI₃/TiO₂ Heterojunction Solar Cells. *J. Am. Chem. Soc.* **2012**, *134* (42), 17396-17399.
19. Kazim, S.; Nazeeruddin, M. K.; Grätzel, M.; Ahmad, S., Perovskit als Lichtabsorptionsmaterial: ein Durchbruch in der Photovoltaik. *Angew. Chem.* **2014**, *126* (11), 2854-2867. Kazim, S.; Nazeeruddin, M. K.; Grätzel, M.; Ahmad, S., Perovskite as Light Harvester: A Game Changer in Photovoltaics. *Angew. Chem., Int. Ed.* **2014**, *53* (11), 2812-2824.
20. Boix, P. P.; Nonomura, K.; Mathews, N.; Mhaisalkar, S. G., Current progress and future perspectives for organic/inorganic perovskite solar cells. *Mater. Today* **2014**, *17* (1), 16-23.
21. Sun, S.; Salim, T.; Mathews, N.; Duchamp, M.; Boothroyd, C.; Xing, G.; Sum, T. C.; Lam, Y. M., The origin of high efficiency in low-temperature solution-processable bilayer organometal halide hybrid solar cells. *Energy Environ. Sci.* **2014**, *7* (1), 399-407.
22. National Renewable Energy Laboratory, Best Research - Cell Efficiencies. <https://www.nrel.gov/pv/assets/images/efficiency-chart.png> (accessed 02/03/2018).
23. Park, N.-G.; Grätzel, M.; Miyasaka, T.; Zhu, K.; Emery, K., Towards stable and commercially available perovskite solar cells. *Nat. Energy* **2016**, *1*, 16152.
24. Wang, Z.; Shi, Z.; Li, T.; Chen, Y.; Huang, W., Stabilität von Perovskit-Solarzellen: Einfluss der Substitution von A-Kation und X-Anion. *Angew. Chem.* **2017**, *129* (5), 1210-1233. Wang, Z.; Shi, Z.; Li, T.; Chen, Y.; Huang, W., Stability of Perovskite Solar Cells: A Prospective on the Substitution of the A Cation and X Anion. *Angew. Chem., Int. Ed.* **2017**, *56* (5), 1190-1212.
25. Li, F.; Liu, M., Recent efficient strategies for improving the moisture stability of perovskite solar cells. *J. Mater. Chem. A* **2017**, *5* (30), 15447-15459.
26. Flora, G.; Gupta, D.; Tiwari, A., Toxicity of lead: a review with recent updates. In *Interdisciplinary Toxicology*, 2012; Vol. 5, p 47.
27. Benmessaoud, I. R.; Mahul-Mellier, A.-L.; Horvath, E.; Maco, B.; Spina, M.; Lashuel, H. A.; Forro, L., Health hazards of methylammonium lead iodide based perovskites: cytotoxicity studies. *Toxicol. Res.* **2016**, *5* (2), 407-419.

28. Babayigit, A.; Duy Thanh, D.; Ethirajan, A.; Manca, J.; Muller, M.; Boyen, H.-G.; Conings, B., Assessing the toxicity of Pb- and Sn-based perovskite solar cells in model organism *Danio rerio*. *Sci. Rep.* **2016**, *6*, 18721.
29. Babayigit, A.; Ethirajan, A.; Muller, M.; Conings, B., Toxicity of organometal halide perovskite solar cells. *Nat. Mater.* **2016**, *15*, 247.
30. Binek, A.; Petrus, M. L.; Huber, N.; Bristow, H.; Hu, Y.; Bein, T.; Docampo, P., Recycling Perovskite Solar Cells To Avoid Lead Waste. *ACS Appl. Mater. Interfaces* **2016**, *8* (20), 12881-12886.
31. Kadro, J. M.; Pellet, N.; Giordano, F.; Ulianov, A.; Muntener, O.; Maier, J.; Gratzel, M.; Hagfeldt, A., Proof-of-concept for facile perovskite solar cell recycling. *Energy Environ. Sci.* **2016**, *9* (10), 3172-3179.
32. Huang, L.; Xu, J.; Sun, X.; Xu, R.; Du, Y.; Ni, J.; Cai, H.; Li, J.; Hu, Z.; Zhang, J., New Films on Old Substrates: Toward Green and Sustainable Energy Production via Recycling of Functional Components from Degraded Perovskite Solar Cells. *ACS Sustainable Chem. Eng.* **2017**, *5* (4), 3261-3269.
33. Espinosa, N.; Serrano-Luján, L.; Urbina, A.; Krebs, F. C., Solution and vapour deposited lead perovskite solar cells: Ecotoxicity from a life cycle assessment perspective. *Sol. Energy Mater. Sol. Cells* **2015**, *137*, 303-310.
34. Alberola-Borràs, J.-A.; Vidal, R.; Juárez-Pérez, E. J.; Mas-Marzá, E.; Guerrero, A.; Mora-Seró, I., Relative impacts of methylammonium lead triiodide perovskite solar cells based on life cycle assessment. *Sol. Energy Mater. Sol. Cells* **2017**, *179*, 169-177.
35. Zhang, J.; Gao, X.; Deng, Y.; Zha, Y.; Yuan, C., Comparison of life cycle environmental impacts of different perovskite solar cell systems. *Sol. Energy Mater. Sol. Cells* **2017**, *166*, 9-17.
36. Gong, J.; Darling, S. B.; You, F., Perovskite photovoltaics: life-cycle assessment of energy and environmental impacts. *Energy Environ. Sci.* **2015**, *8* (7), 1953-1968.
37. Leguy, A. M. A.; Hu, Y.; Campoy-Quiles, M.; Alonso, M. I.; Weber, O. J.; Azarhoosh, P.; van Schilfhaarde, M.; Weller, M. T.; Bein, T.; Nelson, J.; Docampo, P.; Barnes, P. R. F., Reversible Hydration of $\text{CH}_3\text{NH}_3\text{PbI}_3$ in Films, Single Crystals, and Solar Cells. *Chem. Mater.* **2015**, *27* (9), 3397-3407.
38. Niu, G.; Li, W.; Meng, F.; Wang, L.; Dong, H.; Qiu, Y., Study on the stability of $\text{CH}_3\text{NH}_3\text{PbI}_3$ films and the effect of post-modification by aluminum oxide in all-solid-state hybrid solar cells. *J. Mater. Chem. A* **2014**, *2* (3), 705-710.
39. Chen, J.; Cai, X.; Yang, D.; Song, D.; Wang, J.; Jiang, J.; Ma, A.; Lv, S.; Hu, M. Z.; Ni, C., Recent progress in stabilizing hybrid perovskites for solar cell applications. *J. Power Sources* **2017**, *355*, 98-133.

40. Wang, Q.; Dong, Q.; Li, T.; Gruverman, A.; Huang, J., Thin Insulating Tunneling Contacts for Efficient and Water-Resistant Perovskite Solar Cells. *Adv. Mater.* **2016**, *28* (31), 6734-6739.
41. You, J.; Meng, L.; Song, T.-B.; Guo, T.-F.; Yang, Y.; Chang, W.-H.; Hong, Z.; Chen, H.; Zhou, H.; Chen, Q.; Liu, Y.; De Marco, N.; Yang, Y., Improved air stability of perovskite solar cells via solution-processed metal oxide transport layers. *Nat. Nanotechnol.* **2015**, *11*, 75.
42. Zhang, H.; Wang, H.; Chen, W.; Jen, A. K. Y., CuGaO₂: A Promising Inorganic Hole-Transporting Material for Highly Efficient and Stable Perovskite Solar Cells. *Adv. Mater.* **2017**, *29* (8), 1604984.
43. Docampo, P.; Ball, J. M.; Darwich, M.; Eperon, G. E.; Snaith, H. J., Efficient organometal trihalide perovskite planar-heterojunction solar cells on flexible polymer substrates. *Nat. Commun.* **2013**, *4*.
44. Liu, T.; Chen, K.; Hu, Q.; Zhu, R.; Gong, Q., Inverted Perovskite Solar Cells: Progresses and Perspectives. *Adv. Energy Mater.* **2016**, *6* (17), 1600457.
45. Saliba, M.; Matsui, T.; Seo, J.-Y.; Domanski, K.; Correa-Baena, J.-P.; Nazeeruddin, M. K.; Zakeeruddin, S. M.; Tress, W.; Abate, A.; Hagfeldt, A.; Grätzel, M., Cesium-containing triple cation perovskite solar cells: improved stability, reproducibility and high efficiency. *Energy Environ. Sci.* **2016**, *9* (6), 1989-1997.
46. Stoumpos, C. C.; Kanatzidis, M. G., Halide Perovskites: Poor Man's High-Performance Semiconductors. *Adv. Mater.* **2016**, *28* (28), 5778-5793.
47. Smith, I. C.; Hoke, E. T.; Solis-Ibarra, D.; McGehee, M. D.; Karunadasa, H. I., A Layered Hybrid Perovskite Solar-Cell Absorber with Enhanced Moisture Stability. *Angew. Chem.* **2014**, *126* (42), 11414-11417. Smith, I. C.; Hoke, E. T.; Solis-Ibarra, D.; McGehee, M. D.; Karunadasa, H. I., A Layered Hybrid Perovskite Solar-Cell Absorber with Enhanced Moisture Stability. *Angew. Chem., Int. Ed.* **2014**, *53*, 11232-11235.
48. Cheng, Y.; Li, H.-W.; Qing, J.; Yang, Q.-D.; Guan, Z.; Liu, C.; Cheung, S. H.; So, S. K.; Lee, C.-S.; Tsang, S.-W., The detrimental effect of excess mobile ions in planar CH₃NH₃PbI₃ perovskite solar cells. *J. Mater. Chem. A* **2016**, *4* (33), 12748-12755.
49. Bag, M.; Renna, L. A.; Adhikari, R. Y.; Karak, S.; Liu, F.; Lahti, P. M.; Russell, T. P.; Tuominen, M. T.; Venkataraman, D., Kinetics of Ion Transport in Perovskite Active Layers and Its Implications for Active Layer Stability. *J. Am. Chem. Soc.* **2015**, *137* (40), 13130-13137.
50. Lin, Y.; Bai, Y.; Fang, Y.; Wang, Q.; Deng, Y.; Huang, J., Suppressed Ion Migration in Low-Dimensional Perovskites. *ACS Energy Lett.* **2017**, *2* (7), 1571-1572.
51. Yang, T.-Y.; Gregori, G.; Pellet, N.; Grätzel, M.; Maier, J., The Significance of Ion Conduction in a Hybrid Organic-Inorganic Lead-Iodide-Based Perovskite Photosensitizer. *Angew. Chem.* **2015**, *127* (27), 8016-8021. Yang, T.-Y.; Gregori, G.; Pellet, N.; Grätzel, M.; Maier, J., The Significance

of Ion Conduction in a Hybrid Organic–Inorganic Lead-Iodide-Based Perovskite Photosensitizer. *Angew. Chem., Int. Ed.* **2015**, *54* (27), 7905-7910.

52. Petrus, M. L.; Schlipf, J.; Li, C.; Gujar, T. P.; Giesbrecht, N.; Müller-Buschbaum, P.; Thelakkat, M.; Bein, T.; Hüttner, S.; Docampo, P., Capturing the Sun: A Review of the Challenges and Perspectives of Perovskite Solar Cells. *Adv. Energy Mater.* **2017**, *7* (16), 1700264.

53. Frost, J. M.; Butler, K. T.; Walsh, A., Molecular ferroelectric contributions to anomalous hysteresis in hybrid perovskite solar cells. *APL Mater.* **2014**, *2* (8), -.

54. Snaith, H. J.; Abate, A.; Ball, J. M.; Eperon, G. E.; Leijtens, T.; Noel, N. K.; Stranks, S. D.; Wang, J. T.-W.; Wojciechowski, K.; Zhang, W., Anomalous Hysteresis in Perovskite Solar Cells. *J. Phys. Chem. Lett.* **2014**, *5* (9), 1511-1515.

55. Goldschmidt, V. M., Die Gesetze der Krystallochemie. *Naturwissenschaften* **1926**, *14* (21), 477-485.

56. Kieslich, G.; Sun, S.; Cheetham, A. K., Solid-state principles applied to organic-inorganic perovskites: new tricks for an old dog. *Chem. Sci.* **2014**, *5* (12), 4712-4715.

57. Kieslich, G.; Sun, S.; Cheetham, A. K., An extended Tolerance Factor approach for organic-inorganic perovskites. *Chem. Sci.* **2015**.

58. Mitzi, D. B., Templating and structural engineering in organic-inorganic perovskites. *J. Chem. Soc., Dalton Trans.* **2001**, (1), 1-12.

59. Mitzi, D. B., Synthesis, Structure, and Properties of Organic-Inorganic Perovskites and Related Materials. In *Progress in Inorganic Chemistry*; Karlin, K. D., Ed.; John Wiley & Sons, Inc.: New York, NY, 1999; pp 1–121.

60. Cao, D. H.; Stoumpos, C. C.; Farha, O. K.; Hupp, J. T.; Kanatzidis, M. G., 2D Homologous Perovskites as Light-Absorbing Materials for Solar Cell Applications. *J. Am. Chem. Soc.* **2015**, *137* (24), 7843-7850.

61. Dronskowski, R.; Kikkawa, S.; Stein, A., *Handbook of solid state chemistry - Volume 4: Nano and hybrid materials*. Wiley-VCH Verlag GmbH & Co. KGaA: Weinheim, 2017.

62. Dohner, E. R.; Hoke, E. T.; Karunadasa, H. I., Self-Assembly of Broadband White-Light Emitters. *J. Am. Chem. Soc.* **2014**, *136* (5), 1718-1721.

63. Wang, S.; Mitzi, D. B.; Feild, C. A.; Guloy, A., Synthesis and Characterization of $[\text{NH}_2\text{C}(\text{I})\text{:NH}_2]_3\text{MI}_5$ (M = Sn, Pb): Stereochemical Activity in Divalent Tin and Lead Halides Containing Single $\langle 110 \rangle$ Perovskite Sheets. *J. Am. Chem. Soc.* **1995**, *117* (19), 5297-5302.

64. Vincent, B. R.; Robertson, K. N.; Cameron, T. S.; Knop, O., Alkylammonium lead halides. Part 1. Isolated PbI_6^{4-} ions in $(\text{CH}_3\text{NH}_3)_4\text{PbI}_6 \cdot 2\text{H}_2\text{O}$. *Can. J. Chem.* **1987**, *65* (5), 1042-1046.

65. Ibach, H.; Lüth, H., *Festkörperphysik*. 7th ed.; Springer-Verlag: Berlin Heidelberg, 2009.

66. Kittel, C., *Einführung in die Festkörperphysik*. 14th ed.; Oldenbourg Wissenschaftsverlag GmbH: München, 2006.

67. Smith, M. D.; Crace, E. J.; Jaffe, A.; Karunadasa, H. I., The Diversity of Layered Halide Perovskites. *Annu. Rev. Mater. Res.* **2018**, *48* (1).
68. Lin, Q.; Armin, A.; Nagiri, R. C. R.; Burn, P. L.; Meredith, P., Electro-optics of perovskite solar cells. *Nat. Photonics* **2014**, *9*, 106.
69. Umebayashi, T.; Asai, K.; Kondo, T.; Nakao, A., Electronic structures of lead iodide based low-dimensional crystals. *Phys. Rev. B: Condens. Matter Mater. Phys.* **2003**, *67* (15), 155405.
70. Kataoka, T.; Kondo, T.; Ito, R.; Sasaki, S.; Uchida, K.; Miura, N., Magneto-optical study on excitonic spectra in $(C_6H_{13}NH_3)_2PbI_4$. *Phys. Rev. B: Condens. Matter Mater. Phys.* **1993**, *47* (4), 2010-2018.
71. Neogi, I.; Bruno, A.; Bahulayan, D.; Goh, T. W.; Ghosh, B.; Ganguly, R.; Cortecchia, D.; Sum, T. C.; Soci, C.; Mathews, N.; Mhaisalkar, S. G., Broadband-Emitting 2 D Hybrid Organic-Inorganic Perovskite Based on Cyclohexane-bis(methylamonium) Cation. *ChemSusChem* **2017**, *10* (19), 3765-3772.
72. Hong, X.; Ishihara, T.; Nurmikko, A. V., Dielectric confinement effect on excitons in PbI₄-based layered semiconductors. *Phys. Rev. B: Condens. Matter Mater. Phys.* **1992**, *45* (12), 6961-6964.
73. Muljarov, E. A.; Tikhodeev, S. G.; Gippius, N. A.; Ishihara, T., Excitons in self-organized semiconductor/insulator superlattices: Pbl-based perovskite compounds. *Phys. Rev. B: Condens. Matter Mater. Phys.* **1995**, *51* (20), 14370-14378.
74. Shinada, M.; Sugano, S., Interband Optical Transitions in Extremely Anisotropic Semiconductors. I. Bound and Unbound Exciton Absorption. *J. Phys. Soc. Jpn.* **1966**, *21* (10), 1936-1946.
75. Keldysh, L. V., Coulomb interaction in thin semiconductor and semimetal films. *Pis'ma Zh. Eksp. Teor. Fiz.* **1979**, *29* (11), 716-719.
76. Hanamura, E.; Nagaosa, N.; Kumagai, M.; Takagahara, T., Quantum wells with enhanced exciton effects and optical non-linearity. *Mater. Sci. Eng., B* **1988**, *1* (3), 255-258.
77. Smith, M. D.; Karunadasa, H. I., White-Light Emission from Layered Halide Perovskites. *Acc. Chem. Res.* **2018**, *51* (3), 619-627.
78. Smith, M. D.; Jaffe, A.; Dohner, E. R.; Lindenberg, A. M.; Karunadasa, H. I., Structural origins of broadband emission from layered Pb-Br hybrid perovskites. *Chem. Sci.* **2017**, *8* (6), 4497-4504.
79. Hu, T.; Smith, M. D.; Dohner, E. R.; Sher, M.-J.; Wu, X.; Trinh, M. T.; Fisher, A.; Corbett, J.; Zhu, X. Y.; Karunadasa, H. I.; Lindenberg, A. M., Mechanism for Broadband White-Light Emission from Two-Dimensional (110) Hybrid Perovskites. *J. Phys. Chem. Lett.* **2016**, *7* (12), 2258-2263.
80. Kitazawa, N., Excitons in two-dimensional layered perovskite compounds: $(C_6H_5C_2H_4NH_3)_2Pb(Br,I)_4$ and $(C_6H_5C_2H_4NH_3)_2Pb(Cl,Br)_4$. *Mater. Sci. Eng., B* **1997**, *49* (3), 233-238.

81. Tanaka, K.; Takahashi, T.; Kondo, T.; Umeda, K.; Ema, K.; Umebayashi, T.; Asai, K.; Uchida, K.; Miura, N., Electronic and Excitonic Structures of Inorganic–Organic Perovskite-Type Quantum-Well Crystal $(\text{C}_4\text{H}_9\text{NH}_3)_2\text{PbBr}_4$. *Jpn. J. Appl. Phys.* **2005**, *44* (8), 5923.
82. Dohner, E. R.; Jaffe, A.; Bradshaw, L. R.; Karunadasa, H. I., Intrinsic White-Light Emission from Layered Hybrid Perovskites. *J. Am. Chem. Soc.* **2014**, *136* (38), 13154-13157.
83. Thirumal, K.; Chong, W. K.; Xie, W.; Ganguly, R.; Muduli, S. K.; Sherburne, M.; Asta, M.; Mhaisalkar, S.; Sum, T. C.; Soo, H. S.; Mathews, N., Morphology-Independent Stable White-Light Emission from Self-Assembled Two-Dimensional Perovskites Driven by Strong Exciton–Phonon Coupling to the Organic Framework. *Chem. Mater.* **2017**, *29* (9), 3947-3953.
84. Wu, Z.; Ji, C.; Sun, Z.; Wang, S.; Zhao, S.; Zhang, W.; Li, L.; Luo, J., Broadband white-light emission with a high color rendering index in a two-dimensional organic-inorganic hybrid perovskite. *J. Mater. Chem. C* **2018**, *6* (5), 1171-1175.
85. Tongay, S.; Suh, J.; Ataca, C.; Fan, W.; Luce, A.; Kang, J. S.; Liu, J.; Ko, C.; Raghunathanan, R.; Zhou, J.; Ogletree, F.; Li, J.; Grossman, J. C.; Wu, J., Defects activated photoluminescence in two-dimensional semiconductors: interplay between bound, charged, and free excitons. *Sci. Rep.* **2013**, *3*, 2657.
86. Schmidt, T.; Lischka, K.; Zulehner, W., Excitation-power dependence of the near-band-edge photoluminescence of semiconductors. *Phys. Rev. B: Condens. Matter Mater. Phys.* **1992**, *45* (16), 8989-8994.
87. Williams, R. T.; Song, K. S., The self-trapped exciton. *J. Phys. Chem. Solids* **1990**, *51* (7), 679-716.
88. Kitazawa, N.; Aono, M.; Watanabe, Y., Temperature-dependent time-resolved photoluminescence of $(\text{C}_6\text{H}_5\text{C}_2\text{H}_4\text{NH}_3)_2\text{PbX}_4$ (X=Br and I). *Mater. Chem. Phys.* **2012**, *134* (2), 875-880.
89. Yangui, A.; Garrot, D.; Lauret, J. S.; Lusson, A.; Bouchez, G.; Deleporte, E.; Pillet, S.; Bendeif, E. E.; Castro, M.; Triki, S.; Abid, Y.; Boukheddaden, K., Optical Investigation of Broadband White-Light Emission in Self-Assembled Organic–Inorganic Perovskite $(\text{C}_6\text{H}_{11}\text{NH}_3)_2\text{PbBr}_4$. *J. Phys. Chem. C* **2015**, *119* (41), 23638-23647.
90. Pust, P.; Schmidt, P. J.; Schnick, W., A revolution in lighting. *Nat. Mater.* **2015**, *14*, 454.
91. Silver, J.; Withnall, R., Color Conversion Phosphors for LEDs. In *Luminescent Materials and Applications*, John Wiley & Sons, Ltd: Chichester, England, 2008; pp 75-109.
92. Ye, S.; Xiao, F.; Pan, Y. X.; Ma, Y. Y.; Zhang, Q. Y., Phosphors in phosphor-converted white light-emitting diodes: Recent advances in materials, techniques and properties. *Mater. Sci. Eng., R* **2010**, *71* (1), 1-34.

93. Taguchi, T. In *Recent progress and future prospect of high-performance near-UV based white LEDs: from ECO lighting to medical application*, SPIE Optical Engineering + Applications, SPIE: 2009; p 15.
94. Mao, L.; Wu, Y.; Stoumpos, C. C.; Traore, B.; Katan, C.; Even, J.; Wasielewski, M. R.; Kanatzidis, M. G., Tunable White-Light Emission in Single-Cation-Templated Three-Layered 2D Perovskites $(\text{CH}_3\text{CH}_2\text{NH}_3)_4\text{Pb}_3\text{Br}_{10-x}\text{Cl}_x$. *J. Am. Chem. Soc.* **2017**, *139* (34), 11956-11963.
95. Mao, L.; Wu, Y.; Stoumpos, C. C.; Wasielewski, M. R.; Kanatzidis, M. G., White-Light Emission and Structural Distortion in New Corrugated Two-Dimensional Lead Bromide Perovskites. *J. Am. Chem. Soc.* **2017**, *139* (14), 5210-5215.
96. Alonso, J. A.; Martínez-Lope, M. J.; Casais, M. T.; Fernández-Díaz, M. T., Evolution of the Jahn–Teller Distortion of MnO_6 Octahedra in RMnO_3 Perovskites (R = Pr, Nd, Dy, Tb, Ho, Er, Y): A Neutron Diffraction Study. *Inorg. Chem.* **2000**, *39* (5), 917-923.
97. Tsai, H.; Nie, W.; Blancon, J.-C.; Stoumpos, C. C.; Asadpour, R.; Harutyunyan, B.; Neukirch, A. J.; Verduzco, R.; Crochet, J. J.; Tretiak, S.; Pedesseau, L.; Even, J.; Alam, M. A.; Gupta, G.; Lou, J.; Ajayan, P. M.; Bedzyk, M. J.; Kanatzidis, M. G.; Mohite, A. D., High-efficiency two-dimensional Ruddlesden–Popper perovskite solar cells. *Nature* **2016**, *536* (7616), 312-316.
98. Quan, L. N.; Yuan, M.; Comin, R.; Voznyy, O.; Beauregard, E. M.; Hoogland, S.; Buin, A.; Kirmani, A. R.; Zhao, K.; Amassian, A.; Kim, D. H.; Sargent, E. H., Ligand-Stabilized Reduced-Dimensionality Perovskites. *J. Am. Chem. Soc.* **2016**, *138* (8), 2649-2655.
99. Chen, Y.; Sun, Y.; Peng, J.; Zhang, W.; Su, X.; Zheng, K.; Pullerits, T.; Liang, Z., Tailoring Organic Cation of 2D Air-Stable Organometal Halide Perovskites for Highly Efficient Planar Solar Cells. *Adv. Energy Mater.* **2017**, *7* (18), 1700162.
100. Yao, K.; Wang, X.; Xu, Y.-x.; Li, F.; Zhou, L., Multilayered Perovskite Materials Based on Polymeric-Ammonium Cations for Stable Large-Area Solar Cell. *Chem. Mater.* **2016**, *28* (9), 3131-3138.
101. Ma, C.; Leng, C.; Ji, Y.; Wei, X.; Sun, K.; Tang, L.; Yang, J.; Luo, W.; Li, C.; Deng, Y.; Feng, S.; Shen, J.; Lu, S.; Du, C.; Shi, H., 2D/3D perovskite hybrids as moisture-tolerant and efficient light absorbers for solar cells. *Nanoscale* **2016**, *8* (43), 18309-18314.
102. Hu, Y.; Schlipf, J.; Wussler, M.; Petrus, M. L.; Jaegermann, W.; Bein, T.; Müller-Buschbaum, P.; Docampo, P., Hybrid Perovskite/Perovskite Heterojunction Solar Cells. *ACS Nano* **2016**, *10* (6), 5999-6007.
103. Grancini, G.; Roldán-Carmona, C.; Zimmermann, I.; Mosconi, E.; Lee, X.; Martineau, D.; Nabey, S.; Oswald, F.; De Angelis, F.; Graetzel, M.; Nazeeruddin, M. K., One-Year stable perovskite solar cells by 2D/3D interface engineering. *Nat. Commun.* **2017**, *8*, 15684.

104. Juarez-Perez, E. J.; Wußler, M.; Fabregat-Santiago, F.; Lakus-Wollny, K.; Mankel, E.; Mayer, T.; Jaegermann, W.; Mora-Sero, I., Role of the Selective Contacts in the Performance of Lead Halide Perovskite Solar Cells. *J. Phys. Chem. Lett.* **2014**, *5* (4), 680-685.
105. Lee, D. S.; Yun, J. S.; Kim, J.; Soufiani, A. M.; Chen, S.; Cho, Y.; Deng, X.; Seidel, J.; Lim, S.; Huang, S.; Ho-Baillie, A. W. Y., Passivation of Grain Boundaries by Phenethylammonium in Formamidinium-Methylammonium Lead Halide Perovskite Solar Cells. *ACS Energy Lett.* **2018**, *3* (3), 647-654.
106. Yao, K.; Wang, X.; Xu, Y.-x.; Li, F., A general fabrication procedure for efficient and stable planar perovskite solar cells: Morphological and interfacial control by in-situ-generated layered perovskite. *Nano Energy* **2015**, *18*, 165-175.
107. Lin, Y.; Bai, Y.; Fang, Y.; Chen, Z.; Yang, S.; Zheng, X.; Tang, S.; Liu, Y.; Zhao, J.; Huang, J., Enhanced Thermal Stability in Perovskite Solar Cells by Assembling 2D/3D Stacking Structures. *J. Phys. Chem. Lett.* **2018**, *9* (3), 654-658.
108. Cho, K. T.; Grancini, G.; Lee, Y.; Oveisi, E.; Ryu, J.; Almora, O.; Tschumi, M.; Schouwink, P. A.; Seo, G.; Heo, S.; Park, J.; Jang, J.; Paek, S.; Garcia-Belmonte, G.; Nazeeruddin, M. K., Selective growth of layered perovskites for stable and efficient photovoltaics. *Energy Environ. Sci.* **2018**.
109. Ogomi, Y.; Morita, A.; Tsukamoto, S.; Saitho, T.; Shen, Q.; Toyoda, T.; Yoshino, K.; Pandey, S. S.; Ma, T.; Hayase, S., All-Solid Perovskite Solar Cells with HOCO-R-NH₃⁺I⁻ Anchor-Group Inserted between Porous Titania and Perovskite. *J. Phys. Chem. C* **2014**, *118* (30), 16651-16659.
110. Bao, Q.; Liu, X.; Braun, S.; Fahlman, M., Oxygen- and Water-Based Degradation in [6,6]-Phenyl-C61-Butyric Acid Methyl Ester (PCBM) Films. *Adv. Energy Mater.* **2014**, *4* (6), 1301272-n/a.
111. Domanski, K.; Correa-Baena, J.-P.; Mine, N.; Nazeeruddin, M. K.; Abate, A.; Saliba, M.; Tress, W.; Hagfeldt, A.; Grätzel, M., Not All That Glitters Is Gold: Metal-Migration-Induced Degradation in Perovskite Solar Cells. *ACS Nano* **2016**, *10* (6), 6306-6314.
112. Smith, M. D.; Watson, B. L.; Dauskaradt, R. H.; Karunadasa, H. I., Broadband Emission with a Massive Stokes Shift from Sulfonium Pb-Br Hybrids. *Chem. Mater.* **2017**, *29* (17), 7083-7087.
113. Dalvi, V. H.; Rossky, P. J., Molecular origins of fluorocarbon hydrophobicity. *Proc. Natl. Acad. Sci. U. S. A.* **2010**, *107* (31), 13603-13607.
114. Frost, J. M.; Butler, K. T.; Brivio, F.; Hendon, C. H.; van Schilfgaarde, M.; Walsh, A., Atomistic Origins of High-Performance in Hybrid Halide Perovskite Solar Cells. *Nano Lett.* **2014**, *14* (5), 2584-2590.

2. Toward Fluorinated Spacers for MAPI-Derived Hybrid Perovskites: Synthesis, Characterization, and Phase Transitions of $(\text{FC}_2\text{H}_4\text{NH}_3)_2\text{PbCl}_4$

Claudia Lermer, Susanne T. Birkhold, Igor L. Moudrakovski, Peter Mayer, Leslie M. Schoop, Lukas Schmidt-Mende, and Bettina V. Lotsch,

published in: *Chem. Mater.* **2016**, *28*, 6560–6566

DOI: 10.1021/acs.chemmater.6b02151

<http://dx.doi.org/10.1021/acs.chemmater.6b02151>

Formatting and numbering of figures were changed.

Adapted with permission from The American Chemical Society

Abstract

The intrinsic moisture sensitivity of the hybrid perovskite methylammonium lead iodide (MAPI) calls for new synthetic strategies to enhance moisture resistance and, thus, long-term stability. Here, we combine two strategies: (i) transitioning from 3D to 2D hybrid perovskites by inserting larger A-site cations as spacers and (ii) using fluorinated linkers to enhance the hydrophobicity of the material - and identify two new hybrid perovskite-type compounds, $(\text{FC}_2\text{H}_4\text{NH}_3)_2\text{PbCl}_4$ and $(\text{FC}_2\text{H}_4\text{NH}_3)\text{PbBr}_3\cdot\text{DMF}$, carrying 2-fluoroethylammonium $(\text{FC}_2\text{H}_4\text{NH}_3)^+$ as a promising organic cation for the synthesis of moisture-resistant hybrid perovskites. $(\text{FC}_2\text{H}_4\text{NH}_3)_2\text{PbCl}_4$ features a two-dimensional structure and pronounced long-term stability as confirmed by single-crystal and powder X-ray diffraction. The observed reversible phase transitions at 87 and 107 °C investigated with thermal analysis, temperature-dependent powder X-ray diffraction measurements, and ^1H , ^{13}C , and ^{207}Pb solid-state NMR spectroscopy can be assigned to changes in the inorganic lead chloride and organic sublattices, respectively, both having clearly observable fingerprints in the solid-state NMR spectra. DFT calculations trace the origin of the observed severe distortion of the inorganic sublattice in $(\text{FC}_2\text{H}_4\text{NH}_3)_2\text{PbCl}_4$ back to structural features including the formation of hydrogen bonds. The optical properties of $(\text{FC}_2\text{H}_4\text{NH}_3)_2\text{PbCl}_4$ were characterized by optical absorption spectroscopy and time-resolved photoluminescence measurements with a view toward the interaction between the organic and inorganic sublattices. The broad

photoluminescence spectrum as well as specific absorption characteristics are assigned to exciton self-trapping due to a strong coupling of the excited states to lattice distortions.

2.1 Introduction

Research in the field of hybrid perovskites has experienced a rapid revival since the discovery of the superior optical and electronic properties of methylammonium lead iodide (MAPI) as an absorber material in solar cells. Its large absorption coefficient,¹ medium band gap,² and long hole and electron diffusion lengths,³ combined with its solution processability, accelerated the development into one of the most important semiconductor materials for solid-state solar cells.⁴ On the way to commercialization of hybrid perovskite solar cells, some challenges still have to be addressed, including the toxicity of lead and the poor moisture stability of MAPI-type hybrid perovskites.⁵ Recently, Smith et al. reported a promising strategy to increase the moisture resistivity of MAPI-derived compounds significantly. They separated the 3D lead iodide lattice by inserting bulky phenethylammonium cations (PEA) in the fashion of Mitzi's tin-based hybrid perovskites, namely, $(C_4H_9NH_3)_2(CH_3NH_3)_{n-1}Sn_nI_{3n+1}$ (n = number of corner-sharing SnI_6 octahedra forming the perovskite block), where butylammonium cations isolated the conducting perovskite layers to form a 2D quantum well-type structure.⁶ Upon exposure of the as-obtained $(PEA)_2(MA)_2[Pb_3I_{10}]$ ($CH_3NH_3^+ = MA$) to a moist atmosphere, no degradation was observed. This is a testament to the higher stability inherent to many 2D perovskites and at the same time allows for the fabrication of high quality thin films, without sacrificing too much of the inherent optoelectronic properties of MAPI's 3D structure.^{7, 8} Kanatzidis and co-workers explored this concept for the $(CH_3(CH_2)_3NH_3)_2(CH_3NH_3)_{n-1}Pb_nI_{3n+1}$ series and coined the terms *perovskitizer* and *spacer* for the cations forming the hybrid perovskite structure and those separating the quasi-3D perovskite blocks, respectively. Increasing the moisture resistivity is not the only benefit of including bulky organic cations in the structure; it also presents a synthetic tool for precisely tailoring the optical and electronic properties by the choice of the *spacer* cation and the number of layers in the perovskite blocks.⁹

A useful empirical guide for the search of suitable new *perovskitizers* and *spacers* is Goldschmidt's tolerance factor t , which determines the range of existence of the 3D perovskite structure ABX_3 based on the radius ratio of the constituents A, B, and X. t is determined by the following equation:¹⁰

$$t = (r_A + r_X) / \sqrt{2}(r_B + r_X) \quad (1)$$

A cubic perovskite structure can be expected, if t is in the range 0.9–1.0. Additionally, distorted perovskite structures are likely to form for values from 0.80 to 0.89.¹¹ $(CH_3CH_2NH_3)PbI_3$, which

seems to be very similar to MAPI at first sight, contains one-dimensional (1D) face-sharing PbI_6 octahedral chains.¹² The different structures become comprehensible, when taking the tolerance factor, which was calculated to be 1.05(4) by Kieslich et al., into account.¹¹ Thus, cations which have at least the size of an ethylammonium cation are likely to be suitable candidates as spacers. It is widely known that exchanging hydrogen atoms by fluorine atoms in hydrocarbons increases its hydrophobicity immensely.¹³ Thus, applying fluorinated cations as spacers in hybrid perovskites would be a natural choice to further increase the moisture resistivity while potentially increasing the polarity at the same time. Furthermore, the studies by Frost et al. strongly suggest that increasing the dipole moment of the chosen organic cation could improve charge separation and increase carrier lifetimes due to an enhanced polarization of the crystal lattice, resulting in well-separated “ferroelectric highways” for both charge carriers.¹⁴ For these reasons, an investigation of fluorinated A-site cations is the next step for developing new potentially ferroelectric 2D hybrid perovskites with further enhanced moisture resistance. In this work a new two-dimensional (2D) hybrid perovskite, $(\text{FC}_2\text{H}_4\text{NH}_3)_2\text{PbCl}_4$, was synthesized, and its structural, thermal, and optical properties were investigated. The formation of a 2D structure indicates the ability of fluoroethylammonium to act as a spacer for MAPI-based compounds. Exposure to ambient atmosphere for several months did not have any effect on the compound’s integrity. Additionally, the crystal structure of the related DMF solvate $(\text{FC}_2\text{H}_4\text{NH}_3)\text{PbBr}_3\cdot\text{DMF}$ was determined, showing a transition from the 2D structure in $(\text{FC}_2\text{H}_4\text{NH}_3)_2\text{PbCl}_4$ to a 1D chain-like structure in $(\text{FC}_2\text{H}_4\text{NH}_3)\text{PbBr}_3\cdot\text{DMF}$.

2.2 Experimental Section

Materials and Methods. PbCl_2 (Sigma-Aldrich, 98%), PbBr_2 (Sigma-Aldrich, $\geq 98\%$), 2-fluoroethylamine hydrochloride (Sigma-Aldrich, 90%), concentrated hydrochloric acid (Brenntag, purum), concentrated hydrobromic acid (Acros Organics, pure), and dimethylformamide (Alfa Aesar, 99%) were commercially available and used as received without further purification.

Synthesis of $\text{FC}_2\text{H}_4\text{NH}_3\text{Cl}$ and $\text{FC}_2\text{H}_4\text{NH}_3\text{Br}$. 1.16×10^{-1} mL (1.36 mmol) concentrated HCl or 1.55×10^{-1} mL (1.36 mmol) concentrated HBr were added to 150 mg (1.36 mmol) of 2-fluoroethylamine hydrochloride while cooling with an ice bath, respectively. The reaction mixture was stirred for 2.5 h at 0 °C. The solvent was subsequently removed by heating to 50 °C under nitrogen flow. The yellowish product was washed with ether until a white color was obtained. Anal. Calcd for $\text{FC}_2\text{H}_4\text{NH}_3\text{Cl}$: C, 24.13; H, 7.09; N, 14.07 wt %. Found: C, 21.20; H, 7.11; N, 5.53 wt %. IR (cm^{-1}): 3000(m), 2969(m), 2893(m), 2822(m), 2768(m), 2679(m), 2634(m), 2482(w), 2013(w), 1607(m), 1513(m), 1455(w), 1401(w), 1361(w), 1325(w), 1272(w), 1178(w), 1133(w), 1066(m), 994(s), 977(s), 876(w), 825(w). ^1H NMR (DMSO-d_6 , 20 °C) δ = 8.43 (s, 3H, $-\text{NH}_3$), 4.66

(d_t, 2H, F-CH₂), 3.12 (d_t, 2H, H₃N-CH₂) ppm. ¹³C NMR (DMSO-d₆, 20 °C) δ = 80.5 (d, F-CH₂), 39.1 (d, H₃N-CH₂) ppm. Anal. Calcd for FC₂H₄NH₃Br: C, 16.68; H, 4.90; N, 9.73 wt %. Found: C, 15.24; H, 4.81; N, 10.16 wt %. IR (cm⁻¹): 3095(m), 3015(m), 2925(m), 2796(m), 2666(w), 2616(w), 2456(w), 2362(w), 2331(w), 1579(m), 1562(m), 1510(m), 1448(w), 1435(w), 1396(m), 1304(w), 1269(w), 1168(w), 1121(w), 1067(m), 983(s), 951(s), 870(m), 669(w). ¹H NMR (DMSO-d₆, 20 °C) δ = 8.01 (s, 3H, -NH₃), 4.64 (d_t, 2H, F-CH₂), 3.17 (d_t, 2H, H₃N-CH₂) ppm. ¹³C NMR (DMSO-d₆, 20 °C) δ = 80.6 (d, F-CH₂), 39.3 (d, H₃N-CH₂) ppm.

Synthesis of (FC₂H₄NH₃)₂PbCl₄. 71.5 mg (0.72 mmol) FC₂H₄NH₃Cl, 102.0 mg (0.36 mmol) PbCl₂, and 1.2 mL DMF were heated to 80 °C for 2 h, whereupon the solids were dissolved completely. Single crystals suitable for X-ray diffraction analysis were obtained by evaporating the solvent at room temperature.

Synthesis of (FC₂H₄NH₃)PbBr₃·DMF. 28.8 mg (0.2 mmol) FC₂H₄NH₃Br, 74.9 mg (0.2 mmol) PbBr₂, and 1.0 mL DMF were heated to 80 °C for 2 h, whereupon the solids were dissolved completely. Single crystals suitable for X-ray diffraction analysis were obtained by evaporating the solvent at room temperature.

Characterization. Single-crystal X-ray diffraction data of (FC₂H₄NH₃)₂PbCl₄ were collected at -100 °C on a Bruker D8 Venture diffractometer equipped with a rotating anode generator with Mo K_α radiation (λ = 0.71073 Å). The diffraction intensities were integrated using the SAINT software package, and a multiscan absorption correction was applied with SADABS. The crystal structure was solved by direct methods (SIR97)¹⁵ and refined against F² by applying the full-matrix least-squares method (SHELXL-97).^{16, 17} C-bound hydrogen positions were calculated according to geometrical criteria and treated as riding on their parent atoms while N-bound hydrogen atoms were refined freely. All non-hydrogen atoms were refined anisotropically.

Powder X-ray diffraction (PXRD) patterns of (FC₂H₄NH₃)₂PbCl₄ were collected at various temperatures using a Bruker D8-Advance diffractometer in Debye-Scherrer geometry with a Vântec detector with Ge(111)-monochromated Cu K_{α1} radiation (λ = 1.54059 Å). The sample was encapsulated in a capillary under inert atmosphere; nonetheless, air stability was confirmed thereafter. For further PXRD measurements at room temperature, a Huber G670 Guinier imaging plate detector in transmission geometry was used. These measurements were also performed with Ge(111)-monochromated Cu K_{α1} radiation (λ = 1.54059 Å). Full profile fits were obtained using TOPAS Academic.¹⁸

Solid-state NMR spectra were recorded on a Bruker Avance-III WB 400 MHz (H₀ = 9.4 T) instrument. A Bruker double resonance BL4MAS probe and 4 mm zirconia rotors were used for all measurements. ¹³C and ¹H spectra were referenced to the customary standard tetramethylsilane (TMS), using the high frequency signal of solid adamantane at 38.56 ppm as a secondary standard in ¹³C spectra and the signal at 1.74 ppm in ¹H spectra. In experiments with

magic-angle spinning (MAS), the sample was spun between 8000 and 12500 Hz, with the spinning rate controlled by the standard Bruker equipment. The ^1H spectra were acquired in 16 scans with a relaxation delay of 3 s. The ^{13}C cross-polarization (CP) MAS spectra were recorded in 1024 scans with a contact time of 4 ms and a recycle delay of 1 s. All ^{13}C and ^{207}Pb spectra were acquired with high power proton decoupling that was achieved using the SPINAL-64 decoupling method. ^{207}Pb spectra were referenced to tetramethyl lead ($\delta = 0.0$ ppm) with the solid $\text{Pb}(\text{NO}_3)_2$ as a secondary standard ($\delta = -3494$ ppm at 20°C and MAS of 1500 Hz). ^{207}Pb MAS spectra were recorded with rotor-synchronized Hahn-echo. The sample was spun at 8000 Hz for the measurement at 85°C and at 10000 Hz for all of the other measurements. The repetition time was set to 4 s, and the number of scans was 2048.

Differential scanning calorimetry (DSC) data was collected using a Linseis PT10 calorimeter. Samples were heated in sealed aluminum pans under air from room temperature to 125°C with a heating rate of 3 K min^{-1} and subsequently cooled down to room temperature at the same rate. Additionally, DSC measurements were performed using a PerkinElmer Pyris 1. The sample was heated from -46 to 195°C with a heating rate of 3 K min^{-1} and subsequently cooled down to room temperature at the same rate.

Optical samples were prepared by clamping $(\text{FC}_2\text{H}_4\text{NH}_3)_2\text{PbCl}_4$ powder between two quartz glass substrates. Absorption spectra were recorded with an Agilent Technologies 8453 UV-vis spectrometer in an integrating sphere. For steady-state and time-resolved photoluminescence measurements, a PicoQuant FluoTime 300 fluorescence spectrometer was used. Steady-state photoluminescence was measured using a 300 W xenon arc lamp. The excitation source for time-resolved photoluminescence measurements was a picosecond pulsed laser diode of 405 nm, and the decay was recorded on the basis of time-correlated single photon counting.

FTIR spectra were recorded at ambient conditions between 650 and 4000 cm^{-1} on a Spektrum BX II FTIR spectrometer (PerkinElmer) equipped with a DuraSampler diamond ATR device.

Elemental analyses for C, H, and N were performed with the elemental analyzer systems Vario EL and Vario Micro (Elementar Analysensysteme GmbH).

Electronic structure calculations were performed in the framework of density functional theory (DFT) using the Wien2k¹⁹ code with a full-potential linearized augmented planewave and local orbitals [FP-LAPW + lo] basis²⁰⁻²² together with the Perdew-Burke-Ernzerhof (PBE) parametrization²³ of the generalized approximation (GGA) as the exchange-correlation functional. Spin-orbit coupling was included. The plane wave cutoff parameter $R_{\text{MT}}K_{\text{max}}$ was set to 7, and the irreducible Brillouin zone was sampled by 147 k-points.

2.3 Results and Discussion

Structural Investigation of $(\text{FC}_2\text{H}_4\text{NH}_3)_2\text{PbCl}_4$. The stoichiometric reaction of PbCl_2 and 2-fluoroethylammonium chloride in DMF led to phase-pure $(\text{FC}_2\text{H}_4\text{NH}_3)_2\text{PbCl}_4$. The crystal structure of the 2D organic–inorganic perovskite $(\text{FC}_2\text{H}_4\text{NH}_3)_2\text{PbCl}_4$ was determined by single-crystal X-ray diffraction at 173 K. Crystallographic data and details of the structure refinement are shown in Tables SI–SV. The compound crystallizes in a layered 2D perovskite-type structure akin to halide representatives of the Ruddlesden-Popper phases with $n = 1$, where n is the number of corner-sharing octahedral layers in the perovskite blocks $[\text{ABX}_3]_n$, interleaved with n $[\text{AX}]$ blocks with rock-salt-type structure. $(\text{FC}_2\text{H}_4\text{NH}_3)_2\text{PbCl}_4$ comprises layers of trans-connected, corner-sharing PbCl_6 octahedra, which are severely distorted (Figure 1). Possible reasons for this distortion will be discussed in detail later on. The organic cations form a double-layer which is stabilized by weak *intermolecular* hydrogen bonds.²⁴ *Intramolecular* hydrogen bonds between the fluorine substituents and the protonated amine groups lead to the observed *cis*-configuration of the 2-fluoroethylammonium cations (Table SVI). The distance between the PbCl_4^{2-} layers was determined to be 9.51 Å. $(\text{FC}_2\text{H}_4\text{NH}_3)_2\text{PbCl}_4$ exhibits $Pnma$ symmetry. Due to the centrosymmetric nature of the space group, ferroelectric properties cannot be expected for $(\text{FC}_2\text{H}_4\text{NH}_3)_2\text{PbCl}_4$. In contrast to the chloride version discussed above, the reaction of fluoroethylammonium bromide with lead bromide in DMF leads to the formation of a dimensionally reduced DMF solvate in which the 2D lead bromide layers are broken up into 1D double chains consisting of edge-sharing octahedra. A discussion of the crystal structure of the resulting compound, $(\text{FC}_2\text{H}_4\text{NH}_3)\text{PbBr}_3 \cdot \text{DMF}$, and additional experimental details can be found in the Supporting Information S8–S12.

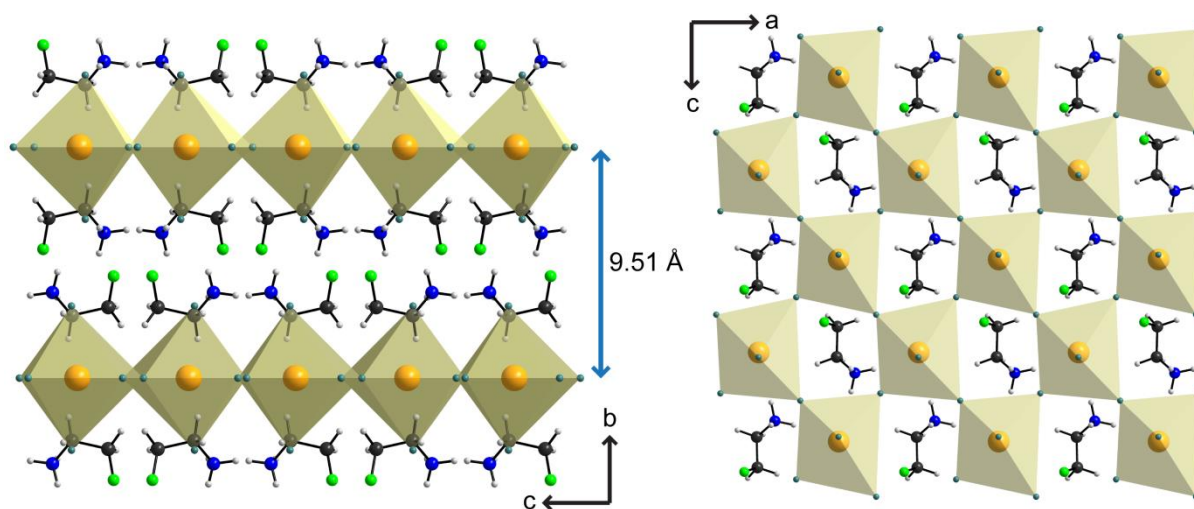


Figure 2.1. Crystal structure of $(\text{FC}_2\text{H}_4\text{NH}_3)_2\text{PbCl}_4$ in projection along $[100]$ (left) and in projection along $[0\bar{1}0]$ (right). C is displayed in black, N is blue, F is green, H is gray, Pb is orange, and Cl is turquoise.

DFT Calculations. The PbCl_6 octahedra in $(\text{FC}_2\text{H}_4\text{NH}_3)_2\text{PbCl}_4$ exhibit Pb–Cl bond lengths between 2.7001(7) and 3.2054(7) Å and bond angles between 86.5° and 93.9° (Tables SIV and SV). Related compounds reported in the literature, namely, $(\text{C}_3\text{H}_7\text{NH}_3)_2\text{PbCl}_4$ and $(\text{C}_6\text{H}_5\text{C}_2\text{H}_4\text{NH}_3)_2\text{PbCl}_4$, show a qualitatively similar, however much smaller, distortion of the Pb atom coordination sphere with Pb-Cl bond lengths in the ranges 2.830(7)-2.899(7) Å and 2.752(2)-3.033(2) Å, respectively.^{25, 26} In order to investigate the origin of this rather severe distortion present in $(\text{FC}_2\text{H}_4\text{NH}_3)_2\text{PbCl}_4$, electronic structure calculations on the DFT level including spin-orbit coupling were performed. If the origin was due to a sterically active Pb 6s lone pair, we would expect to see hybridization between *s* and *p* states at the Fermi level. This hybridization would result in a stereochemically active lone pair that is not centrosymmetric and could therefore reside off-center within an octahedron, causing distortion. Analysis of the partial density of states (PDOS) reveals that the valence band consists mostly of Cl 3*p* states, mixed with Pb 6*s* and Pb 6*p* states. The Pb 6*s* states are found in the upper valence band whereas the Pb 6*p* states are located in the lower valence band. Additional Pb 6*s* states are localized below -6 eV. The conduction band is dominated by Pb 6*p* states. Taking a closer look at the upper valence band, a small fraction of 6*p* states can be observed at the same energy level as 6*s* states which allows for hybridization of these states (Figure 2a,b). This could suggest the presence of a steric effect of the lone pair that can follow from canceling out the centrosymmetry of the *s* orbital by adding *p* character. However, in our case this effect is presumably very small, since the density of Pb *p* states in the upper valence band is below 0.014 states (formula unit)⁻¹ eV⁻¹. Therefore, the octahedral distortions seem to be of structural rather than electronic origin, which becomes apparent when projecting the crystal structure down the *b* axis (Figure 1). The size of the organic cations exactly matches the vacancies within the octahedral network; therefore, the octahedral distortion results in an optimal dense packing. Additionally, moderate and weak hydrogen bonds²⁴ between the organic cations and the Cl atoms of the inorganic lattice might contribute to the observed structural distortions (Table SVI). The calculated bandgap is 2.51 eV which is significantly lower than the measured band gap of 3.27 eV. The PBE functional used for our calculations is, however, well-known to underestimate band gaps, and the discrepancy of 0.75 eV is within the usual range of underestimation. The organic cations do not seem to have any influence on the band gap as an analysis of the respective states shows (Figure S2a). The band structure plot (Figure 2c) reveals the band gap to be indirect, with the valence band maximum located at Γ and the conduction band minimum located between Γ and Z. Fat band plots also show the presence of a Pb 6*s* lone pair (Figure S2b).

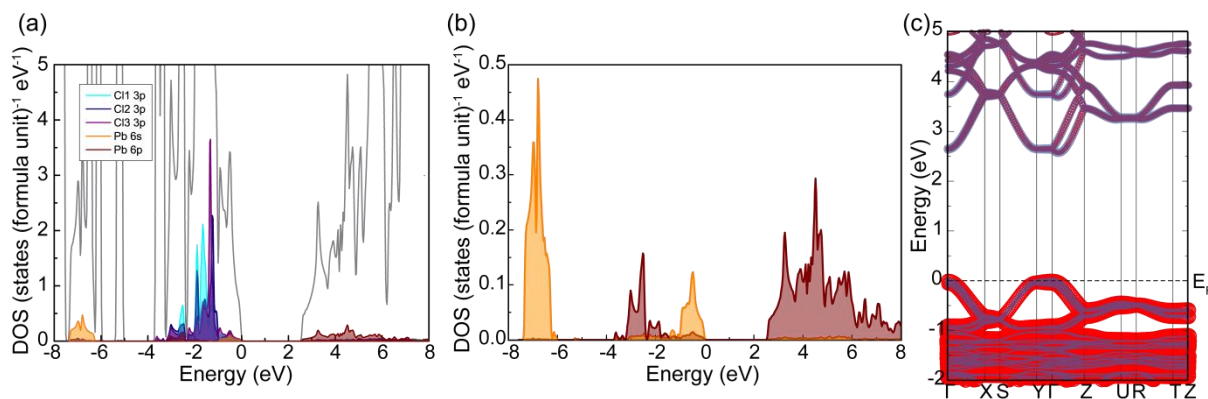


Figure 2.2. (a) Partial density of states (PDOS) plot for $(\text{FC}_2\text{H}_4\text{NH}_3)_2\text{PbCl}_4$, showing 3p states of the three different Cl sites as well as Pb 6s and 6p states. The total DOS is plotted in gray in the background. The positions of the Pb 6s and 6p states are highlighted in part b. (c) Band structure of $(\text{FC}_2\text{H}_4\text{NH}_3)_2\text{PbCl}_4$. Contributions from Cl states are indicated in red, whereas Pb states are shown in blue (all orbitals). The overlay of the red and blue bands results in the color purple. The thickness of the bands is a measure for the contribution of those states.

Phase Transitions in $(\text{FC}_2\text{H}_4\text{NH}_3)_2\text{PbCl}_4$. DSC measurements indicate two reversible phase transitions at 87 °C and at 107 °C, which were determined from the heating cycle (Figure S3). These were investigated more closely using solid-state NMR spectroscopy. To probe both the effect of structural distortions and rearrangements in the organic and inorganic sublattices, the spectra of ^1H , ^{13}C , and ^{207}Pb were monitored. While $(\text{FC}_2\text{H}_4\text{NH}_3)_2\text{PbCl}_4$ was heated up to 112.5 °C followed by cooling down to room temperature, several ^{207}Pb solid-state NMR spectra were recorded (Figure 3b). ^{207}Pb is a spin 1/2 nucleus with an extremely wide chemical shift range, with Pb(II) covering a range between 3000 and -6000 ppm. The observed chemical shifts are in agreement with the oxidation state Pb(II), while the highly anisotropic shape of the signal observed below the first phase transition points to an asymmetrical coordination sphere of the Pb atoms. This observation is in accordance with the above-described severely distorted PbCl_6 octahedra. The first phase transition is therefore most likely connected to a change in the inorganic sublattice producing a more symmetrical lead environment, and accompanied by a substantially reduced anisotropy and a shift of the signal from -237 ± 2 ppm to -971 ± 2 ppm. These changes are found to be reversible upon cooling the sample down to room temperature. Apart from a small downfield shift, the second phase transition is not observed in the ^{207}Pb spectrum, which essentially excludes an involvement of the Pb-Cl lattice in the phase transition. Presumably, the second phase transition is related to small changes in the mobility or orientation of the A-site cation. ^1H solid-state NMR spectra show three overlapping signals that can be assigned to the protons of the NH_3 -group and the two methylene groups, respectively (Figure 3a). The assignment is based on the relative integrated intensities, and expected relative shifts in ^1H resonances of $-\text{CH}_2-$ and $-\text{CH}_2\text{F}$ signals. The first phase transition leads to a downfield shift and a

narrowing of the observed signals, which supports the assumption that the 2-fluorethylammonium cations become more mobile due to the change in the heavy lattice. As a consequence, they can rotate more freely. The second phase transition does not have a visible fingerprint in the ^1H NMR spectra.

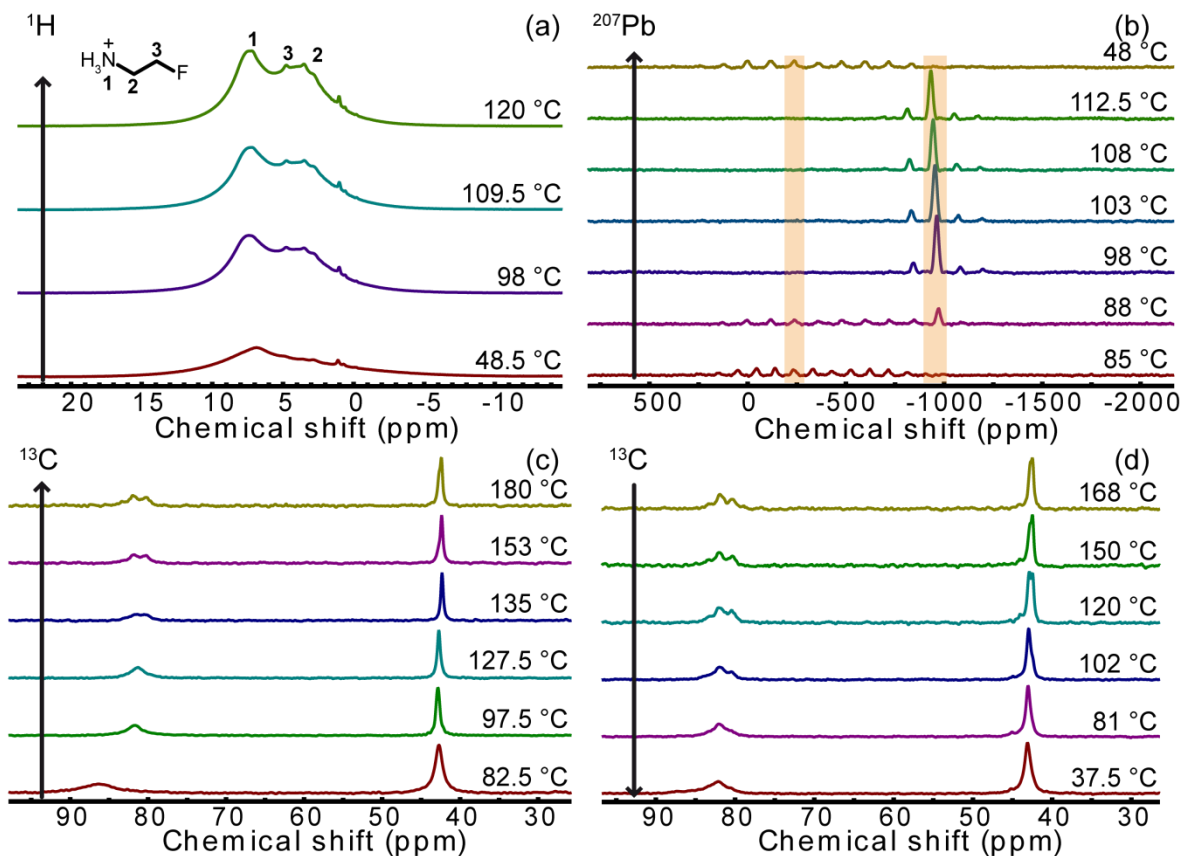


Figure 2.3. (a) ^1H MAS, (b) ^{207}Pb MAS, and (c, d) ^{13}C CP MAS solid-state NMR spectra of $(\text{FC}_2\text{H}_4\text{NH}_3)_2\text{PbCl}_4$. The arrows indicate the course of the temperature program. The isotropic signals are highlighted for the ^{207}Pb NMR spectra. The remaining signals (b) are spinning side bands.

Finally, a temperature-dependent structural investigation using ^{13}C solid-state NMR spectroscopy was performed (Figure 3c,d). The recorded ^{13}C solid-state NMR spectra show two distinct signals which are assigned to the carbon atoms of the methylene groups. Upon heating the sample above the first transition temperature, a narrowing of the signals can be observed besides a significant upfield shift of the signal detected at 86.4 ppm. This signal splits up into two when the temperature is increased above 127.5 °C. It is conceivable that this signature at 127.5 °C is associated with a delayed second phase transition which is seen at 107 °C in the DSC measurements. A possible reason for the splitting is the direct spin-spin J-coupling between adjacent F and C atoms. However, the doublet should be more distinct in this case. Therefore, it is most likely that what we see is not entirely due to ^{19}F - ^{13}C J-coupling, but also due to melting of the organic sublattice above the transition temperature, giving rise to dynamical disorder of the

organic cations. The signal at 42.4 ppm starts splitting up only at 180 °C. These later changes are partly reversible upon cooling down and are not distinctly related to either of the structural phase transitions. The changes associated with the first phase transition, however, are persistent. To summarize, heating $(\text{FC}_2\text{H}_4\text{NH}_3)_2\text{PbCl}_4$ above 130 °C leads to a permanent structural change, but the compound is not decomposed upon heating it up to 180 °C.

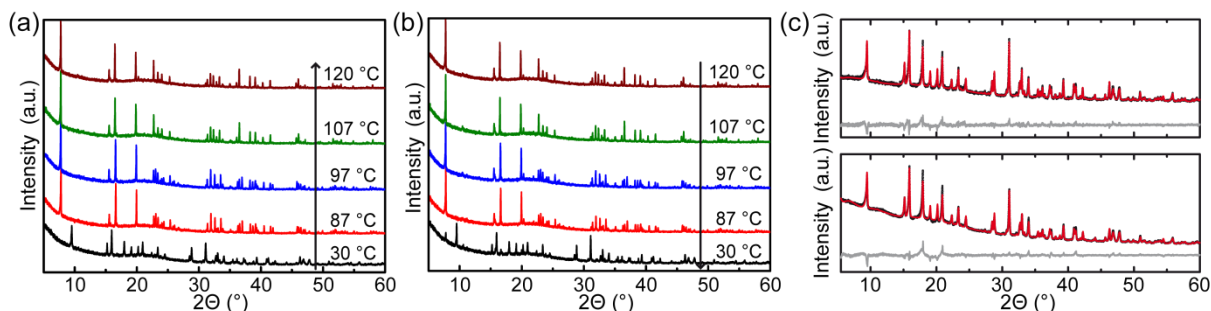


Figure 2.4. Powder X-ray diffraction patterns monitoring the phase transitions upon (a) heating the sample to 120 °C and (b) cooling the sample back down to 30 °C. X-ray powder diffraction data of $(\text{FC}_2\text{H}_4\text{NH}_3)_2\text{PbCl}_4$ acquired at room temperature right after synthesis (bottom) and after 4 months exposure to ambient conditions (top) represented by open circles. (c) Rietveld profile fits (red solid lines) confirm phase purity. The difference curves are displayed in gray.

Powder X-ray Diffraction (PXRD). PXRD was used to complement the above-described insights into the reversibility and local structural changes during the temperature dependent structural phase transitions of $(\text{FC}_2\text{H}_4\text{NH}_3)_2\text{PbCl}_4$ (Figure 4a,b). The structural change connected to the first phase transition becomes obvious on comparing the dissimilar diffractograms recorded at 30 and 87 °C. Only small additional changes can be observed when the sample is heated to 120 °C, which consolidates the assumption that the second phase transition is not connected to any significant structural changes in the inorganic sublattice. When cooling the sample back down to 30 °C, the initial diffractogram recorded at 30 °C is regained almost completely. Only the reflection at 7.75° which is very prominent in the diffractograms of the high temperature phase has not vanished completely despite a significant loss in intensity. Recording another diffractogram of the sample 1 year after conducting the heating cycle shows that the phase transition is indeed fully reversible: the reflection at 7.75° cannot be observed anymore (Figure S4). These results indicate that the conversion from the high temperature to the low temperature phase might be kinetically delayed.

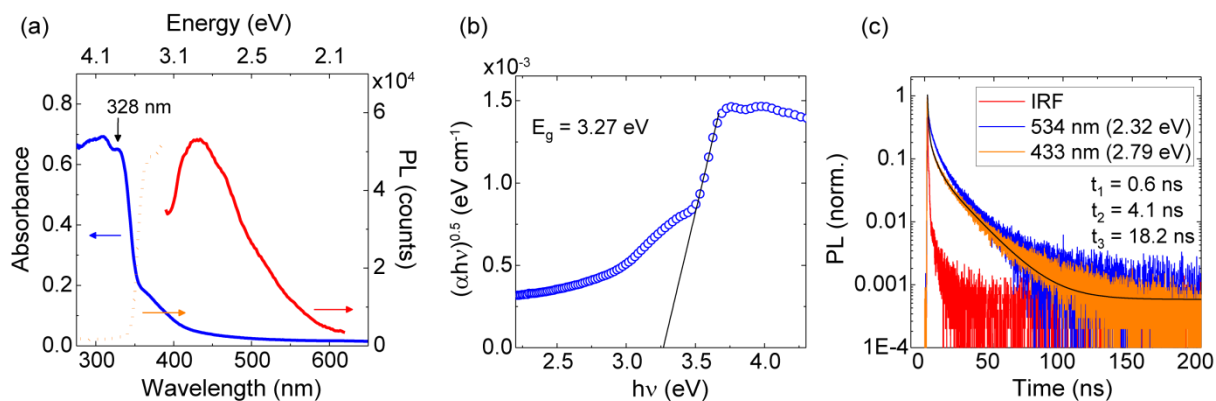


Figure 2.5. (a) Absorbance (blue solid line), photoluminescence (red solid line, $\lambda_{\text{excitation}} = 375$ nm), and photoluminescence excitation spectrum (orange dots, $\lambda_{\text{emission}} = 443$ nm) of $(\text{FC}_2\text{H}_4\text{NH}_3)_2\text{PbCl}_4$ at 295 K. (b) Tauc plot with an indirect band gap of 3.27 eV. (c) PL decay of $(\text{FC}_2\text{H}_4\text{NH}_3)_2\text{PbCl}_4$ at different emission energies at 295 K and the instrument response function (IRF). The PL decay at 2.79 eV is fitted with a three-exponential decay function (black line).

Optical Properties. Absorption and photoluminescence measurements were performed to investigate the optical properties of $(\text{FC}_2\text{H}_4\text{NH}_3)_2\text{PbCl}_4$. The absorbance spectrum of $(\text{FC}_2\text{H}_4\text{NH}_3)_2\text{PbCl}_4$ is presented in Figure 5a. With the assumption of an indirect band gap (also confirmed by DFT calculations, see above), a band gap of 3.27 eV is determined with a Tauc plot, which is comparable to other organic-inorganic layered perovskite compounds (Figure 5b).^{1, 27, 28} Typically, these layered perovskites feature a sharp excitonic absorption peak below the band edge, as the dielectric mismatch between organic and inorganic layer causes a high exciton binding energy and strongly bound excitons within the inorganic layer.²⁷⁻²⁹ As can be seen in Figure 5a, a clear separation between the absorption band edge and the excitonic peak for $(\text{FC}_2\text{H}_4\text{NH}_3)_2\text{PbCl}_4$ cannot be observed, but there is an overlap of a peak at 328 nm and the band edge. Such a close occurrence of an excitonic absorption peak and the band edge has already been reported for other organic-inorganic layered perovskite compounds³⁰ and can be explained by the fact that the optical properties strongly depend on the organic moiety. Possible effects of the organic layer on excited states within the inorganic layer include a change of the exciton binding energy depending on the organic layer's dielectric constant, a potential energy transfer into the organic layer,³¹ and structural distortions of the inorganic layer imposed by the organic layer.^{30, 32, 33} Consequently, differences in optical properties for different organic-inorganic layered perovskite compounds can be expected. While for excitation above the bandgap, no significant photoluminescence can be detected (Figure S5a); excitation into the sub-bandgap absorption feature between 350 and 400 nm leads to a strong and broad photoluminescence (PL) spectrum (Figure 5a). As the PL excitation spectrum for the PL emission peak at 443 nm coincides well with the sub-bandgap absorption feature for wavelengths above 350 nm, it can be assumed that excitation of these sub-bandgap states leads to enhanced radiative recombination. The origin of

such a broad emission has already been discussed by Dohner et al.,²⁸ who assigned the broad PL to strong coupling of excited states to lattice distortions and the inhomogeneous broadening of the PL spectrum to additional contributions of trap states. Similarly, Papavassiliou et al.³² investigated the impact of the organic moiety on PL properties and found that organic layers consisting of short alkyl chains lead to a broad PL spectrum due to self-trapped excitons, whereas longer alkyl chains lead to sharp excitonic PL peaks. These observations are consistent with the data presented here, as the crystal structure of $(\text{FC}_2\text{H}_4\text{NH}_3)_2\text{PbCl}_4$ features severe structural distortions of the inorganic sublattice at room temperature, which is assumed to induce self-trapping of excitons due to a coupling to lattice distortions. Moreover, an impact of the fluorine in the organic moiety on the PL properties cannot be excluded either. The fact that the PL spectrum can be excited by excitation energies that are almost as small as the emission energy indicates a continuum of initial states that can contribute to the broad PL spectrum. Such a broad distribution of emitting states cannot be explained by a specific crystal defect, but rather by a continuous energy distribution of lattice distortions. The inhomogeneous broadening of the PL spectrum of $(\text{FC}_2\text{H}_4\text{NH}_3)_2\text{PbCl}_4$ can be fitted with two Gaussian functions with peak positions at 2.79 and 2.32 eV, respectively (Figure S6b). Both the lower energy shoulder and the broad PL emission can be excited by the same absorption features (Figure S5b) and have similar lifetimes (Figure 5c), suggesting the same physical nature of these states and thermal equilibrium between them.²⁸ However, as Figure S6b displays an increase of the lower energy shoulder for a decrease in temperature, an enhanced trapping rate of excited states can be assumed for lower temperatures. The photoluminescence decay displayed in Figure 5c can be fitted with a three-exponential decay function with lifetimes of $t_1 = 0.6$ ns, $t_2 = 4$ ns, and $t_3 = 18$ ns. PL lifetimes of several nanoseconds are characteristic for organic–inorganic layered perovskites.^{28, 33} In contrast to 3D organic–inorganic perovskites, where charge recombination of free electrons and holes determines the PL characteristics at room temperature, leading to lifetimes on the order of hundreds of nanoseconds,^{3, 34} the PL of layered perovskites predominantly originates from confined excitons within the inorganic layer. On the basis of the multiexponential decay, it is suggested that several dynamical processes take place after photoexcitation, including the intrinsic lifetime of free excitons and the formation of self-trapped excitons, as well as their interaction with interface states and potential permanent lattice defects, or intersystem crossing with triplet states.^{33, 35}

Stability. An important finding is that, in contrast to other 2D and 3D hybrid perovskites, $(\text{FC}_2\text{H}_4\text{NH}_3)_2\text{PbCl}_4$ shows pronounced long-term stability. When exposed to ambient conditions over several months, no visible changes can be observed. Rietveld analyses of PXRD data of

(FC₂H₄NH₃)₂PbCl₄ right after synthesis and after 4 months exposure confirm this observation (Figure 4c and Figure S2).

2.4 Conclusions

The crystal structures of the new hybrid compounds, (FC₂H₄NH₃)₂PbCl₄ and (FC₂H₄NH₃)PbBr₃·DMF, were discussed with a special focus on the influence of hydrogen bonds and the origin of structural distortions in the inorganic sublattice on the arrangement of the organic cations. Moreover, the phase transitions of (FC₂H₄NH₃)₂PbCl₄ were investigated closely by combining solid-state NMR spectroscopy, DSC measurements, and PXRD. It could be shown that the first phase transition at 87°C is due to structural changes in the heavy lattice whereas the second phase transition is likely related to orientational changes in the organic sublattice. DFT calculations suggested that the observed distortion of the PbCl₆ octahedra predominantly is of structural origin connected to a dense packing of the organic cations and the inorganic lattice and the formation of hydrogen bonds between the inorganic and organic sublattice, rather than of electronic origin based on hybridization of the Pb 6s lone pair. Optical measurements were applied to study the nature of the photogenerated states and their interaction with the crystal lattice. A strong and broad PL spectrum for excitations below the bandgap is assigned to a coupling of excited states to lattice distortions. The resulting self-trapped excitons lead to a temperature-dependent inhomogeneous broadening of the PL spectrum and a multiexponential PL decay with lifetimes in the nanosecond range. Additionally, it was shown that (FC₂H₄NH₃)₂PbCl₄ features long-term stability under ambient conditions. These findings suggest that the fluoroethylammonium cation is a promising candidate as a spacer for moisture-resistant MAPI-derived compounds due to its ability to create 2-dimensional structures and the demonstrated stability of (FC₂H₄NH₃)₂PbCl₄. Synthesizing a compound that contains several layers of MAPI separated by layers of (FC₂H₄NH₃)⁺ might have the potential for combining the favorable optical properties of MAPI with the better stability of a 2D hybrid perovskite. Additionally, (FC₂H₄NH₃)⁺ features a large dipole moment which might lead to an enhanced polarity of the lattice and with it an increase in charge separation and improved carrier lifetimes as theoretical studies by Frost et al. indicate.¹⁴ These factors point to a number of design criteria which when synergistically combined may give rise to powerful absorber materials for solar cells and related optoelectronic devices.

Acknowledgements

Financial support by the Max Planck Society, “Deutsche Telekom Stiftung” (scholarship for C.L.), the cluster of excellence “Nanosystems Initiative Munich” (NIM), and the Center for NanoScience

(CeNS) is gratefully acknowledged. The authors thank the group of Prof. Thomas Klapötke for the possibility to use their DSC calorimeter and Marc Bölter, M.Sc., for assistance. We also thank Christine Stefani (Dinnebier group, MPI-FKF) for carrying out the temperature-dependent PXRD measurements and Ewald Schmitt (Maier department, MPIFKF) for performing further DSC measurements. L.M.S. gratefully acknowledges financial support by the Minerva fast track program.

2.5 References

1. Mitzi, D. B., Synthesis, Structure, and Properties of Organic-Inorganic Perovskites and Related Materials. In *Progress in Inorganic Chemistry*; Karlin, K. D., Ed.; John Wiley & Sons, Inc.: New York, NY, 1999; pp 1–121.
2. Baikie, T.; Fang, Y.; Kadro, J. M.; Schreyer, M.; Wei, F.; Mhaisalkar, S. G.; Graetzel, M.; White, T. J., Synthesis and crystal chemistry of the hybrid perovskite (CH₃NH₃)PbI₃ for solid-state sensitised solar cell applications. *J. Mater. Chem. A* **2013**, 1, (18), 5628-5641.
3. Stranks, S. D.; Eperon, G. E.; Grancini, G.; Menelaou, C.; Alcocer, M. J. P.; Leijtens, T.; Herz, L. M.; Petrozza, A.; Snaith, H. J., Electron-Hole Diffusion Lengths Exceeding 1 Micrometer in an Organometal Trihalide Perovskite Absorber. *Science* **2013**, 342, (6156), 341-344.
4. Shi, S.; Li, Y.; Li, X.; Wang, H., Advancements in all-solid-state hybrid solar cells based on organometal halide perovskites. *Mater. Horiz.* **2015**, 2, (4), 378-405.
5. Service, R. F., Turning Up the Light. *Science* **2013**, 342, (6160), 794-797.
6. Mitzi, D. B.; Feild, C. A.; Harrison, W. T. A.; Guloy, A. M., Conducting tin halides with a layered organic-based perovskite structure. *Nature* **1994**, 369, (6480), 467-469.
7. Smith, I. C.; Hoke, E. T.; Solis-Ibarra, D.; McGehee, M. D.; Karunadasa, H. I., A Layered Hybrid Perovskite Solar-Cell Absorber with Enhanced Moisture Stability. *Angew. Chem.* **2014**, 126, (42), 11414-11417. Smith, I. C.; Hoke, E. T.; Solis-Ibarra, D.; McGehee, M. D.; Karunadasa, H. I., A Layered Hybrid Perovskite Solar-Cell Absorber with Enhanced Moisture Stability. *Angew. Chem., Int. Ed.* **2014**, 53, 11232–11235.
8. Quan, L. N.; Yuan, M.; Comin, R.; Voznyy, O.; Beauregard, E. M.; Hoogland, S.; Buin, A.; Kirmani, A. R.; Zhao, K.; Amassian, A.; Kim, D. H.; Sargent, E. H., Ligand-Stabilized Reduced-Dimensionality Perovskites. *J. Am. Chem. Soc.* **2016**, 138, (8), 2649-2655.
9. Cao, D. H.; Stoumpos, C. C.; Farha, O. K.; Hupp, J. T.; Kanatzidis, M. G., 2D Homologous Perovskites as Light-Absorbing Materials for Solar Cell Applications. *J. Am. Chem. Soc.* **2015**, 137, (24), 7843-7850.
10. Goldschmidt, V. M., Die Gesetze der Krystallochemie. *Naturwissenschaften* **1926**, 14, (21), 477-485.

11. Kieslich, G.; Sun, S.; Cheetham, A. K., Solid-state principles applied to organic-inorganic perovskites: new tricks for an old dog. *Chem. Sci.* **2014**, 5, (12), 4712-4715.
12. Im, J. H.; Chung, J.; Kim, S. J.; Park, N. G., Synthesis, structure, and photovoltaic property of a nanocrystalline 2H perovskite-type novel sensitizer (CH₃CH₂NH₃)PbI₃. *Nanoscale Res. Lett.* **2012**, 7, 353.
13. Dalvi, V. H.; Rossky, P. J., Molecular origins of fluorocarbon hydrophobicity. *Proc. Natl. Acad. Sci. U. S. A.* **2010**, 107, (31), 13603-13607.
14. Frost, J. M.; Butler, K. T.; Brivio, F.; Hendon, C. H.; van Schilfgaarde, M.; Walsh, A., Atomistic Origins of High-Performance in Hybrid Halide Perovskite Solar Cells. *Nano Lett.* **2014**, 14, (5), 2584-2590.
15. Altomare, A.; Burla, M. C.; Camalli, M.; Cascarano, G. L.; Giacovazzo, C.; Guagliardi, A.; Moliterni, A. G. G.; Polidori, G.; Spagna, R., SIR97: a new tool for crystal structure determination and refinement. *J. Appl. Crystallogr.* **1999**, 32, (1), 115-119.
16. Sheldrick, G. M., A short history of SHELX. *Acta Crystallogr., Sect. A: Found. Crystallogr.* **2008**, 64, (1), 112-122.
17. Sheldrick, G. M., SHELXL-97: *Program for the Refinement of Crystal Structures*; Universität Göttingen, 1997.
18. *Topas Academic, version 4.1*; Coelho Software: Brisbane, Australia, 2007.
19. Blaha, P.; Schwarz, K.; Madsen, G.; Kvasnicka, D.; Luitz, J. *WIEN2k, An Augmented Plane Wave+ Local Orbitals Program for Calculating Crystal Properties*; Technische Universität: Wien, Austria, 2001.
20. Singh, D. J.; Nordstroem, L., *Planewaves, Pseudopotentials, and the LAPW Method*; Springer: New York, NY, 2006.
21. Madsen, G. K. H.; Blaha, P.; Schwarz, K.; Sjöstedt, E.; Nordström, L., Efficient linearization of the augmented plane-wave method. *Phys. Rev. B: Condens. Matter Mater. Phys.* **2001**, 64, (19), 195134.
22. Sjöstedt, E.; Nordström, L.; Singh, D. J., An alternative way of linearizing the augmented plane-wave method. *Solid State Commun.* **2000**, 114, (1), 15-20.
23. Perdew, J. P.; Burke, K.; Ernzerhof, M., Generalized Gradient Approximation Made Simple. *Phys. Rev. Lett.* **1996**, 77, (18), 3865-3868.
24. Steiner, T., Die Wasserstoffbrücke im Festkörper. *Angew. Chem.* **2002**, 114, (1), 50-80. Steiner, T., The Hydrogen Bond in the Solid State. *Angew. Chem., Int. Ed.* **2002**, 41, 48-76.
25. Meresse, A.; Daoud, A., Bis(n-propylammonium) tetrachloroplumbate. *Acta Crystallogr., Sect. C: Cryst. Struct. Commun.* **1989**, 45, (2), 194-196.
26. Mitzi, D. B., A Layered Solution Crystal Growth Technique and the Crystal Structure of (C₆H₅C₂H₄NH₃)₂PbCl₄. *J. Solid State Chem.* **1999**, 145, (2), 694-704.

27. Mousdis, G. A.; Papavassiliou, G. C.; Raptopoulou, C. P.; Terzis, A., Preparation and characterization of $[\text{H}_3\text{N}(\text{CH}_2)_6\text{NH}_3]\text{PbI}_4$ and similar compounds with a layered perovskite structure. *J. Mater. Chem.* **2000**, 10, (2), 515-518.
28. Dohner, E. R.; Jaffe, A.; Bradshaw, L. R.; Karunadasa, H. I., Intrinsic White-Light Emission from Layered Hybrid Perovskites. *J. Am. Chem. Soc.* **2014**, 136, (38), 13154-13157.
29. Muljarov, E. A.; Tikhodeev, S. G.; Gippius, N. A.; Ishihara, T., Excitons in self-organized semiconductor/insulator superlattices: PbI-based perovskite compounds. *Phys. Rev. B: Condens. Matter Mater. Phys.* **1995**, 51, (20), 14370-14378.
30. Kawano, N.; Koshimizu, M.; Sun, Y.; Yahaba, N.; Fujimoto, Y.; Yanagida, T.; Asai, K., Effects of Organic Moieties on Luminescence Properties of Organic-Inorganic Layered Perovskite-Type Compounds. *J. Phys. Chem. C* **2014**, 118, (17), 9101-9106.
31. Braun, M.; Tuffentsammer, W.; Wachtel, H.; Wolf, H. C., Tailoring of energy levels in lead chloride based layered perovskites and energy transfer between the organic and inorganic planes. *Chem. Phys. Lett.* **1999**, 303, (1-2), 157-164.
32. Papavassiliou, G. C.; Vidali, M.-S.; Pagona, G.; Mousdis, G. A.; Karousis, N.; Koutselas, I., Effects of organic moieties on the photoluminescence spectra of perovskite-type tin bromide based compounds. *J. Phys. Chem. Solids* **2015**, 79, 1-6.
33. Kitazawa, N.; Watanabe, Y., Optical properties of natural quantum-well compounds $(\text{C}_6\text{H}_5\text{-C}_n\text{H}_{2n}\text{-NH}_3)_2\text{PbBr}_4$ ($n=1-4$). *J. Phys. Chem. Solids* **2010**, 71, (5), 797-802.
34. Stranks, S. D.; Burlakov, V. M.; Leijtens, T.; Ball, J. M.; Goriely, A.; Snaith, H. J., Recombination Kinetics in Organic-Inorganic Perovskites: Excitons, Free Charge, and Subgap States. *Phys. Rev. Appl.* **2014**, 2, (3), 034007.
35. Hu, T.; Smith, M. D.; Dohner, E. R.; Sher, M.-J.; Wu, X.; Trinh, M. T.; Fisher, A.; Corbett, J.; Zhu, X. Y.; Karunadasa, H. I.; Lindenberg, A. M., Mechanism for Broadband White-Light Emission from Two-Dimensional (110) Hybrid Perovskites. *J. Phys. Chem. Lett.* **2016**, 7, (12), 2258-2263.

3. Benzimidazolium Lead Halide Perovskites: Effects of Anion Substitution and Dimensionality on the Bandgap

Claudia Lermer, Sascha P. Harm, Susanne T. Birkhold, Julian A. Jaser, Christopher M. Kutz, Peter Mayer, Lukas Schmidt-Mende, and Bettina V. Lotsch

Dedicated to Professor Anthony K. Cheetham FRS on the Occasion of His 70th Birthday

published in: Z. Anorg. Allg. Chem. 2016, 1369–1376
DOI: 10.1002/zaac.201600371
<http://dx.doi.org/10.1002/zaac.201600371>
Formatting and numbering of figures were changed.
Adapted with permission from WILEY-VCH Verlag GmbH & Co. KGaA

Abstract

We present the synthesis and structural characterization of a series of benzimidazolium-based lead halide perovskites including $(\text{C}_7\text{H}_7\text{N}_2)_2\text{PbCl}_4$, $(\text{C}_7\text{H}_7\text{N}_2)_2\text{PbBr}_4$, $(\text{C}_7\text{H}_7\text{N}_2)_2\text{PbI}_4$, and $(\text{C}_7\text{H}_7\text{N}_2)\text{PbI}_3$, which serves as a platform to investigate the change in optical properties as a function of the halide and the dimensionality of the inorganic sublattice. The structural similarity of the layered systems with $A_2\text{MX}_4$ stoichiometry was verified by single-crystal X-ray diffraction and solid-state NMR spectroscopy. The optical properties were analyzed by absorption and photoluminescence (PL) measurements, confirming the decrease in bandgap when exchanging the chloride with its higher homologues Br and I. In addition, comparison of the layered compound $(\text{C}_7\text{H}_7\text{N}_2)_2\text{PbI}_4$ with the known compound $(\text{C}_7\text{H}_7\text{N}_2)\text{PbI}_3$ reveals an increase in bandgap on going from a 2D to a dimensionally reduced 1D topology. Besides, significant differences in the PL spectra of the halides are observed, which likely are due to recombination of self-trapped excitons stabilized through lattice distortions or permanent lattice defects in the compounds featuring broad PL emission bands.

3.1 Introduction

Research in the field of 2D lead-halide hybrid perovskites is largely motivated by the great promise they hold as low-cost, chemically tunable absorber, transport and light-emitting materials in optoelectronic applications. The alternating arrangement of high dielectric lead halide layers and low dielectric organic layers in 2D hybrid perovskites gives rise to an inherent multiple-quantum-well structure, which results in the formation of excitons with large exciton binding energies in the metal halide sheets.¹⁻³ The dielectric confinement effect entailing a sharp excitonic absorption peak can lead to interesting optical properties including electroluminescence^{4, 5} and strong room temperature photoluminescence,⁶ making applications in solid-state lighting conceivable as put forward by *Karunadasa* and co-workers. These authors reported 2D lead halide hybrid perovskites featuring broadband white-light emission at room temperature with photoluminescence quantum efficiencies (PLQE) as high as 9%.^{7, 8} The hallmark of hybrid perovskites and related structures - their variability in structure and composition allowing for the exchange of the organic cation, the metal and the halide in hybrid perovskites - makes this class of compounds a versatile platform for various applications in optoelectronics and beyond.⁹ Hybrid perovskites have been represented most notably by methylammonium lead iodide (MAPI), which features a high absorption coefficient and long ambipolar charge carrier diffusion lengths, thus rendering MAPI a promising solar cell absorber material.^{10, 11} However, in the case of 2D perovskite materials with $n = 1$ (n = number of corner-sharing octahedral layers in each inorganic block), the strong confinement of their excitons accompanied by short charge carrier diffusion lengths has hampered their application in photovoltaics so far. An interesting development is the incorporation of halides into the organic layer of several layered hybrid perovskites,^{12, 13} which could serve as a handle to increase the dielectric constant in the organic layer which at the same time decreases the overall dielectric confinement.¹³ In principle, this modification could bring 2D hybrid perovskites back into the play when searching for future solar cell absorber materials. Herein we focus on the structural and optical investigation of the novel 2:1 benzimidazolium lead halide compounds $(C_7H_7N_2)_2PbCl_4$, $(C_7H_7N_2)_2PbBr_4$, and $(C_7H_7N_2)_2PbI_4$ featuring a 2D perovskite-type structure. This series of structurally related compounds enables us to systematically analyze the effect of exchanging the halide on the optical properties, while the crystal structure is maintained. In addition, the influence of the dimensionality of the lead halide sublattice on the optical bandgap is discussed by comparison with the compound $(C_7H_7N_2)PbI_3$. The crystal structure and optical properties of $(C_7H_7N_2)PbI_3$ were already reported by *Wang* et al., but studies on the bulk properties of the phase-pure material are still elusive.¹⁴ Note that the only benzimidazole lead halide compound described so far in the literature besides $(C_7H_7N_2)PbI_3$ - $Pb(C_7H_6N_2)_2Cl_4$ - is a molecular coordination compound based on Pb^{IV} and neutral benzimidazole, rather than an extended hybrid solid.¹⁵

3.2 Results and Discussion

Synthesis of $(\text{C}_7\text{H}_7\text{N}_2)_2\text{PbCl}_4$, $(\text{C}_7\text{H}_7\text{N}_2)_2\text{PbBr}_4$, $(\text{C}_7\text{H}_7\text{N}_2)_2\text{PbI}_4$, and $(\text{C}_7\text{H}_7\text{N}_2)\text{PbI}_3$

Phase-pure $(\text{C}_7\text{H}_7\text{N}_2)_2\text{PbCl}_4$, $(\text{C}_7\text{H}_7\text{N}_2)_2\text{PbBr}_4$, and $(\text{C}_7\text{H}_7\text{N}_2)\text{PbI}_3$ were obtained by the stoichiometric reaction of benzimidazole with PbX_2 ($X = \text{Cl}, \text{Br}, \text{I}$) in the respective hydrohalic acid. $(\text{C}_7\text{H}_7\text{N}_2)_2\text{PbCl}_4$ was only obtained by evaporating the solvent in a nitrogen flow (Figure 1a). $(\text{C}_7\text{H}_7\text{N}_2)_2\text{PbBr}_4$ and $(\text{C}_7\text{H}_7\text{N}_2)\text{PbI}_3$ could also be obtained by adding ethyl acetate to the reaction mixture, which led to precipitation of the phase-pure product (Figure S1, Supporting Information). Besides, an alternative solvent-free synthesis procedure was explored for $(\text{C}_7\text{H}_7\text{N}_2)_2\text{PbBr}_4$ and $(\text{C}_7\text{H}_7\text{N}_2)\text{PbI}_3$. The precursors, benzimidazole and PbX_2 ($X = \text{Br}, \text{I}$), were mixed and ground with a few drops of the respective hydrohalic acid. $(\text{C}_7\text{H}_7\text{N}_2)\text{PbI}_3$ was obtained phase-pure, whereas $(\text{C}_7\text{H}_7\text{N}_2)_2\text{PbBr}_4$ contained a small impurity (Figure S2, Supporting Information), which was further analyzed by energy-dispersive X-ray spectroscopy (EDX) and found to be a Pb-rich phase displaying a needle-like morphology (Supporting Information S5).

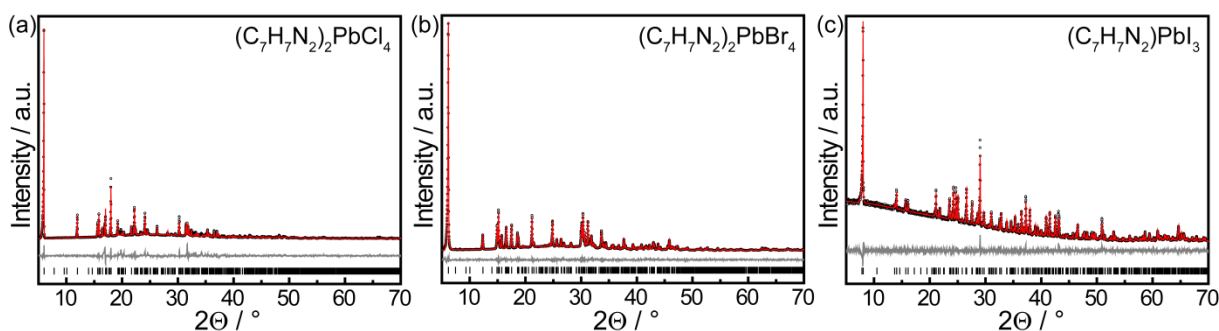


Figure 3.1. X-ray powder diffraction data and Rietveld refinements of $(\text{C}_7\text{H}_7\text{N}_2)_2\text{PbCl}_4$ (a), $(\text{C}_7\text{H}_7\text{N}_2)_2\text{PbBr}_4$ (b), and $(\text{C}_7\text{H}_7\text{N}_2)\text{PbI}_3$ (c). The experimental patterns are represented by black open circles; the Rietveld profile fit (red solid line) and the difference profile (grey solid line) confirm phase purity. $(\text{C}_7\text{H}_7\text{N}_2)_2\text{PbCl}_4$, $(\text{C}_7\text{H}_7\text{N}_2)_2\text{PbBr}_4$, and $(\text{C}_7\text{H}_7\text{N}_2)\text{PbI}_3$ were obtained by evaporating the solvent under nitrogen flow from the precursor solution.

We attempted to prepare phase-pure $(\text{C}_7\text{H}_7\text{N}_2)_2\text{PbI}_4$ by solvent-free mechanochemical reactions of benzimidazolium iodide monohydrate, $(\text{C}_7\text{H}_7\text{N}_2)\text{I}\cdot\text{H}_2\text{O}$, with PbI_2 , and of $(\text{C}_7\text{H}_7\text{N}_2)\text{I}\cdot\text{H}_2\text{O}$ with $(\text{C}_7\text{H}_7\text{N}_2)\text{PbI}_3$ using a mortar and pestle. Another attempt included the in situ protonation of benzimidazole with a few drops of HI while grinding the reagents benzimidazole and PbI_2 . We also attempted to synthesize the desired product in solution by reacting $(\text{C}_7\text{H}_7\text{N}_2)\text{I}$ and PbI_2 in dimethylformamide (DMF). In all cases, the main product $(\text{C}_7\text{H}_7\text{N}_2)_2\text{PbI}_4$ was accompanied by $(\text{C}_7\text{H}_7\text{N}_2)\text{PbI}_3$ as a side phase, as evidenced by powder X-ray diffraction (PXRD). In addition, PbI_2 was detected as a second minor phase when used as a starting material in the synthesis. Therefore, we chose to focus on $(\text{C}_7\text{H}_7\text{N}_2)\text{I}\cdot\text{H}_2\text{O}$ and $(\text{C}_7\text{H}_7\text{N}_2)\text{PbI}_3$ as precursors, which were ground in a

vibratory ball mill for 5 d. Grinding the starting materials with a mortar gave similar results. The obtained bright red powder (Figure S4, Supporting Information) contains $(\text{C}_7\text{H}_7\text{N}_2)_2\text{PbI}_4$ (red phase) and $(\text{C}_7\text{H}_7\text{N}_2)\text{PbI}_3$ (yellow phase) in a ratio of 10 to 1 (hereafter BzImPbI4/3) as determined by Rietveld refinement of the collected PXRD data (Figure S3, Supporting Information). All details on the Rietveld analysis can be found in the Supporting Information S3. In addition, thermal stability data of $(\text{C}_7\text{H}_7\text{N}_2)_2\text{PbCl}_4$, $(\text{C}_7\text{H}_7\text{N}_2)_2\text{PbBr}_4$, and $(\text{C}_7\text{H}_7\text{N}_2)\text{PbI}_3$ is reported in Supporting Information S8, revealing thermal stabilities up to 300 °C for the chloride and bromide and up to 350 °C for the iodide.

Structural Investigation of $(\text{C}_7\text{H}_7\text{N}_2)_2\text{PbCl}_4$, $(\text{C}_7\text{H}_7\text{N}_2)_2\text{PbBr}_4$, and $(\text{C}_7\text{H}_7\text{N}_2)_2\text{PbI}_4$

The hybrid compounds $(\text{C}_7\text{H}_7\text{N}_2)_2\text{PbCl}_4$, $(\text{C}_7\text{H}_7\text{N}_2)_2\text{PbBr}_4$, and $(\text{C}_7\text{H}_7\text{N}_2)_2\text{PbI}_4$ exhibit layers of corner-sharing PbX_6 octahedra separated by a double layer of protonated benzimidazolium cations, which protrude into the “cavities” formed by the PbX_6 octahedra with their imidazolium termini (Figure 2). The distance between the inorganic layers decreases from 14.48 Å in $(\text{C}_7\text{H}_7\text{N}_2)_2\text{PbCl}_4$ to 14.16 Å in $(\text{C}_7\text{H}_7\text{N}_2)_2\text{PbBr}_4$ and to 13.90 Å in $(\text{C}_7\text{H}_7\text{N}_2)_2\text{PbI}_4$, which seems counterintuitive at first sight given the increasing size of the halides. However, this trend can be rationalized by taking into account the increasing size of the cavities formed by the inorganic layers with increasing size of the respective halide ion from $(\text{C}_7\text{H}_7\text{N}_2)_2\text{PbCl}_4$ to $(\text{C}_7\text{H}_7\text{N}_2)_2\text{PbI}_4$. In this way, the organic and inorganic sublattices can interdigitate more closely such that the distance between the layers decreases.

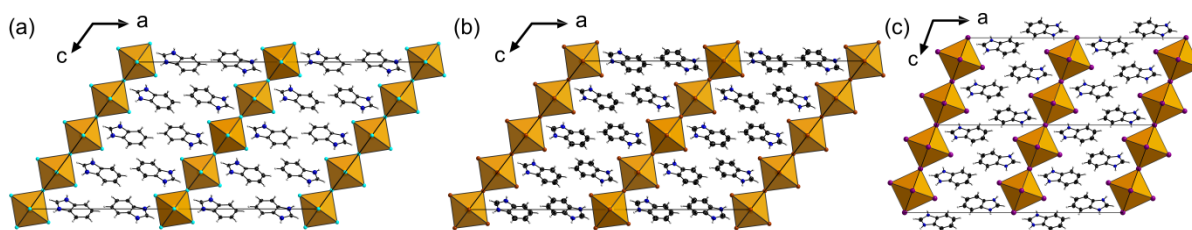


Figure 3.2. Crystal structures of $(\text{C}_7\text{H}_7\text{N}_2)_2\text{PbCl}_4$ (a) and $(\text{C}_7\text{H}_7\text{N}_2)_2\text{PbI}_4$ (c) measured at 100 K and $(\text{C}_7\text{H}_7\text{N}_2)_2\text{PbBr}_4$ (b) measured at 173 K in projection along [010]. Thermal ellipsoids for carbon and nitrogen are drawn at the 70% probability level. C is displayed in black, N is blue, H is grey, Pb is orange, Cl is turquoise, Br is brown and I is purple. Cell edges are marked with black solid lines.

The described orientation of the organic cations is most likely due to the formation of moderate to weak hydrogen bonds between the nitrogen atoms of the imidazolium moiety and the halide atoms of the PbX_6 octahedra; no π - π interactions between the heteroaromatic units are observed (Figure 3, Tables SVI, SXI, SXVI, Supporting Information). The structure is stabilized further by ionic interactions between the negatively charged inorganic sublattice and the positively charged organic sublattice. All of the compounds discussed so far crystallize in the monoclinic space group

$C2/c$. However, the arrangement of the benzimidazolium cations in $(C_7H_7N_2)_2PbI_4$ differs from that in the isotypic compounds $(C_7H_7N_2)_2PbCl_4$ and $(C_7H_7N_2)_2PbBr_4$ as depicted in Figure 3. $(C_7H_7N_2)_2PbCl_4$ and $(C_7H_7N_2)_2PbBr_4$ feature two crystallographically distinct benzimidazolium cations: One comprising the atoms N1 and N3 (BzIm-N1N3) and the other one N2 and N4 (BzIm-N2N4). The cations alternate within the organic layer, whereby the π -planes of BzIm-N1N3 and BzIm-N2N4 comprise an angle of 7.3° and 7.0° , respectively. The complete arrangement of benzimidazolium cations is obtained when applying a c glide plane to the A and A' layers, which results in the formation of the B and B' layers, respectively (Figure 3a). In contrast, the “zigzag” pattern in $(C_7H_7N_2)_2PbI_4$ containing only one unique benzimidazolium cation arises from applying the c glide plane to the A layer. Consequently, the lattice parameter in c direction is halved compared to the chloride and bromide version (Figure 3). The observed distortion of the PbX_6 octahedra, which is similar for all compounds and becomes primarily apparent in the $X-Pb-X$ bond angles [$82.83(3)$ – $97.17(3)^\circ$ in $(C_7H_7N_2)_2PbCl_4$, $83.523(6)$ – $96.477(6)^\circ$ in $(C_7H_7N_2)_2PbBr_4$, and $83.928(4)$ – $96.072(4)^\circ$ in $(C_7H_7N_2)_2PbI_4$] is likely connected to the benzimidazolium cations pushing into the cavities of the inorganic lattice and the formation of hydrogen bonds between the organic cations and the PbX_6 octahedra's halide atoms as discussed above. Another source of the observed lattice distortion may be the stereochemically active 6s Pb lone pair as observed for other layered lead-based hybrid perovskites.¹⁶ However, electronic structure calculations would be needed to further analyze the origin of the observed distortion. Crystallographic data and details of the structure refinements are shown in Tables SI–SV, SVII–SX, and SXII–SXV (Supporting Information).

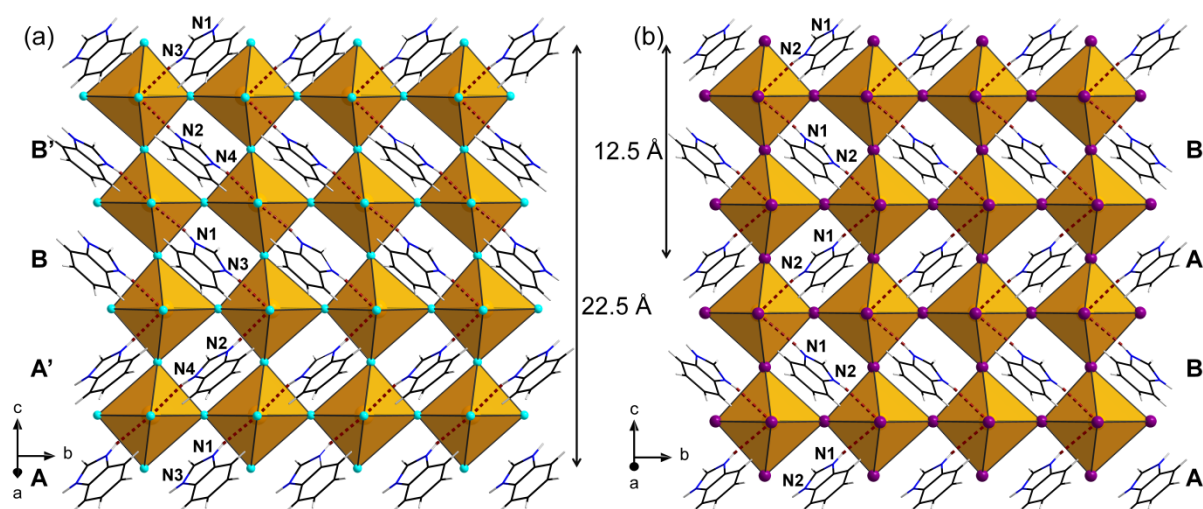


Figure 3.3. Crystal structures of $(C_7H_7N_2)_2PbCl_4$ (a) and $(C_7H_7N_2)_2PbI_4$ (b), view onto the (100) plane. The length of the respective c axis is emphasized. Hydrogen bonds are marked with red dashed lines. Nitrogen atoms are labeled exemplarily. C is displayed in black, N is blue, H is grey, Pb is orange, Cl is turquoise, and I is purple.

Structural Investigation of $(\text{C}_7\text{H}_7\text{N}_2)\text{PbI}_3$

Since the structure of $(\text{C}_7\text{H}_7\text{N}_2)\text{PbI}_3$ was already determined by Wang et al.,¹⁴ it is only described briefly here for completeness. The hybrid compound $(\text{C}_7\text{H}_7\text{N}_2)\text{PbI}_3$ exhibits $P2_12_12_1$ symmetry and features double chains of edge-sharing PbI_6 octahedra, which are surrounded by benzimidazolium cations arranged in stacks of two (Figure 4a); the structure can thus be considered as quasi one-dimensional. The benzimidazolium cations are parallel to each other when belonging to the same stack but tilted by 89.8° with respect to the cations of the associated stack (Figure 4b). Besides apparent ionic interactions between the negatively charged inorganic layer and the protonated benzimidazole cations, weak hydrogen bonds ($\text{N-H}\cdots\text{I} = 3.537$ and 3.638 Å) between the benzimidazolium N atoms and the I3 atoms of the inorganic sublattice could be identified as the predominant interactions in $(\text{C}_7\text{H}_7\text{N}_2)\text{PbI}_3$. Also, a distortion of the PbI_6 octahedra is apparent which is likely due to structural features, specifically the formation of hydrogen bonds, or possible Pb lone pair effects as mentioned above (Figure 4c, Table XXII). Crystallographic data and details of the structure refinements are shown in Tables SXVII-SXXI (Supporting Information).

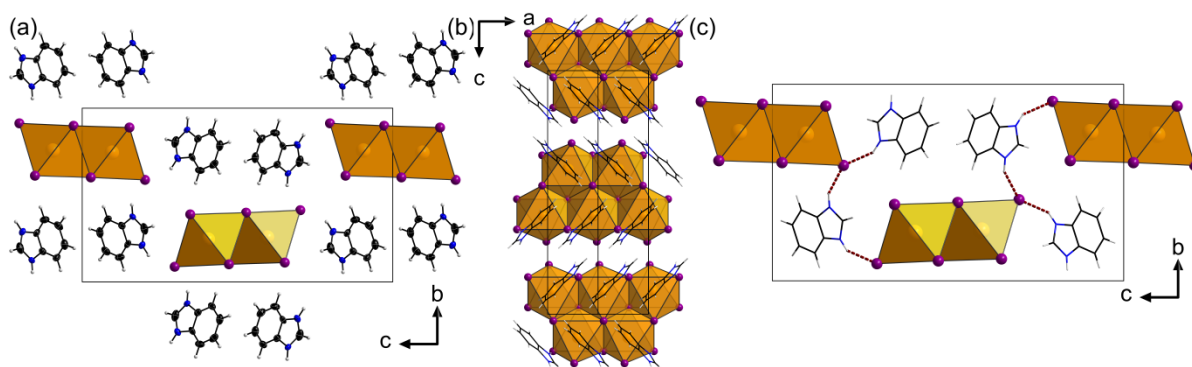


Figure 3.4. Crystal structure of $(\text{C}_7\text{H}_7\text{N}_2)\text{PbI}_3$ in projection along $[100]$ (a, c), and $[010]$ (b). Thermal ellipsoids for carbon and nitrogen are drawn at the 70% probability level. Hydrogen bonds are marked with red dashed lines. C is displayed in black, N is blue, H is grey, Pb is orange, and I is purple. Cell edges are marked with black solid lines.

Solid-state NMR Spectroscopy

^1H , ^{13}C , and ^{15}N solid-state NMR spectroscopy was applied as a tool to access the local structure of the organic sublattice and to confirm the integrity of the benzimidazolium cation in $(\text{C}_7\text{H}_7\text{N}_2)_2\text{PbCl}_4$, $(\text{C}_7\text{H}_7\text{N}_2)_2\text{PbBr}_4$, and $(\text{C}_7\text{H}_7\text{N}_2)\text{PbI}_3$ (Figure 5). The ^1H spectra of the chloride and the bromide compound show three distinguishable signals at 13.18 (N-H), 9.21 (C_2 -H) and 6.86 ($\text{C}_{4/7,5/6}$ -H) ppm and at 12.66 (N-H), 9.04 (C_2 -H) and 7.54 ($\text{C}_{4/7,5/6}$ -H) ppm, respectively. In contrast, only two signals at 11.18 (N-H) and 7.89 ($\text{C}_{2,4/7,5/6}$ -H) ppm are resolved for $(\text{C}_7\text{H}_7\text{N}_2)\text{PbI}_3$. The differences in local structure and hydrogen bonding between the isotopic compounds $(\text{C}_7\text{H}_7\text{N}_2)_2\text{PbCl}_4$ and $(\text{C}_7\text{H}_7\text{N}_2)_2\text{PbBr}_4$ and the 1D compound $(\text{C}_7\text{H}_7\text{N}_2)\text{PbI}_3$ are reflected in

differences in the ^{13}C chemical shifts by as much as 4.5 ppm. The chemical shifts are in good agreement with a study by *Pugmire* et al., who investigated molecular benzimidazole hydrochloride in a saturated aqueous solution.¹⁷ The ^{13}C spectra of the investigated compounds show four distinct signals, in line with the mirror plane intersecting the benzimidazolium cation along its longest axis. The protonation of benzimidazole becomes also obvious in the observed upfield shifts for C_4 and C_9 as compared to neutral benzimidazole.¹⁸ Notably, C_2 is downfield shifted on going from the iodide to the bromide to the chloride, which is consistent with increasingly strong hydrogen-bonding interactions along this series, leading to a deshielding of the carbon neighboring the protonated nitrogen atoms. The splitting of the $\text{C}_{5/6}$ signal visible for $(\text{C}_7\text{H}_7\text{N}_2)_2\text{PbBr}_4$ is likely due to the presence of the two crystallographically distinct benzimidazolium cations, whose chemical environments are so similar that all other signals coalesce in $(\text{C}_7\text{H}_7\text{N}_2)_2\text{PbBr}_4$ and $(\text{C}_7\text{H}_7\text{N}_2)_2\text{PbCl}_4$. The ^{15}N spectra show only one signal between -221.15 and -222.39 ppm, which confirms the presence of two chemically equivalent protonated imidazolium nitrogen atoms as well as the similar local environments of the crystallographically different benzimidazolium units.¹⁸ The assignment of the signals in the ^{13}C and ^{15}N spectra is displayed in detail in the Supporting Information S6.

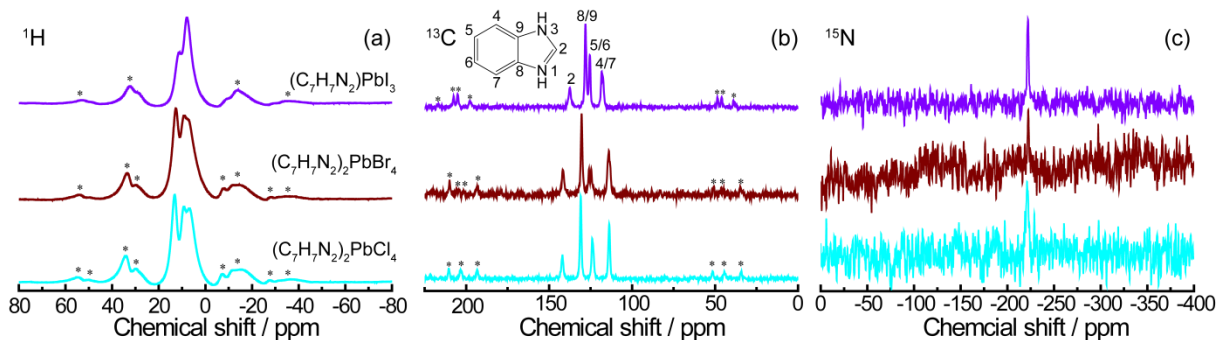


Figure 3.5. ^1H MAS (a), ^{13}C CP MAS (b) and ^{15}N CP MAS (c) solid-state NMR spectra of $(\text{C}_7\text{H}_7\text{N}_2)_2\text{PbCl}_4$ (cyan), $(\text{C}_7\text{H}_7\text{N}_2)_2\text{PbBr}_4$ (brown) and $(\text{C}_7\text{H}_7\text{N}_2)\text{PbI}_3$ (purple). Spinning side bands are marked with asterisks.

Optical Properties

The optical properties of $(\text{C}_7\text{H}_7\text{N}_2)_2\text{PbCl}_4$, $(\text{C}_7\text{H}_7\text{N}_2)_2\text{PbBr}_4$, $(\text{C}_7\text{H}_7\text{N}_2)\text{PbI}_3$, and $\text{BzImPbI}_4/3$ [containing $(\text{C}_7\text{H}_7\text{N}_2)_2\text{PbI}_4$ and $(\text{C}_7\text{H}_7\text{N}_2)\text{PbI}_3$ in a ratio of 10 to 1, see above], were investigated by absorbance and photoluminescence (PL) measurements, as presented in Figure 6. The bandgaps E_g , as determined by Tauc plots (see S7, Supporting Information) decrease on going from the chloride ($E_g = 3.08$ eV) to the bromide ($E_g = 2.60$ eV) to the iodide ($E_g = 1.99$ eV), which becomes clearly visible in the color change from white to yellow to red for $(\text{C}_7\text{H}_7\text{N}_2)_2\text{PbCl}_4$, $(\text{C}_7\text{H}_7\text{N}_2)_2\text{PbBr}_4$, and $(\text{C}_7\text{H}_7\text{N}_2)_2\text{PbI}_4$, respectively (Figure 7a, b, and d).

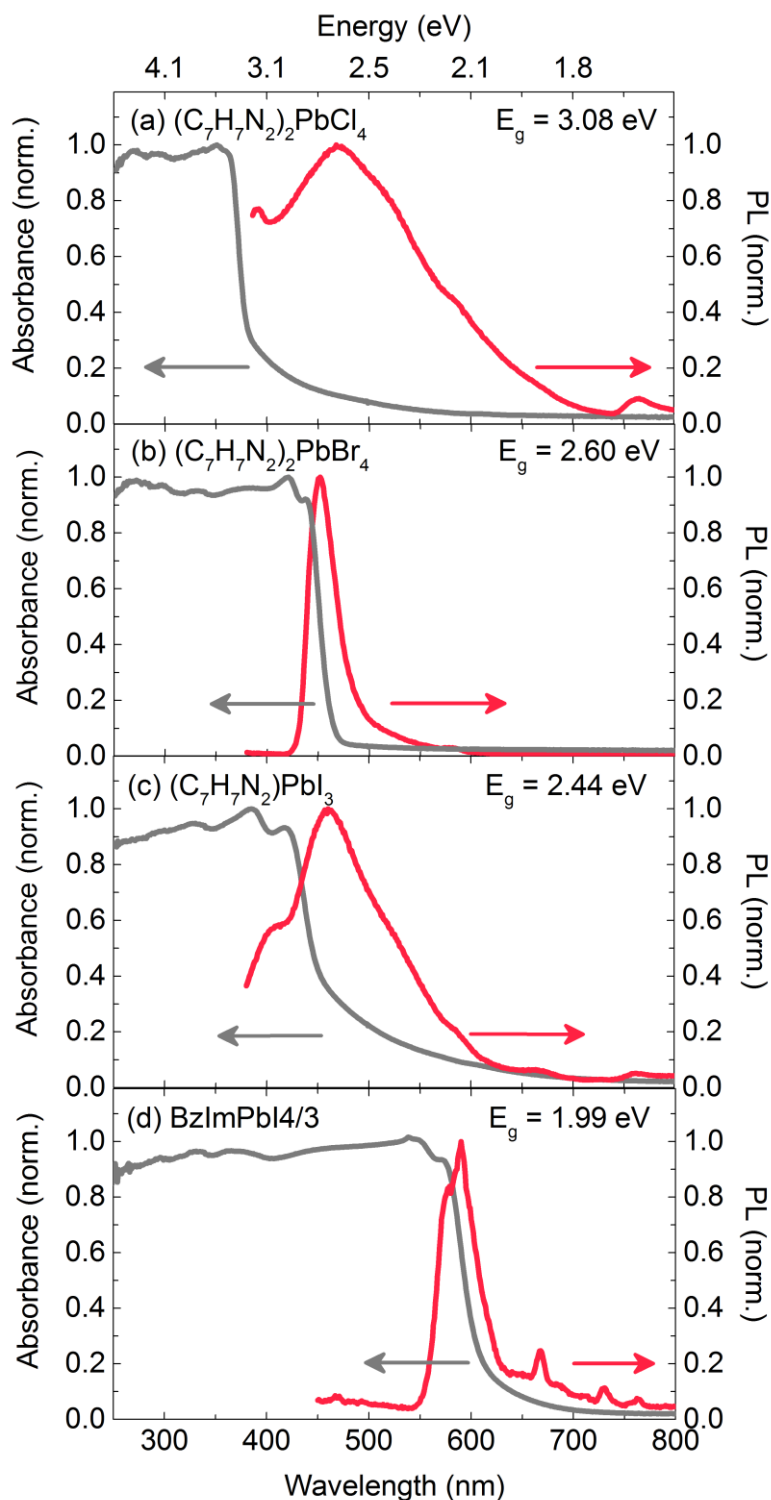


Figure 3.6. Absorbance (grey line) and photoluminescence spectra (red line, $\lambda_{\text{excitation}} = 350 \text{ nm}$) of $(\text{C}_7\text{H}_7\text{N}_2)_2\text{PbCl}_4$ (a), $(\text{C}_7\text{H}_7\text{N}_2)_2\text{PbBr}_4$ (b), $(\text{C}_7\text{H}_7\text{N}_2)\text{PbI}_3$ (c), and $\text{BzImPbI}_{4/3}$ (d) at room temperature. Bandgaps E_g are extracted from Tauc plots presented in S7 (Supporting Information).

Bandgap tuning of metal halide perovskites has been widely investigated for solar cell applications of 3D perovskites, where variations in the halide as in $\text{CH}_3\text{NH}_3\text{Pb}(\text{I}_{1-x}\text{Br}_x)_3$,^{19, 20} or in the organic cation²¹ lead to changes in the bandgap, which were found to correlate with changes

in the metal-halide bond length. Besides the lattice parameters, the bandgap of perovskites is also influenced by the compound's dimensionality as can be seen for the iodide based compounds in Figure 6c and d. A decrease in the dimensionality from 2D (in BzImPbI₄/3) to 1D [in (C₇H₇N₂)PbI₃] increases the bandgap E_g from 1.99 eV to 2.44 eV and is accompanied by a color change from red to yellow (Figure 7c, d). The bandgap of (C₇H₇N₂)PbI₃ has been reported by Wang et al. to be 2.76 eV, which may point to the presence of impurity phases since the precursors for (C₇H₇N₂)PbI₃, where reacted at off-stoichiometric ratios by Wang et al.¹⁴ The impact of halide exchange and dimensionality on the bandgap energy can also be seen by comparison of the herein presented perovskite compounds to the 3D perovskites (CH₃NH₃)PbCl₃, (CH₃NH₃)PbBr₃, and (CH₃NH₃)PbI₃ with bandgaps of 2.88 eV, 2.2 eV, and 1.5 eV, respectively.^{22, 23}



Figure 3.7. Photographs of (C₇H₇N₂)₂PbCl₄ (a), (C₇H₇N₂)₂PbBr₄ (b), and (C₇H₇N₂)PbI₃ powder (c) and of (C₇H₇N₂)₂PbI₄ crystals (d).

Concerning the PL spectra, striking variations in the spectral width occur for the different structures. For both (C₇H₇N₂)₂PbBr₄ and BzImPbI₄/3, a relatively narrow PL emission coincides well with the absorbance edge. Yet, additional PL emission peaks appear for BzImPbI₄/3, which can be related to impurity states, as the sample contains about 10% (C₇H₇N₂)PbI₃ impurities. In general, photo-excited states relax to the energetically lowest accessible states before recombination into the ground state, which gives rise to PL emission. The absent emission of (C₇H₇N₂)PbI₃ at 460 nm in the PL of BzImPbI₄/3 might be due to a reabsorption by (C₇H₇N₂)₂PbI₄ components. However, both samples have minor PL signals at 580 nm and 668 nm, which indicates emission of (C₇H₇N₂)PbI₃ states within BzImPbI₄/3, likely due to a hindered charge transfer from these low energy states into (C₇H₇N₂)₂PbI₄. In contrast to the sharp band-to-band transition of (C₇H₇N₂)₂PbBr₄ and BzImPbI₄/3, the PL spectra of (C₇H₇N₂)₂PbCl₄ and (C₇H₇N₂)PbI₃ are characterized by a broad and strongly Stokes shifted PL emission that includes multiple emission peaks. Likewise, the absorbance spectra of (C₇H₇N₂)₂PbCl₄ and (C₇H₇N₂)PbI₃ also possess significant intensity below their absorbance edges. The origin of this broad, white light PL emission for layered organic-inorganic perovskites has been identified by Dohner et al. to originate from self-trapped excitons that strongly couple to a deformable lattice and structural distortions, driven by strong electron-phonon coupling.⁸ The transient, photo-induced formation of these self-trapped excitons has been observed to occur on a femtosecond (fs) - timescale and

its multicomponent nature has been confirmed by temperature dependent and time-resolved PL measurements.²⁴⁻²⁶ Note that all compounds studied here show similar levels of distortions of the inorganic sublattice, which is why the observed differences in the PL emission may result from different degrees of lattice “softness” or permanent lattice defects rather than (static) structural distortions.

In case of $(\text{C}_7\text{H}_7\text{N}_2)\text{PbI}_3$, we propose that the occurrence of the broad PL emission is based on its 1D lattice topology (see Figure 4) which assists the rapid formation of self-trapped excitons without potential barrier.^{27, 28} We also assign the broad PL emission of $(\text{C}_7\text{H}_7\text{N}_2)_2\text{PbCl}_4$ to the recombination of self-trapped excitons due to its broad emission profile with a FWHM of 190 nm and a large Stokes shift of over 100 nm, which is typical for the emission of self-trapped excitons.^{7, 8, 24} Based on this broad emission profile and the additionally absorbing states below the bandgap, we propose that for $(\text{C}_7\text{H}_7\text{N}_2)_2\text{PbCl}_4$ either facile electron-phonon coupling occurs or a small defect concentration must be present that cannot be resolved by PXRD measurements. In order to fully understand the different nature and origin of the emitting states in $(\text{C}_7\text{H}_7\text{N}_2)_2\text{PbCl}_4$ compared to $(\text{C}_7\text{H}_7\text{N}_2)_2\text{PbBr}_4$, further studies such as temperature dependent or time-resolved PL measurements are required. We also would like to note that a comparable impact of halide exchange from bromide to chloride on the optical properties has previously been observed in 2D hybrid perovskites by the appearance of inhomogeneous PL emission²⁹ or by increasing Stokes shifts and spectral emission widths for 3D perovskites of $\text{MAPbBr}_{3-x}\text{Cl}_x$.³⁰

3.3 Conclusions

The crystal structures of the compounds $(\text{C}_7\text{H}_7\text{N}_2)_2\text{PbCl}_4$, $(\text{C}_7\text{H}_7\text{N}_2)_2\text{PbBr}_4$, and $(\text{C}_7\text{H}_7\text{N}_2)_2\text{PbI}_4$, a new series of closely related 2D hybrid perovskites, are reported for the first time and discussed with respect to interactions between the inorganic and organic sublattices. In addition, we confirmed the crystal structure of $(\text{C}_7\text{H}_7\text{N}_2)\text{PbI}_3$, which has been obtained as phase-pure bulk material for the first time.¹⁴ Several low-temperature routes for the synthesis of the benzimidazolium lead halides were shown to be feasible with excellent yields [except for $(\text{C}_7\text{H}_7\text{N}_2)_2\text{PbI}_4$], including solvent-free mechanochemical reactions and in-situ protonation of benzimidazole using hydrohalic acids as a solvent. The local structure and stability of $(\text{C}_7\text{H}_7\text{N}_2)_2\text{PbCl}_4$, $(\text{C}_7\text{H}_7\text{N}_2)_2\text{PbBr}_4$, and $(\text{C}_7\text{H}_7\text{N}_2)\text{PbI}_3$ were studied with solid-state NMR spectroscopy and thermal analysis, respectively, revealing thermal stabilities up to 300 °C for the chloride and bromide and up to 350 °C for the iodide. Due to the close structural relationship between the 2:1 compounds, the decrease in bandgap from $(\text{C}_7\text{H}_7\text{N}_2)_2\text{PbCl}_4$ to $(\text{C}_7\text{H}_7\text{N}_2)_2\text{PbBr}_4$ to $(\text{C}_7\text{H}_7\text{N}_2)_2\text{PbI}_4$ determined by optical absorption measurements can be ascribed to the choice of the halide, which is the only variable. The influence of dimensionality on the bandgap was demonstrated by comparing E_g for yellow $(\text{C}_7\text{H}_7\text{N}_2)\text{PbI}_3$ featuring a 1D chain-like structure and for

the 2D red compound $(\text{C}_7\text{H}_7\text{N}_2)_2\text{PbI}_4$. PL measurements revealed a sharp PL emission for $(\text{C}_7\text{H}_7\text{N}_2)_2\text{PbBr}_4$ and $\text{BzImPbI}_{4/3}$, whereas $(\text{C}_7\text{H}_7\text{N}_2)_2\text{PbCl}_4$ and $(\text{C}_7\text{H}_7\text{N}_2)\text{PbI}_3$ show a rather broad and unstructured PL emission. We suggest that the differences in PL emission can be traced back to a more efficient coupling of self-trapped excitons to phonons or lattice defects in the compounds featuring broad PL emission bands.

3.4 Experimental Section

Materials and Methods: PbCl_2 (Sigma-Aldrich, 98%), PbBr_2 (Sigma-Aldrich, $\geq 98\%$), PbI_2 (Acros Organics, 99%), benzimidazole (Alfa Aesar, 99%), concentrated hydrochloric acid (Brenntag, purum), concentrated hydrobromic acid (Acros Organics, pure), concentrated hydriodic acid (Acros Organics, for analysis), ethyl acetate (Staub & Co. Silbermann, 99.8%), ether (Bernd Kraft, 95.5%), and dimethylformamide (Alfa Aesar, 99%) were commercially available and used as received without further purification.

Synthesis of $(\text{C}_7\text{H}_7\text{N}_2)_2\text{PbCl}_4$: Benzimidazole (47.7 mg, 0.4 mmol), PbCl_2 (56.8 mg, 0.2 mmol), and 4 mL HCl were heated to 80 °C for 2 h, whereupon the solids were dissolved completely. The solvent was subsequently removed in a nitrogen flow, whereupon a white solid precipitated. Single crystals suitable for X-ray diffraction analysis were obtained by evaporating the solvent at room temperature instead. $(\text{C}_7\text{H}_7\text{N}_2)_2\text{PbCl}_4$: calcd. C 28.63; H 2.40; N 9.54; Cl 24.14%; found: C 28.41; H 2.34; N 9.46; Cl 24.28%. **IR:** $\tilde{\nu} = 3146$ (m), 3096 (m), 3070 (m), 3038 (m), 3006 (m), 2962 (m), 2940 (m), 2854 (m), 2814 (m), 2748 (w), 1817 (w), 1623 (w), 1522 (w), 1496 (w), 1447 (s), 1398 (w), 1370 (vs), 1282 (w), 1256 (s), 1235 (w), 1171 (w), 1160 (w), 1140 (w), 1101 (w), 1003 (m), 944 (w), 910 (w), 882 (w), 773 (s), 742 (vs) cm^{-1} .

Synthesis of $(\text{C}_7\text{H}_7\text{N}_2)_2\text{PbBr}_4$: Benzimidazole (47.7 mg, 0.4 mmol), PbBr_2 (74.9 mg, 0.2 mmol) and 4 mL HBr were heated to 80 °C for 2 h, whereupon the solids were dissolved completely. The solvent was subsequently removed under nitrogen flow. The obtained yellow solid was washed with ethyl acetate. Single yellow crystals suitable for X-ray diffraction analysis were obtained by evaporating the solvent at room temperature instead. $(\text{C}_7\text{H}_7\text{N}_2)_2\text{PbBr}_4$: calcd. C 21.98; H 1.84; N 7.32; Br 41.77%; found: C 21.95; H 1.86; N 7.32; Br 40.44%. **IR:** $\tilde{\nu} = 3140$ (m), 3103 (m), 3077 (m), 3009 (m), 2971 (m), 2846 (m), 2810 (w), 1792 (w), 1619 (m), 1524 (w), 1496 (w), 1446 (s), 1397 (w), 1365 (vs), 1346 (m), 1277 (w), 1255 (vs), 1170 (w), 1158 (w), 1133 (m), 1100 (w), 1001 (m), 939 (m), 774 (m), 746 (vs) cm^{-1} .

Additionally, $(\text{C}_7\text{H}_7\text{N}_2)_2\text{PbBr}_4$ can be obtained by heating benzimidazole (179 mg, 1.5 mmol), PbBr_2 (281 mg, 0.75 mmol) and 15 mL HBr to 80 °C for 2 h. The product was obtained by adding ethyl acetate to the reaction mixture after it was cooled down to room temperature.

Synthesis of $(\text{C}_7\text{H}_7\text{N}_2)\text{PbI}_3$: Benzimidazole (89.5 mg, 0.75 mmol), PbI_2 (349 mg, 0.75 mmol), and 15 mL HI were heated to 80 °C for 2 h. A clear solution could not be obtained at any time. After

cooling the reaction mixture down to room temperature dissolved product was precipitated by adding ethyl acetate. Afterwards, the yellow solid was filtered and washed with ethyl acetate. $(C_7H_7N_2)PbI_3$: calcd. C 11.89; H 1.00; N 3.96; I 53.84%; found: C 11.92; H 1.04; N 4.01; I 51.83%. **IR**: $\tilde{\nu}$ = 3254 (m), 3227 (m), 3133 (m), 1612 (m), 1522 (w), 1485 (m), 1444 (s), 1421 (w), 1366 (s), 1346 (w), 1258 (m), 1206 (m), 1176 (w), 1155 (m), 1134 (s), 1103 (s), 1003 (w), 939 (w), 923 (s), 887 (w), 879 (w), 850 (w), 773 (w), 750 (vs), 687 (vs) cm^{-1} .

$(C_7H_7N_2)PbI_3$ was also synthesized by heating benzimidazole (23.9 mg, 0.2 mmol), PbI_2 (93.1 mg, 0.2 mmol) and 4 mL HI to 80 °C for 2 h. A yellow solid was gained by evaporating the solvent in a nitrogen flow after the reaction mixture was cooled down to room temperature. Subsequently, the product was washed with ethyl acetate. Single yellow crystals suitable for X-ray diffraction analysis were obtained by evaporating the solvent at room temperature instead.

Solvent-free Synthesis of $(C_7H_7N_2)_2PbBr_4$ and $(C_7H_7N_2)PbI_3$: Benzimidazole (51.1 mg, 0.43 mmol) and $PbBr_2$ (80 mg, 0.21 mmol) were mixed and ground with a few drops of HBr. Subsequently, the powder was washed by adding a little ethyl acetate, grinding the mixture and removing the ethyl acetate afterwards. This procedure was repeated a couple of times. In a last step the solvent was removed in a nitrogen flow. The same experimental procedure was performed to synthesize $(C_7H_7N_2)PbI_3$. Here, benzimidazole (25.7 mg, 0.21 mmol), PbI_2 (100 mg, 0.22 mmol), and a few drops of HI were mixed and ground.

Synthesis of $(C_7H_7N_2)I \cdot H_2O$: HI (0.6 mL) was added to benzimidazole (200 mg, 1.68 mmol), while cooling with an ice bath. Subsequently, the solvent was evaporated in a nitrogen flow. The product was washed with ethyl acetate and ether. $(C_7H_7N_2)I \cdot H_2O$: calcd. C 31.84; H 3.44; N 10.61%; found: C 31.80; H 3.47; N 10.62 %. **IR**: $\tilde{\nu}$ = 3468 (w), 3403 (m), 3154 (w), 3123 (m), 3099 (m), 3064 (m), 3036 (m), 3008 (m), 2970 (m), 2929 (m), 2844 (m), 2812 (m), 2751 (m), 1607 (m), 1520 (w), 1494 (w), 1442 (s), 1372 (s), 1349 (m), 1258 (s), 1232 (m), 1178 (w), 1161 (w), 1145 (w), 1124 (w), 1100 (w), 1005 (w), 934 (m), 878 (m), 852 (s), 772 (s), 762 (s), 740 (vs) cm^{-1} . **1H NMR** ($[D_6]DMSO$, 20 °C): δ = 9.57 (s, 1 H, $-C_2-H$), 7.87 (d_d, 2 H, $C_{4/7}-H$) 7.60 (d_d, 2 H, $C_{5/6}-H$). **^{13}C NMR** ($[D_6]DMSO$, 20 °C): δ = 140.68 (s, C_2), 130.50 (s, $C_{8/9}$), 126.12 (s, $C_{5/6}$), 114.47 (s, $C_{4/7}$) ppm.

Synthesis of $(C_7H_7N_2)_2PbI_4$: Single crystals suitable for X-ray diffraction analysis were obtained by dissolving $(C_7H_7N_2)I \cdot H_2O$ (20 mg, 0.076 mmol) and PbI_2 (9.5 mg, 0.02 mmol) in 0.3 mL DMF at room temperature and subsequently, evaporating the solvent at room temperature. Attempting to synthesize $(C_7H_7N_2)_2PbI_4$ as a bulk material $(C_7H_7N_2)PbI_3$ (212 mg, 0.3 mmol) was mixed with $(C_7H_7N_2)I \cdot H_2O$ (73.6 mg, 0.28 mmol) and ground for 5 d with a Specamill vibratory ball mill (Specac). A red powder was obtained.

Single-crystal X-ray diffraction: Single-crystal X-ray diffraction data of $(C_7H_7N_2)_2PbCl_4$ and $(C_7H_7N_2)_2PbI_4$ were collected with a Bruker D8 Venture diffractometer equipped with a rotating anode generator with Mo- K_α radiation (λ = 0.71073 Å) at 100 K. Both compounds crystallized as

two-component twins, hence TWINABS was applied for data reduction and absorption correction.³¹ The reflection data were merged in Laue class 2/m [$R_{\text{int}} = 0.0367$ ((C₇H₇N₂)₂PbCl₄), $R_{\text{int}} = 0.0430$ ((C₇H₇N₂)₂PbI₄)]. A D8 Quest I μ S diffractometer with a Mo-Microsource generator was used to collect single-crystal X-ray diffraction data of (C₇H₇N₂)₂PbBr₄ and (C₇H₇N₂)PbI₃ at 173 K. The diffraction intensities were integrated using the SAINT software package³² and a multi-scan absorption correction was applied with SADABS.³³ The crystal structure was solved by direct methods (SIR97)³⁴ and refined against F^2 by applying the full-matrix least-squares method (SHELXL-2014/7).³⁵ Only for (C₇H₇N₂)₂PbI₄ the program SHELXT-2014 was used for the structure solution.³⁶ Hydrogen positions were calculated according to geometrical criteria and treated as riding on their parent atoms with the exception of the N-bound hydrogen positions in (C₇H₇N₂)PbI₃, which were refined with a restrained N–H bond distance of 0.88(1) Å. Their atomic displacement parameters were constraint to 1.2 times the value of their parent atom. All non-hydrogen atoms were refined anisotropically.

Crystallographic data (excluding structure factors) for the structures in this paper have been deposited with the Cambridge Crystallographic Data Centre, CCDC, 12 Union Road, Cambridge CB21EZ, UK. Copies of the data can be obtained free of charge on quoting the depository numbers CCDC-1507154, CCDC-1507155, CCDC-1507156 and CCDC-1507157 (Fax: +44-1223-336-033; E-Mail: deposit@ccdc.cam.ac.uk, <http://www.ccdc.cam.ac.uk>).

Powder X-ray Diffraction (PXRD): Powder X-ray diffraction patterns were collected with STOE Stadi P diffractometers in a modified Debye-Scherrer set-up equipped with a Mythen1K detector using Ge(111)-monochromated Cu- $K_{\alpha 1}$ radiation ($\lambda = 1.54059$ Å). Samples were encapsulated into capillaries under ambient conditions prior to the measurement. Rietveld refinements were performed using TOPAS academic.³⁷

Infrared (IR) Spectroscopy: FT-IR spectra were recorded at ambient conditions between 650 and 4000 cm⁻¹ on a Spektrum BX II FTIR spectrometer (Perkin-Elmer) equipped with a DuraSampler diamond ATR device.

Absorption and Photoluminescence (PL) Measurements: For optical measurements, samples were clamped between two quartz substrates. Absorption spectra were measured with an Agilent Technologies 8453 UV/Vis spectrometer in an integrating sphere. Steady-state photoluminescence measurements were recorded with a PicoQuant FluoTime 300 fluorescence spectrometer, using a 300 W xenon arc lamp as excitation source. All measurements were done in air under ambient conditions.

Solid-state NMR Spectroscopy: ¹H, ¹³C and ¹⁵N MAS solid-state NMR spectra were recorded with a Bruker Avance III-500 ($H_0 = 11.74$ T) spectrometer at room temperature using a 4 mm probe, with the sample spinning at 10 kHz. All spectra were referenced to 0.1% Si(CH₃)₄ ($\delta = 0.0$ ppm) in CDCl₃. ¹H spectra were obtained in one scan. ¹³C cross-polarization (CP) MAS spectra were

recorded with a contact time of 3 ms in 496, 1024, and 136 scans for $(\text{C}_7\text{H}_7\text{N}_2)_2\text{PbCl}_4$, $(\text{C}_7\text{H}_7\text{N}_2)_2\text{PbBr}_4$ and $(\text{C}_7\text{H}_7\text{N}_2)\text{PbI}_3$, respectively. The repetition time was set to 128 s for $(\text{C}_7\text{H}_7\text{N}_2)_2\text{PbCl}_4$ and to 64 s for $(\text{C}_7\text{H}_7\text{N}_2)_2\text{PbBr}_4$ and $(\text{C}_7\text{H}_7\text{N}_2)\text{PbI}_3$. ^{15}N CP MAS spectra were acquired with a contact time of 1 ms and a recycle delay of 64 s in 2752, 4104 and 1344 scans for $(\text{C}_7\text{H}_7\text{N}_2)_2\text{PbCl}_4$, $(\text{C}_7\text{H}_7\text{N}_2)_2\text{PbBr}_4$, and $(\text{C}_7\text{H}_7\text{N}_2)\text{PbI}_3$, respectively. All ^{13}C and ^{15}N spectra were recorded with proton decoupling using the TPPM method.³⁸

Solution-state NMR Spectroscopy: ^1H and ^{13}C NMR spectra were recorded with a Bruker 400 TR spectrometer in $[\text{D}_6]$ DMSO at room temperature.

Energy Dispersive X-ray Spectroscopy (EDX): A FEI Helios G3 UC scanning electron microscope (SEM) operating at 20 kV was used to determine the content of Pb and Br in $(\text{C}_7\text{H}_7\text{N}_2)_2\text{PbBr}_4$ locally.

Thermal Analysis: DTA and TG data were collected simultaneously with a NETZSCH STA 409C/CD thermoanalyzer. Samples were heated in an argon flow of $100 \text{ mL}\cdot\text{min}^{-1}$ in aluminium oxide crucibles from room temperature to $800 \text{ }^\circ\text{C}$ for $(\text{C}_7\text{H}_7\text{N}_2)_2\text{PbCl}_4$ and to $900 \text{ }^\circ\text{C}$ for $(\text{C}_7\text{H}_7\text{N}_2)_2\text{PbBr}_4$ and $(\text{C}_7\text{H}_7\text{N}_2)\text{PbI}_3$ with a heating rate of $10 \text{ K}\cdot\text{min}^{-1}$.

Elemental Analysis: The elemental analyzer systems Vario EL and Vario Micro (Elementar Analysensysteme GmbH) were used to determine the content of C, H, and N. The percentage of Cl, Br and I was analysed with the titrator 888 Titrand (Metrohm).

Acknowledgements

We gratefully acknowledge financial support by the Max Planck Gesellschaft, Deutsche Telekom Stiftung (scholarship for *CL*), Carl Zeiss Stiftung (scholarship for *STB*), the cluster of excellence Nanosystems Initiative Munich (NIM) and the Center for NanoScience (CeNS). Thanks to *Christian Minke* (Schnick group, LMU Munich) for performing the solid state NMR spectroscopy measurements and to *Daniel Weber*, M.Sc. and *Willi Hölle* for collecting the thermal analysis data. We also thank *Viola Duppel*, *Dr. Sophia Betzler* and *Dr. Ramona Hoffmann* (Bein group, LMU Munich) for performing the EDX measurements. Thanks to *Christine Stefani* (Dinnebier group, MPI-FKF) for collecting additional PXRD data.

3.5 References

1. Muljarov, E. A.; Tikhodeev, S. G.; Gippius, N. A.; Ishihara, T., Excitons in self-organized semiconductor/insulator superlattices: PbI-based perovskite compounds. *Phys. Rev. B: Condens. Matter Mater. Phys.* **1995**, 51, (20), 14370-14378.

2. Mousdis, G. A.; Papavassiliou, G. C.; Raptopoulou, C. P.; Terzis, A., Preparation and characterization of $[\text{H}_3\text{N}(\text{CH}_2)_6\text{NH}_3]\text{PbI}_4$ and similar compounds with a layered perovskite structure. *J. Mater. Chem.* **2000**, 10, (2), 515-518.
3. Ishihara, T.; Takahashi, J.; Goto, T., Exciton state in two-dimensional perovskite semiconductor $(\text{C}_{10}\text{H}_{21}\text{NH}_3)_2\text{PbI}_4$. *Solid State Commun.* **1989**, 69, (9), 933-936.
4. Era, M.; Morimoto, S.; Tsutsui, T.; Saito, S., Organic-inorganic heterostructure electroluminescent device using a layered perovskite semiconductor $(\text{C}_6\text{H}_5\text{C}_2\text{H}_4\text{NH}_3)_2\text{PbI}_4$. *Appl. Phys. Lett.* **1994**, 65, (6), 676-678.
5. Chondroudis, K.; Mitzi, D. B., Electroluminescence from an Organic-Inorganic Perovskite Incorporating a Quaterthiophene Dye within Lead Halide Perovskite Layers. *Chem. Mater.* **1999**, 11, (11), 3028-3030.
6. Hong, X.; Ishihara, T.; Nurmikko, A. V., Dielectric confinement effect on excitons in PbI_4 -based layered semiconductors. *Phys. Rev. B: Condens. Matter Mater. Phys.* **1992**, 45, (12), 6961-6964.
7. Dohner, E. R.; Hoke, E. T.; Karunadasa, H. I., Self-Assembly of Broadband White-Light Emitters. *J. Am. Chem. Soc.* **2014**, 136, (5), 1718-1721.
8. Dohner, E. R.; Jaffe, A.; Bradshaw, L. R.; Karunadasa, H. I., Intrinsic White-Light Emission from Layered Hybrid Perovskites. *J. Am. Chem. Soc.* **2014**, 136, (38), 13154-13157.
9. Chen, Q.; De Marco, N.; Yang, Y.; Song, T.-B.; Chen, C.-C.; Zhao, H.; Hong, Z.; Zhou, H.; Yang, Y., Under the spotlight: The organic-inorganic hybrid halide perovskite for optoelectronic applications. *Nano Today* **2015**, 10, (3), 355-396.
10. Mitzi, D. B., Synthesis, Structure, and Properties of Organic-Inorganic Perovskites and Related Materials. In *Progress in Inorganic Chemistry*; Karlin, K. D., Ed.; John Wiley & Sons, Inc.: New York, NY, 1999; pp 1-121.
11. Stranks, S. D.; Eperon, G. E.; Grancini, G.; Menelaou, C.; Alcocer, M. J. P.; Leijtens, T.; Herz, L. M.; Petrozza, A.; Snaith, H. J., Electron-Hole Diffusion Lengths Exceeding 1 Micrometer in an Organometal Trihalide Perovskite Absorber. *Science* **2013**, 342, (6156), 341-344.
12. Solis-Ibarra, D.; Karunadasa, H. I., Reversible and Irreversible Chemisorption in Nonporous-Crystalline Hybrids. *Angew. Chem.* **2014**, 126, (4), 1057-1060. Solis-Ibarra, D.; Karunadasa, H. I., Reversible and Irreversible Chemisorption in Nonporous-Crystalline Hybrids. *Angew. Chem., Int. Ed.* **2014**, 53, (4), 1039-1042.
13. Solis-Ibarra, D.; Smith, I. C.; Karunadasa, H. I., Post-synthetic halide conversion and selective halogen capture in hybrid perovskites. *Chem. Sci.* **2015**, 6, (7), 4054-4059.
14. Wang, G.-E.; Wang, M.-S.; Jiang, X.-M.; Liu, G.-N.; Cai, L.-Z.; Guo, G.-C.; Huang, J.-S., Crystal structures and optical properties of 1-D PbI_3 -based hybrid materials templated by in situ synthesized benzimidazole derivatives. *Sci. Sin. Chim.* **2011**, 41, (4), 717-725.

15. Biradar, N. S.; Sirmokadam, N. N., Benzimidazole complexes of lead(IV). *J. Inorg. Nucl. Chem.* **1973**, 35, (10), 3639-3641.
16. Mitzi, D. B., Synthesis, Crystal Structure, and Optical and Thermal Properties of $(C_4H_9NH_3)_2MI_4$ (M = Ge, Sn, Pb). *Chem. Mater.* **1996**, 8, (3), 791-800.
17. Pugmire, R. J.; Grant, D. M., Carbon-13 magnetic resonance. XIX. Benzimidazole, purine, and their anionic and cationic species. *J. Am. Chem. Soc.* **1971**, 93, (8), 1880-1887.
18. Nieto, C. I.; Cabildo, P.; García, M. Á.; Claramunt, R. M.; Alkorta, I.; Elguero, J., An experimental and theoretical NMR study of NH-benzimidazoles in solution and in the solid state: proton transfer and tautomerism. *Beilstein J. Org. Chem.* **2014**, 10, 1620-1629.
19. Kulkarni, S. A.; Baikie, T.; Boix, P. P.; Yantara, N.; Mathews, N.; Mhaisalkar, S., Band-gap tuning of lead halide perovskites using a sequential deposition process. *J. Mater. Chem. A* **2014**, 2, (24), 9221-9225.
20. Noh, J. H.; Im, S. H.; Heo, J. H.; Mandal, T. N.; Seok, S. I., Chemical Management for Colorful, Efficient, and Stable Inorganic–Organic Hybrid Nanostructured Solar Cells. *Nano Lett.* **2013**, 13, (4), 1764-1769.
21. Eperon, G. E.; Stranks, S. D.; Menelaou, C.; Johnston, M. B.; Herz, L. M.; Snaith, H. J., Formamidinium lead trihalide: a broadly tunable perovskite for efficient planar heterojunction solar cells. *Energy Environ. Sci.* **2014**, 7, (3), 982-988.
22. Smith, I. C.; Hoke, E. T.; Solis-Ibarra, D.; McGehee, M. D.; Karunadasa, H. I., A Layered Hybrid Perovskite Solar-Cell Absorber with Enhanced Moisture Stability. *Angew. Chem.* **2014**, 126, (42), 11414-11417. Smith, I. C.; Hoke, E. T.; Solis-Ibarra, D.; McGehee, M. D.; Karunadasa, H. I., A Layered Hybrid Perovskite Solar-Cell Absorber with Enhanced Moisture Stability. *Angew. Chem., Int. Ed.* **2014**, 53, 11232–11235.
23. Maculan, G.; Sheikh, A. D.; Abdelhady, A. L.; Saidaminov, M. I.; Haque, M. A.; Murali, B.; Alarousu, E.; Mohammed, O. F.; Wu, T.; Bakr, O. M., $CH_3NH_3PbCl_3$ Single Crystals: Inverse Temperature Crystallization and Visible-Blind UV-Photodetector. *J. Phys. Chem. Lett.* **2015**, 6, (19), 3781-3786.
24. Hu, T.; Smith, M. D.; Dohner, E. R.; Sher, M.-J.; Wu, X.; Trinh, M. T.; Fisher, A.; Corbett, J.; Zhu, X. Y.; Karunadasa, H. I.; Lindenberg, A. M., Mechanism for Broadband White-Light Emission from Two-Dimensional (110) Hybrid Perovskites. *J. Phys. Chem. Lett.* **2016**, 7, (12), 2258-2263.
25. Lermer, C.; Birkhold, S. T.; Moudrakovski, I. L.; Mayer, P.; Schoop, L. M.; Schmidt-Mende, L.; Lotsch, B. V., Toward Fluorinated Spacers for MAPI-Derived Hybrid Perovskites: Synthesis, Characterization, and Phase Transitions of $(FC_2H_4NH_3)_2PbCl_4$. *Chem. Mater.* **2016**, 28, (18), 6560-6566.
26. Yangui, A.; Garrot, D.; Lauret, J. S.; Lusson, A.; Bouchez, G.; Deleporte, E.; Pillet, S.; Bendeif, E. E.; Castro, M.; Triki, S.; Abid, Y.; Boukheddaden, K., Optical Investigation of Broadband White-

Light Emission in Self-Assembled Organic–Inorganic Perovskite $(\text{C}_6\text{H}_{11}\text{NH}_3)_2\text{PbBr}_4$. *J. Phys. Chem. C* **2015**, 119, (41), 23638-23647.

27. Kabanov, V. V.; Mashtakov, O. Y., Electron localization with and without barrier formation. *Phys. Rev. B: Condens. Matter Mater. Phys.* **1993**, 47, (10), 6060-6064.
28. Emin, D.; Holstein, T., Adiabatic Theory of an Electron in a Deformable Continuum. *Phys. Rev. Lett.* **1976**, 36, (6), 323-326.
29. Dou, L.; Wong, A. B.; Yu, Y.; Lai, M.; Kornienko, N.; Eaton, S. W.; Fu, A.; Bischak, C. G.; Ma, J.; Ding, T.; Ginsberg, N. S.; Wang, L.-W.; Alivisatos, A. P.; Yang, P., Atomically thin two-dimensional organic-inorganic hybrid perovskites. *Science* **2015**, 349, (6255), 1518-1521.
30. Comin, R.; Walters, G.; Thibau, E. S.; Voznyy, O.; Lu, Z.-H.; Sargent, E. H., Structural, optical, and electronic studies of wide-bandgap lead halide perovskites. *J. Mater. Chem. C* **2015**, 3, (34), 8839-8843.
31. *TWINABS*, Bruker: Madison, Wisconsin, USA, 2001.
32. *SAINT*, Bruker: Madison, Wisconsin, USA, 2012.
33. *SADABS*, Bruker: Madison, Wisconsin, USA, 2001.
34. Altomare, A.; Burla, M. C.; Camalli, M.; Casciarano, G. L.; Giacovazzo, C.; Guagliardi, A.; Moliterni, A. G. G.; Polidori, G.; Spagna, R., SIR97: a new tool for crystal structure determination and refinement. *J. Appl. Crystallogr.* **1999**, 32, (1), 115-119.
35. Sheldrick, G., Crystal structure refinement with SHELXL. *Acta Crystallogr., Sect. C* **2015**, 71, (1), 3-8.
36. Sheldrick, G., SHELXT - Integrated space-group and crystal-structure determination. *Acta Crystallogr., Sect. A* **2015**, 71, (1), 3-8.
37. *Topas Academic, version 5*; Coelho Software: Brisbane, Australia, 2012.
38. Bennett, A. E.; Rienstra, C. M.; Auger, M.; Lakshmi, K. V.; Griffin, R. G., Heteronuclear decoupling in rotating solids. *J. Chem. Phys.* **1995**, 103, (16), 6951-6958.

4. Completing the picture of 2-(aminomethylpyridinium) lead hybrid perovskites – Insights into structure, conductivity behavior and optical properties

Claudia Lermer, Alessandro Senocrate, Igor L. Moudrakovski, Tobias Seewald, Anna-Katharina Hatz, Peter Mayer, Florian Pielhofer, Julian A. Jaser, Lukas Schmidt-Mende, Joachim Maier, Bettina V. Lotsch

This chapter is a pre-peer reviewed version of a manuscript submitted to *Chem. Mater.*

Abstract

Hybrid perovskites have evolved into an exciting materials platform supporting a wide variety of optoelectronic applications including solar cells and light-emitting devices. In spite of their rapid deployment in devices, a detailed understanding of their structure – property relationships is scarce. In this study, we comprehensively analyze the crystal and electronic structures, as well as thermal, optical and electronic properties of a series of 2-(aminomethylpyridinium) lead halides including the isotypic hybrid perovskites $(\text{C}_6\text{H}_{10}\text{N}_2)\text{PbX}_4$ ($X = \text{Cl}, \text{Br}$ and I) and the hybrid compound $(\text{C}_6\text{H}_{10}\text{N}_2)_6\text{IPb}_5\text{I}_{21} \cdot 3 \text{H}_2\text{O}$. The thermal transformation of $(\text{C}_6\text{H}_{10}\text{N}_2)_6\text{IPb}_5\text{I}_{21} \cdot 3 \text{H}_2\text{O}$ into $(\text{C}_6\text{H}_{10}\text{N}_2)\text{PbI}_4$ was studied by thermal analysis and powder X-ray diffraction and used to reverse engineer a synthesis route for phase-pure $(\text{C}_6\text{H}_{10}\text{N}_2)\text{PbI}_4$. The very broad PL emission of $(\text{C}_6\text{H}_{10}\text{N}_2)_6\text{IPb}_5\text{I}_{21} \cdot 3 \text{H}_2\text{O}$ is traced back to the largest octahedral distortion found in this compound amongst all studied 2-(aminomethylpyridinium) lead halides. We further find that $(\text{C}_6\text{H}_{10}\text{N}_2)\text{PbI}_4$ and $(\text{C}_6\text{H}_{10}\text{N}_2)_6\text{IPb}_5\text{I}_{21} \cdot 3 \text{H}_2\text{O}$ are mixed ionic-electronic conductors and identify the diffusing ionic species as iodine and protons, respectively, by combining solid-state NMR measurements with a.c. impedance spectroscopy and d.c. galvanostatic polarization measurements.

4.1 Introduction

The pace of development in the field of hybrid halide perovskites has surged since methylammonium lead iodide (MAPI) was discovered as a highly promising solar cell material, thanks to its remarkable absorption properties and charge carrier dynamics.¹⁻⁴ At the same time, layered (2D) hybrid perovskites came into the limelight showing not only higher stability than the related 3D compounds, but also intriguing optical properties including broad-band

photoluminescence (PL).⁵⁻⁸ This property results from their inherent 2D quantum well structure giving rise to the formation of excitons with high exciton binding energies within the inorganic layers.⁹ Subsequent thorough investigations elucidated design principles for white-light emitting phosphors. It was found that the PL lifetime and the width of emission can be enhanced by increasing the distortion of the metal halide octahedra the inorganic layer is built on. This principle can be implemented by exploiting the templating effect of the organic cations separating the metal halide octahedra sheets.^{8, 10}

The vast majority of possible applications for layered hybrid perovskites (including light-emitting devices,⁸ field-effect transistors¹¹ and solar cell devices⁵⁻⁶) follows from their variability in composition and structure. Additional design principles might be derived when exploring and expanding the rich phase space of hybrid perovskites further.

While the optical properties of such layered compounds have been investigated extensively,¹² only one study, to our knowledge, explored the mixed ionic-electronic conduction in a 2D lead-based hybrid perovskite so far.¹³ The importance of such studies originates from investigations on MAPI that show how ion migration is a key factor in polarization and hysteresis phenomena,^{14-16, 52} as well as degradation processes¹⁷⁻¹⁸ taking place in MAPI-based solar cells. Notably, ref. 16 pointed out that such polarization process has to affect the entire bulk and not only space charge zones. On the contrary, Lin et al. discovered that ion migration in the 2D hybrid perovskite $(C_4H_9NH_3)_2(CH_3NH_3)_3Pb_4I_{13}$ is suppressed, which might be one of the reasons for the higher stability inherent to 2D hybrid perovskites.¹³ Yet, additional data from other layered hybrid perovskites is needed to generalize this important observation.

In this paper we synthesize and comprehensively characterize the hybrid perovskite series $(C_6H_{10}N_2)PbX_4$ ($X = Cl, Br$ and I) and the complex lead iodide hydrate $(C_6H_{10}N_2)_6IPb_5I_{21} \cdot 3 H_2O$ covering structural aspects, optical properties and conductivity experiments. The crystal structure of $(C_6H_{10}N_2)PbBr_4$ has been described by Li et al. alongside a basic optical characterization.¹⁹ The crystal structure of $(C_6H_{10}N_2)_6IPb_5I_{21} \cdot 3 H_2O$, including optical absorption as well as TG and DSC data, was reported just recently by Yu and coworkers.²⁰ Our study broadens the family of hybrid perovskite halides based on the 2-(aminomethylpyridinium) cation, and allows us to derive structure-property relationships by studying trends in this materials system. We apply photoluminescence spectroscopy and absorption measurements supported by density functional theory (DFT) calculations to analyze the optical properties in detail. Due to the favorable band gap of the iodine-based compounds and the pronounced stability of $(C_6H_{10}N_2)_6IPb_5I_{21} \cdot 3 H_2O$ under ambient conditions, these compounds were subjected to further investigations including a.c. impedance spectroscopy, d.c. galvanostatic polarization and solid-state NMR spectroscopy to gain information on their conductivity behavior and the diffusing ionic species. This study thus

expands the family of hybrid perovskites and contributes to the fundamental understanding of their underlying properties.

4.2 Experimental Section

Materials & Methods. PbCl₂ (Sigma-Aldrich, 98 %), PbBr₂ (Sigma-Aldrich, ≥98 %), PbI₂ (Acros Organics, 99 %), 2-(aminomethyl)pyridine (Sigma-Aldrich, 99 %), concentrated hydrochloric acid (Brenntag, purum), concentrated hydrobromic acid (Acros Organics, pure), concentrated hydriodic acid (Acros Organics, for analysis), concentrated deuterium iodide (60%) in D₂O (Deutero, 99.5 %) and ethyl acetate (Staub & Co. Silbermann, 99.8%) were commercially available and used as received without further purification.

Synthesis of (C₆H₁₀N₂)₆IPb₅I₂₁ · 3 H₂O and (C₆D₁₀N₂)₆IPb₅I₂₁ · 3 D₂O. 0.05 mL (0.48 mmol) 2-picolylamine was added to a clear solution of 186 mg (0.40 mmol) PbI₂ in 1.7 mL concentrated HI and concentrated DI, respectively. The reaction mixture was stirred for 30 min which led to the precipitation of a dark yellow solid. The reaction product was washed thoroughly with ethyl acetate and was stored under ambient conditions. Single crystals for X-ray diffraction were obtained by evaporating the solvent of a less concentrated reaction mixture containing 4 mL HI at room temperature. Anal. Calcd: C, 9.52; H, 1.46; N, 3.70; I, 61.46 wt%. Found: C, 9.54; H, 1.56; N, 3.72; I, 59.54 wt%.

Synthesis of (C₆H₁₀N₂)PbCl₄. 0.05 mL (0.48 mmol) 2-picolylamine was added to a clear solution of 136 mg (0.48 mmol) PbCl₂ in 5 mL concentrated HCl. The reaction mixture was stirred for 30 min, which led to precipitation of a white solid. The reaction product was washed thoroughly with ethyl acetate and was stored under Argon atmosphere. Two methods were applied to obtain single crystals suitable for X-ray diffraction. First, evaporation of the solvent from the reaction mixture at room temperature. Second, vapor diffusion with ethyl acetate led to single crystals of good quality. Here, ethyl acetate slowly diffused into the reaction mixture within a closed system. Anal. Calcd: C, 15.70; H, 2.20; N, 6.10; Cl, 30.88 wt%. Found: C, 15.92; H, 2.36; N, 6.26; Cl, 31.04 wt%.

Synthesis of (C₆H₁₀N₂)PbBr₄. 0.045 mL (0.432 mmol) 2-picolylamine was added to a clear solution of 162 mg (0.432 mmol) PbBr₂ in 4 mL concentrated HBr. The reaction mixture was stirred for 30 min, which led to precipitation of a lemon yellow solid. The reaction product was washed thoroughly with ethyl acetate and was stored under Argon atmosphere. Single crystals suitable for X-ray diffraction could be obtained by the same methods as described for (C₆H₁₀N₂)PbBr₄. Anal. Calcd: C, 11.31; H, 1.58; N, 4.40; Br, 50.18 wt%. Found: C, 11.45; H, 1.74; N, 4.45; Br, 49.79 wt%.

Synthesis of (C₆H₁₀N₂)PbI₄. (C₆H₁₀N₂)₆IPb₅I₂₁ · 3 H₂O was thinly spread in a Petri dish and heated to 160 °C for 2.5 h in a muffle furnace (Themconcept) which led to a color change from yellow to red. The reaction product was quickly transferred to a Schlenk tube and stored under Argon

atmosphere. Single crystals suitable for X-ray diffraction were obtained by adding ethyl acetate to a reaction mixture containing 4 mL HI, 179 mg (0.384 mmol) PbI_2 and 0.04 mL (0.384 mmol) 2-(aminomethyl)amine. As a result, red crystals precipitated which were washed with ethyl acetate. Anal. Calcd: C, 8.74; H, 1.22; N, 3.40; I, 61.53 wt%. Found: C, 9.19; H, 1.36; N, 3.32; I, 59.54 wt%.

Conductivity measurements. In order to assess the electrical properties of $(\text{C}_6\text{H}_{10}\text{N}_2)_6\text{IPb}_5\text{I}_{21} \cdot 3\text{H}_2\text{O}$ and $(\text{C}_6\text{H}_{10}\text{N}_2)\text{PbI}_4$, the powders were uniaxially cold-pressed with a pressure of 11 kN resulting in dense pellets with a diameter of 5 mm. Graphite pellets, which are blocking for ionic carriers, were prepared using the same procedure and served as electrodes. D.c. polarization experiments were conducted with a high impedance current source and electrometer (Keithley 2634B). Measurements were carried out in dark, under dynamic Ar flow and the oxygen content was recorded with a sensor (Cambridge Sensotec Rapidox 2100). To control $p(\text{I}_2)$ over the samples, Argon was flown in a container with iodine chips, kept in a thermostat at fixed temperature. Iodine partial pressure was assumed to correspond to the equilibrium pressure of iodine at the thermostat temperature, which was calculated based on the Gibbs free energy of sublimation of solid iodine. The extraction of ionic and electronic conductivity values from the polarization curves was performed according to literature.²¹

Solid-state NMR spectroscopy. All NMR measurements reported in this work were performed on a Bruker Avance III 400 MHz instrument in a magnetic field of 9.4 T. Measurements were performed on a Bruker BL4 double resonance MAS probe with 4mm outside diameter ZrO_2 spinners. Dry nitrogen was used as spinning, bearing, and cooling gas. The spinning rate was normally kept between 10 and 14 kHz. The temperature in the probe was regulated with a Bruker BVT3000 temperature controller. Actual temperature inside the spinner was calibrated on the ^{207}Pb signal of powdered $\text{Pb}(\text{NO}_3)_2$.²² ^1H MAS NMR spectra were acquired in 16 scans with a relaxation delay of 5 s. ^{13}C cross polarization (CP) MAS NMR spectra were recorded in 1024 - 2048 scans with a contact time of 4 ms and a recycle delay of 1 s. ^{13}C direct excitation MAS NMR spectra were acquired in 80 - 120 scans with a recycle delay of 1000 s. All ^{13}C and ^{15}N spectra were acquired using high power composite proton decoupling achieved with the SPINAL-64 decoupling method. ^{15}N CP MAS NMR spectra were recorded in 20000 - 30000 scans with a contact time of 6 ms and a recycle delay of 2 - 4 s. ^{15}N - ^1H 2D heteronuclear correlation CP MAS spectra were acquired using a **Frequency Switched Lee Goldberg Heteronuclear Correlation** (FSLG HETCOR) experiment.²³ A total of 48 increments in f1-dimension were acquired with 600 scans per increment and relaxation delay of 3 s. The ^2H solid-state NMR spectra were obtained using a 90° - τ - 90° solid-echo pulse sequence and RF power of 65 kHz. While attempted, no signals have been detected from ^{207}Pb , nor ^{127}I . This is not entirely surprising given a distribution of sites for lead and large quadrupolar interactions for ^{127}I . Chemical shifts were referenced externally relative to

TMS (^1H and ^{13}C , $\delta_{\text{iso}} = 0.0$ ppm), and nitromethane (^{15}N , $\delta_{\text{iso}} = 0.0$ ppm, set with the secondary reference of NH_4Cl , $\delta_{\text{iso}} = -341.2.0$ ppm).

DFT Calculations. All calculations concerning the NMR parameters were performed with the Castep code²⁴⁻²⁵ integrated within the Biovia Materials Studio 2017 suite. The computations use the generalized gradient approximation (GGA) and Perdew-Burke-Ernzerhof (PBE) functional,²⁶ with the core-valence interactions described by ultra-soft pseudopotentials.²⁵ A Monkhorst-Pack grid²⁷ was used to realize integrations over the Brillouin zone, with k point spacings generally being less than 0.04 \AA^{-1} . The convergence of the calculated NMR parameters was tested for both the size of a Monkhorst-Pack k-grid and a basis set cut-off energy, with cut-off energies being in the range of 550-610 eV. To account for relativistic effects in such heavy elements as lead and iodine, all calculations were performed including the zeroth-order regular approximation (ZORA)²⁸⁻²⁹ through scalar-relativistic pseudopotentials.³⁰ Geometry optimization calculations were performed using the Broyden-Fletcher-Goldfarb-Shanno (BFGS) algorithm, with the same functional, k-grid spacings and cut-off energies as in the single-point energy calculations. Convergence tolerance parameters for geometry optimization were as follows: maximum energy 2×10^{-5} eV/atom, maximum force 0.05 eV/\AA , maximum stress 0.1 GPa and maximum displacement 0.002 \AA . Crystallographic data used in the calculations were taken from the literature.

Spectral simulations and fitting. Analytical simulations of the experimental spectra were carried out with the DMFit³¹ simulation package and the SOLAGuide module in TopSpin 3.2 processing software from Bruker.

Further, band structure calculations were performed using a linear combination of Gaussian type functions (LCGTF) scheme as implemented in CRYSTAL14.³²⁻³³ To avoid the well-known underestimation of experimental band gaps by standard DFT exchange correlation functionals, the Fock-exchange containing hybrid-functional HSE06³⁴ was applied. The energy convergence criterion was set to 10^{-7} a.u. with a *k*-mesh sampling of $4 \times 4 \times 4$. Pseudo potential basis sets³⁵⁻³⁶ as well as all electron basis sets were used.³⁷⁻⁴⁰

Single crystal X-ray diffraction. Single-crystal X-ray diffraction data were collected on a Bruker D8 Venture diffractometer equipped with a rotating anode generator with Mo $K\alpha$ radiation ($\lambda = 0.71073 \text{ \AA}$). The diffraction intensities were integrated using the SAINT software package⁴¹ and a multi-scan absorption correction was applied with SADABS.⁴² Various programs were applied for structure solution. The crystal structure of $(\text{C}_6\text{H}_{10}\text{N}_2)\text{PbBr}_4$ at 100 K was solved by Direct Methods with the program SIR97.⁴³ SHELXT-2014 was used to solve the crystal structures of $(\text{C}_6\text{H}_{10}\text{N}_2)_6\text{IPb}_5\text{I}_{21} \cdot 3 \text{ H}_2\text{O}$ and $(\text{C}_6\text{H}_{10}\text{N}_2)\text{PbX}_4$, ($X = \text{Cl}, \text{Br}$ and I) at 296 K and the crystal structure of $(\text{C}_6\text{H}_{10}\text{N}_2)\text{PbI}_4$ at 153 K.⁴⁴ Finally, the crystal structures of $(\text{C}_6\text{H}_{10}\text{N}_2)_6\text{IPb}_5\text{I}_{21} \cdot 3 \text{ H}_2\text{O}$ and $(\text{C}_6\text{H}_{10}\text{N}_2)_4\text{Pb}_4\text{Cl}_{16}$ at 100 K were solved with SHELXS-97.⁴⁵ All crystal structures were refined against F^2 by applying the full-matrix least-squares method (SHELXL-2014/7).⁴⁶ The organic

cation in $(\text{C}_6\text{H}_{10}\text{N}_2)\text{PbBr}_4$ is disordered over two sets of sites at 100 K and was refined using a split model (site occupation factor ratio 0.68:0.32). The less occupied C and N sites were only refined isotropically with a common temperature factor. All other non-hydrogen atoms were refined anisotropically. Hydrogen positions were calculated according to geometrical criteria and treated as riding on their parent atoms, whereby N-H distances were refined freely.

Powder X-ray diffraction (PXRD). Powders of $(\text{C}_6\text{H}_{10}\text{N}_2)\text{PbX}_4$ ($X = \text{Cl}, \text{Br}$ and I) were filled into glass capillaries (Hilgenberg, diameter 0.2 - 0.3 mm) in an argon-filled glovebox. $(\text{C}_6\text{H}_{10}\text{N}_2)\text{PbCl}_4$ and $(\text{C}_6\text{H}_{10}\text{N}_2)_6\text{IPb}_5\text{I}_{21} \cdot 3 \text{H}_2\text{O}$ were ground under addition of diamond powder. The sample preparation for $(\text{C}_6\text{H}_{10}\text{N}_2)_6\text{IPb}_5\text{I}_{21} \cdot 3 \text{H}_2\text{O}$ was executed under ambient conditions. Powder X-ray diffraction patterns were collected with STOE Stadi-P diffractometers in Debye-Scherrer geometry equipped with a Mythen1K detector (Dectris) using Ge(111)-monochromated Cu $K_{\alpha 1}$ radiation ($\lambda = 1.54059 \text{ \AA}$), Mo $K_{\alpha 1}$ radiation ($\lambda = 0.70930 \text{ \AA}$) and Ag $K_{\alpha 1}$ ($\lambda = 0.55941 \text{ \AA}$), respectively. Additionally, a temperature-dependent PXRD study was performed for $(\text{C}_6\text{H}_{10}\text{N}_2)_6\text{IPb}_5\text{I}_{21} \cdot 3 \text{H}_2\text{O}$. For that $(\text{C}_6\text{H}_{10}\text{N}_2)_6\text{IPb}_5\text{I}_{21} \cdot 3 \text{H}_2\text{O}$ was gently ground and filled into an open quartz capillary (Hilgenberg, diameter 0.3 mm). Temperature dependent PXRD patterns were recorded in the range of $2 - 112^\circ 2\theta$ within 4 hours each on a Mo $K_{\alpha 1}$ radiation Stoe Stadi-P powder diffractometer in Debye-Scherrer geometry, equipped with a primary Ge(111) Johann-type monochromator (Stoe & CIE) and an array of 3 Mythen-2K detectors (Dectris Ltd.). The sample was measured at 30°C , then heated from 90° to 160°C in 10°C steps and then cooled down to 30°C . The PXRD patterns were analyzed using TOPAS-Academic V4.1.⁴⁷

Thermal analysis. TG data of $(\text{C}_6\text{H}_{10}\text{N}_2)_6\text{IPb}_5\text{I}_{21} \cdot 3 \text{H}_2\text{O}$ were collected using a NETZSCH TG 209F1 Libra thermobalance. The sample was heated from 34°C to 500°C in an aluminium oxide crucible with a heating rate of 1 K min^{-1} under nitrogen atmosphere.

Absorption and photoluminescence (PL) measurements. All optical measurements were performed at room temperature on powdered samples enclosed between quartz slides in nitrogen atmosphere, packed to yield optical densities of approximately 0.9 above the band gap. Absorbance spectra were recorded within an integrating sphere on an Agilent Cary5000 UV-vis-NIR spectrometer. Time-resolved photoluminescence data was collected on a Hamamatsu C10910 streak camera equipped with a phase-locked M10911 synchroscan unit using frequency-doubled pulses from an 800 nm, 120 fs Titanium:Sapphire oscillator (Coherent Mira-HP) for excitation, resulting in an instrument response function of as short as 2 ps FWHM depending on the selected time range. Sample excitation took place at fluences of $5\text{-}20 \text{ nJ cm}^{-2}$ in a cryostat evacuated down to a pressure of 10^{-5} mbar . Scattered excitation light was blocked from entering the detection by means of a 420 nm longpass filter.

Elemental analysis. The content of C, H, and N was determined by using the elemental analyzer systems Vario EL and Vario Micro (Elementar Analysensysteme GmbH). The percentage of Cl, Br and I was assayed with the titrator 888 Titrand (Metrohm).

4.3 Results and Discussion

The hybrid compound $(\text{C}_6\text{H}_{10}\text{N}_2)_6\text{IPb}_5\text{I}_{21} \cdot 3 \text{H}_2\text{O}$ and the hybrid perovskites $(\text{C}_6\text{H}_{10}\text{N}_2)\text{PbCl}_4$ and $(\text{C}_6\text{H}_{10}\text{N}_2)\text{PbBr}_4$ self-assemble at room temperature in reaction mixtures containing 2-(aminomethyl)pyridine, PbX_2 ($X = \text{Cl}, \text{Br}$ and I) and the respective hydrohalic acid. After precipitation from the reaction mixture and washing with ethyl acetate, the phase-pure compounds were isolated (Figures 2a, S6). Phase-pure $(\text{C}_6\text{H}_{10}\text{N}_2)\text{PbI}_4$ could be obtained by heating $(\text{C}_6\text{H}_{10}\text{N}_2)_6\text{IPb}_5\text{I}_{21} \cdot 3 \text{H}_2\text{O}$ to $160 \text{ }^\circ\text{C}$ in air for 2.5 h (Figure 2b). The crystal structure of $(\text{C}_6\text{H}_{10}\text{N}_2)_6\text{IPb}_5\text{I}_{21} \cdot 3 \text{H}_2\text{O}$, space group $Pnma$ (no. 62), was recently reported by Yu et al,²⁰ therefore we will only discuss it briefly here.

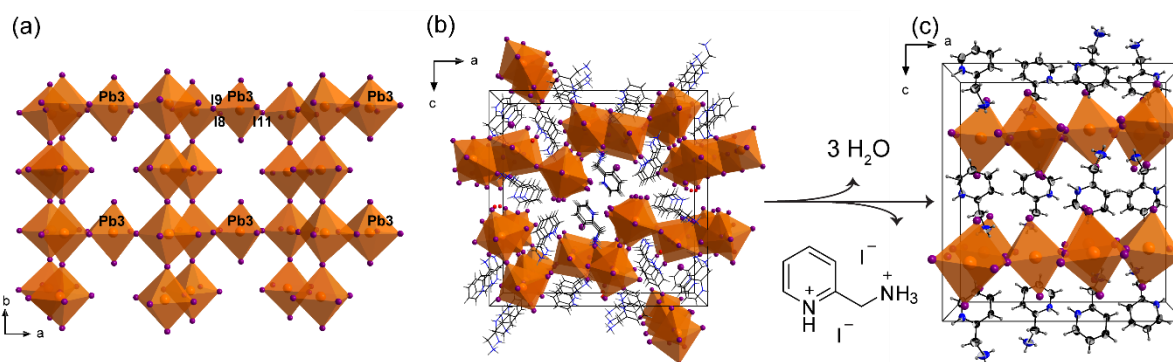


Figure 4.1. (a) Inorganic layer of $(\text{C}_6\text{H}_{10}\text{N}_2)_6\text{IPb}_5\text{I}_{21} \cdot 3 \text{H}_2\text{O}$ projected along the c axis. Conversion of (b) $(\text{C}_6\text{H}_{10}\text{N}_2)_6\text{IPb}_5\text{I}_{21} \cdot 3 \text{H}_2\text{O}$ to (c) $(\text{C}_6\text{H}_{10}\text{N}_2)\text{PbI}_4$ upon heating to $160 \text{ }^\circ\text{C}$ for 2.5 h. The crystal structures of (b) $(\text{C}_6\text{H}_{10}\text{N}_2)_6\text{IPb}_5\text{I}_{21} \cdot 3 \text{H}_2\text{O}$ and (c) $(\text{C}_6\text{H}_{10}\text{N}_2)\text{PbI}_4$ at room temperature are projected along the b axis. For clarity the hydrogen atoms of the water molecules are omitted and a wire-frame model is applied for the organic cations in (b). Thermal ellipsoids for carbon and nitrogen are drawn at the 50% probability level. Pb is displayed in orange, I is purple, N is blue, C is black, O is red, and H is grey.

The hybrid compound is built up from “perforated” inorganic layers which can be described as interconnected corner-sharing double chains of PbI_6^{2-} octahedra. However, only every other octahedron of these building blocks is linked to the adjacent chain by an additional single PbI_6^{4-} octahedron (Pb3). The connection takes place via edges on one side (I8, I9) and corners on the opposing side (I11) (Figure 1a). Monolayers of double protonated 2-(aminomethyl)pyridinium cations separate the inorganic layers. Besides ionic interactions, a dense network of weak to moderate hydrogen bonds plays an important role in stabilizing the structure (Figure S1, Table SVI).⁴⁸ Furthermore, the structure accommodates some additional iodide ions which are not part

of the PbI_6^{2-} octahedra (Figure 1b). This observation raises the question whether these “free” iodide ions are mobile and as such can diffuse through the solid. This will be discussed later on and studied by conductivity measurements. $(\text{C}_6\text{H}_{10}\text{N}_2)_6\text{IPb}_5\text{I}_{21} \cdot 3 \text{H}_2\text{O}$ shows long-term stability as shown by a PXRD measurement after storing the material for 9 months under ambient conditions (Figure S5). Yu et al. already noted a change in color from yellow to red when heating $(\text{C}_6\text{H}_{10}\text{N}_2)_6\text{IPb}_5\text{I}_{21} \cdot 3 \text{H}_2\text{O}$ to higher temperatures and assigned it to structural changes. We have comprehensively analyzed this process and find that rather than a simple dehydration, as described previously, a structural conversion into a 2D hybrid perovskite structure with composition $(\text{C}_6\text{H}_{10}\text{N}_2)\text{PbI}_4$ takes place upon heating. We then used these insights to develop a synthesis route for phase-pure $(\text{C}_6\text{H}_{10}\text{N}_2)\text{PbI}_4$. The stepwise transformation of $(\text{C}_6\text{H}_{10}\text{N}_2)_6\text{IPb}_5\text{I}_{21} \cdot 3 \text{H}_2\text{O}$ was monitored by a TG measurement with a heating rate of 1 K min^{-1} (Figure S8). In the first step the crystal water evaporates with an observed mass loss of 1.9% (calculated loss for the 3 H_2O molecules is 1.2%). In the second step, 2-(aminomethyl)pyridinium iodide leaves the crystal structure with a mass loss of 7.6% (calculated loss due to $(\text{C}_6\text{H}_{10}\text{N}_2)\text{I}_2$ is 8.0%), resulting in the formation of $(\text{C}_6\text{H}_{10}\text{N}_2)\text{PbI}_4$. Further heating leads to complete degradation of the material. To complement our findings, we performed temperature-dependent PXRD measurements using an open system (Figure 2c). The conversion from the yellow hybrid compound $(\text{C}_6\text{H}_{10}\text{N}_2)_6\text{IPb}_5\text{I}_{21} \cdot 3 \text{H}_2\text{O}$ to the red hybrid perovskite $(\text{C}_6\text{H}_{10}\text{N}_2)\text{PbI}_4$ starts at $90 \text{ }^\circ\text{C}$ and is completed at $160 \text{ }^\circ\text{C}$. As expected, the crystal structure of $(\text{C}_6\text{H}_{10}\text{N}_2)\text{PbI}_4$ is maintained upon cooling the sample back to room temperature (Figure S7), since the crystallization water and the evaporated 2-(aminomethyl)pyridinium iodide are no longer available for reincorporation during cooling.

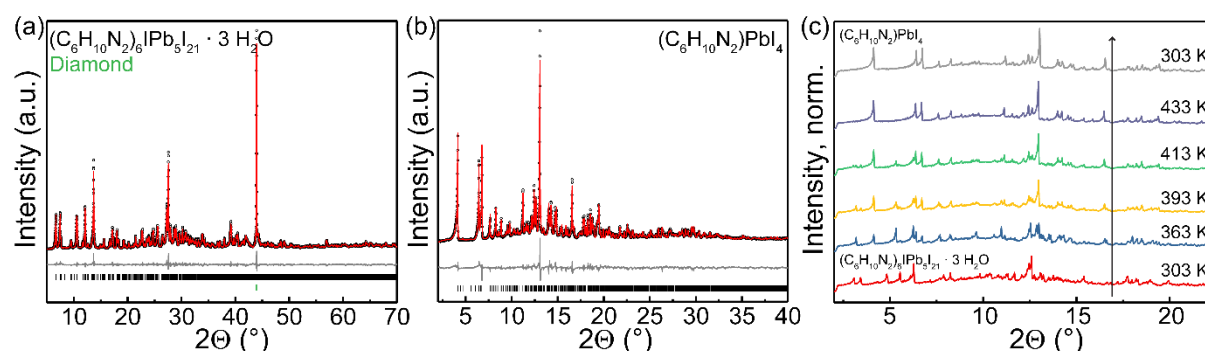


Figure 4.2. Powder X-ray diffraction data (black open circles) of (a) $(\text{C}_6\text{H}_{10}\text{N}_2)_6\text{IPb}_5\text{I}_{21} \cdot 3 \text{H}_2\text{O}$ ($\lambda = \text{Cu K}\alpha_1$) and (b) $(\text{C}_6\text{H}_{10}\text{N}_2)\text{PbI}_4$ ($\lambda = \text{Mo K}\alpha_1$). The Rietveld profile fits (red solid lines) confirm phase purity. The difference curves are displayed in grey. $(\text{C}_6\text{H}_{10}\text{N}_2)_6\text{IPb}_5\text{I}_{21} \cdot 3 \text{H}_2\text{O}$ was diluted with diamond (green tick). (c) PXRD patterns ($\lambda = \text{Mo K}\alpha_1$) monitoring the irreversible conversion of $(\text{C}_6\text{H}_{10}\text{N}_2)_6\text{IPb}_5\text{I}_{21} \cdot 3 \text{H}_2\text{O}$ to $(\text{C}_6\text{H}_{10}\text{N}_2)\text{PbI}_4$ when heating $(\text{C}_6\text{H}_{10}\text{N}_2)_6\text{IPb}_5\text{I}_{21} \cdot 3 \text{H}_2\text{O}$ in an open system to $160 \text{ }^\circ\text{C}$. The arrow indicates the course of the temperature program.

$(C_6H_{10}N_2)PbI_4$ belongs to the series $(C_6H_{10}N_2)PbX_4$ ($X = Cl, Br$ and I) of isotypic hybrid perovskites crystallizing in the orthorhombic space group $Pbca$ (no. 61) at room temperature. The compound $(C_6H_{10}N_2)PbBr_4$ was already described by Li et al.¹⁹ The 2D perovskite structure comprises layers of corner-sharing PbX_6^{4-} octahedra which are separated by monolayers of double-protonated 2-(aminomethyl)pyridinium cations. As for many hybrid perovskites, hydrogen bonds have a crucial impact on the structure.⁴⁹ The protonated primary amino groups protrude into the cavities formed by the inorganic lattice, whereby weak to moderate hydrogen bonds between the halide atoms of the PbX_6^{4-} octahedra and both kinds of amino groups are formed (Figure S2, Tables SXVII, SXXII, SXXVII). Looking at the organic cations lining up the a axis, the orientation of the primary amino group alternates by 180° for every molecule within the line (Figure 1c). Additionally, we investigated the crystal structure of the compounds described in this work at 100 K and 153 K, respectively. Only the chloride containing compound $(C_6H_{10}N_2)_4Pb_4Cl_{16}$ exhibits a different space group at low temperatures, crystallizing in the polar space group $Pna2_1$ (no. 33) at 100 K. Even though the inorganic layers composed of corner-sharing octahedra and the arrangement of organic cations are maintained, differences in the tilting pattern of the octahedra at room temperature and 100 K can be observed (Figure S4b,c). The symmetry relations between the space groups are illustrated with the aid of a Bärnighausen tree (Figure S4a).⁵⁰ First, we can deduce a *translationengleiche* symmetry reduction of index 2 from $Pbca$ to $Pca2_1$ (no. 29), which includes the loss of the inversion center. As a consequence, we observed an inversion twin at 100 K. The subsequent *klassengleiche* transformation of index 2 from $Pca2_1$ to $Pna2_1$ is connected to a doubling of the b axis explaining the expansion of the unit cell when cooling $(C_6H_{10}N_2)PbCl_4$ to 100 K. For $(C_6H_{10}N_2)PbBr_4$ we found that the 2-(aminomethyl)pyridinium cations are disordered at 100 K (Figure S3).

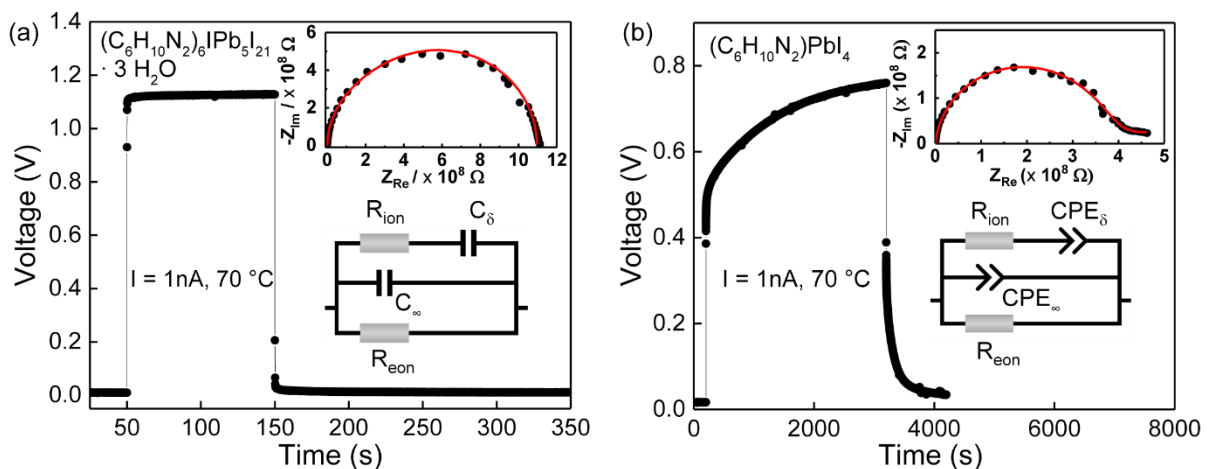


Figure 4.3. D.c. galvanostatic polarization measurement and a.c impedance spectroscopy under Ar with ion-blocking carbon electrodes at 70 °C after 10 h of equilibration for (a) $(C_6H_{10}N_2)_6IPb_5I_{21} \cdot 3 H_2O$ and (b) $(C_6H_{10}N_2)PbI_4$. The inset shows the equivalent circuit model⁵¹⁻⁵² used in the analysis of the impedance data.

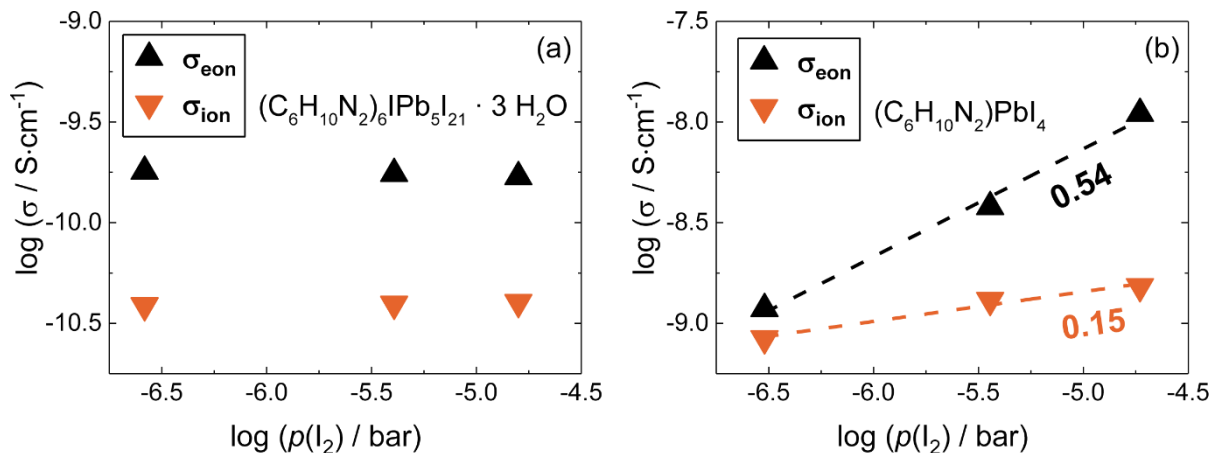


Figure 4.4. Ionic and electronic conductivity as a function of iodine partial pressure ($p(\text{I}_2)$) for (a) $(\text{C}_6\text{H}_{10}\text{N}_2)_6\text{IPb}_5\text{I}_{21} \cdot 3 \text{H}_2\text{O}$ and (b) $(\text{C}_6\text{H}_{10}\text{N}_2)\text{PbI}_4$. The conductivity measurement were carried out using d.c. galvanostatic polarization with ion-blocking graphite electrodes at 70 °C. Argon was used as a carrier gas ($p(\text{O}_2) = 15 \text{ ppm}$).

By means of a.c. impedance spectroscopy and d.c. galvanostatic polarization under Argon atmosphere, shown in Figure 3, we observe that both materials are mixed ionic-electronic conductors, as common for many halide perovskites.^{16, 53} $(\text{C}_6\text{H}_{10}\text{N}_2)_6\text{IPb}_5\text{I}_{21} \cdot 3 \text{H}_2\text{O}$ presents a substantially lower ionic conductivity ($8 \cdot 10^{-11} \text{ S cm}^{-1}$) than its dehydrated counterpart ($2 \cdot 10^{-10} \text{ S cm}^{-1}$), while the electronic conductivity values are similar (about $2 \cdot 10^{-10} \text{ S cm}^{-1}$). A comparison to literature shows that, in the dark, both compositions have a smaller electronic and ionic conductivity than MAPI,¹⁶ but a higher conductivity than 2D $(\text{C}_4\text{H}_9\text{NH}_3)_2(\text{CH}_3\text{NH}_3)_3\text{Pb}_4\text{I}_{13}$.¹³ Next, we investigated the nature of the mobile ionic species by performing conductivity measurements as a function of iodine partial pressure, which can modify the compound stoichiometry and thus its charge carrier concentrations.⁵² As known for several other halide perovskites, these materials are very often halide conductors^{16, 52-53} and, due to simple size considerations, we can rule out a significant mobility of the organic cations. The question is therefore whether the ionic conductivity stems from iodide ions or from a fraction of the protons present in the structure that, once dissociated, could have a high mobility. We start by considering $(\text{C}_6\text{H}_{10}\text{N}_2)_6\text{IPb}_5\text{I}_{21} \cdot 3 \text{H}_2\text{O}$ that, as stated previously, has a quantity of non-bound iodine atoms that could potentially diffuse through the structure. As shown in Figure 4a, both ionic and electronic conductivity are unchanged by iodine exposure. This indicates that no iodine incorporation takes place for this material. Assuming sufficient surface kinetics this occurrence implies absence of mobile iodine defects. As discussed in more detail below, this is consistent with NMR measurements showing mobile protons in this phase. In contrast, $(\text{C}_6\text{H}_{10}\text{N}_2)\text{PbI}_4$ shows a clear increasing trend in both ionic and electronic conductivity (Figure 4b) with $p(\text{I}_2)$, indicating perceptible iodine incorporation. In conjunction with NMR experiments that show absence of mobile protons, this is indicative of significant iodine motion. Also, the increasing trend of electronic conductivity is suggestive of p-

type conduction, while the rise in ionic conductivity could be interpreted with the presence of mobile iodine interstitials, the concentration of which is increased by iodine incorporation. We note that, presently, this latter statement is only preliminary and more analyses are required for confirmation.

Insight in the nature of the diffusing ion species was further obtained by solid-state NMR. First of all, the phase purity of $(\text{C}_6\text{H}_{10}\text{N}_2)_6\text{IPb}_5\text{I}_{21} \cdot 3 \text{H}_2\text{O}$ and $(\text{C}_6\text{H}_{10}\text{N}_2)\text{PbI}_4$ was confirmed by recording ^1H , ^{13}C and ^{15}N solid-state NMR spectra at room temperature. The NMR spectra are discussed in the supporting information S9. The ^1H NMR spectrum of $(\text{C}_6\text{H}_{10}\text{N}_2)\text{PbI}_4$ gives no direct indications of proton conduction. The hydroxyl ions can be excluded to be the ionic charge carriers, since no mobile species can be observed in the range of 3 ppm - 0 ppm in the ^1H spectrum.⁵⁴⁻⁵⁵ As a consequence, the bulk of ionic conductivity in $(\text{C}_6\text{H}_{10}\text{N}_2)\text{PbI}_4$ is likely due to iodine motion, in agreement with conductivity measurements.

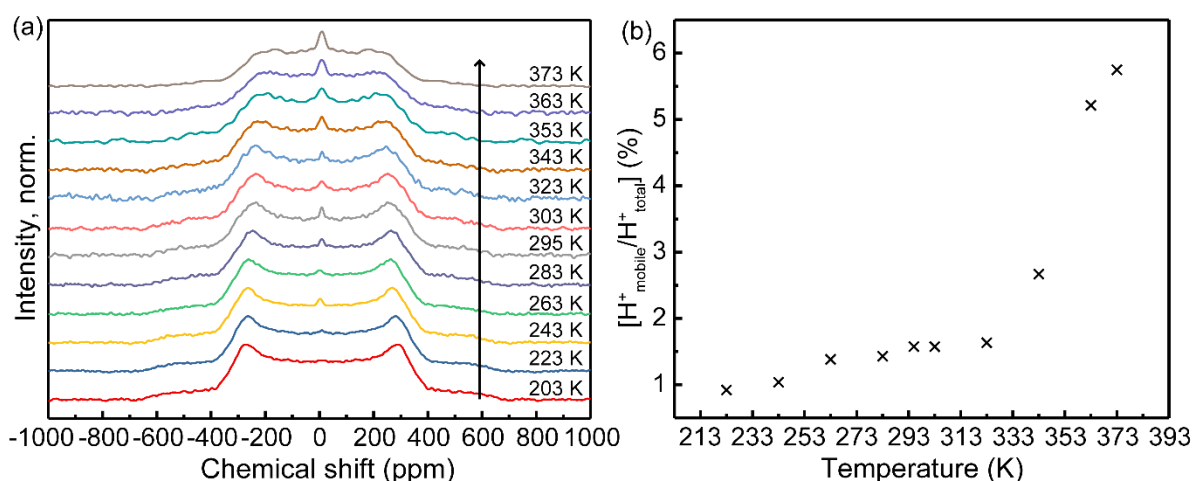


Figure 4.5. (a) Temperature-dependent ^2H static solid-state NMR spectra of $(\text{C}_6\text{H}_{10}\text{N}_2)_6\text{IPb}_5\text{I}_{21} \cdot 3 \text{H}_2\text{O}$. The arrow indicates the course of the temperature program. (b) Ratio of mobile protons to the total amount of protons in $(\text{C}_6\text{H}_{10}\text{N}_2)_6\text{IPb}_5\text{I}_{21} \cdot 3 \text{H}_2\text{O}$ as a function of temperature. The sudden increase is due to loss of crystal water.

A detailed analysis of the ^2H spectra of $(\text{C}_6\text{D}_{10}\text{N}_2)_6\text{IPb}_5\text{I}_{21} \cdot 3 \text{H}_2\text{O}$ suggests that a small fraction of protons may experience fast (on the NMR time scale) translational motion through the solid. These mobile protons appear in the stationary spectra as a low intensity narrow signal with a chemical shift near 8.0 ppm, as obtained from the ^2H MAS NMR measurements. This chemical shift of 8.0 ppm is within the generally accepted range of moderately acidic protons.⁵⁴ In order to estimate the number of mobile protons, we recorded temperature-dependent ^2H MAS and stationary NMR spectra (Figure 5). Static spectra demonstrate a sharp signal from the translationally mobile protons on top of the broad signal generated by the protons with low mobility. An estimate of the ratio of the mobile protons to the total number of protons in the sample was derived by fitting the

spectra with a combination of Lorentzian/Gaussian lines for the mobile protons and a first order quadrupolar line shape for the relatively immobile molecules of D_2O , respectively (Figure S16). A slow increase in the fraction of mobile protons can be observed upon heating $(C_6H_{10}N_2)_6IPb_5I_{21} \cdot 3 H_2O$ from 203 K to about 323 K, which is followed by a leap when the temperature is rising above 333 K. This jump concurs with the evaporation of crystal water as elucidated by thermal analysis (Figure S8) and this is most likely the reason for the observed behavior. We can thus state that protons are likely to be responsible for the measured ionic conductivity of $(C_6H_{10}N_2)_6IPb_5I_{21} \cdot 3 H_2O$.

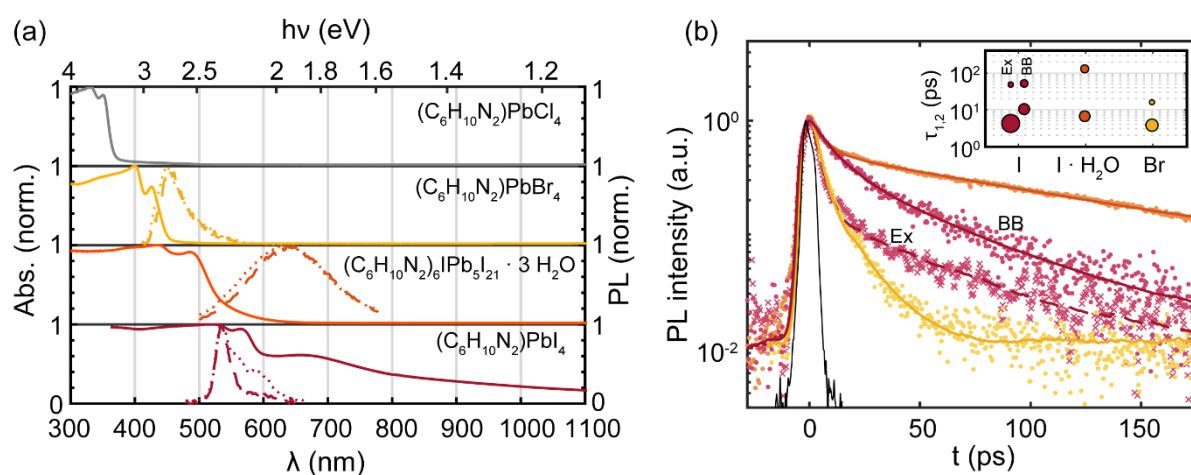


Figure 4.6. (a) Absorbance (solid lines) and PL spectra ($\lambda_{\text{excitation}} = 400 \text{ nm}$) immediately upon excitation (dotted lines) and later during the decay (dashed lines). (b) Time-resolved PL intensity data (dots) and biexponential fits (colored lines) convoluted with the instrument resolution function (IRF) (black line) of $(C_6H_{10}N_2)PbI_4$ (red), $(C_6H_{10}N_2)_6IPb_5I_{21} \cdot 3 H_2O$ (orange), and $(C_6H_{10}N_2)PbBr_4$ (yellow). The inset shows the corresponding time constants. The marker size is proportional to the fractional weighing of the decay components. BB is decay of band-to-band transition and Ex is excitonic decay.

Absorption and photoluminescence measurements were applied to gain insight into the optical properties of all discussed materials. As expected, the optical absorption onsets of the $(C_6H_{10}N_2)PbX_4$ ($X = Cl, Br$ and I) series shift towards the red with increasing halide size.⁵⁶⁻⁵⁷ The band gaps extracted from the absorption spectra are 3.40 eV, 2.95 eV, and 1.96 eV for $X = Cl, Br$, and I , respectively (Figure S18). The values show the same trend as the band gaps obtained from electronic structure calculations, which predict 3.07 eV, 2.78 eV and 2.45 eV for the chloride, bromide and iodide-based compound, respectively (Figure S21). In addition, the band gap was revealed to be direct and located at the Γ point (Figure S22). The large size of the unit cell of $(C_6H_{10}N_2)_6IPb_5I_{21} \cdot 3 H_2O$ made calculations impracticable. However, the band gap was measured optically to be 2.45 eV and thus ranges between those of the bromide and iodide representatives

of the $(\text{C}_6\text{H}_{10}\text{N}_2)\text{PbX}_4$ series. Contrary to the prevailing observation that the conduction and the valence band of lead-halide perovskites are mainly composed of halide and lead orbitals, the conduction band of all members of the $(\text{C}_6\text{H}_{10}\text{N}_2)\text{PbX}_4$ ($X = \text{Cl}, \text{Br}$ and I) series only comprises states assigned to 2-(aminomethyl)pyridinium.⁵⁸⁻⁵⁹ Thus, the organic molecule influences the size of the band gap which opens up design possibilities regarding the electronic structure of hybrid perovskites based on the organic component. The absorbance spectra for each compound (Figure 6a) feature a distinct excitonic peak near the band edge. $(\text{C}_6\text{H}_{10}\text{N}_2)\text{PbI}_4$ shows a broad sub-band gap absorption, along with a wide peak around 700 nm. The origin of this absorption was narrowed down by synthesizing $(\text{C}_6\text{H}_{10}\text{N}_2)\text{PbI}_4$ under nitrogen atmosphere which led to the disappearance of the broad sub-band gap feature (Figure S20). The influence of the ambient atmosphere during the conversion process probably leads to an additional distribution of intra-band gap states, likely due to defects. Temporally resolved photoluminescence (PL) spectroscopy was applied for further insight into the contributing photoactive states. Immediately upon excitation, the PL spectrum of $(\text{C}_6\text{H}_{10}\text{N}_2)\text{PbI}_4$ exhibits one dominant peak at 535 nm near the absorption maximum attributed to band-to-band recombination, as well as a second one, red-shifted by 100 meV from the energetic position of the exciton (Figure S19). The dynamics of the spectral contributions allow additional conclusions regarding their origins, the lower energy feature being dominated (92%) by a fast decay component with a lifetime of 3.6(4) ps, similar to a corresponding signature in $(\text{C}_6\text{H}_{10}\text{N}_2)\text{PbBr}_4$ (85% with 3.0(3) ps) located at 450 nm, 195 meV below the respective exciton peak. We therefore assign these fast components to excitonic recombination of the $(\text{C}_6\text{H}_{10}\text{N}_2)\text{PbX}_4$ materials. Similarly short lifetimes and low fluorescence quantum yields have been attributed to thermal quenching by Gan et al. for a series of two-dimensional lead iodide hybrid perovskites featuring aromatic phenylalkylammonium cations.⁶⁰ In contrast, $(\text{C}_6\text{H}_{10}\text{N}_2)_6\text{IPb}_5\text{I}_{21} \cdot 3 \text{H}_2\text{O}$ shows longer lifetimes (127 ps contributing 38%) and a much broader PL spectrum (FWHM of 0.43 eV) centered at 640 nm, with a large Stokes shift of 540 meV. These findings are indicative of self-trapped excitons as described by Hu et al.⁶¹ The PL emission of 2D lead bromide perovskites was found to broaden with increasing octahedral distortion in the inorganic layer, along with increased lifetimes.⁸ Calculation of Δd , which is the magnitude of distortion, for all compounds discussed above confirmed the rather severe distortion in $(\text{C}_6\text{H}_{10}\text{N}_2)_6\text{IPb}_5\text{I}_{21} \cdot 3 \text{H}_2\text{O}$ ($\Delta d_{\text{avg}} = 17.5 \cdot 10^{-4}$), while $(\text{C}_6\text{H}_{10}\text{N}_2)\text{PbCl}_4$, $(\text{C}_6\text{H}_{10}\text{N}_2)\text{PbBr}_4$ and $(\text{C}_6\text{H}_{10}\text{N}_2)\text{PbI}_4$ are significantly less distorted, as shown by the respective Δd values of $6.8 \cdot 10^{-4}$, $2.3 \cdot 10^{-4}$ and $1.1 \cdot 10^{-4}$, respectively. This is in accordance with the more broadband PL emission of $(\text{C}_6\text{H}_{10}\text{N}_2)_6\text{IPb}_5\text{I}_{21} \cdot 3 \text{H}_2\text{O}$ compared to $(\text{C}_6\text{H}_{10}\text{N}_2)\text{PbX}_4$ ($X = \text{Br}, \text{I}$). Details on the calculations can be found in the supporting information. The band-to-band transition of $(\text{C}_6\text{H}_{10}\text{N}_2)\text{PbBr}_4$ could not be observed due to the spectral proximity to the pump pulse, while excitation of $(\text{C}_6\text{H}_{10}\text{N}_2)\text{PbCl}_4$ in the UV was experimentally unavailable.

4.4 Conclusions

The isotopic hybrid perovskite series $(\text{C}_6\text{H}_{10}\text{N}_2)\text{PbX}_4$ ($X = \text{Cl}, \text{Br}$ and I) was completed by developing synthesis routes for the chloride and the iodide compounds. In addition, a detailed structural analysis including a discussion of the role of hydrogen bonds for structure formation was reported. The phase transition observed for $(\text{C}_6\text{H}_{10}\text{N}_2)\text{PbCl}_4$ when cooling the sample to 100 K was backtracked using group-subgroup-relations. In addition, the structure and the thermal behavior of the related hybrid compound $(\text{C}_6\text{H}_{10}\text{N}_2)_6\text{IPb}_5\text{I}_{21} \cdot 3 \text{H}_2\text{O}$, serving as a starting material for the synthesis of $(\text{C}_6\text{H}_{10}\text{N}_2)\text{PbI}_4$, was discussed. Spectral broadening and an increase in lifetime of the PL were found to correlate with the octahedral distortion of the crystal structures, achieving an emission bandwidth spanning about 150 nm (0.43 eV) FWHM in the visible for $(\text{C}_6\text{H}_{10}\text{N}_2)_6\text{IPb}_5\text{I}_{21} \cdot 3 \text{H}_2\text{O}$. The iodide-based compounds $(\text{C}_6\text{H}_{10}\text{N}_2)\text{PbI}_4$ and $(\text{C}_6\text{H}_{10}\text{N}_2)_6\text{IPb}_5\text{I}_{21} \cdot 3 \text{H}_2\text{O}$ featuring band gaps of 1.96 eV and 2.45 eV, respectively, were found to be mixed ionic-electronic conductors whereby the conductivity values for both compounds and both charge carriers are very low. This virtually suppressed ion migration is likely to be beneficial in terms of stability of these materials when used for optoelectronic applications. Moreover, the combination of NMR measurements and conductivity experiments as a function of iodine partial pressure points towards predominant iodine conduction in $(\text{C}_6\text{H}_{10}\text{N}_2)\text{PbI}_4$ and predominant proton conduction in $(\text{C}_6\text{H}_{10}\text{N}_2)_6\text{IPb}_5\text{I}_{21} \cdot 3 \text{H}_2\text{O}$.

Acknowledgements

Financial support by the Max Planck Society, “Deutsche Telekom Stiftung” (scholarship for CL), the cluster of excellence *Nanosystems Initiative Munich* (NIM) and the Center for NanoScience (CeNS) is gratefully acknowledged. We thank Dr. Michael Schöneich for collecting the thermal analysis data. The authors are grateful to Christine Stefani and Luzia S. Germann (Dinnebier group, MPI-FKF) for collecting additional PXR data. In addition, we thank Luzia S. Germann for her advice regarding Rietveld refinements.

4.5 References

1. Kojima, A.; Teshima, K.; Shirai, Y.; Miyasaka, T., Organometal Halide Perovskites as Visible-Light Sensitizers for Photovoltaic Cells. *J. Am. Chem. Soc.* **2009**, *131* (17), 6050-6051.
2. Kim, H.-S.; Lee, C.-R.; Im, J.-H.; Lee, K.-B.; Moehl, T.; Marchioro, A.; Moon, S.-J.; Humphry-Baker, R.; Yum, J.-H.; Moser, J. E.; Gratzel, M.; Park, N.-G., Lead Iodide Perovskite Sensitized All-Solid-State Submicron Thin Film Mesoscopic Solar Cell with Efficiency Exceeding 9%. *Sci. Rep.* **2012**, *2*.

3. Stranks, S. D.; Eperon, G. E.; Grancini, G.; Menelaou, C.; Alcocer, M. J. P.; Leijtens, T.; Herz, L. M.; Petrozza, A.; Snaith, H. J., Electron-Hole Diffusion Lengths Exceeding 1 Micrometer in an Organometal Trihalide Perovskite Absorber. *Science* **2013**, *342* (6156), 341-344.
4. Stoumpos, C. C.; Kanatzidis, M. G., Halide Perovskites: Poor Man's High-Performance Semiconductors. *Adv. Mater.* **2016**, *28* (28), 5778-5793.
5. Smith, I. C.; Hoke, E. T.; Solis-Ibarra, D.; McGehee, M. D.; Karunadasa, H. I., A Layered Hybrid Perovskite Solar-Cell Absorber with Enhanced Moisture Stability. *Angew. Chem.* **2014**, *126* (42), 11414-11417. Smith, I. C.; Hoke, E. T.; Solis-Ibarra, D.; McGehee, M. D.; Karunadasa, H. I., A Layered Hybrid Perovskite Solar-Cell Absorber with Enhanced Moisture Stability. *Angew. Chem., Int. Ed.* **2014**, *53*, 11232–11235.
6. Tsai, H.; Nie, W.; Blancon, J.-C.; Stoumpos, C. C.; Asadpour, R.; Harutyunyan, B.; Neukirch, A. J.; Verduzco, R.; Crochet, J. J.; Tretiak, S.; Pedesseau, L.; Even, J.; Alam, M. A.; Gupta, G.; Lou, J.; Ajayan, P. M.; Bedzyk, M. J.; Kanatzidis, M. G.; Mohite, A. D., High-efficiency two-dimensional Ruddlesden–Popper perovskite solar cells. *Nature* **2016**, *536* (7616), 312-316.
7. Dohner, E. R.; Jaffe, A.; Bradshaw, L. R.; Karunadasa, H. I., Intrinsic White-Light Emission from Layered Hybrid Perovskites. *J. Am. Chem. Soc.* **2014**, *136* (38), 13154-13157.
8. Mao, L.; Wu, Y.; Stoumpos, C. C.; Wasielewski, M. R.; Kanatzidis, M. G., White-Light Emission and Structural Distortion in New Corrugated Two-Dimensional Lead Bromide Perovskites. *J. Am. Chem. Soc.* **2017**, *139* (14), 5210-5215.
9. Ishihara, T.; Takahashi, J.; Goto, T., Exciton state in two-dimensional perovskite semiconductor $(\text{C}_{10}\text{H}_{21}\text{NH}_3)_2\text{PbI}_4$. *Solid State Commun.* **1989**, *69* (9), 933-936.
10. Smith, M. D.; Jaffe, A.; Dohner, E. R.; Lindenberg, A. M.; Karunadasa, H. I., Structural origins of broadband emission from layered Pb-Br hybrid perovskites. *Chem. Sci.* **2017**, *8* (6), 4497-4504.
11. Chondroudis, K.; Mitzi, D. B., Electroluminescence from an Organic–Inorganic Perovskite Incorporating a Quaterthiophene Dye within Lead Halide Perovskite Layers. *Chem. Mater.* **1999**, *11* (11), 3028-3030.
12. Smith, M. D.; Karunadasa, H. I., White-Light Emission from Layered Halide Perovskites. *Acc. Chem. Res.* **2018**, *51* (3), 619-627.
13. Lin, Y.; Bai, Y.; Fang, Y.; Wang, Q.; Deng, Y.; Huang, J., Suppressed Ion Migration in Low-Dimensional Perovskites. *ACS Energy Lett.* **2017**, *2* (7), 1571-1572.
14. Snaith, H. J.; Abate, A.; Ball, J. M.; Eperon, G. E.; Leijtens, T.; Noel, N. K.; Stranks, S. D.; Wang, J. T.-W.; Wojciechowski, K.; Zhang, W., Anomalous Hysteresis in Perovskite Solar Cells. *J. Phys. Chem. Lett.* **2014**, *5* (9), 1511-1515.
15. Juarez-Perez, E. J.; Sanchez, R. S.; Badia, L.; Garcia-Belmonte, G.; Kang, Y. S.; Mora-Sero, I.; Bisquert, J., Photoinduced Giant Dielectric Constant in Lead Halide Perovskite Solar Cells. *J. Phys. Chem. Lett.* **2014**, *5* (13), 2390-2394.

16. Yang, T.-Y.; Gregori, G.; Pellet, N.; Grätzel, M.; Maier, J., The Significance of Ion Conduction in a Hybrid Organic–Inorganic Lead-Iodide-Based Perovskite Photosensitizer. *Angew. Chem.* **2015**, *127* (27), 8016-8021. Yang, T.-Y.; Gregori, G.; Pellet, N.; Grätzel, M.; Maier, J., The Significance of Ion Conduction in a Hybrid Organic–Inorganic Lead-Iodide-Based Perovskite Photosensitizer. *Angew. Chem., Int. Ed.* **2015**, *54* (27), 7905-7910.
17. Cheng, Y.; Li, H.-W.; Qing, J.; Yang, Q.-D.; Guan, Z.; Liu, C.; Cheung, S. H.; So, S. K.; Lee, C.-S.; Tsang, S.-W., The detrimental effect of excess mobile ions in planar CH₃NH₃PbI₃ perovskite solar cells. *J. Mater. Chem. A* **2016**, *4* (33), 12748-12755.
18. Bag, M.; Renna, L. A.; Adhikari, R. Y.; Karak, S.; Liu, F.; Lahti, P. M.; Russell, T. P.; Tuominen, M. T.; Venkataraman, D., Kinetics of Ion Transport in Perovskite Active Layers and Its Implications for Active Layer Stability. *J. Am. Chem. Soc.* **2015**, *137* (40), 13130-13137.
19. Li, Y.; Zheng, G.; Lin, C.; Lin, J., Synthesis, structure and optical properties of different dimensional organic–inorganic perovskites. *Solid State Sci.* **2007**, *9* (9), 855-861.
20. Yu, H.; Wei, Z.; Hao, Y.; Liang, Z.; Fu, Z.; Cai, H., Reversible solid-state thermochromism of a 2D organic-inorganic hybrid perovskite structure based on iodoplumbate and 2-aminomethylpyridine. *New J. Chem.* **2017**, *41* (18), 9586-9589.
21. Maier, J., *Physical Chemistry of Ionic Materials: Ions and Electrons in Solids*. John Wiley & Sons, Ltd: Chichester, UK, 2004.
22. Bielecki, A.; Burum, D. P., Temperature Dependence of ²⁰⁷Pb MAS Spectra of Solid Lead Nitrate. An Accurate, Sensitive Thermometer for Variable-Temperature MAS. *J. Magn. Reson., Ser. A* **1995**, *116* (2), 215-220.
23. Burum, D. P.; Bielecki, A., An improved experiment for heteronuclear-correlation 2D NMR in Solids. *J. Magn. Reson.* **1991**, *94* (3), 645-652.
24. Segall, M. D.; Lindan, P. J. D.; Probert, M. J.; Pickard, C. J.; Hasnip, P. J.; Clark, S. J.; Payne, M. C., First-principles simulation: Ideas, illustrations and the CASTEP code. *J. Phys.: Condens. Matter* **2002**, *14* (11), 2717-2744.
25. Yates, J. R.; Pickard, C. J.; Mauri, F., Calculation of NMR chemical shifts for extended systems using ultrasoft pseudopotentials. *Physical Review B - Condensed Matter and Materials Physics* **2007**, *76* (2), 024401-11.
26. Perdew, J. P.; Burke, K.; Wang, Y., Generalized gradient approximation for the exchange-correlation hole of a many-electron system. *Phys. Rev. B* **1996**, *54* (23), 16533-16539.
27. Monkhorst, H. J.; Pack, J. D., Special points for Brillouin-zone integrations. *Phys. Rev. B* **1976**, *13* (12), 5188-5192.
28. van Lenthe, E.; Snijders, J. G.; Baerends, E. J., The zero-order regular approximation for relativistic effects: The effect of spin–orbit coupling in closed shell molecules. *J. Chem. Phys.* **1996**, *105* (15), 6505-6516.

29. van Lenthe, E.; Baerends, E. J.; Snijders, J. G., Relativistic total energy using regular approximations. *J. Chem. Phys.* **1994**, *101* (11), 9783-9792.
30. Bonhomme, C.; Gervais, C.; Babonneau, F.; Coelho, C.; Pourpoint, F.; Azais, T.; Ashbrook, S. E.; Griffin, J. M.; Yates, J. R.; Mauri, F.; Pickard, C. J., First-Principles Calculation of NMR Parameters Using the Gauge Including Projector Augmented Wave Method: A Chemist's Point of View. *Chem. Rev.* **2012**, *112* (11), 5733-5779.
31. Massiot, D.; Fayon, F.; Capron, M.; King, I.; Le Calvé, S.; Alonso, B.; Durand, J. O.; Bujoli, B.; Gan, Z.; Hoatson, G., Modelling one- and two-dimensional solid-state NMR spectra. *Magn. Reson. Chem* **2002**, *40* (1), 70-76.
32. Dovesi, R.; Orlando, R.; Erba, A.; Zicovich-Wilson, C. M.; Civalleri, B.; Casassa, S.; Maschio, L.; Ferrabone, M.; De La Pierre, M.; D'Arco, P.; Noël, Y.; Causà, M.; Rérat, M.; Kirtman, B., CRYSTAL14: A program for the ab initio investigation of crystalline solids. *Int. J. Quantum Chem.* **2014**, *114* (19), 1287-1317.
33. Dovesi, R.; Saunders, V. R.; Roetti, C.; Orlando, R.; Zicovich-Wilson, C. M.; Pascale, F.; Civalleri, B.; Doll, K.; Harrison, N. M.; Bush, I. J.; D'Arco, P.; Llunell, M.; Causà, M.; Noël, Y., *CRYSTAL14 User's Manual*. University of Torino, Torino, 2014.
34. Heyd, J.; Scuseria, G. E.; Ernzerhof, M., Hybrid functionals based on a screened Coulomb potential. *J. Chem. Phys.* **2003**, *118* (18), 8207-8215.
35. Sophia, G.; Baranek, P.; Sarrazin, C.; Rérat, M.; Dovesi, R., First-principles study of the mechanisms of the pressure-induced dielectric anomalies in ferroelectric perovskites. *Phase Transitions* **2013**, *86* (11), 1069-1084.
36. Doll, K.; Stoll, H., Ground-state properties of heavy alkali halides. *Phys. Rev. B* **1998**, *57* (8), 4327-4331.
37. Apra, E.; Causa, M.; Prencipe, M.; Dovesi, R.; Saunders, V. R., On the structural properties of NaCl: an ab initio study of the B1-B2 phase transition. *J. Phys. Condens. Matter* **1993**, *5* (18), 2969.
38. Catti, M.; Pavese, A.; Dovesi, R.; Saunders, V. R., Static lattice and electron properties of MgCO₃ (magnesite) calculated by ab initio periodic Hartree-Fock methods. *Phys. Rev. B* **1993**, *47* (15), 9189-9198.
39. Dovesi, R.; Causa, M.; Orlando, R.; Roetti, C.; Saunders, V. R., Ab initio approach to molecular crystals: A periodic Hartree-Fock study of crystalline urea. *J. Chem. Phys.* **1990**, *92* (12), 7402-7411.
40. Gatti, C.; Saunders, V. R.; Roetti, C., Crystal field effects on the topological properties of the electron density in molecular crystals: The case of urea. *J. Chem. Phys.* **1994**, *101* (12), 10686-10696.
41. *SAINT*, Bruker: Madison, Wisconsin, USA, 2012.
42. *SADABS*, Bruker: Madison, Wisconsin, USA, 2001.

43. Altomare, A.; Burla, M. C.; Camalli, M.; Cascarano, G. L.; Giacovazzo, C.; Guagliardi, A.; Moliterni, A. G. G.; Polidori, G.; Spagna, R., SIR97: a new tool for crystal structure determination and refinement. *J. Appl. Crystallogr.* **1999**, *32* (1), 115-119.
44. Sheldrick, G., SHELXT - Integrated space-group and crystal-structure determination. *Acta Crystallogr. A* **2015**, *71* (1), 3-8.
45. Sheldrick, G. M. *SHELXS-97 - Program for Crystal Structure Solution*, University of Göttingen, Göttingen, Germany, 1997.
46. Sheldrick, G., Crystal structure refinement with SHELXL. *Acta Crystallogr. C* **2015**, *71* (1), 3-8.
47. Coelho, A. A. *Topas Academic V4.1, Software, Coelho Software*, Brisbane, Australia, 2007.
48. Steiner, T., Die Wasserstoffbrücke im Festkörper. *Angew. Chem.* **2002**, *114*, 50–80. Steiner, T., The Hydrogen Bond in the Solid State. *Angew. Chem., Int. Ed.* **2002**, *41* (1), 48-76.
49. Lee, J.-H.; Bristowe, N. C.; Lee, J. H.; Lee, S.-H.; Bristowe, P. D.; Cheetham, A. K.; Jang, H. M., Resolving the Physical Origin of Octahedral Tilting in Halide Perovskites. *Chem. Mater.* **2016**, *28* (12), 4259-4266.
50. Bärnighausen, H., Group-Subgroup Relations between Space Groups: A Useful Tool in Crystal Chemistry. *Commun. Math. Chem.* **1980**, *8*, 139 - 175.
51. Huggins, R. A., Simple method to determine electronic and ionic components of the conductivity in mixed conductors a review. *Ionics* **2002**, *8* (3), 300-313.
52. Senocrate, A.; Moudrakovski, I.; Kim, G. Y.; Yang, T.-Y.; Gregori, G.; Grätzel, M.; Maier, J., The Nature of Ion Conduction in Methylammonium Lead Iodide: A Multimethod Approach. *Angew. Chem.* **2017**, *129* (27), 7863-7867. Senocrate, A.; Moudrakovski, I.; Kim, G. Y.; Yang, T.-Y.; Gregori, G.; Grätzel, M.; Maier, J., The Nature of Ion Conduction in Methylammonium Lead Iodide: A Multimethod Approach. *Angew. Chem., Int. Ed.* **2017**, *56* (27), 7755-7759.
53. Mizusaki, J.; Arai, K.; Fueki, K., Ionic conduction of the perovskite-type halides. *Solid State Ionics* **1983**, *11* (3), 203-211.
54. Xue, X.; Kanzaki, M., Proton Distributions and Hydrogen Bonding in Crystalline and Glassy Hydrous Silicates and Related Inorganic Materials: Insights from High-Resolution Solid-State Nuclear Magnetic Resonance Spectroscopy. *J. Am. Ceram. Soc.* **2009**, *92* (12), 2803-2830.
55. Mastikhin, V. M.; Mudrakovsky, I. L.; Nosov, A. V., ¹H NMR magic angle spinning (MAS) studies of heterogeneous catalysis. *Prog. Nucl. Magn. Reson. Spectrosc.* **1991**, *23* (3), 259-299.
56. Lermer, C.; Harm, S. P.; Birkhold, S. T.; Jaser, J. A.; Kutz, C. M.; Mayer, P.; Schmidt-Mende, L.; Lotsch, B. V., Benzimidazolium Lead Halide Perovskites: Effects of Anion Substitution and Dimensionality on the Bandgap. *Z. Anorg. Allg. Chem.* **2016**, *642* (23), 1369-1376.

57. Kulkarni, S. A.; Baikie, T.; Boix, P. P.; Yantara, N.; Mathews, N.; Mhaisalkar, S., Band-gap tuning of lead halide perovskites using a sequential deposition process. *J. Mater. Chem. A* **2014**, *2* (24), 9221-9225.
58. Mitzi, D. B., Synthesis, Structure, and Properties of Organic-Inorganic Perovskites and Related Materials. In *Progress in Inorganic Chemistry*; Karlin, K. D., Ed.; John Wiley & Sons, Inc.: New York, NY, 1999; pp 1–121.
59. Smith, M. D.; Crace, E. J.; Jaffe, A.; Karunadasa, H. I., The Diversity of Layered Halide Perovskites. *Annu. Rev. Mater. Res.* **2018**, *48* (1).
60. Gan, L.; Li, J.; Fang, Z.; He, H.; Ye, Z., Effects of Organic Cation Length on Exciton Recombination in Two-Dimensional Layered Lead Iodide Hybrid Perovskite Crystals. *J. Phys. Chem. Lett.* **2017**, *8* (20), 5177-5183.
61. Hu, T.; Smith, M. D.; Dohner, E. R.; Sher, M.-J.; Wu, X.; Trinh, M. T.; Fisher, A.; Corbett, J.; Zhu, X. Y.; Karunadasa, H. I.; Lindenberg, A. M., Mechanism for Broadband White-Light Emission from Two-Dimensional (110) Hybrid Perovskites. *J. Phys. Chem. Lett.* **2016**, *7* (12), 2258-2263.

5. Summary

The compound class of hybrid perovskites is forging ahead in various fields including photovoltaics and solid-state lighting. Research on the frontrunner material methylammonium lead iodide (MAPI) yielded solar cells with efficiencies above 22% within less than a decade. However, its inherent instability towards moisture is a hindrance which needs to be overcome on the way to commercialization.

An approved strategy for stability enhancement is the reduction of the 3D topology of MAPI to a 2D structure by applying larger hydrophobic hydrocarbons. This work synergistically combines this approach with enhancing the overall hydrophobicity of the organic lattice by employing the fluorinated organic cation 2-fluoroethylammonium ($\text{FC}_2\text{H}_4\text{NH}_3^+$). As a result, the new hybrid perovskite $(\text{FC}_2\text{H}_4\text{NH}_3)_2\text{PbCl}_4$ was obtained showing distinct long-term stability. Single-crystal X-ray diffraction proved the layered structure of $(\text{FC}_2\text{H}_4\text{NH}_3)_2\text{PbCl}_4$ consisting of corner-sharing lead chloride octahedra sheets separated by a double layer of 2-fluoroethylammonium cations. Moreover, a severe distortion of the $[\text{PbCl}_6]^{4-}$ octahedra became apparent whose origin was examined by DFT calculations. A possible hybridization between Pb 6s and Pb 6p states was found to be marginal which prompts the conclusion that a structural origin is more likely than a sterically active Pb 6s lone pair. Hydrogen bonds between the organic and inorganic sublattice may play a major role here. Thermal analysis elucidated two reversible phase transitions at 87 and 107 °C which were followed by means of temperature-dependent powder X-ray diffraction measurements, and ^1H , ^{13}C , and ^{207}Pb solid-state NMR spectroscopy. While the first phase transition is associated to a change in the heavy lattice, the second phase transition is found to affect the organic lattice leaving only traces in the ^{13}C NMR spectra. The excitonic feature present in the absorption spectrum of $(\text{FC}_2\text{H}_4\text{NH}_3)_2\text{PbCl}_4$ is analyzed more closely with photoluminescence (PL) measurements. The broad PL hints towards a trapping of excitons mediated by a strong coupling of excited states to the severely distorted lattice. In addition, the synthesis and the crystal structure of the hybrid compound $(\text{FC}_2\text{H}_4\text{NH}_3)\text{PbBr}_3\cdot\text{DMF}$ were described for the first time.

The revelation of structure-property relations is key for the rational development of novel hybrid perovskite materials. In this context, we chose families of structurally closely related hybrid perovskites and analyzed their optical properties as a function of composition, dimensionality and octahedral distortion.

First of all, a series of benzimidazolium lead halides including $(\text{C}_7\text{H}_7\text{N}_2)_2\text{PbCl}_4$, $(\text{C}_7\text{H}_7\text{N}_2)_2\text{PbBr}_4$, $(\text{C}_7\text{H}_7\text{N}_2)_2\text{PbI}_4$ and $(\text{C}_7\text{H}_7\text{N}_2)\text{PbI}_3$, was subject of a comprehensive investigation with respect to their crystal structure, local interactions between the inorganic and organic sublattices and the

influence of the change in halide and dimensionality on the bandgap. The compounds $(C_7H_7N_2)_2PbX_4$ ($X = Cl, Br$ and I) feature a 2D structure in contrast to the 1D benzimidazolium lead halide $(C_7H_7N_2)PbI_3$ exhibiting double chains of edge-sharing $[PbI_6]^{4-}$ octahedra. This reduction in dimensionality is reflected in an increase in bandgap when moving from $(C_7H_7N_2)_2PbI_4$ to $(C_7H_7N_2)PbI_3$. We explored several synthesis routes including solvent-free mechanochemical reactions and in-situ protonation of benzimidazole using the respective hydrohalic acid as a solvent. While phase-pure $(C_7H_7N_2)_2PbCl_4$, $(C_7H_7N_2)_2PbBr_4$ and $(C_7H_7N_2)PbI_3$ were accessible in bulk quantities, $(C_7H_7N_2)_2PbI_4$ was always accompanied by $(C_7H_7N_2)PbI_3$ as a side phase. NMR spectroscopy measurements probed the chemical environment of the benzimidazolium cations in $(C_7H_7N_2)_2PbCl_4$, $(C_7H_7N_2)_2PbBr_4$ and $(C_7H_7N_2)PbI_3$, which confirmed the high similarity of the layered structures. Finally, optical measurements showed a decrease in bandgap by going from chloride to bromide and to iodide as expected. More strikingly, distinct differences in the PL features are observed. While $(C_7H_7N_2)_2PbBr_4$ and BzImPbI_{4/3} ($(C_7H_7N_2)_2PbI_4$ with 10% $(C_7H_7N_2)PbI_3$) show narrow PL with a small Stokes shift, $(C_7H_7N_2)PbI_3$ and $(C_7H_7N_2)_2PbCl_4$ show a rather broad PL signal with a large Stokes shift. We assume that excitons are able to couple more efficiently to the lattice or permanent defects in the latter cases causing a broadening of the PL.

Broad emission is the basis for applying layered hybrid perovskites as phosphors in solid-state lighting which is currently investigated intensively. In contrast, research on the conductivity behavior of 2D hybrid perovskites has been neglected so far.

This work tackles this deficiency and provides conductivity data for the mixed ionic-electronic conductors $(C_6H_{10}N_2)PbI_4$ and $(C_6H_{10}N_2)_6IPb_5I_{21} \cdot 3 H_2O$. In addition, we were able to identify the diffusing ionic species by combining NMR spectroscopy with conductivity experiments under various iodine partial pressures. The synthesis route, which we developed for the fabrication of $(C_6H_{10}N_2)PbI_4$, is based on a heat-induced transformation of $(C_6H_{10}N_2)_6IPb_5I_{21} \cdot 3 H_2O$ which we investigated in detail by thermal analysis and temperature-dependent PXRD measurements. Furthermore, we completed the isotopic 2D hybrid perovskite series $(C_6H_{10}N_2)PbX_4$ ($X = Cl, Br$ and I) by describing the synthesis and structure of $(C_6H_{10}N_2)PbCl_4$ and $(C_6H_{10}N_2)PbI_4$ for the first time. Additional single-crystal X-ray diffraction measurements at low temperatures pointed towards phase transitions in $(C_6H_{10}N_2)PbCl_4$ associated with the loss of its inversion center and an expansion of the unit cell. PL measurements showed diverging PL width and lifetimes for $(C_6H_{10}N_2)PbBr_4$, $(C_6H_{10}N_2)PbI_4$ and $(C_6H_{10}N_2)_6IPb_5I_{21} \cdot 3 H_2O$ which could be correlated to the extent of $[PbX_6]^{4-}$ octahedral distortion.

6. Conclusions & Outlook

The interest in hybrid perovskites was reawakened by the phenomenal development of solar cells based on the 3D hybrid perovskite methylammonium lead iodide (MAPI). MAPI fulfills the majority of requirements imposed on solar cell materials including long diffusion lengths,¹⁻² a large absorption coefficient,³ a small exciton binding energy⁴ and ambipolar charge transport.⁵ Yet, industrial usage is still hindered by MAPI's lacking stability in atmospheric moisture. Current strategies to tackle this issue comprise the insertion of protection layers, a transformation to 2D and quasi-2D hybrid perovskites and the encapsulation of the whole device.⁶

We add another synthetic approach to this portfolio by proposing the incorporation of fluorinated organic cations as *spacers* in layered hybrid perovskites to enhance the hydrophobicity of the material. We illustrated this idea's prospects of success with the fluorinated cation 2-fluoroethylammonium ($\text{FC}_2\text{H}_4\text{NH}_3$)⁺ which induces the layered structure found for the new hybrid perovskite $(\text{FC}_2\text{H}_4\text{NH}_3)_2\text{PbCl}_4$. Most importantly, a pronounced long-term stability was demonstrated. A simultaneously published study by Slavney et al. proved our hypothesis accurate that MAPI-derived hybrid perovskites with fluorinated *spacers* would show enhanced moisture resistance. They compared the degradation rates of MAPI, $(\text{PEA})_2(\text{MA})_2\text{Pb}_3\text{I}_{10}$ (PEA = phenethylammonium; MA = methylammonium) and $(\text{FPEA})_2(\text{MA})_2\text{Pb}_3\text{I}_{10}$ (FPEA = 4-fluorophenethylammonium) and found the lowest sensitivity towards humidity for the fluorinated compound.⁷

Our research in this field was also motivated by a theoretical study by Frost et al. which proposed that the efficient charge separation and long carrier lifetimes found for MAPI are a result of its highly polarized lattice caused by methylammonium's dipole moment. Thus, increasing the dipole moment of the organic molecule by fluorination is suggested to enhance these charge carrier characteristics.⁸ We paved the way for a study on the photovoltaic properties of fluorinated hybrid perovskites by the synthesis and comprehensive characterization of $(\text{FC}_2\text{H}_4\text{NH}_3)_2\text{PbCl}_4$.

The expansion of the family of hybrid perovskites by seven new hybrid materials including $(\text{FC}_2\text{H}_4\text{NH}_3)_2\text{PbCl}_4$, $(\text{FC}_2\text{H}_4\text{NH}_3)\text{PbBr}_3\cdot\text{DMF}$, $(\text{C}_7\text{H}_7\text{N}_2)_2\text{PbCl}_4$, $(\text{C}_7\text{H}_7\text{N}_2)_2\text{PbBr}_4$, $(\text{C}_7\text{H}_7\text{N}_2)_2\text{PbI}_4$, $(\text{C}_6\text{H}_{10}\text{N}_2)\text{PbCl}_4$ and $(\text{C}_6\text{H}_{10}\text{N}_2)\text{PbI}_4$ reinforced several structure-property relations which may support the rational design of new hybrid perovskites. First of all, we illustrated with the aid of the layered hybrid perovskite series $(\text{C}_6\text{H}_{10}\text{N}_2)\text{PbX}_4$ ($X = \text{Cl}, \text{Br}$ and I) and $(\text{C}_7\text{H}_7\text{N}_2)_2\text{PbX}_4$ ($X = \text{Cl}, \text{Br}$ and I) that the bandgap can be easily tailored by the choice of the halide. In addition, investigation of the optical properties of the 2D hybrid perovskite $(\text{C}_7\text{H}_7\text{N}_2)_2\text{PbI}_4$ and the 1D benzimidazolium

lead halide $(C_7H_7N_2)PbI_3$ showed that a reduction in dimensionality entails an increase in bandgap.

Lately, a group of layered broadband white-light emitting hybrid perovskites has been discovered which have the potential to start the development of a new generation of semiconductors for white light-emitting diodes.⁹⁻¹⁰ Since 2D hybrid perovskites usually show narrow photoluminescence, guiding principles for the targeted synthesis of broadband emitters are sought. A study by Mao et. revealed that an increase in distortion of the metal halide octahedra is accompanied by a broadening of the PL emission and an enhancement in PL lifetimes.¹¹ We investigated a family of 2-(aminomethylpyridinium) lead halides and found that this correlation is reflected in their optical properties. The hybrid compound $(C_6H_{10}N_2)_6IPb_5I_{21} \cdot 3 H_2O$ exhibiting the largest octahedral distortion shows the broadest PL width and the longest PL lifetime. In addition, this relation also makes the broad emission of $(FC_2H_4NH_3)_2PbCl_4$ comprehensible considering its highly distorted inorganic lattice. We expanded the phase space of hybrid perovskites by several new representatives contributing to a better understanding of their properties.

The potential of layered hybrid perovskites in the photovoltaic field is not only based on their higher moisture stability but also on suppressed ion migration found for the quasi-2D hybrid perovskite $(C_4H_9NH_3)_2(CH_3NH_3)_3Pb_4I_{13}$.¹² Ion conduction was found to be involved in the degradation of MAPI causing a decline in photovoltaic performance.¹³⁻¹⁴ Since data on the conductivity behavior of layered hybrid compounds is still scarce, we investigated $(C_6H_{10}N_2)_6IPb_5I_{21} \cdot 3 H_2O$ and $(C_6H_{10}N_2)PbI_4$ by means of a.c. impedance spectroscopy, d.c. galvanostatic polarization measurements and NMR measurements. Both 2-(aminomethylpyridinium) lead halides show very low ionic and electronic conduction whereby protons and iodine ions are the predominant ionic species in $(C_6H_{10}N_2)_6IPb_5I_{21} \cdot 3 H_2O$ and $(C_6H_{10}N_2)PbI_4$, respectively. These findings encourage the application of layered hybrid perovskites in the photovoltaic field and beyond.

6.1 References

1. Xing, G.; Mathews, N.; Sun, S.; Lim, S. S.; Lam, Y. M.; Grätzel, M.; Mhaisalkar, S.; Sum, T. C., Long-Range Balanced Electron- and Hole-Transport Lengths in Organic-Inorganic $\text{CH}_3\text{NH}_3\text{PbI}_3$. *Science* **2013**, *342* (6156), 344-347.
2. Dong, Q.; Fang, Y.; Shao, Y.; Mulligan, P.; Qiu, J.; Cao, L.; Huang, J., Electron-hole diffusion lengths > 175 μm in solution-grown $\text{CH}_3\text{NH}_3\text{PbI}_3$ single crystals. *Science* **2015**, *347* (6225), 967-970.
3. De Wolf, S.; Holovsky, J.; Moon, S.-J.; Löper, P.; Niesen, B.; Ledinsky, M.; Haug, F.-J.; Yum, J.-H.; Ballif, C., Organometallic Halide Perovskites: Sharp Optical Absorption Edge and Its Relation to Photovoltaic Performance. *J. Phys. Chem. Lett.* **2014**, *5* (6), 1035-1039.
4. Herz, L. M., Charge-Carrier Dynamics in Organic-Inorganic Metal Halide Perovskites. *Annu. Rev. Phys. Chem.* **2016**, *67* (1), 65-89.
5. Ball, J. M.; Lee, M. M.; Hey, A.; Snaith, H. J., Low-temperature processed meso-superstructured to thin-film perovskite solar cells. *Energy Environ. Sci.* **2013**, *6* (6), 1739-1743.
6. Li, F.; Liu, M., Recent efficient strategies for improving the moisture stability of perovskite solar cells. *J. Mater. Chem. A* **2017**, *5* (30), 15447-15459.
7. Slavney, A. H.; Smaha, R. W.; Smith, I. C.; Jaffe, A.; Umeyama, D.; Karunadasa, H. I., Chemical Approaches to Addressing the Instability and Toxicity of Lead-Halide Perovskite Absorbers. *Inorg. Chem.* **2017**, *56* (1), 46-55.
8. Frost, J. M.; Butler, K. T.; Brivio, F.; Hendon, C. H.; van Schilfgaarde, M.; Walsh, A., Atomistic Origins of High-Performance in Hybrid Halide Perovskite Solar Cells. *Nano Lett.* **2014**, *14* (5), 2584-2590.
9. Dohner, E. R.; Hoke, E. T.; Karunadasa, H. I., Self-Assembly of Broadband White-Light Emitters. *J. Am. Chem. Soc.* **2014**, *136* (5), 1718-1721.
10. Smith, M. D.; Karunadasa, H. I., White-Light Emission from Layered Halide Perovskites. *Acc. Chem. Res.* **2018**, *51* (3), 619-627.
11. Mao, L.; Wu, Y.; Stoumpos, C. C.; Wasielewski, M. R.; Kanatzidis, M. G., White-Light Emission and Structural Distortion in New Corrugated Two-Dimensional Lead Bromide Perovskites. *J. Am. Chem. Soc.* **2017**, *139* (14), 5210-5215.
12. Lin, Y.; Bai, Y.; Fang, Y.; Wang, Q.; Deng, Y.; Huang, J., Suppressed Ion Migration in Low-Dimensional Perovskites. *ACS Energy Lett.* **2017**, *2* (7), 1571-1572.
13. Cheng, Y.; Li, H.-W.; Qing, J.; Yang, Q.-D.; Guan, Z.; Liu, C.; Cheung, S. H.; So, S. K.; Lee, C.-S.; Tsang, S.-W., The detrimental effect of excess mobile ions in planar $\text{CH}_3\text{NH}_3\text{PbI}_3$ perovskite solar cells. *J. Mater. Chem. A* **2016**, *4* (33), 12748-12755.

14. Bag, M.; Renna, L. A.; Adhikari, R. Y.; Karak, S.; Liu, F.; Lahti, P. M.; Russell, T. P.; Tuominen, M. T.; Venkataraman, D., Kinetics of Ion Transport in Perovskite Active Layers and Its Implications for Active Layer Stability. *J. Am. Chem. Soc.* **2015**, *137* (40), 13130-13137.

7. Appendix

The following section comprises

- supporting information for Chapter 2, 3 and 4
- list of publications within this thesis
- CCDC deposition numbers
- list of presentations
- list of abbreviations.

A Supporting Information for Chapter 2

A.1 Crystallographic data for $(\text{FC}_2\text{H}_4\text{NH}_3)_2\text{PbCl}_4$ **Table SI.** Crystallographic data and details of the structure refinement for $(\text{FC}_2\text{H}_4\text{NH}_3)_2\text{PbCl}_4$ (CCDC 1479690).

Formula	$(\text{FC}_2\text{H}_4\text{NH}_3)_2\text{PbCl}_4$
Molar mass (g mol^{-1})	477.2
Crystal system	Orthorhombic
Space group	<i>Pnma</i> (no. 62)
T ($^{\circ}\text{C}$)	-100
Radiation, λ (\AA)	Mo $\text{K}\alpha$, 0.71073
<i>a</i> (\AA)	7.7059(3)
<i>b</i> (\AA)	18.4574(7)
<i>c</i> (\AA)	8.7525(3)
α, β, γ ($^{\circ}$)	90
<i>V</i> (\AA^3)	1244.88(8)
<i>Z</i>	4
Calculated density (g cm^{-3})	2.54604(16)
Crystal size (mm^3)	$0.060 \times 0.020 \times 0.010$
Absorption coefficient (mm^{-1})	14.398
F(000)	880
Absorption correction	multi-scan
θ range	3.52° to 28.33°
Index range	$-10 \leq h \leq 10$, $-24 \leq k \leq 24$, $-11 \leq l \leq 11$
Parameters/restraints	76 / 0
Total No. of reflections	38015
No. of independent reflections	1597 [$R_{\text{int}} = 0.0343$]
No. of observed reflections	1362
Min./max. residual electron density (e \AA^{-3})	-0.424 / 0.644
Goof	1.080
wR2	0.0250
R1 (for observed reflections)	0.0115
$w = [\sigma^2(F_o^2) + (0.0113P)^2 + 0.4700P]^{-1}$, with $P = (F_o^2 + 2F_c^2)/3$	

Table SII. Atomic coordinates and equivalent isotropic displacement parameters of the non-hydrogen atoms for $(\text{FC}_2\text{H}_4\text{NH}_3)_2\text{PbCl}_4$ at $-100\text{ }^\circ\text{C}$ with standard deviations in parentheses. $U(\text{eq})$ is defined as one third of the trace of the orthogonalized U Tensor.

Atom	x	y	z	$U(\text{eq}) / \text{Å}^2$
Pb1	0.35105(1)	0.25	0.50508(1)	0.0112(1)
Cl1	0.59091(9)	0.25	0.72997(7)	0.0206(2)
Cl2	0.61665(9)	0.25	0.29746(8)	0.0197(2)
Cl3	0.35234(6)	0.40596(3)	0.53155(5)	0.0166(1)
F1	0.94134(16)	0.47077(6)	0.33875(12)	0.0232(3)
N1	0.7499(2)	0.43540(10)	0.6183(2)	0.0174(5)
C1	0.8636(3)	0.38566(11)	0.5302(2)	0.0180(6)
C2	0.8592(3)	0.40343(11)	0.3633(2)	0.0204(6)

Table SIII. Anisotropic displacement parameters for $(\text{FC}_2\text{H}_4\text{NH}_3)_2\text{PbCl}_4$ at $-100\text{ }^\circ\text{C}$ with standard deviations in parentheses.

Atom	U_{11}	U_{22}	U_{33}	U_{23}	U_{13}	U_{12}
Pb1	0.0107(1)	0.0119(1)	0.0108(1)	0	0.0000(1)	0
Cl1	0.0161(3)	0.0290(4)	0.0166(3)	0	-0.0048(3)	0
Cl2	0.0174(3)	0.0208(4)	0.0209(3)	0	0.0057(3)	0
Cl3	0.0187(2)	0.0144(2)	0.0167(2)	0.0007(2)	0.0002(2)	0.0015(2)
F1	0.0289(6)	0.0189(6)	0.0219(6)	0.0026(5)	0.0013(5)	-0.0058(6)
N1	0.0166(9)	0.0204(10)	0.0152(9)	0.0020(7)	0.0017(7)	-0.0001(8)
C1	0.0181(10)	0.0151(10)	0.0208(10)	0.0022(8)	0.0007(8)	0.0027(8)
C2	0.0276(11)	0.0158(10)	0.0178(10)	-0.0029(8)	0.0034(8)	-0.0056(9)

Table SIV. Selected bond distances for $(\text{FC}_2\text{H}_4\text{NH}_3)_2\text{PbCl}_4$ at $-100\text{ }^\circ\text{C}$ with standard deviations in parentheses.

Bond	Distance / Å	Bond	Distance / Å
Pb1-Cl1	2.7001(7)	N1-H1	0.93(2)
Pb1-Cl2	2.7370(7)	N1-H2	0.86(3)
Pb1-Cl3	2.8879(6)	N1-H3	0.92(3)
Pb1-Cl1^b	3.0653(7)	C1-C2	1.498(2)
Pb1-Cl2^a	3.2054(7)	C1-H1A	0.9900
Pb1-Cl3ⁱ	2.8879(6)	C1-H1B	0.9900
F1-C2	1.411(2)	C2-H2A	0.9900
N1-C1	1.485(3)	C2-H2A	0.9900

$a = -1/2+x, 1/2-y, 1/2-z$; $b = -1/2+x, 1/2-y, 3/2-z$; $i = x, 1/2-y, z$

Table SV. Selected bond angles for $(\text{FC}_2\text{H}_4\text{NH}_3)_2\text{PbCl}_4$ at $-100\text{ }^\circ\text{C}$ with standard deviations in parentheses.

Bond	Angle / $^\circ$	Bond	Angle / $^\circ$
Cl1-Pb1-Cl2	88.40(2)	C1-N1-H3	108.2(14)
Cl1-Pb1-Cl3	86.51(1)	C1-N1-H1	109.5(16)
Cl1-Pb1-Cl2 ^a	171.10(2)	C1-N1-H2	109.6(17)
Cl1-Pb1-Cl1 ^b	84.04(2)	H1-N1-H2	111(2)
Cl1-Pb1-Cl3 ⁱ	86.51(1)	H1-N1-H3	111(2)
Cl2-Pb1-Cl3	92.91(1)	N1-C1-C2	110.96(17)
Cl2-Pb1-Cl2 ^a	82.70(2)	F1-C2-C1	109.35(15)
Cl1 _b -Pb1-Cl2	172.44(2)	N1-C1-H1A	109.00
Cl2-Pb1-Cl3 _i	92.91(1)	N1-C1-H1B	109.00
Cl2 ^a -Pb1-Cl3	93.91(1)	C2-C1-H1A	109.00
Cl1 ^b -Pb1-Cl3	86.65(1)	C2-C1-H1B	109.00
Cl3-Pb1-Cl3 ⁱ	170.79(1)	H1A-C1-H1B	108.00
Cl1 ^b -Pb1-Cl2 ^a	104.86(2)	F1-C2-H2A	110.00
Cl2 ^a -Pb1-Cl3 ⁱ	93.91(1)	F1-C2-H2B	110.00
Cl1 ^b -Pb1-Cl3 ⁱ	86.65(1)	C1-C2-H2A	110.00
Pb1-Cl1-Pb1 ^d	177.64(3)	C1-C2-H2B	110.00
Pb1-Cl2-Pb1 ^c	165.90(3)	H2A-C2-H2B	108.00
H2-N1-H3	108(2)		

a = $-1/2+x, 1/2-y, 1/2-z$; b = $-1/2+x, 1/2-y, 3/2-z$; c = $1/2+x, 1/2-y, 1/2-z$; d = $1/2+x, 1/2-y, 3/2-z$; i = $x, 1/2-y, z$

Table SVI. Hydrogen bond distances (in \AA) and angles (in $^\circ$) for $(\text{FC}_2\text{H}_4\text{NH}_3)_2\text{PbCl}_4$ at $-100\text{ }^\circ\text{C}$ with standard deviations in parentheses. The intramolecular hydrogen bond is marked with an asterisk. Symmetry codes: i = $1-x, 1-y, 1-z$; ii = $2-x, 1-y, 1-z$; iii = $1/2+x, y, 3/2-z$; iv = $1/2+x, 1/2-y, 1/2-z$.

D-H...A	H...A	D...A	$\angle\text{D-H...A}$
N1-H2...F1 _{ii}	2.4465(1)	2.9667(1)	119.5
N1-H2...F1*	2.5965(1)	2.9308(1)	104.3
N1-H1...Cl3	2.2695(1)	3.2026(1)	175.8
N1-H2...Cl3 _i	2.5761(1)	3.3038(1)	142.8
N1-H3...Cl3 _{iii}	2.2967(1)	3.2110(1)	174.7
C2-H2A...Cl2 _{iv}	2.7606(1)	3.7332(1)	167.5

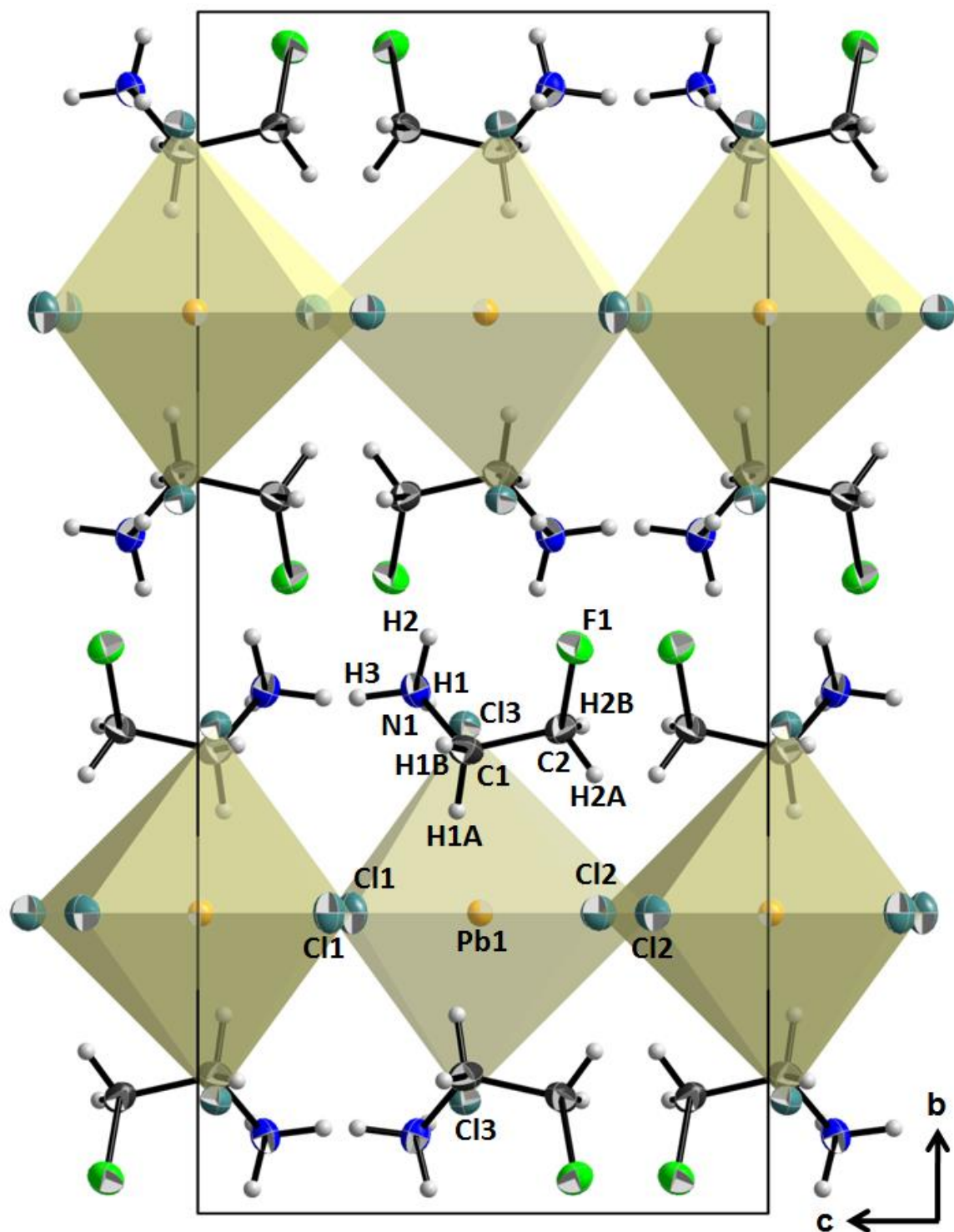


Figure S1. Crystal structure of $(\text{FC}_2\text{H}_4\text{NH}_3)_2\text{PbCl}_4$, measured at $-100\text{ }^\circ\text{C}$, in projection along $[100]$. Thermal ellipsoids (except for hydrogen) are drawn at the 70% probability level. Atoms are labelled exemplarily. C is displayed in black, N is blue, F is green, H is grey, Pb is orange and Cl is turquoise. Cell edges are marked with black solid lines.

A.2 Rietveld refinement results for $(\text{FC}_2\text{H}_4\text{NH}_3)_2\text{PbCl}_4$

The Rietveld refinement results for the RT PXRD data of $(\text{FC}_2\text{H}_4\text{NH}_3)_2\text{PbCl}_4$ acquired right after synthesis and after 4 months exposure to ambient conditions are listed below. Only the heavy atoms Pb and Cl were subject of refinement. The isotropic temperature factor B_{eq} was solely refined for Pb, the heaviest atom.

 $(\text{FC}_2\text{H}_4\text{NH}_3)_2\text{PbCl}_4$, 0 days exposure to ambient conditionsradiation: Cu $K_{\alpha 1}$ space group: *Pnma*orthorhombic, $a = 7.7588(2) \text{ \AA}$, $b = 18.5433(4) \text{ \AA}$, $c = 8.7734(2) \text{ \AA}$

Atom	Wyck.	x	y	z	occ.	$B_{\text{eq}} (\text{\AA}^2)$
Pb1	4c	0.3545(2)	0.25	0.5063(4)	1	0.77(4)
Cl1	4c	0.5974(25)	0.25	0.7204(15)	1	1
Cl2	4c	0.5962(24)	0.25	0.2850(15)	1	1
Cl3	8d	0.3422(8)	0.4058(2)	0.5495(6)	1	1

 $R_{\text{exp}} = 2.03 \%$, $R_{\text{wp}} = 3.36$, $R_{\text{p}} = 2.33 \%$, $R_{\text{Bragg}} = 3.20 \%$, $\text{GooF} = 1.66$ **$(\text{FC}_2\text{H}_4\text{NH}_3)_2\text{PbCl}_4$, 4 months exposure to ambient conditions**radiation: Cu $K_{\alpha 1}$ space group: *Pnma*orthorhombic, $a = 7.7590(1) \text{ \AA}$, $b = 18.5429(3) \text{ \AA}$, $c = 8.7790(1) \text{ \AA}$

Atom	Wyck.	x	y	z	occ.	$B_{\text{eq}} (\text{\AA}^2)$
Pb1	4c	0.3546(2)	0.25	0.5084(3)	1	0.22(4)
Cl1	4c	0.6006(25)	0.25	0.7237(14)	1	1
Cl2	4c	0.6052(25)	0.25	0.2812(14)	1	1
Cl3	8d	0.3479(7)	0.4070(2)	0.5430(6)	1	1

 $R_{\text{exp}} = 2.874 \%$, $R_{\text{wp}} = 2.496 \%$, $R_{\text{p}} = 1.768 \%$, $R_{\text{Bragg}} = 1.95 \%$, $\text{GooF} = 0.87$

A.3 Partial density of states (PDOS) plot for $(\text{FC}_2\text{H}_4\text{NH}_3)_2\text{PbCl}_4$ and band structure of $(\text{FC}_2\text{H}_4\text{NH}_3)_2\text{PbCl}_4$

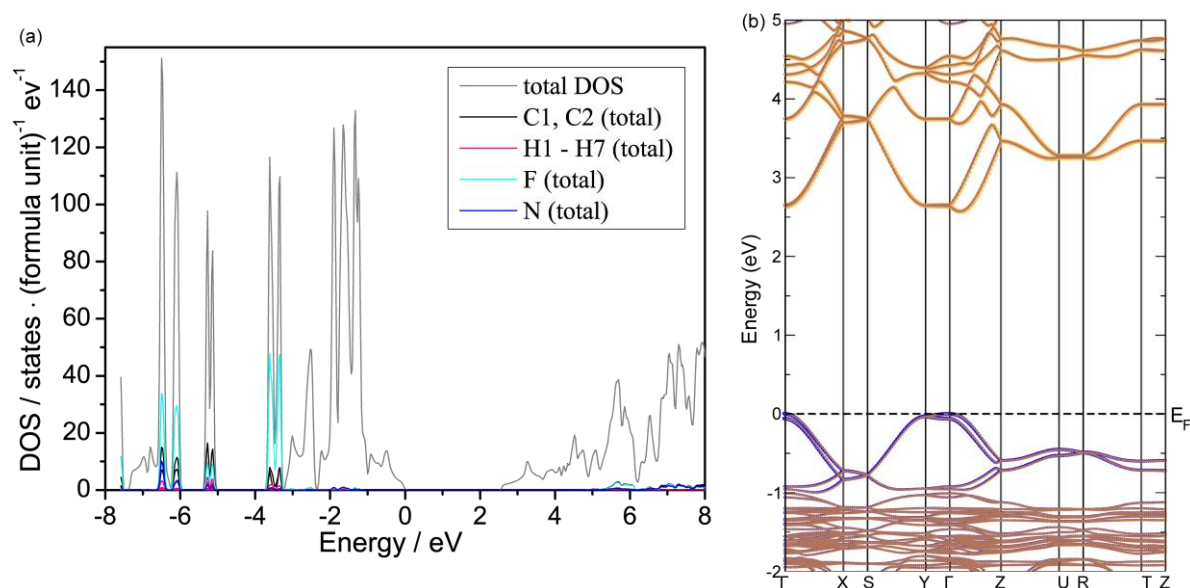


Figure S2. (a) Partial density of states (PDOS) plot for $(\text{FC}_2\text{H}_4\text{NH}_3)_2\text{PbCl}_4$, showing all states of the atoms belonging to the organic cations. C states are displayed in black, H states are pink, F states are turquoise and N states are blue. The total DOS is plotted in gray in the background. (b) Band structure of $(\text{FC}_2\text{H}_4\text{NH}_3)_2\text{PbCl}_4$ showing the contribution of different Pb states. The conduction band consists of Pb p states (orange) and all Pb s states (purple) are filled.

A.4 DSC measurements of $(\text{FC}_2\text{H}_4\text{NH}_3)_2\text{PbCl}_4$

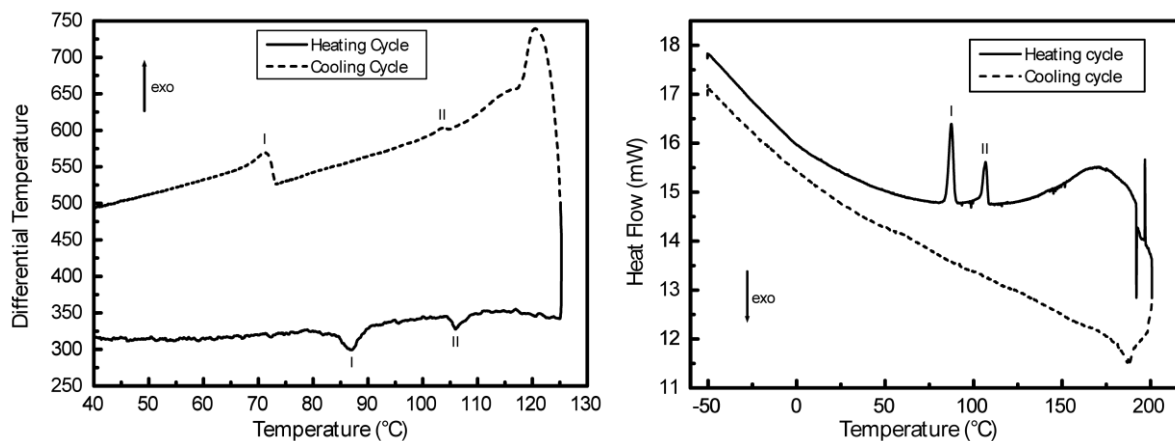


Figure S3. DSC curves of $(\text{FC}_2\text{H}_4\text{NH}_3)_2\text{PbCl}_4$ recorded at a heating rate of 3 K min^{-1} showing the reversible phase transitions at 87 °C (I) and 107 °C (II) (left). The feature between 113 °C and 125 °C is device-related (left). A DSC measurement on a Perkin Elmer Pyris 1 calorimeter (right) confirms the phase transitions at 87 °C (I) and 107 °C (II).

A.5 Temperature-dependent PXRD investigation of $(\text{FC}_2\text{H}_4\text{NH}_3)_2\text{PbCl}_4$ illustrating the reversibility of the first phase transition

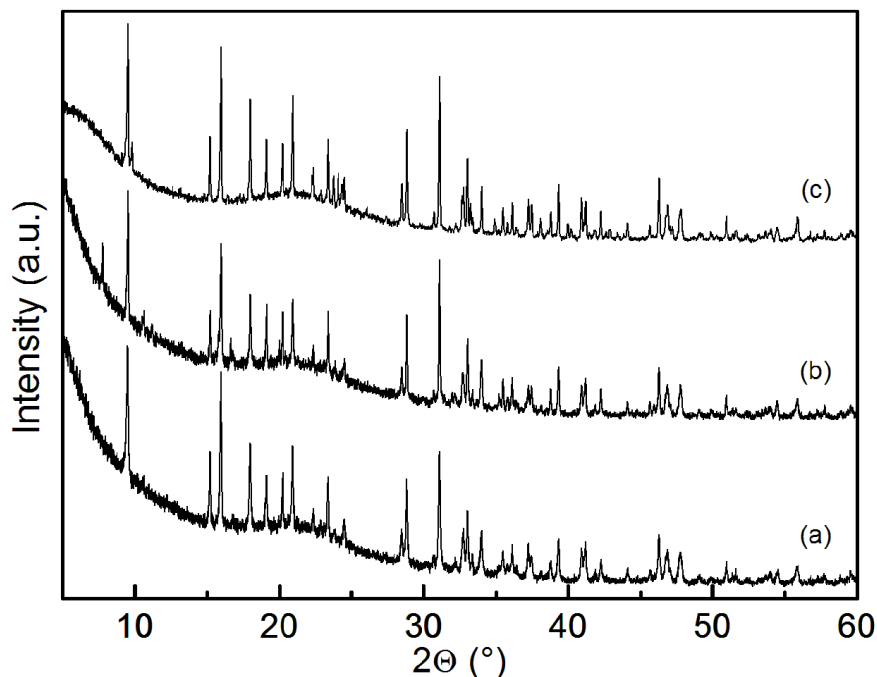


Figure S4. Powder X-ray diffraction investigation of $(\text{FC}_2\text{H}_4\text{NH}_3)_2\text{PbCl}_4$ showing the reversibility of the phase transition at 87 °C. Measurements were performed before heating the sample to 120 °C (a), right after cooling to 30 °C (b) and 1 year after conducting the heating cycle (c). The reflection at 7.75 °C belonging to the high-temperature phase is not visible anymore after an appropriate waiting time at room temperature.

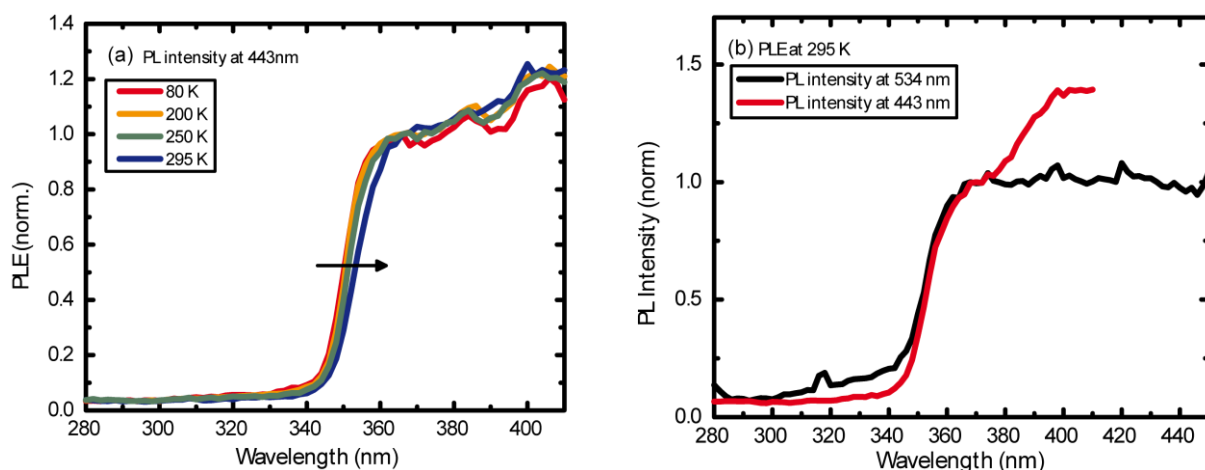
A.6 Photoluminescence spectra of $(\text{FC}_2\text{H}_4\text{NH}_3)_2\text{PbCl}_4$ 

Figure S5. A) PL spectra of $(\text{FC}_2\text{H}_4\text{NH}_3)_2\text{PbCl}_4$ for different excitation wavelengths at 295 K. Inset: Normalized PL spectra for excitation wavelengths of 360 nm, 380 nm and 400 nm. B) PL spectra of $(\text{FC}_2\text{H}_4\text{NH}_3)_2\text{PbCl}_4$ at 295 K and 80 K, excited with 375 nm (3.3 eV). Spectra are fitted with two Gaussian functions (solid lines) with peak positions at 2.33 eV/2.79 eV and 2.32 eV/2.79 eV for 295K and 80 K, respectively.

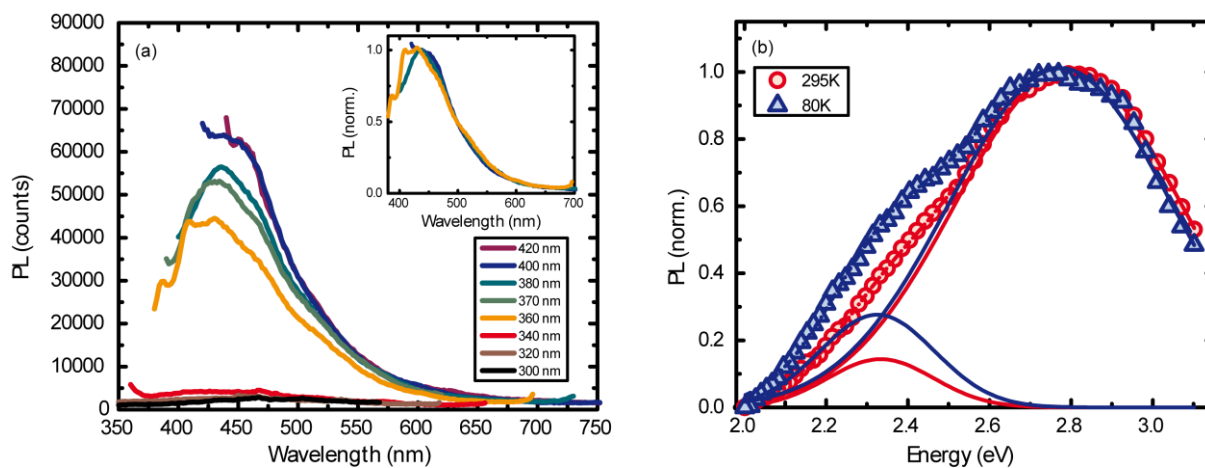
A.7 Photoluminescence excitation spectra of $(\text{FC}_2\text{H}_4\text{NH}_3)_2\text{PbCl}_4$ 

Figure S6. A) PL excitation spectra of $(\text{FC}_2\text{H}_4\text{NH}_3)_2\text{PbCl}_4$ at different temperatures ($\lambda_{\text{emission}} = 443\text{nm}$). B) PL excitation spectra of $(\text{FC}_2\text{H}_4\text{NH}_3)_2\text{PbCl}_4$ for two different PL emission wavelengths at 295K.

A.8 Discussion of the crystal structure of $(\text{FC}_2\text{H}_4\text{NH}_3)\text{PbBr}_3 \cdot \text{DMF}$

In addition to $(\text{FC}_2\text{H}_4\text{NH}_3)_2\text{PbCl}_4$ the crystal structure of the related DMF solvate $(\text{FC}_2\text{H}_4\text{NH}_3)\text{PbBr}_3 \cdot \text{DMF}$ was determined, showing a transition from the 2D structure in $(\text{FC}_2\text{H}_4\text{NH}_3)_2\text{PbCl}_4$ to a 1D chain-like structure in $(\text{FC}_2\text{H}_4\text{NH}_3)\text{PbBr}_3 \cdot \text{DMF}$. The new compound $(\text{FC}_2\text{H}_4\text{NH}_3)\text{PbBr}_3 \cdot \text{DMF}$ was obtained by the reaction of fluoroethylammonium bromide with lead bromide in DMF. Crystallographic data and details of the structure refinement for $(\text{FC}_2\text{H}_4\text{NH}_3)\text{PbBr}_3 \cdot \text{DMF}$ are displayed in Tables SVII – SXI. $(\text{FC}_2\text{H}_4\text{NH}_3)\text{PbBr}_3 \cdot \text{DMF}$ contains double chains formed by edge-sharing PbBr_4^{2-} octahedra. 2-fluoroethylammonium cations and DMF molecules are located in between the chains (Figure S7). Incorporation of the solvate molecules into the structure is most likely due to the energetically favourable formation of moderately strong intermolecular $\text{N1-H1C} \cdots \text{O1}$ and $\text{N1-H1E} \cdots \text{O1}$ hydrogen bonds between 2-fluoroethylammonium cations and DMF molecules, which determine the arrangement of these molecules and seem to break up the inorganic sublattice. Weak intramolecular and intermolecular hydrogen bonds between the organic molecules and bromide atoms also contribute to the stabilization of the structure. A complete overview of all hydrogen bonds can be found in Table SXII. Rietveld analyses confirm the phase purity of the obtained bulk material (Figure S8).

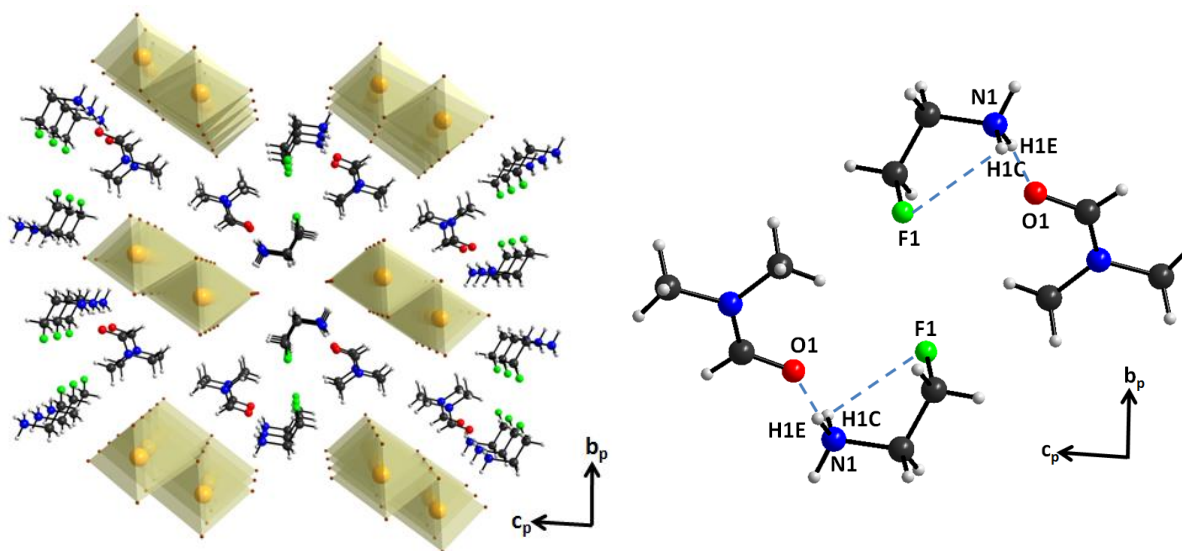
A.9 Crystal structure of $(\text{FC}_2\text{H}_4\text{NH}_3)\text{PbBr}_3 \cdot \text{DMF}$ 

Figure S7. Crystal Structure of $(\text{FC}_2\text{H}_4\text{NH}_3)\text{PbBr}_3 \cdot \text{DMF}$ in projection along $[\bar{1}00]$ (left). Hydrogen bonds are marked exemplarily with dashed lines (right). C is displayed in black, N is blue, F is green, H is grey, Pb is orange and Br is brown.

A.10 Crystallographic data for (FC₂H₄NH₃)PbBr₃ · DMF**Table SVII.** Crystallographic data and details of the structure refinement for (FC₂H₄NH₃)PbBr₃ · DMF (CCDC 1479691).

Formula	(FC ₂ H ₄ NH ₃)PbBr ₃ · C ₃ H ₇ NO
Molar mass (g mol ⁻¹)	584.1
Crystal system	triclinic
Space group	<i>P</i> 1 (no. 2)
T (°C)	-100
Radiation, λ (Å)	Mo Kα, 0.71073
<i>a</i> (Å)	4.4434(2)
<i>b</i> (Å)	11.2688(6)
<i>c</i> (Å)	13.7677(7)
α (°)	83.8913(14)
β (°)	81.4800(17)
γ (°)	83.1354(17)
<i>V</i> (Å ³)	674.11(6)
<i>Z</i>	2
Calculated density (g cm ⁻³)	2.8776(3)
Crystal size (mm ³)	0.050 × 0.040 × 0.020
Absorption coefficient (mm ⁻¹)	21.388
F(000)	524
Absorption correction	multi-scan
θ range	3.00° to 28.31°
Index range	-5 ≤ <i>h</i> ≤ 5, -14 ≤ <i>k</i> ≤ 15, 0 ≤ <i>l</i> ≤ 18
Parameters/restraints	123 / 0
Total No. of reflections	8838
No. of independent reflections	3330 [R _{int} = 0.0000]*
No. of observed reflections	2932
Min./max. residual electron density (e Å ⁻³)	-0.920 / 1.036
Goof	1.052
wR2	0.0523
R1 (for observed reflections)	0.0247
$w = [\sigma^2(F_o^2) + (0.0211P)^2 + 0.9657P]^{-1}$, with $P = (F_o^2 + 2F_c^2)/3$	

*This structure has been refined as a 2-component twin (BASF 0.07).

Table SVIII. Atomic coordinates and equivalent isotropic displacement parameters of the non-hydrogen atoms for (FC₂H₄NH₃)PbBr₃ · DMF at -100 °C with standard deviations in parentheses. U(eq) is defined as one third of the trace of the orthogonalized U Tensor.

Atom	x	y	z	U(eq) / Å ²
Pb1	0.65368(4)	0.09149(1)	0.62667(1)	0.0176(1)
Br1	0.09070(11)	0.26946(4)	0.63125(4)	0.0307(1)
Br2	1.21328(11)	-0.10049(4)	0.61507(3)	0.0207(1)
Br3	0.56665(11)	0.05122(4)	0.83390(3)	0.0250(1)
O1	0.2867(8)	0.3066(3)	0.1936(2)	0.0286(10)
N1	0.1301(9)	0.8187(3)	-0.1291(3)	0.0241(11)
N2	0.4448(9)	0.4250(3)	0.2948(3)	0.0229(11)
C1	-0.0044(14)	0.7057(5)	0.0313(4)	0.0440(17)
C2	0.0347(13)	0.8262(5)	-0.0211(3)	0.0305(16)
C3	0.3099(11)	0.3339(4)	0.2767(4)	0.0244(12)
C4	0.5781(13)	0.5071(4)	0.2152(4)	0.0317(16)
C5	0.4774(14)	0.4461(4)	0.3946(3)	0.0326(16)
F1	0.2692(10)	0.6331(4)	0.0186(3)	0.0642(14)

Table SIX. Anisotropic displacement parameters for (FC₂H₄NH₃)PbBr₃ · DMF at -100 °C with standard deviations in parentheses.

Atom	U ₁₁	U ₂₂	U ₃₃	U ₂₃	U ₁₃	U ₁₂
Pb1	0.0152(1)	0.0208(1)	0.0173(1)	-0.0025(1)	-0.0021(1)	-0.0034(1)
Br1	0.0224(2)	0.0198(2)	0.0505(3)	-0.0028(2)	-0.0053(2)	-0.0044(2)
Br2	0.0226(2)	0.0207(2)	0.0191(2)	-0.0004(2)	-0.0032(2)	-0.0038(2)
Br3	0.0242(2)	0.0349(2)	0.0169(2)	-0.0044(2)	-0.0023(2)	-0.0057(2)
O1	0.0227(17)	0.0364(17)	0.0308(18)	-0.0129(14)	-0.0079(15)	-0.0057(15)
N1	0.021(2)	0.0252(19)	0.027(2)	-0.0074(16)	-0.0009(17)	-0.0045(17)
N2	0.027(2)	0.0216(17)	0.0214(19)	-0.0015(15)	-0.0064(16)	-0.0039(16)
C1	0.039(3)	0.055(3)	0.032(3)	0.010(3)	0.000(3)	0.001(3)
C2	0.032(3)	0.043(3)	0.017(2)	-0.004(2)	-0.004(2)	-0.004(2)
C3	0.019(2)	0.023(2)	0.031(2)	-0.0024(18)	-0.0034(19)	-0.0011(19)
C4	0.036(3)	0.028(2)	0.032(3)	0.003(2)	-0.006(2)	-0.010(2)
C5	0.046(3)	0.027(2)	0.027(3)	-0.0044(19)	-0.010(2)	-0.005(2)
F1	0.065(3)	0.067(2)	0.048(2)	0.0146(18)	-0.006(2)	0.024(2)

Table SX. Selected bond distances for (FC₂H₄NH₃)PbBr₃ · DMF at -100 °C with standard deviations in parentheses.

Bond	Distance / Å	Bond	Distance / Å
Pb1-Br2	3.0917(5)	N1-H1D	0.93(2)
Pb1-Br3	2.8169(5)	C3-H3	0.9500
Pb1-Br1	3.0108(5)	C4-H4B	0.9800
Pb1-Br2 ^a	3.1166(5)	C4-H4A	0.9800
Pb1-Br1 ^b	2.9650(5)	C4-H4C	0.9800
Pb1-Br2 ^c	3.2858(5)	C5-H5C	0.9800
F1-C1	1.381(8)	C5-H5B	0.9800
O1-C3	1.238(6)	C5-H5A	0.9800
N2-C4	1.460(6)	C1-C2	1.485(8)
N2-C5	1.450(6)	C1-H1A	0.9900
N2-C3	1.312(6)	C1-H1B	0.9900
N1-C2	1.493(6)	C2-H2A	0.9900
N1-H1E	0.93(3)	C2-H2B	0.9900
N1-H1C	0.93(3)		

a = -1+x,y,z; b = 1+x,y,z; c = 2-x,-y,1-z

Table SXI. Selected bond angles for (FC₂H₄NH₃)PbBr₃ · DMF at -100 °C with standard deviations in parentheses.

Bond	Angle / °	Bond	Angle / °
Br2-Pb1-Br3	90.39(1)	O1-C3-N2	125.2(5)
Br2-Pb1-Br1	176.63(1)	O1-C3-H3	117.00
Br2-Pb1-Br2 ^a	91.40(1)	N2-C3-H3	117.00
Br2-Pb1-Br1 ^b	86.86(1)	H4B-C4-H4C	110.00
Br2-Pb1-Br2 ^c	83.31(1)	N2-C4-H4B	109.00
Br3-Pb1-Br1	91.18(1)	N2-C4-H4A	109.00
Br2 ^a -Pb1-Br3	89.86(1)	H4A-C4-H4C	110.00
Br3-Pb1-Br1 ^b	91.76(2)	N2-C4-H4C	109.00
Br2 ^c -Pb1-Br3	172.43(1)	H4A-C4-H4B	109.00
Br2 ^a -Pb1-Br1	85.62(1)	N2-C5-H5A	109.00
Br1-Pb1-Br1 ^b	96.07(1)	H5A-C5-H5B	110.00
Br2 ^c -Pb1-Br1	94.90(1)	N2-C5-H5B	109.00
Br2 ^a -Pb1-Br1 ^b	177.63(1)	N2-C5-H5C	109.00
Br2 ^a -Pb1-Br2 ^c	86.11(1)	H5A-C5-H5C	110.00
Br2 ^c -Pb1-Br1 ^b	92.09(1)	H5B-C5-H5C	110.00
Pb1-Br2-Pb1 ^b	91.40(1)	F1-C1-C2	109.7(5)
Pb1-Br2-Pb1 ^c	96.69(1)	N1-C2-C1	111.3(4)
Pb1 ^b -Br2-Pb1 ^c	93.89(1)	F1-C1-H1A	110.00
Pb1-Br1-Pb1 ^a	96.07(1)	F1-C1-H1B	110.00
C3-N2-C4	121.5(4)	F1-C1-H1B	110.00

Table SXI. Continuation.

C3-N2-C5	121.4(4)	C2-C1-H1B	110.00
C4-N2-C5	117.1(4)	H1A-C1-H1B	108.00
H1D-N1-H1E	110(2)	N1-C2-H2A	109.00
C2-N1-H1E	109.5(11)	N1-C2-H2B	109.00
C2-N1-H1C	109.4(6)	C1-C2-H2A	109.00
C2-N1-H1D	109.3(11)	C1-C2-H2A	109.00
H1C-N1-H1D	110(3)	H2A-C2-H2B	108.00
H1C-N1-H1E	110(3)		

a = -1+x,y,z; b = 1+x,y,z; c = 2-x,-y,1-z

Table SXII. Hydrogen bond distances (in Å) and angles (in °) for (FC₂H₄NH₃)PbBr₃ · DMF at -100 °C with standard deviations in parentheses. The intramolecular hydrogen bond is marked with an asterisk. Symmetry codes: i = 1-x,1-y,-z; ii = -x,1-y,-z; iii = -1+x,1+y,-1+z; iv = x,1+y,-1+z; v = 1-x,1-y,1-z; vi = -x,1-y,1-z;

D-H...A	H...A	D...A	∠D-H...A
N1-H1C...O1ⁱ	1.9524(1)	2.8653(1)	166.4
N1-H1E...O1ⁱⁱ	1.8294(1)	2.7551(1)	172.8
N1-H1C...F1[*]	2.5503(1)	2.8366(1)	98.2
N1-H1D...Br3ⁱⁱⁱ	2.9312(1)	3.4525(1)	116.8
N1-H1D...Br3^{iv}	2.7100(1)	3.3952(1)	131.1
C2-H2A...Br3^v	2.8847(1)	3.7925(1)	152.8
C2-H2B...Br3^{vi}	2.9261(1)	3.6774(1)	133.4

A.11 Rietveld analysis for $(\text{FC}_2\text{H}_4\text{NH}_3)\text{PbBr}_3 \cdot \text{DMF}$

The Rietveld refinement results for the RT PXRD data of $(\text{FC}_2\text{H}_4\text{NH}_3)\text{PbBr}_3 \cdot \text{DMF}$ are listed below. Only the heavy atoms Pb and Br were subject of refinement. The isotropic temperature factor B_{eq} was solely refined for Pb, the heaviest atom.

 $(\text{FC}_2\text{H}_4\text{NH}_3)\text{PbBr}_3 \cdot \text{DMF}$ radiation: Cu $K_{\alpha 1}$ space group: $P1$

triclinic, $a = 4.4643(1) \text{ \AA}$, $b = 11.4003(2) \text{ \AA}$, $c = 13.7967(2) \text{ \AA}$, $\alpha = 83.9431(15)$, $\beta = 81.3575(16)$, $\gamma = 83.3882(9)$

Atom	Wyck.	x	y	z	occ.	$B_{\text{eq}} (\text{\AA}^2)$
Pb1	2i	0.6594(5)	0.0928(2)	0.6198(3)	1	1.17(6)
Br1	2i	0.0915(10)	0.2729(4)	0.6356(3)	1	1
Br2	2i	1.2192(10)	-0.1042(4)	0.6198(3)	1	1
Br3	2i	0.5671(9)	0.0513(3)	0.8346(3)	1	1

$R_{\text{exp}} = 1.93 \%$, $R_{\text{wp}} = 2.97 \%$, $R_p = 2.25 \%$, $R_{\text{Bragg}} = 2.04 \%$, $\text{GooF} = 1.54$

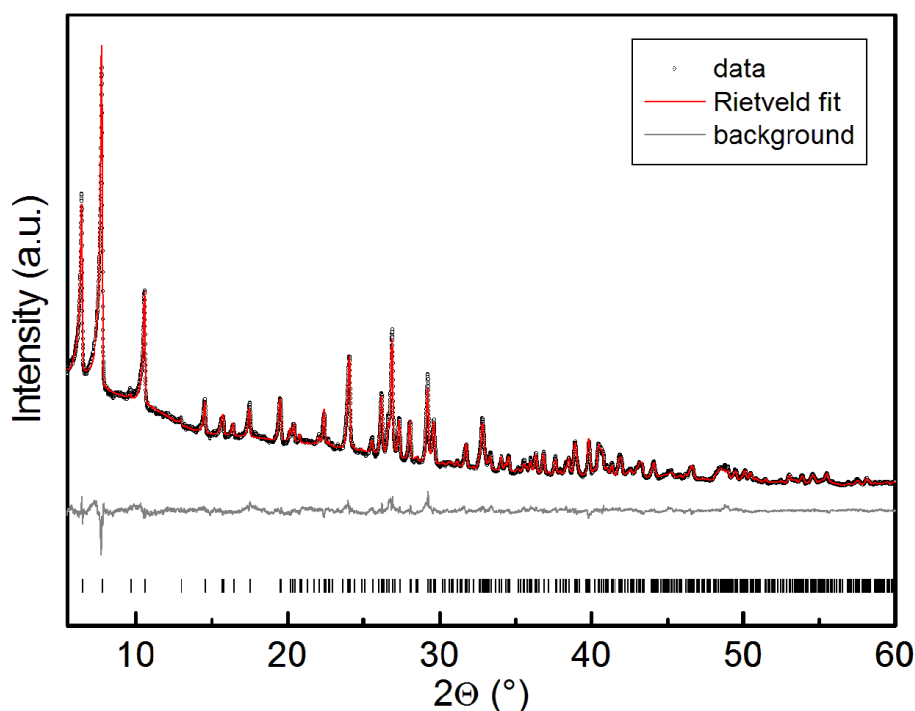


Figure S8. X-ray powder diffraction data of $(\text{FC}_2\text{H}_4\text{NH}_3)\text{PbBr}_3 \cdot \text{DMF}$ represented by open circles. The Rietveld profile fit (red solid line) and the difference profile (grey solid line) confirm phase purity.

A.12 Characterization of $(\text{FC}_2\text{H}_4\text{NH}_3)\text{PbBr}_3 \cdot \text{DMF}$

Characterization. Single-crystal X-ray diffraction data of $(\text{FC}_2\text{H}_4\text{NH}_3)\text{PbBr}_3 \cdot \text{DMF}$ was collected at $-100\text{ }^\circ\text{C}$ on a Bruker D8 Venture diffractometer equipped with a rotating anode generator with Mo K_α radiation ($\lambda = 0.71073\text{ \AA}$). The diffraction intensities were integrated using the SAINT software package and a multi-scan absorption correction was applied with SADABS. The crystal structure was solved by direct methods (SIR97)¹ and refined against F^2 by applying the full-matrix least-squares method (SHELXL-97).^{2, 3} C-bound hydrogen positions were calculated according to geometrical criteria and treated as riding on their parent atoms. The N-bound hydrogen atoms have also been located geometrically, but with additional refinement of the N-H distance. All non-hydrogen atoms were refined anisotropically.

Powder X-ray diffraction (PXRD) patterns of $(\text{FC}_2\text{H}_4\text{NH}_3)\text{PbBr}_3 \cdot \text{DMF}$ were collected at room temperature using a Huber G670 Guinier imaging plate detector in transmission geometry. These measurements were performed with $\text{Ge}(111)$ -monochromated $\text{Cu-K}_{\alpha 1}$ radiation ($\lambda = 1.54059\text{ \AA}$). Full profile fits were obtained using TOPAS Academic.⁴

FTIR spectra were recorded at ambient conditions between 650 and 4000 cm^{-1} on a Spektrum BX II FTIR spectrometer (Perkin Elmer) equipped with a DuraSampler diamond ATR device.

Elemental analyses for C, H, and N were performed with the elemental analyzer systems Vario EL and Vario Micro (Elementar Analysensysteme GmbH).

A.13 References

1. Altomare, A.; Burla, M. C.; Camalli, M.; Cascarano, G. L.; Giacovazzo, C.; Guagliardi, A.; Moliterni, A. G. G.; Polidori, G.; Spagna, R. SIR97: a new tool for crystal structure determination and refinement. *J. Appl. Crystallogr.* **1999**, *32*, 115-119.
2. Sheldrick, G. M., A short history of SHELX. *Acta Crystallogr., Sect. A: Found. Adv.* **2008**, *64*, 112-122.
3. Sheldrick, G. M. SHELXL-97: Program for the Refinement of Crystal Structures, Universität Göttingen, 1997.
4. *Topas Academic*, version 4.1, Coelho Software: Brisbane, Australia, 2007.

B Supporting Information for Chapter 3

B.1 Crystallographic data for $(C_7H_7N_2)_2PbCl_4$, $(C_7H_7N_2)_2PbBr_4$ and $(C_7H_7N_2)_2PbI_4$ **Table SI.** Crystallographic data and details of the structure refinement for $(C_7H_7N_2)_2PbCl_4^*$, $(C_7H_7N_2)_2PbBr_4$ and $(C_7H_7N_2)_2PbI_4^{**}$ (CCDC 1507155, CCDC 1507157 and CCDC 1507154).

Formula	$(C_7H_7N_2)_2PbCl_4$	$(C_7H_7N_2)_2PbBr_4$	$(C_7H_7N_2)_2PbI_4$
Molar mass (g mol ⁻¹)	587.28	765.12	953.08
Crystal system	Monoclinic	Monoclinic	Monoclinic
Space group	<i>C2/c</i> (no. 15)	<i>C2/c</i> (no. 15)	<i>C2/c</i> (no. 15)
T (K)	100	173	100
Radiation, λ (Å)	Mo K α , 0.71073	Mo K α , 0.71073	Mo K α , 0.71073
<i>a</i> (Å)	35.9216(13)	35.7693(13)	29.5955(14)
<i>b</i> (Å)	5.6589(2)	5.9455(2)	6.2908(3)
<i>c</i> (Å)	22.5343(8)	23.6768(8)	12.5412(6)
α, γ (°)	90	90	90
β (°)	126.2572(8)	127.6495(10)	110.022(2)
<i>V</i> (Å ³)	3693.7(2)	3986.7(2)	2193.79(18)
<i>Z</i>	8	8	4
Calculated density (g cm ⁻³)	2.112	2.549	2.886
Crystal size (mm ³)	0.03 × 0.04 × 0.05	0.04 × 0.05 × 0.07	0.01 × 0.03 × 0.04
Absorption coefficient (mm ⁻¹)	9.716	16.484	13.323
F(000)	2208	2784	1680
Absorption correction	multi-scan	multi-scan	multi-scan
θ range	2.2° to 26.4°	2.2° to 27.5°	3.3° to 34.0°
Index range	-44 ≤ <i>h</i> ≤ 36, 0 ≤ <i>k</i> ≤ 7, 0 ≤ <i>l</i> ≤ 28	-42 ≤ <i>h</i> ≤ 46, -7 ≤ <i>k</i> ≤ 7, -30 ≤ <i>l</i> ≤ 30	-46 ≤ <i>h</i> ≤ 43, 0 ≤ <i>k</i> ≤ 9, 0 ≤ <i>l</i> ≤ 19
Parameters/restraints	213 / 0	212 / 0	108 / 0
Total No. of reflections	6834	31986	3830
No. of independent reflections	3762 [R _{int} = 0.0367]	4608 [R _{int} = 0.038]	3830 [R _{int} = 0.0430]
No. of observed reflections	3337	3811	3268
Min./max. residual electron density (e Å ⁻³)	-1.25 / 1.40	-1.17 / 0.65	-1.78 / 1.71
Goof	1.18	1.12	1.08
Final R indices [<i>I</i> > 2σ(<i>I</i>)]	R1 = 0.0279 wR2 = 0.0486 ^a	R1 = 0.0204 wR2 = 0.0384 ^b	R1 = 0.0321 wR2 = 0.0618 ^c
Final R indices (all data)	R1 = 0.0353 wR2 = 0.0502 ^a	R1 = 0.0301 wR2 = 0.0409 ^b	R1 = 0.0475 wR2 = 0.0682 ^c

^a $w = [\sigma^2(F_0^2) + (0.0128P)^2 + 25.1665P]^{-1}$, with $P = (F_0^2 + 2F_c^2)/3$

^b $w = [\sigma^2(F_0^2) + (0.0145)^2 + 2.0915P]^{-1}$, with $P = (F_0^2 + 2F_c^2)/3$

^c $w = [\sigma^2(F_0^2) + (0.0148)^2 + 27.4190P]^{-1}$, with $P = (F_0^2 + 2F_c^2)/3$

*This structure has been refined as a 2-component twin (BASF 0.45988(132)).

** This structure has been refined as a 2-component twin (BASF 0.17251(170)).

Table SII. Atomic coordinates and equivalent isotropic displacement parameters for $(C_7H_7N_2)_2PbCl_4$ at 100 K with standard deviations in parentheses. $U(eq)$ is defined as one third of the trace of the orthogonalized U Tensor.

Atom	Wyck.	x	y	z	$U(eq) / \text{\AA}^2$
C1	8f	0.0791(3)	0.0475(19)	0.2033(5)	0.014(2)
H1	8f	0.0477	0.0239	0.1846	0.016
C2	8f	0.0780(3)	0.095(2)	0.4551(6)	0.017(2)
H2	8f	0.0476	0.1413	0.4376	0.021
N1	8f	0.1020(3)	0.0828(15)	0.0007(4)	0.0182(19)
H3	8f	0.0921	0.1775	0.0195	0.022
Cl1	8f	0.09865(4)	0.4971(6)	0.09135(15)	0.0172(3)
N2	8f	0.1052(2)	0.2172(15)	0.2488(4)	0.0148(17)
H4	8f	0.0966	0.3265	0.2662	0.018
N3	8f	0.1041(2)	0.1990(14)	0.4381(4)	0.0149(16)
H5	8f	0.0960	0.3214	0.4087	0.018
C3	8f	0.1462(2)	-0.0819(11)	-0.0257(4)	0.0154(13)
C4	8f	0.1446(2)	-0.0977(12)	0.5142(3)	0.0133(14)
C5	8f	0.1464(2)	0.0007(11)	0.2248(3)	0.0141(13)
C6	8f	0.1815(2)	0.2542(12)	0.0562(3)	0.0170(13)
H6	8f	0.1807	0.3778	0.0839	0.020
C7	8f	0.1838(2)	0.1199(12)	0.4726(3)	0.0178(14)
H7	8f	0.1845	0.2437	0.4448	0.021
C8	8f	0.1888(2)	0.3283(12)	0.3091(4)	0.0178(14)
H8	8f	0.1901	0.4624	0.3357	0.021
C9	8f	0.2193(2)	0.2193(12)	0.0552(3)	0.0193(14)
H9	8f	0.2452	0.3219	0.0827	0.023
C10	8f	0.2201(2)	0.0354(13)	0.0143(4)	0.0193(15)
H10	8f	0.2468	0.0167	0.0153	0.023
C11	8f	0.2243(2)	0.0606(12)	0.2716(4)	0.0197(14)
H11	8f	0.2510	0.0178	0.2748	0.024
C12	8f	0.2263(2)	0.2560(12)	0.3121(4)	0.0195(14)
H12	8f	0.2545	0.3402	0.3424	0.023
C13	8f	0.3158(2)	0.4289(12)	0.2731(4)	0.0173(14)
H13	8f	0.3174	0.2973	0.3006	0.021
C14	8f	0.3515(2)	0.6950(12)	0.2350(3)	0.0122(13)
Cl2	8f	0.40078(4)	0.1156(2)	0.15981(13)	0.0140(3)
N4	8f	0.3983(3)	0.4140(14)	0.3133(4)	0.0138(19)
H14	8f	0.4095	0.2917	0.3432	0.017
Cl3	8f	0.50120(14)	0.0626(2)	0.12598(14)	0.0169(3)
Cl4	4e	0	0.1304(3)	$\frac{1}{4}$	0.0165(3)
Pb1	4e	0	0.62392(4)	$\frac{1}{4}$	0.00841(7)
Pb2	4b	0	$\frac{1}{2}$	0	0.00844(7)
Cl5	4a	0	0	0	0.0183(4)

Table SIII. (An)isotropic displacement parameters for $(C_7H_7N_2)_2PbCl_4$ at 100 K with standard deviations in parentheses.

Atom	U₁₁	U₂₂	U₃₃	U₂₃	U₁₃	U₁₂
C1	0.012(4)	0.011(4)	0.014(4)	0.005(3)	0.006(3)	0.004(3)
C2	0.019(4)	0.018(5)	0.020(4)	-0.002(4)	0.014(4)	0.004(3)
N1	0.023(4)	0.012(5)	0.030(5)	-0.001(4)	0.022(4)	-0.001(4)
Cl1	0.0156(6)	0.0180(6)	0.0161(13)	-0.0086(9)	0.0084(11)	-0.0026(14)
N2	0.020(3)	0.015(4)	0.012(3)	-0.001(3)	0.010(3)	0.006(3)
N3	0.020(3)	0.013(4)	0.010(3)	0.001(3)	0.008(3)	-0.002(3)
C3	0.017(3)	0.015(3)	0.012(3)	0.004(3)	0.008(3)	0.006(3)
C4	0.014(3)	0.010(3)	0.009(3)	0.004(3)	0.004(3)	0.000(3)
C5	0.019(3)	0.013(3)	0.007(3)	0.002(2)	0.005(3)	0.001(3)
C6	0.018(3)	0.016(3)	0.015(3)	-0.002(3)	0.009(3)	0.001(3)
C7	0.022(4)	0.021(4)	0.014(3)	-0.005(3)	0.013(3)	-0.007(3)
C8	0.024(3)	0.014(3)	0.018(3)	-0.006(3)	0.014(3)	-0.004(3)
C9	0.012(3)	0.022(4)	0.016(3)	0.003(3)	0.004(3)	-0.004(3)
C10	0.010(3)	0.030(4)	0.017(3)	0.010(3)	0.007(3)	0.009(3)
C11	0.021(4)	0.021(3)	0.021(4)	0.000(3)	0.015(3)	0.000(3)
C12	0.020(3)	0.019(3)	0.019(3)	-0.004(3)	0.011(3)	-0.009(3)
C13	0.020(3)	0.013(3)	0.020(4)	0.003(3)	0.012(3)	-0.001(3)
C14	0.016(3)	0.009(3)	0.015(3)	0.002(2)	0.011(3)	0.001(3)
Cl2	0.0184(6)	0.0115(5)	0.0123(11)	0.0005(9)	0.0092(9)	0.0020(4)
N4	0.010(3)	0.016(5)	0.016(4)	0.013(4)	0.008(3)	0.008(3)
Cl3	0.0253(6)	0.0186(6)	0.0075(14)	-0.0022(12)	0.0101(12)	-0.002(2)
Cl4	0.0256(9)	0.0058(7)	0.023(2)	0	0.0171(19)	0
Pb1	0.01458(13)	0.00542(12)	0.0085(3)	0	0.0087(3)	0
Pb2	0.01262(13)	0.00698(12)	0.0093(4)	-0.0015(2)	0.0085(3)	-0.0010(3)
Cl5	0.0233(9)	0.0086(8)	0.024(2)	0.0009(14)	0.015(2)	-0.002(2)

7. Appendix

Table SIV. Bond distances for $(C_7H_7N_2)_2PbCl_4$ at 100 K with standard deviations in parentheses.

Atom 1	Atom 2	Distance / Å	Atom 1	Atom 2	Distance / Å
C1	N2	1.310(13)	C9	C10	1.401(10)
	N4	1.314(12) ⁱ		H9	0.9500
	H1	0.9500	C10	C7	1.381(10) ⁱⁱⁱ
C2	N1	1.330(13) ⁱⁱ		H10	0.9500
	N3	1.341(12)	C11	C13	1.388(10) ⁱ
	H2	0.9500		C12	1.408(10)
N1	C2	1.330(13) ⁱⁱⁱ		H11	0.9500
	C4	1.375(9) ⁱⁱⁱ	C12	H12	0.9500
	H3	0.8800	C13	C11	1.388(10) ^{iv}
Cl1	Pb2	2.8579(12)		C5	1.390(9) ^{iv}
N2	C14	1.377(9) ⁱ		H13	0.9500
	H4	0.8800	C14	N2	1.377(9) ^{iv}
N3	C3	1.388(9) ⁱⁱ		C8	1.397(9) ^{iv}
	H5	0.8800		C5	1.398(9) ^{iv}
C3	C4	1.379(9) ⁱⁱⁱ	Cl2	Pb1	2.8755(12) ^v
	N3	1.388(9) ⁱⁱⁱ	N4	C1	1.314(12) ^{iv}
	C7	1.392(9) ⁱⁱⁱ		C5	1.388(10) ^{iv}
C4	N1	1.375(10) ⁱⁱ		H14	0.8800
	C3	1.379(9) ⁱⁱ	Cl3	Pb2	2.8357(12) ^v
	C6	1.396(9) ⁱⁱ		Pb1	2.8418(12) ^v
C5	N4	1.388(10) ⁱ	Cl4	Pb1	2.7927(15)
	C13	1.390(9) ⁱ		Pb1	2.8662(15) ^{vi}
	C14	1.398(9) ⁱ	Pb1	Cl3	2.8418(12) ^{vii}
C6	C9	1.388(9)		Cl3	2.8418(12) ^{iv}
	C4	1.396(9) ⁱⁱⁱ		Cl4	2.8662(15) ^{viii}
	H6	0.9500		Cl2	2.8755(12) ^{vii}
C7	C10	1.381(10) ⁱⁱ		Cl2	2.8755(12) ^{iv}
	C3	1.392(9) ⁱⁱ	Pb2	Cl5	2.8294 ^{viii}
	H7	0.9500		Cl5	2.8294
C8	C12	1.372(9)		Cl3	2.8357(12) ^{ix}
	C14	1.397(9) ⁱ		Cl3	2.8357(12) ^{vii}
	H8	0.9500		Cl1	2.8579(12) ^x
			Cl5	Pb2	2.8294 ^{vi}
i	$-x+\frac{1}{2}, y-\frac{1}{2}, -z+\frac{1}{2}$		vi	$x, y-1, z$	
ii	$x, -y, z+\frac{1}{2}$		vii	$x-\frac{1}{2}, y+\frac{1}{2}, z$	
iii	$x, -y, z-\frac{1}{2}$		viii	$x, y+1, z$	
iv	$-x+\frac{1}{2}, y+\frac{1}{2}, -z+\frac{1}{2}$		ix	$-x+\frac{1}{2}, -y+\frac{1}{2}, -z$	
v	$x+\frac{1}{2}, y-\frac{1}{2}, z$		x	$-x, -y+1, -z$	

Table SV. Bond angles for $(C_7H_7N_2)_2PbCl_4$ at 100 K with standard deviations in parentheses.

Bond	Angle / °	Bond	Angle / °	Bond	Angle / °
N2-C1-N4 ⁱ	111.6(8)	C3-C7 ⁱⁱ -H7	122.4	Cl3-Pb1 ^{vii} -Cl3 ^{iv}	165.97(6)
N2-C1-H1	124.2	C12-C8-C14 ⁱ	116.7(6)	Cl4-Pb1-Cl4 ^{viii}	180.000(1)
N4-C1 ⁱ -H1	124.2	C12-C8-H8	121.7	Cl3-Pb1 ^{vii} -Cl4 ^{viii}	97.02(3)
N1-C2 ⁱⁱ -N3	107.9(8)	C14-C8 ⁱ -H8	121.7	Cl3-Pb1 ^{iv} -Cl4 ^{viii}	97.02(3)
N1-C2 ⁱⁱ -H2	126.0	C6-C9-C10	121.1(6)	Cl4-Pb1-Cl2 ^{vii}	89.06(2)
N3-C2-H2	126.0	C6-C9-H9	119.4	Cl3-Pb1 ^{vii} -Cl2 ^{vii}	92.08(10)
C2-N1 ⁱⁱⁱ -C4 ⁱⁱⁱ	110.2(8)	C10-C9-H9	119.4	Cl3-Pb1 ^{iv} -Cl2 ^{vii}	87.69(10)
C2-N1 ⁱⁱⁱ -H3	124.9	C7-C10 ⁱⁱⁱ -C9	122.8(6)	Cl4-Pb1 ^{viii} -Cl2 ^{vii}	90.94(2)
C4-N1 ⁱⁱⁱ -H3	124.9	C7-C10 ⁱⁱⁱ -H10	118.6	Cl4-Pb1-Cl2 ^{iv}	89.06(2)
C1-N2-C14 ⁱ	108.3(8)	C9-C10-H10	118.6	Cl3-Pb1 ^{vii} -Cl2 ^{iv}	87.69(10)
C1-N2-H4	125.9	C13-C11 ⁱ -C12	121.7(6)	Cl3-Pb1 ^{iv} -Cl2 ^{iv}	92.08(10)
C14-N2 ⁱ -H4	125.9	C13-C11 ⁱ -H11	119.1	Cl4-Pb1 ^{viii} -Cl2 ^{iv}	90.94(2)
C2-N3-C3 ⁱⁱ	109.0(8)	C12-C11-H11	119.1	Cl2-Pb1 ^{vii} -Cl2 ^{iv}	178.12(5)
C2-N3-H5	125.5	C8-C12-C11	122.0(6)	Cl5-Pb2 ^{viii} -Cl5	180.0
C3-N3 ⁱⁱ -H5	125.5	C8-C12-H12	119.0	Cl5-Pb2 ^{viii} -Cl3 ^{ix}	97.17(3)
C4-C3 ⁱⁱⁱ -N3 ⁱⁱⁱ	106.7(6)	C11-C12-H12	119.0	Cl5-Pb2-Cl3 ^{ix}	82.83(3)
C4-C3 ⁱⁱⁱ -C7 ⁱⁱⁱ	123.1(6)	C11-C13 ^{iv} -C5 ^{iv}	116.2(6)	Cl5-Pb2 ^{viii} -Cl3 ^{vii}	82.83(3)
N3-C3 ⁱⁱⁱ -C7 ⁱⁱⁱ	130.3(7)	C11-C13 ^{iv} -H13	121.9	Cl5-Pb2-Cl3 ^{vii}	97.17(3)
N1-C4 ⁱⁱ -C3 ⁱⁱ	106.2(6)	C5-C13 ^{iv} -H13	121.9	Cl3-Pb2 ^{ix} -Cl3 ^{vii}	180.00(15)
N1-C4 ⁱⁱ -C6 ⁱⁱ	132.3(7)	N2-C14 ^{iv} -C8 ^{iv}	132.2(7)	Cl5-Pb2 ^{viii} -Cl1	90.33(7)
C3-C4 ⁱⁱ -C6 ⁱⁱ	121.4(6)	N2-C14 ^{iv} -C5 ^{iv}	106.3(6)	Cl5-Pb2-Cl1	89.67(7)
N4-C5-C13 ⁱ	131.9(6)	C8-C14 ^{iv} -C5 ^{iv}	121.4(6)	Cl3-Pb2 ^{ix} -Cl1	89.92(10)
N4-C5-C14 ⁱ	106.1(6)	C1-N4 ^{iv} -C5 ^{iv}	107.7(7)	Cl3-Pb2 ^{vii} -Cl1	90.08(10)
C13-C5 ⁱ -C14 ⁱ	122.0(6)	C1-N4 ^{iv} -H14	126.1	Cl5-Pb2 ^{viii} -Cl1 ^x	89.67(7)
C9-C6-C4 ⁱⁱⁱ	116.4(6)	C5-N4 ^{iv} -H14	126.1	Cl5-Pb2-Cl1 ^x	90.33(7)
C9-C6-H6	121.8	Pb2-Cl3 ^v -Pb1 ^v	178.58(16)	Cl3-Pb2 ^{ix} -Cl1 ^x	90.08(10)
C4-C6 ⁱⁱⁱ -H6	121.8	Pb1-Cl4-Pb1 ^{vi}	180.0	Cl3-Pb2 ^{vii} -Cl1 ^x	89.92(10)
C10-C7 ⁱⁱ -C3 ⁱⁱ	115.2(6)	Cl4-Pb1-Cl3 ^{vii}	82.98(3)	Cl1-Pb2-Cl1 ^x	180.00(4)
C10-C7 ⁱⁱ -H7	122.4	Cl4-Pb1-Cl3 ^{iv}	82.98(3)	Pb2-Cl5 ^{vi} -Pb2	180.0
i	$-x+\frac{1}{2}, y-\frac{1}{2}, -z+\frac{1}{2}$	vi	$x, y-1, z$		
ii	$x, -y, z+\frac{1}{2}$	vii	$x-\frac{1}{2}, y+\frac{1}{2}, z$		
iii	$x, -y, z-\frac{1}{2}$	viii	$x, y+1, z$		
iv	$-x+\frac{1}{2}, y+\frac{1}{2}, -z+\frac{1}{2}$	ix	$-x+\frac{1}{2}, -y+\frac{1}{2}, -z$		
v	$x+\frac{1}{2}, y-\frac{1}{2}, z$	x	$-x, -y+1, -z$		

Table SVI. Hydrogen bond distances (in Å) and angles (in °) for (C₇H₇N₂)₂PbCl₄ at 100 K with standard deviations in parentheses.

D-H...A	H...A	D...A	∠D-H...A
N1-H3...Cl1	2.344	3.159(9)	154.07
N2-H4...Cl2 ⁱ	2.298	3.144(8)	161.48
N3-H5...Cl2 ⁱ	2.319	3.161(8)	160.06
N4-H14...Cl1 ⁱⁱ	2.357	3.150(8)	149.93
i	-x+ $\frac{1}{2}$, y- $\frac{1}{2}$, -z+ $\frac{1}{2}$		
ii	x, -y, z+ $\frac{1}{2}$		

Table SVII. Atomic coordinates and equivalent isotropic displacement parameters for (C₇H₇N₂)₂PbBr₄ at 173 K with standard deviations in parentheses. U(eq) is defined as one third of the trace of the orthogonalized U Tensor.

Atom	Wyck.	x	y	z	U(eq) / Å ²
C1	8f	0.08038(13)	0.0322(6)	0.20469(18)	0.0306(8)
H1	8f	0.0483	0.0074	0.1849	0.037
C2	8f	0.08153(14)	0.0914(6)	0.45692(19)	0.0342(8)
H2	8f	0.0504	0.1357	0.4383	0.041
N1	8f	0.10530(10)	0.0771(4)	0.00181(15)	0.0293(6)
H3	8f	0.0949	0.1640	0.0196	0.035
Br1	8f	0.105465(12)	0.49529(5)	0.096509(18)	0.02966(9)
N2	8f	0.10740(10)	0.1964(4)	0.24966(14)	0.0281(6)
H4	8f	0.0984	0.2992	0.2659	0.034
N3	8f	0.10792(10)	0.1882(5)	0.44214(15)	0.0323(7)
H5	8f	0.0996	0.3050	0.4139	0.039
C3	8f	0.15087(13)	-0.0764(5)	-0.02175(17)	0.0275(7)
C4	8f	0.14905(12)	-0.0956(5)	0.51645(17)	0.0234(7)
C5	8f	0.15045(12)	-0.0051(5)	0.22939(17)	0.0234(7)
C6	8f	0.18637(13)	0.2448(5)	0.05822(18)	0.0325(8)
H6	8f	0.1851	0.3624	0.0841	0.039
C7	8f	0.19003(14)	0.1043(6)	0.47967(19)	0.0350(9)
H7	8f	0.1914	0.2199	0.4533	0.042
C8	8f	0.19193(13)	0.3083(6)	0.30991(18)	0.0337(8)
H8	8f	0.1927	0.4351	0.3350	0.040
C9	8f	0.22492(13)	0.2144(6)	0.06022(19)	0.0390(9)
H9	8f	0.2513	0.3115	0.0889	0.047
C10	8f	0.22655(14)	0.0435(6)	0.0211(2)	0.0405(9)
H10	8f	0.2539	0.0296	0.0233	0.049
C11	8f	0.22930(13)	0.0599(6)	0.27697(19)	0.0377(8)
H11	8f	0.2567	0.0224	0.2810	0.045
C12	8f	0.23069(13)	0.2446(6)	0.31483(19)	0.0389(9)

Table SVII. Continuation.

H12	8 <i>f</i>	0.2592	0.3278	0.3447	0.047
C13	8 <i>f</i>	0.31056(12)	0.4321(6)	0.26573(18)	0.0329(8)
H13	8 <i>f</i>	0.3113	0.3056	0.2909	0.039
C14	8 <i>f</i>	0.34800(11)	0.6802(5)	0.23296(16)	0.0232(7)
Br2	8 <i>f</i>	0.393767(12)	0.10534(5)	0.155156(16)	0.02581(8)
N4	8 <i>f</i>	0.39479(10)	0.4083(4)	0.30825(15)	0.0270(6)
H14	8 <i>f</i>	0.4054	0.2898	0.3363	0.032
Br3	8 <i>f</i>	0.500273(12)	0.05649(5)	0.125202(16)	0.02623(8)
Br4	4 <i>e</i>	0	0.10998(6)	$\frac{1}{4}$	0.02702(11)
Pb1	4 <i>e</i>	0	0.60908(2)	$\frac{1}{4}$	0.01653(5)
Pb2	4 <i>b</i>	0	$\frac{1}{2}$	0	0.01528(5)
Br5	4 <i>a</i>	0	0	0	0.02711(11)

Table SVIII. (An)isotropic displacement parameters for (C₇H₇N₂)₂PbBr₄ at 173 K with standard deviations in parentheses.

Atom	U₁₁	U₂₂	U₃₃	U₂₃	U₁₃	U₁₂
C1	0.025(2)	0.0355(19)	0.0309(19)	-0.0061(15)	0.0168(18)	-0.0044(15)
C2	0.032(2)	0.034(2)	0.036(2)	0.0060(16)	0.0203(19)	0.0038(16)
N1	0.0333(18)	0.0257(14)	0.0337(16)	-0.0075(12)	0.0229(15)	0.0008(12)
Br1	0.0262(2)	0.03011(19)	0.02951(19)	-0.0119(2)	0.01542(17)	0.00011(13)
N2	0.0291(17)	0.0265(14)	0.0297(15)	-0.0095(12)	0.0185(14)	-0.0007(12)
N3	0.0403(19)	0.0282(15)	0.0296(15)	0.0085(12)	0.0220(15)	0.0019(14)
C3	0.039(2)	0.0235(16)	0.0244(17)	0.0033(14)	0.0213(17)	0.0068(15)
C4	0.0275(19)	0.0205(16)	0.0241(17)	-0.0022(13)	0.0167(16)	-0.0041(13)
C5	0.0228(19)	0.0235(17)	0.0221(17)	-0.0022(12)	0.0128(16)	-0.0018(12)
C6	0.036(2)	0.0269(17)	0.0327(19)	-0.0024(15)	0.0201(18)	-0.0010(15)
C7	0.046(3)	0.034(2)	0.037(2)	-0.0086(16)	0.031(2)	-0.0164(17)
C8	0.037(2)	0.0296(18)	0.0325(19)	-0.0078(15)	0.0204(18)	-0.0059(16)
C9	0.030(2)	0.042(2)	0.039(2)	0.0074(17)	0.0183(19)	0.0009(17)
C10	0.033(2)	0.050(2)	0.048(2)	0.020(2)	0.029(2)	0.0161(19)
C11	0.027(2)	0.047(2)	0.038(2)	-0.0047(18)	0.0191(19)	-0.0011(17)
C12	0.030(2)	0.042(2)	0.038(2)	-0.0074(17)	0.0173(19)	-0.0127(16)
C13	0.032(2)	0.0356(18)	0.034(2)	0.0063(16)	0.0216(19)	-0.0015(16)
C14	0.0243(18)	0.0238(16)	0.0200(15)	0.0043(13)	0.0127(15)	0.0031(14)
Br2	0.0328(2)	0.02148(16)	0.02398(17)	0.00383(12)	0.01780(16)	0.00478(12)
N4	0.0283(17)	0.0242(14)	0.0312(16)	0.0104(12)	0.0195(15)	0.0046(12)
Br3	0.0384(2)	0.02998(16)	0.01986(15)	-0.0039(2)	0.02270(16)	-0.0055(2)
Br4	0.0423(3)	0.00915(19)	0.0402(3)	0	0.0306(3)	0
Pb1	0.02888(10)	0.01002(8)	0.01733(8)	0	0.01752(8)	0
Pb2	0.02446(10)	0.01060(8)	0.01517(8)	-0.00057(5)	0.01436(8)	-0.00001(6)
Br5	0.0403(3)	0.0097(2)	0.0361(3)	0.00173(16)	0.0257(3)	0.00028(17)

Table SIX. Bond distances for (C₇H₇N₂)₂PbBr₄ at 173 K with standard deviations in parentheses.

Atom 1	Atom 2	Distance / Å	Atom 1	Atom 2	Distance / Å
C1	N4	1.326(4) ⁱ	C9	C10	1.401(5)
	N2	1.328(4)		H9	0.9500
	H1	0.9500		C10	C7
C2	N3	1.322(4)	H10		0.9500
	N1	1.324(4) ⁱⁱ	C11	C13	1.368(5) ⁱ
	H2	0.9500		C12	1.399(5)
N1	C2	1.324(4) ⁱⁱⁱ		H11	0.9500
	C4	1.385(4) ⁱⁱⁱ	C12	H12	0.9500
	H3	0.8800		C13	C11
Br1	Pb2	2.9870(4)	C5		1.378(4) ^{iv}
N2	C14	1.386(4) ⁱ	H13	0.9500	
	H4	0.8800	C14	C8	1.371(5) ^{iv}
N3	C3	1.389(4) ⁱⁱ		N2	1.386(4) ^{iv}
	H5	0.8800		C5	1.397(4) ^{iv}
C3	N3	1.389(4) ⁱⁱⁱ	Br2	Pb1	3.0096(4) ^v
	C7	1.391(5) ⁱⁱⁱ	N4	C1	1.326(4) ^{iv}
	C4	1.393(4) ⁱⁱⁱ		C5	1.384(4) ^{iv}
C4	N1	1.385(4) ⁱⁱ	H14	0.8800	
	C6	1.391(5) ⁱⁱ	Br3	Pb1	2.9773(3) ^v
	C3	1.393(4) ⁱⁱ		Pb2	2.9774(3) ^v
C5	C13	1.378(4) ⁱ	Br4	Pb1	2.9674(4)
	N4	1.384(4) ⁱ	Pb1	2.9781(4) ^{vi}	
	C14	1.397(4) ⁱ	Pb1	Br3	2.9773(3) ^{vii}
C6	C9	1.362(5)		Br3	2.9773(3) ^{iv}
	C4	1.391(5) ⁱⁱⁱ		Br4	2.9781(4) ^{viii}
	H6	0.9500	Br2	3.0096(4) ^{vii}	
C7	C10	1.369(5) ⁱⁱ	Br2	3.0096(4) ^{iv}	
	C3	1.391(5) ⁱⁱ	Pb2	Br5	2.9728 ^{viii}
	H7	0.9500		Br5	2.9728
C8	C14	1.371(5) ⁱ		Br3	2.9774(3) ^{ix}
	C12	1.372(5)	Br3	2.9774(3) ^{vii}	
	H8	0.9500	Br1	2.9870(4) ^x	
			Br5	Pb2	2.9728 ^{vi}
i	$-x+\frac{1}{2}, y-\frac{1}{2}, -z+\frac{1}{2}$		vi	$x, y-1, z$	
ii	$x, -y, z+\frac{1}{2}$		vii	$x-\frac{1}{2}, y+\frac{1}{2}, z$	
iii	$x, -y, z-\frac{1}{2}$		viii	$x, y+1, z$	
iv	$-x+\frac{1}{2}, y+\frac{1}{2}, -z+\frac{1}{2}$		ix	$-x+\frac{1}{2}, -y+\frac{1}{2}, -z$	
v	$x+\frac{1}{2}, y-\frac{1}{2}, z$		x	$-x, -y+1, -z$	

Table SX. Bond angles for (C₇H₇N₂)₂PbBr₄ at 173 K with standard deviations in parentheses.

Bond	Angle / °	Bond	Angle / °	Bond	Angle / °
N4-C1 ⁱ -N2	109.4(3)	C3-C7 ⁱⁱ -H7	121.7	Br3-Pb1 ^{vii} -Br3 ^{iv}	167.943(13)
N4-C1 ⁱ -H1	125.3	C14-C8 ⁱ -C12	116.8(3)	Br4-Pb1-Br4 ^{viii}	180.0
N2-C1-H1	125.3	C14-C8 ⁱ -H8	121.6	Br3-Pb1 ^{vii} -Br4 ^{viii}	96.029(7)
N3-C2-N1 ⁱⁱ	109.3(3)	C12-C8-H8	121.6	Br3-Pb1 ^{iv} -Br4 ^{viii}	96.029(7)
N3-C2-H2	125.4	C6-C9-C10	121.6(4)	Br4-Pb1-Br2 ^{vii}	89.576(6)
N1-C2 ⁱⁱ -H2	125.4	C6-C9-H9	119.2	Br3-Pb1 ^{vii} -Br2 ^{vii}	91.533(9)
C2-N1 ⁱⁱⁱ -C4 ⁱⁱⁱ	109.5(3)	C10-C9-H9	119.2	Br3-Pb1 ^{iv} -Br2 ^{vii}	88.378(9)
C2-N1 ⁱⁱⁱ -H3	125.2	C7-C10 ⁱⁱⁱ -C9	122.1(3)	Br4-Pb1 ^{viii} -Br2 ^{vii}	90.424(6)
C4-N1 ⁱⁱⁱ -H3	125.2	C7-C10 ⁱⁱⁱ -H10	118.9	Br4-Pb1-Br2 ^{iv}	89.576(6)
C1-N2-C14 ⁱ	109.2(3)	C9-C10-H10	118.9	Br3-Pb1 ^{vii} -Br2 ^{iv}	88.378(9)
C1-N2-H4	125.4	C13-C11 ⁱ -C12	121.5(3)	Br3-Pb1 ^{iv} -Br2 ^{iv}	91.533(9)
C14-N2 ⁱ -H4	125.4	C13-C11 ⁱ -H11	119.3	Br4-Pb1 ^{viii} -Br2 ^{iv}	90.424(6)
C2-N3-C3 ⁱⁱ	109.2(3)	C12-C11-H11	119.3	Br2-Pb1 ^{vii} -Br2 ^{iv}	179.152(11)
C2-N3-H5	125.4	C8-C12-C11	121.6(3)	Br5-Pb2 ^{viii} -Br5	180.0
C3-N3 ⁱⁱ -H5	125.4	C8-C12-H12	119.2	Br5-Pb2 ^{viii} -Br3 ^{ix}	96.477(6)
N3-C3 ⁱⁱⁱ -C7 ⁱⁱⁱ	132.6(3)	C11-C12-H12	119.2	Br5-Pb2-Br3 ^{ix}	83.523(6)
N3-C3 ⁱⁱⁱ -C4 ⁱⁱⁱ	106.2(3)	C11-C13 ^{iv} -C5 ^{iv}	117.1(3)	Br5-Pb2 ^{viii} -Br3 ^{vii}	83.523(6)
C7-C3 ⁱⁱⁱ -C4 ⁱⁱⁱ	121.2(3)	C11-C13 ^{iv} - H13	121.4	Br5-Pb2-Br3 ^{vii}	96.477(6)
N1-C4 ⁱⁱ -C6 ⁱⁱ	132.5(3)	C5-C13 ^{iv} -H13	121.4	Br3-Pb2 ^{ix} -Br3 ^{vii}	180.000(17)
N1-C4 ⁱⁱ -C3 ⁱⁱ	105.8(3)	C8-C14 ^{iv} -N2 ^{iv}	132.1(3)	Br5-Pb2 ^{viii} -Br1	90.537(6)
C6-C4 ⁱⁱ -C3 ⁱⁱ	121.7(3)	C8-C14 ^{iv} -C5 ^{iv}	121.9(3)	Br5-Pb2-Br1	89.463(6)
C13-C5 ⁱ -N4 ⁱ	132.7(3)	N2-C14 ^{iv} -C5 ^{iv}	106.0(3)	Br3-Pb2 ^{ix} -Br1	89.721(9)
C13-C5 ⁱ -C14 ⁱ	121.1(3)	C1-N4 ^{iv} -C5 ^{iv}	109.2(3)	Br3-Pb2 ^{vii} -Br1	90.279(9)
N4-C5 ⁱ -C14 ⁱ	106.2(3)	C1-N4 ^{iv} -H14	125.4	Br5-Pb2 ^{viii} -Br1 ^x	89.463(6)
C9-C6-C4 ⁱⁱⁱ	116.9(3)	C5-N4 ^{iv} -H14	125.4	Br5-Pb2-Br1 ^x	90.537(6)
C9-C6-H6	121.6	Pb1-Br3 ^v -Pb2 ^v	179.462(13)	Br3-Pb2 ^{ix} -Br1 ^x	90.279(9)
C4-C6 ⁱⁱⁱ -H6	121.6	Pb1-Br4-Pb1 ^{vi}	180.0	Br3-Pb2 ^{vii} -Br1 ^x	89.721(9)
C10-C7 ⁱⁱ -C3 ⁱⁱ	116.6(3)	Br4-Pb1-Br3 ^{vii}	83.971(7)	Br1-Pb2-Br1 ^x	180.000(10)
C10-C7 ⁱⁱ -H7	121.7	Br4-Pb1-Br3 ^{iv}	83.971(7)	Pb2-Br5 ^{vi} -Pb2	180.0
i	$-x+\frac{1}{2}, y-\frac{1}{2}, -z+\frac{1}{2}$	vi	$x, y-1, z$		
ii	$x, -y, z+\frac{1}{2}$	vii	$x-\frac{1}{2}, y+\frac{1}{2}, z$		
iii	$x, -y, z-\frac{1}{2}$	viii	$x, y+1, z$		
iv	$-x+\frac{1}{2}, y+\frac{1}{2}, -z+\frac{1}{2}$	ix	$-x+\frac{1}{2}, -y+\frac{1}{2}, -z$		
v	$x+\frac{1}{2}, y-\frac{1}{2}, z$	x	$-x, -y+1, -z$		

Table SXI. Hydrogen bond distances (in Å) and angles (in °) for (C₇H₇N₂)₂PbBr₄ at 173 K with standard deviations in parentheses.

D-H...A	H...A	D...A	∠D-H...A
N1-H3...Br1	2.549	3.346(3)	150.97
N2-H4...Br2 ⁱ	2.500	3.333(2)	158.11
N3-H5...Br2 ⁱ	2.529	3.360(3)	157.89
N4-H14...Br1 ⁱⁱ	2.549	3.338(2)	149.49
i	-x+ $\frac{1}{2}$, y- $\frac{1}{2}$, -z+ $\frac{1}{2}$		
ii	x, -y, z+ $\frac{1}{2}$		

Table SXII. Atomic coordinates and equivalent isotropic displacement parameters for (C₇H₇N₂)₂PbI₄ at 100 K with standard deviations in parentheses. U(eq) is defined as one third of the trace of the orthogonalized U Tensor.

Atom	Wyck.	x	y	z	U(eq) / Å ²
C1	8f	0.0857(2)	0.0301(10)	0.5809(6)	0.0236(13)
H1	8f	0.0536	0.0655	0.5736	0.028
N1	8f	0.1107(2)	0.1275(9)	0.1422(5)	0.0211(11)
H2	8f	0.1002	0.2163	0.1828	0.025
N2	8f	0.1123(2)	0.1322(9)	0.5307(4)	0.0210(11)
H3	8f	0.1030	0.2419	0.4849	0.025
C2	8f	0.1559(2)	0.1323(9)	0.1333(5)	0.0170(11)
C3	8f	0.1575(2)	0.0361(9)	0.5629(5)	0.0171(11)
C4	8f	0.1974(2)	0.0770(10)	0.5319(5)	0.0222(12)
H4	8f	0.1978	0.1894	0.4817	0.027
C5	8f	0.1953(2)	0.2655(10)	0.1806(5)	0.0228(13)
H5	8f	0.1948	0.3783	0.2305	0.027
C6	8f	0.2349(2)	0.2238(11)	0.1506(6)	0.0266(14)
H6	8f	0.2624	0.3126	0.1798	0.032
C7	8f	0.2364(2)	0.0554(11)	0.0784(6)	0.0258(13)
H7	8f	0.2649	0.0321	0.0613	0.031
I1	8f	0.385136(12)	0.06134(5)	0.16068(4)	0.01585(8)
I2	4e	0	0.04796(7)	$\frac{1}{4}$	0.01746(10)
Pb	4e	0	0.55302(4)	$\frac{1}{4}$	0.01060(7)
I3	4b	0	$\frac{1}{2}$	0	0.01704(10)

Table SXIII. (An)isotropic displacement parameters for $(C_7H_7N_2)_2PbI_4$ at 100 K with standard deviations in parentheses.

Atom	U_{11}	U_{22}	U_{33}	U_{23}	U_{13}	U_{12}
C1	0.021(3)	0.025(3)	0.024(3)	0.005(3)	0.006(2)	0.003(3)
N1	0.023(3)	0.019(3)	0.025(3)	-0.002(2)	0.012(2)	0.002(2)
N2	0.021(3)	0.022(3)	0.019(3)	0.006(2)	0.005(2)	0.002(2)
C2	0.014(3)	0.018(3)	0.018(3)	-0.003(2)	0.004(2)	0.003(2)
C3	0.016(3)	0.019(3)	0.017(3)	-0.001(2)	0.006(2)	-0.003(2)
C4	0.017(3)	0.026(3)	0.025(3)	0.001(2)	0.010(2)	-0.004(2)
C5	0.025(3)	0.020(3)	0.021(3)	-0.004(2)	0.006(2)	-0.002(2)
C6	0.022(3)	0.028(3)	0.026(3)	-0.001(3)	0.003(3)	-0.006(3)
C7	0.018(3)	0.028(3)	0.033(3)	0.003(3)	0.010(3)	0.002(3)
I1	0.01395(15)	0.01604(15)	0.01674(17)	0.00079(14)	0.00418(15)	0.00084(12)
I2	0.0251(2)	0.00664(18)	0.0228(3)	0	0.0110(2)	0
Pb	0.01502(13)	0.00802(11)	0.00930(12)	0	0.00487(11)	0
I3	0.0237(2)	0.0190(2)	0.0098(2)	-0.0016(2)	0.0076(2)	-0.0032(2)

Table SXIV. Bond distances for $(C_7H_7N_2)_2PbI_4$ at 100 K with standard deviations in parentheses.

Atom 1	Atom 2	Distance / Å	Atom 1	Atom 2	Distance / Å
C1	N1	1.317(8) ⁱ	C5	C6	1.372(10)
	N2	1.330(9)		H5	0.9500
	H1	0.9500		C6	C7
N1	C1	1.317(8) ⁱⁱ	H6		0.9500
	C2	1.379(8)	C7	C4	1.381(9) ⁱⁱ
	H2	0.8800		H7	0.9500
N2	C3	1.394(8)	I1	Pb	3.1947(4) ⁱⁱⁱ
	H3	0.8800	I2	Pb	3.1136(5) ^{iv}
C2	C3	1.390(8) ⁱⁱ	Pb	Pb	3.1772(5)
	C5	1.393(9)		I2	3.1136(5) ^v
C3	C4	1.389(8)	I3	I3	3.15299(15)
	C2	1.390(8) ⁱ		I3	3.15299(15) ^{vi}
C4	C7	1.381(9) ⁱ	I1	I1	3.1947(4) ^{vii}
	H4	0.9500		I1	3.1947(4) ^{viii}
			I3	Pb	3.15299(15) ^{ix}
i	$x, -y, z + \frac{1}{2}$		vi	$-x, y, -z + \frac{1}{2}$	
ii	$x, -y, z - \frac{1}{2}$		vii	$-x + \frac{1}{2}, y + \frac{1}{2}, -z + \frac{1}{2}$	
iii	$x + \frac{1}{2}, y - \frac{1}{2}, z$		viii	$x - \frac{1}{2}, y + \frac{1}{2}, z$	
iv	$x, y - 1, z$		ix	$-x, -y + 1, -z$	
v	$x, y + 1, z$				

Table SXV. Bond angles for $(C_7H_7N_2)_2PbI_4$ at 100 K with standard deviations in parentheses.

Bond	Angle / °	Bond	Angle / °	Bond	Angle / °
N1-C1 ⁱ -N2	109.5(6)	C2-C3 ⁱ -N2	106.1(5)	I2-Pb ^{iv} -I3 ^v	96.072(4)
N1-C1 ⁱ -H1	125.2	C7-C4 ⁱ -C3	116.0(6)	I3-Pb-I3 ^v	167.856(9)
N2-C1-H1	125.2	C7-C4 ⁱ -H4	122.0	I2-Pb ^{iv} -I2	180.0
C1-N1 ⁱⁱ -C2	109.7(5)	C3-C4-H4	122.0	I3-Pb-I2	83.928(4)
C1-N1 ⁱⁱ -H2	125.2	C6-C5-C2	116.0(6)	I3-Pb ^v -I2	83.928(4)
C2-N1-H2	125.2	C6-C5-H5	122.0	I2-Pb ^{iv} -I1 ^{vi}	89.061(7)
C1-N2-C3	108.5(5)	C2-C5-H5	122.0	I3-Pb-I1 ^{vi}	89.319(8)
C1-N2-H3	125.7	C5-C6-C7	122.6(6)	I3-Pb ^v -I1 ^{vi}	90.879(8)
C3-N2-H3	125.7	C5-C6-H6	118.7	I2-Pb-I1 ^{vi}	90.939(7)
N1-C2-C3 ⁱⁱ	106.2(5)	C7-C6-H6	118.7	I2-Pb ^{iv} -I1 ^{vii}	89.061(7)
N1-C2-C5	132.3(6)	C4-C7 ⁱⁱ -C6	121.4(6)	I3-Pb-I1 ^{vii}	90.879(8)
C3-C2 ⁱⁱ -C5	121.5(6)	C4-C7 ⁱⁱ -H7	119.3	I3-Pb ^v -I1 ^{vii}	89.319(8)
C4-C3-C2 ⁱ	122.4(6)	C6-C7-H7	119.3	I2-Pb-I1 ^{vii}	90.939(7)
C4-C3-N2	131.4(6)	Pb-I2 ⁱⁱⁱ -Pb	180.0	I1-Pb ^{vi} -I1 ^{vii}	178.123(14)
i	$x, -y, z + \frac{1}{2}$	v	$-x, y, -z + \frac{1}{2}$		
ii	$x, -y, z - \frac{1}{2}$	vi	$-x + \frac{1}{2}, y + \frac{1}{2}, -z + \frac{1}{2}$		
iii	$x, y-1, z$	vii	$x - \frac{1}{2}, y + \frac{1}{2}, z$		
iv	$x, y+1, z$	viii	$-x, -y+1, -z$		

Table SXVI. Hydrogen bond distances (in Å) and angles (in °) for $(C_7H_7N_2)_2PbI_4$ at 100 K with standard deviations in parentheses.

D-H...A	H...A	D...A	$\angle D-H...A$
N1-H2...I1 ⁱ	2.859	3.656(5)	151.41
N2-H3...I1 ⁱ	2.816	3.630(5)	154.46
i	$-x + \frac{1}{2}, y + \frac{1}{2}, -z + \frac{1}{2}$		
ii	$-x + \frac{1}{2}, y - \frac{1}{2}, -z + \frac{1}{2}$		

B.2 Crystallographic data for (C₇H₇N₂)PbI₃**Table SXVII.** Crystallographic data and details of the structure refinement for (C₇H₇N₂)PbI₃ (CCDC 1507156).

Formula	(C ₇ H ₇ N ₂)PbI ₃
Molar mass (g mol ⁻¹)	707.04
Crystal system	Orthorhombic
Space group	<i>P</i> 2 ₁ 2 ₁ 2 ₁ (no. 19)
T (K)	173
Radiation, λ (Å)	Mo K _α , 0.71073
<i>a</i> (Å)	4.6368(3)
<i>b</i> (Å)	12.4753(8)
<i>c</i> (Å)	22.3577(16)
α, β, γ (°)	90
<i>V</i> (Å ³)	1293.29(15)
<i>Z</i>	4
Calculated density (g cm ⁻³)	3.631
Crystal size (mm ³)	0.01 × 0.02 × 0.10
Absorption coefficient (mm ⁻¹)	20.170
F(000)	1216
Absorption correction	multi-scan
θ range	2.4° to 27.5°
Index range	-6 ≤ <i>h</i> ≤ 5, -16 ≤ <i>k</i> ≤ 16, -29 ≤ <i>l</i> ≤ 29
Parameters/restraints	127 / 2
Total No. of reflections	22305
No. of independent reflections	2956 [R _{int} = 0.033]
No. of observed reflections	2841
Min./max. residual electron density (e Å ⁻³)	-0.74 / 0.56
Goof	1.08
Final R indices [I > 2σ(I)]	R1 = 0.0148, wR2 = 0.0281
Final R indices (all data)	R1 = 0.0168, wR2 = 0.0286

$$w = [\sigma^2(F_0^2) + (0.0112P)^2 + 0.0133P]^{-1}, \text{ with } P = (F_0^2 + 2F_c^2)/3$$

Table SXVIII. Atomic coordinates and equivalent isotropic displacement parameters for $(C_7H_7N_2)PbI_3$ at 173 K with standard deviations in parentheses. $U(eq)$ is defined as one third of the trace of the orthogonalized U Tensor.

Atom	Wyck.	x	y	z	$U(eq) / \text{\AA}^2$
N1	4a	0.0133(7)	0.2884(3)	0.19264(14)	0.0273(8)
H1	4a	0.0541	0.3463	0.2134	0.033
N2	4a	0.0206(7)	0.1246(2)	0.16256(13)	0.0227(7)
H2	4a	0.0681	0.0565	0.1601	0.027
I1	4a	0.10962(6)	0.611344(19)	0.152150(11)	0.02481(7)
C1	4a	0.1322(8)	0.1943(3)	0.20006(18)	0.0290(9)
H3	4a	0.2783	0.1786	0.2285	0.035
C2	4a	0.1889(8)	0.7822(3)	0.35358(16)	0.0186(8)
I2	4a	0.39024(6)	0.101407(19)	0.527661(11)	0.02154(6)
Pb1	4a	0.40678(3)	0.256194(11)	0.404723(6)	0.02004(5)
C3	4a	0.8156(8)	0.1760(3)	0.12753(17)	0.0196(9)
C4	4a	0.4564(8)	0.2155(3)	0.05695(17)	0.0259(9)
H4	4a	0.3304	0.1942	0.0257	0.031
I3	4a	0.47467(5)	0.412681(19)	0.297767(11)	0.02118(6)
C5	4a	0.4531(9)	0.3224(3)	0.07609(18)	0.0261(9)
H5	4a	0.3255	0.3715	0.0573	0.031
C6	4a	0.6384(9)	0.1399(3)	0.08234(16)	0.0225(9)
H6	4a	0.6408	0.0674	0.0693	0.027
C7	4a	0.6284(9)	0.3579(3)	0.12107(18)	0.0270(9)
H7	4a	0.6255	0.4303	0.1343	0.032

Table SXIX. (An)isotropic displacement parameters for $(C_7H_7N_2)PbI_3$ at 173 K with standard deviations in parentheses.

Atom	U_{11}	U_{22}	U_{33}	U_{23}	U_{13}	U_{12}
N1	0.0252(19)	0.0311(19)	0.0256(19)	-0.0070(15)	-0.0029(15)	-0.0028(15)
N2	0.0230(19)	0.0217(17)	0.0236(18)	0.0047(14)	0.0019(14)	0.0030(14)
I1	0.02244(14)	0.02047(13)	0.03152(14)	0.00388(10)	0.00205(11)	0.00114(11)
C1	0.018(2)	0.047(3)	0.022(2)	0.007(2)	0.0028(18)	-0.004(2)
C2	0.0158(19)	0.023(2)	0.0171(19)	0.0070(16)	0.0043(15)	0.0047(15)
I2	0.02251(13)	0.01908(12)	0.02304(13)	0.00119(10)	0.00219(11)	0.00091(11)
Pb1	0.01909(8)	0.02071(8)	0.02033(7)	0.00069(6)	-0.00003(5)	-0.00065(6)
C3	0.018(2)	0.021(2)	0.020(2)	0.0030(16)	0.0041(15)	0.0005(16)
C4	0.018(2)	0.041(2)	0.019(2)	0.0026(17)	0.0014(16)	-0.0021(18)
I3	0.02292(13)	0.02059(12)	0.02004(12)	0.00060(10)	-0.0027(1)	-0.0014(1)
C5	0.021(2)	0.028(2)	0.029(2)	0.0107(18)	0.0062(18)	0.0048(18)
C6	0.025(2)	0.0203(19)	0.022(2)	-0.0048(16)	0.0058(17)	-0.0063(18)
C7	0.030(2)	0.0177(19)	0.034(2)	-0.0030(17)	0.005(2)	-0.0007(18)

7. Appendix

Table SXX. Bond distances for (C₇H₇N₂)PbI₃ at 173 K with standard deviations in parentheses.

Atom 1	Atom 2	Distance / Å	Atom 1	Atom 2	Distance / Å
N1	C1	1.307(5)	Pb1	I3	3.1030(3)
	C2	1.397(5) ⁱ		I1	3.1481(3) ^{vii}
	H1	0.870(10)		I2	3.2352(3) ^{vi}
N2	C1	1.311(5)	C3	I1	3.2582(3) ⁱ
	C3	1.392(5) ⁱⁱ		I2	3.3433(3) ^v
	H2	0.868(10)		C6	1.378(5)
I1	Pb1	3.1481(3) ⁱⁱⁱ	N2	C2	1.392(5) ^{viii}
	Pb1	3.2582(3) ^{iv}		C6	1.390(5) ^{vii}
C1	H3	0.9500	C4	C6	1.387(6)
C2	C7	1.390(6) ⁱⁱⁱ		C5	1.400(5)
	C3	1.390(5) ⁱⁱⁱ	H4	0.9500	
	N1	1.397(5) ^{iv}	C5	C7	1.366(6)
I2	Pb1	3.2352(3) ^v		H5	0.9500
	Pb1	3.3433(3) ^{vi}	C6	H6	0.9500
	Pb1	3.3600(3)		C2	1.390(5) ^{vii}
			C7	H7	0.9500
i	$-x, y-\frac{1}{2}, -z+\frac{1}{2}$		v	$x-\frac{1}{2}, -y+\frac{1}{2}, -z+1$	
ii	$x-1, y, z$		vi	$x+\frac{1}{2}, -y+\frac{1}{2}, -z+1$	
iii	$-x+1, y+\frac{1}{2}, -z+\frac{1}{2}$		vii	$-x+1, y-\frac{1}{2}, -z+\frac{1}{2}$	
iv	$-x, y+\frac{1}{2}, -z+\frac{1}{2}$		viii	$x+1, y, z$	

Table SXXI. Bond angles for (C₇H₇N₂)PbI₃ at 173 K with standard deviations in parentheses.

Bond	Angle / °	Bond	Angle / °	Bond	Angle / °
C1-N1-C2 ⁱ	109.1(3)	Pb1-I2 ^{vi} -Pb1	92.760(8)	I2-Pb1 ^v -I2	85.361(8)
C1-N1-H1	124(3)	I3-Pb1-I1 ^{vii}	88.717(8)	C6-C3-N2 ^{viii}	132.2(4)
C2-N1 ⁱ -H1	127(3)	I3-Pb1-I2 ^{vi}	86.810(8)	C6-C3-C2 ^{vii}	121.6(4)
C1-N2-C3 ⁱⁱ	108.8(3)	I1-Pb1 ^{vii} -I2 ^{vi}	90.596(9)	N2-C3 ^{viii} -C2 ^{vii}	106.1(3)
C1-N2-H2	135(3)	I3-Pb1-I1 ⁱ	97.050(8)	C6-C4-C5	121.9(4)
C3-N2 ⁱⁱ -H2	116(3)	I1-Pb1 ^{vii} -I1 ⁱ	92.721(9)	C6-C4-H4	119.0
Pb1-I1 ⁱⁱⁱ -Pb1 ^{iv}	92.721(9)	I2-Pb1 ^{vi} -I1 ⁱ	174.962(8)	C5-C4-H4	119.0
N1-C1-N2	110.5(4)	I3-Pb1-I2 ^v	94.982(8)	C7-C5-C4	121.8(4)
N1-C1-H3	124.8	I1-Pb1 ^{vii} -I2 ^v	176.301(8)	C7-C5-H5	119.1
N2-C1-H3	124.8	I2-Pb1 ^{vi} -I2 ^v	89.618(8)	C4-C5-H5	119.1
C7-C2 ⁱⁱⁱ -C3 ⁱⁱⁱ	122.2(4)	I1-Pb1 ⁱ -I2 ^v	86.828(8)	C3-C6-C4	116.1(4)
C7-C2 ⁱⁱⁱ -N1 ^{iv}	132.3(3)	I3-Pb1-I2	173.883(8)	C3-C6-H6	121.9
C3-C2 ⁱⁱⁱ -N1 ^{iv}	105.5(3)	I1-Pb1 ^{vii} -I2	90.962(8)	C4-C6-H6	121.9
Pb1-I2 ^v -Pb1 ^{vi}	89.618(8)	I2-Pb1 ^{vi} -I2	87.085(8)	C5-C7-C2 ^{vii}	116.2(4)
Pb1-I2 ^v -Pb1	94.732(8)	I1-Pb1 ⁱ -I2	89.067(8)	C5-C7-H7	121.9
				C2-C7 ^{vii} -H7	121.9
i	$-x, y-\frac{1}{2}, -z+\frac{1}{2}$	v	$x-\frac{1}{2}, -y+\frac{1}{2}, -z+1$		
ii	$x-1, y, z$	vi	$x+\frac{1}{2}, -y+\frac{1}{2}, -z+1$		
iii	$-x+1, y+\frac{1}{2}, -z+\frac{1}{2}$	vii	$-x+1, y-\frac{1}{2}, -z+\frac{1}{2}$		
iv	$-x, y+\frac{1}{2}, -z+\frac{1}{2}$	viii	$x+1, y, z$		

Table SXXII. Hydrogen bond distances (in Å) and angles (in °) for (C₇H₇N₂)PbI₃ at 173 K with standard deviations in parentheses.

D-H...A	H...A	D...A	∠D-H...A
N1-H1...I3	2.82(3)	3.537(3)	140(3)
N2-H2...I3ⁱ	3.04(3)	3.638(3)	128(3)
i	$-x+\frac{1}{2}, y-\frac{1}{2}, -z+\frac{1}{2}$		

B.3 Rietveld refinement results

The Rietveld refinement results for the RT PXRD data of $(C_7H_7N_2)_2PbCl_4$, $(C_7H_7N_2)_2PbBr_4$, $(C_7H_7N_2)PbI_3$ and $BzImPbI_{4/3}$ are listed below. It was premised that the atomic displacement parameters of all C and N atoms in one sample have the same value ($B_{eq}(C,N)$). Besides, the atomic displacement parameter of the hydrogen atoms was constrained to 1.2 times the value of their parent atom ($B_{eq}(H) = 1.2 B_{eq}(C,N)$) as applied in the crystal structure refinement. Additionally, the positions of the heavy atoms, Pb, Cl, Br and I, were subject of refinement unless stated otherwise.

Synthesis of $(C_7H_7N_2)_2PbCl_4$, $(C_7H_7N_2)_2PbBr_4$ and $(C_7H_7N_2)PbI_3$ in HX (X = Br, I) – product obtained by evaporation of the solvent

Only one atomic displacement parameter was refined for all Cl atoms ($B_{eq}(Cl) = 1.00(62)$).

$(C_7H_7N_2)_2PbCl_4$

radiation: Cu $K_{\alpha 1}$

space group: $C2/c$

monoclinic, $a = 36.3204(20) \text{ \AA}$, $b = 5.6870(3) \text{ \AA}$, $c = 22.6911(11) \text{ \AA}$, $\alpha = \gamma = 90^\circ$, $\beta = 125.7117(30)^\circ$

Atom	Wyck.	x	y	z	occ.	$B_{eq} (\text{\AA}^2)$
Cl1	8f	0.0928(10)	0.4667(96)	0.0846(18)	1	1.00(62)
Cl2	8f	0.3853(12)	0.0792(74)	0.1616(19)	1	= $B_{eq}(Cl1)$
Cl3	8f	0.5021(23)	0.0665(70)	0.1288(34)	1	= $B_{eq}(Cl1)$
Cl4	4e	0	0.2518(131)	$\frac{1}{4}$	1	= $B_{eq}(Cl1)$
Pb1	4e	0	0.5757(38)	$\frac{1}{4}$	1	12.51(91)
Pb2	4b	0	$\frac{1}{2}$	0	1	5.87(60)
Cl5	4a	0	0	0	1	= $B_{eq}(Cl1)$

$B_{eq}(C,N) = 4.71(1.09)$

$R_{exp} = 1.66 \%$, $R_{wp} = 10.57 \%$, $R_p = 6.82 \%$, $R_{Bragg} = 2.90 \%$, $Goof = 6.35$

7. Appendix

(C₇H₇N₂)₂PbBr₄radiation: Cu K_{α1}space group: *C2/c*monoclinic, $a = 35.9478(8) \text{ \AA}$, $b = 5.9582(1) \text{ \AA}$, $c = 23.7770(5) \text{ \AA}$, $\alpha = \gamma = 90^\circ$, $\beta = 127.2432(12)^\circ$

Atom	Wyck.	x	y	z	occ.	B _{eq} (Å ²)
Br1	8 <i>f</i>	0.1062(3)	0.4998(11)	0.0953(5)	1	2.87(30)
Br2	8 <i>f</i>	0.3967(3)	0.0975(12)	0.1596(6)	1	4.74(34)
Br3	8 <i>f</i>	0.5007(6)	0.0625(11)	0.1252(7)	1	3.88(18)
Br4	4 <i>e</i>	0	0.1016(12)	$\frac{1}{4}$	1	1.88(36)
Pb1	4 <i>e</i>	0	0.5966(8)	$\frac{1}{4}$	1	4.18(21)
Pb2	4 <i>b</i>	0	$\frac{1}{2}$	0	1	3.77(21)
Br5	4 <i>a</i>	0	0	0	1	5.36(45)

B_{eq}(C,N) = 1.76(28)R_{exp} = 1.57589697 %, R_{wp} = 3.715233 %, R_p = 2.75735746 %, R_{Bragg} = 1.42335843 %, GooF = 2.35753547**(C₇H₇N₂)PbI₃**radiation: Cu K_{α1}space group: *P2₁2₁2₁*orthorhombic, $a = 4.6446(1) \text{ \AA}$, $b = 12.5810(2) \text{ \AA}$, $c = 22.5412(4) \text{ \AA}$, $\alpha = \beta = \gamma = 90^\circ$

Atom	Wyck.	x	y	z	occ.	B _{eq} (Å ²)
I1	4 <i>a</i>	0.1100(19)	0.6091(4)	0.1530(2)	1	4.03(18)
I2	4 <i>a</i>	0.3849(18)	0.1015(4)	0.5278(2)	1	2.76(17)
Pb1	4 <i>a</i>	0.4027(9)	0.2554(4)	0.4044(2)	1	3.29(9)
I3	4 <i>a</i>	0.4742(16)	0.4108(4)	0.2981(2)	1	2.99(15)

B_{eq}(C,N) = 1.53(54)R_{exp} = 0.84 %, R_{wp} = 3.35 %, R_p = 2.53 %, R_{Bragg} = 2.70 %, GooF = 3.96

Synthesis of $(C_7H_7N_2)_2PbBr_4$ and $(C_7H_7N_2)PbI_3$ in HX ($X = Br, I$) - precipitation of the product with ethyl acetate

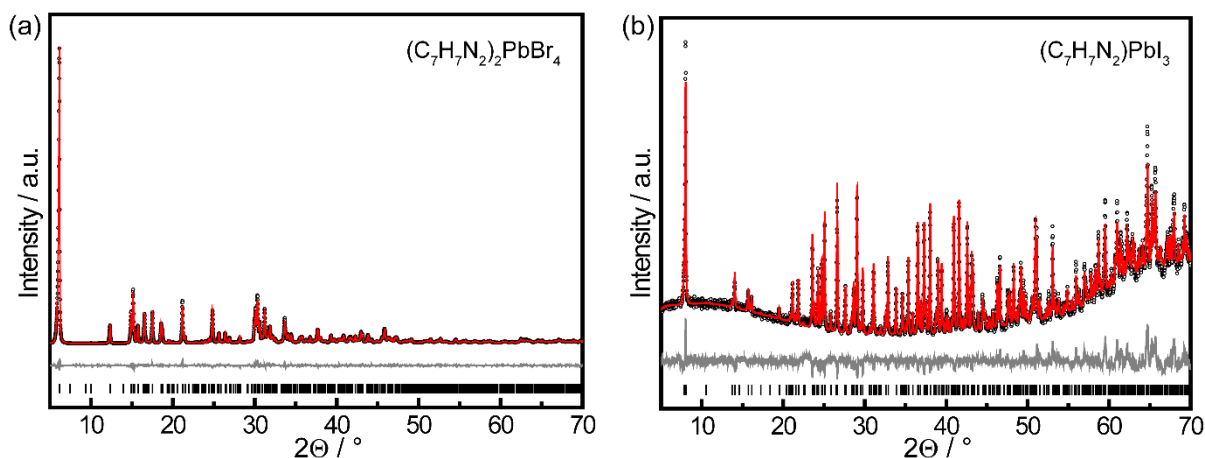


Figure S1. X-ray powder diffraction data of $(C_7H_7N_2)_2PbBr_4$ (a) and $(C_7H_7N_2)PbI_3$ (b) represented by black open circles. The Rietveld profile fit (red solid line) and the difference profile (grey solid line) confirm phase purity. $(C_7H_7N_2)_2PbBr_4$ and $(C_7H_7N_2)PbI_3$ were obtained by precipitation with ethyl acetate from the precursor solution.

$(C_7H_7N_2)_2PbBr_4$

radiation: Cu $K_{\alpha 1}$

space group: $C2/c$

monoclinic, $a = 35.9436(7) \text{ \AA}$, $b = 5.9575(1) \text{ \AA}$, $c = 23.7748(4) \text{ \AA}$, $\alpha = \gamma = 90^\circ$, $\beta = 127.2470(13)^\circ$

Atom	Wyck.	x	y	z	occ.	$B_{eq} (\text{\AA}^2)$
Br1	8f	0.1056(3)	0.4981(9)	0.0943(5)	1	1.86(28)
Br2	8f	0.3964(3)	0.0987(10)	0.1581(5)	1	4.18(30)
Br3	8f	0.5006(5)	0.0634(9)	0.1253(6)	1	3.39(17)
Br4	4e	0	0.0999(11)	$\frac{1}{4}$	1	1.19(31)
Pb1	4e	0	0.5963(7)	$\frac{1}{4}$	1	3.38(18)
Pb2	4b	0	$\frac{1}{2}$	0	1	2.80(19)
Br5	4a	0	0	0	1	4.87(39)

$B_{eq}(C,N) = 3.90(29)$

$R_{exp} = 1.39 \%$, $R_{wp} = 5.31 \%$, $R_p = 4.02 \%$, $R_{Bragg} = 1.97 \%$, $Goof = 3.83$

Due to strong absorption effects the atomic displacement parameter was not refined and set to a value of 2.

(C₇H₇N₂)PbI₃radiation: Cu K_{α1}space group: *P*2₁2₁2₁orthorhombic, *a* = 4.6392(2) Å, *b* = 12.5683(6) Å, *c* = 22.5157(11) Å, α = β = γ = 90°

Atom	Wyck.	x	y	z	occ.	B _{eq} (Å ²)
I1	4 <i>a</i>	0.1106(16)	0.6109(5)	0.1509(3)	1	2
I2	4 <i>a</i>	0.3911(16)	0.1044(5)	0.5284(3)	1	2
Pb1	4 <i>a</i>	0.4058(9)	0.2558(4)	0.4054(2)	1	2
I3	4 <i>a</i>	0.4681(13)	0.4072(5)	0.2997(3)	1	2

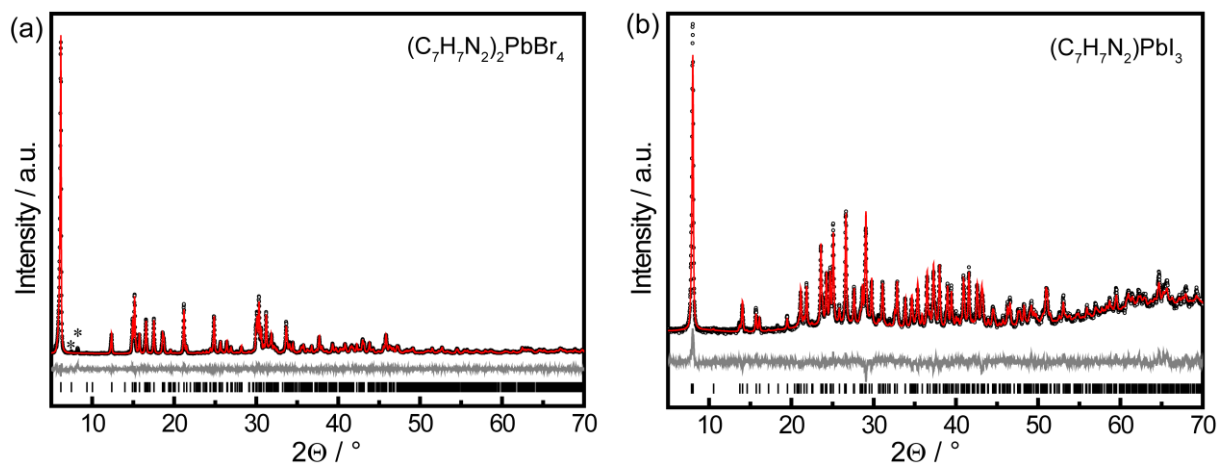
R_{exp} = 3.75 %, R_{wp} = 6.11 %, R_p = 4.84 %, R_{Bragg} = 4.63 %, GooF = 1.63**Solvent-free synthesis of (C₇H₇N₂)₂PbBr₄ and (C₇H₇N₂)PbI₃**

Figure S2. X-ray powder diffraction data of (C₇H₇N₂)₂PbBr₄ (a) and (C₇H₇N₂)PbI₃ (b) represented by black open circles. The Rietveld profile fit is displayed in red and the difference profile in grey. (C₇H₇N₂)₂PbBr₄ and (C₇H₇N₂)PbI₃ were obtained by grinding benzimidazole and PbX₂ (X = Br, I) with a few drops of the respective hydrohalic acid. The reflections attributed to a small impurity in (a) are marked with asterisks.

(C₇H₇N₂)₂PbBr₄radiation: Cu K_{α1}space group: *C2/c*monoclinic, $a = 35.9435(13) \text{ \AA}$, $b = 5.9577(2) \text{ \AA}$, $c = 23.7755(8) \text{ \AA}$, $\alpha = \gamma = 90^\circ$, $\beta = 127.2468(23)^\circ$

Atom	Wyck.	x	y	z	occ.	B _{eq} (Å ²)
Br1	8 <i>f</i>	0.1062(4)	0.4975(17)	0.0954(8)	1	0.76(44)
Br2	8 <i>f</i>	0.3965(5)	0.1005(17)	0.1583(8)	1	2.90(50)
Br3	8 <i>f</i>	0.4998(9)	0.0677(17)	0.1253(11)	1	2.90(30)
Br4	4 <i>e</i>	0	0.1030(19)	$\frac{1}{4}$	1	0.90(55)
Pb1	4 <i>e</i>	0	0.5934(12)	$\frac{1}{4}$	1	2.75(32)
Pb2	4 <i>b</i>	0	$\frac{1}{2}$	0	1	2.32(33)
Br5	4 <i>a</i>	0	0	0	1	2.02(59)

B_{eq}(C,N) = 2.06(50)R_{exp} = 6.04 %, R_{wp} = 9.39 %, R_p = 6.09 %, R_{Bragg} = 3.82 %, GooF = 1.55**(C₇H₇N₂)PbI₃**radiation: Cu K_{α1}space group: *P2₁2₁2₁*orthorhombic, $a = 4.6406(2) \text{ \AA}$, $b = 12.5757(5) \text{ \AA}$, $c = 22.5304(10) \text{ \AA}$, $\alpha = \beta = \gamma = 90^\circ$

Atom	Wyck.	x	y	z	occ.	B _{eq} (Å ²)
I1	4 <i>a</i>	0.1116(18)	0.6086(5)	0.1507(3)	1	9.26(25)
I2	4 <i>a</i>	0.3931(17)	0.1080(4)	0.5296(3)	1	5.27(19)
Pb1	4 <i>a</i>	0.4070(8)	0.2585(5)	0.4048(2)	1	7.48(14)
I3	4 <i>a</i>	0.4723(18)	0.4099(5)	0.3018(3)	1	10.49(26)

B_{eq}(C,N) = 11.69(98)R_{exp} = 4.05 %, R_{wp} = 5.33 %, R_p = 4.27 %, R_{Bragg} = 3.25 %, GooF = 1.31

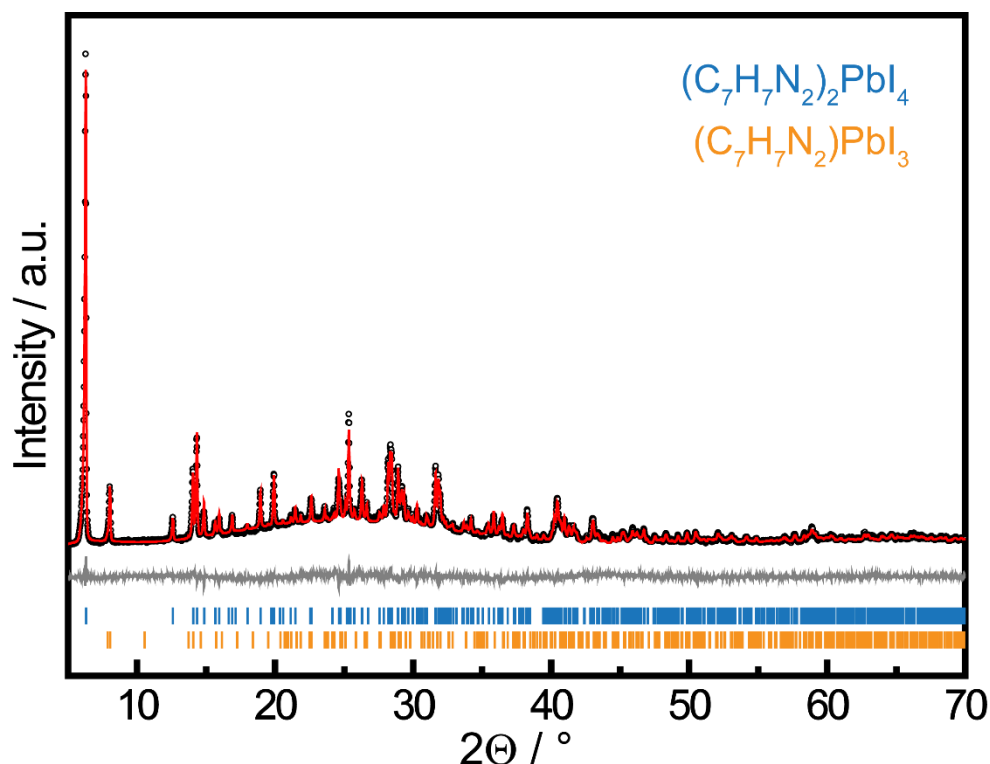
Synthesis of BzImPbI_{4/3}

Figure S3. X-ray powder diffraction data, represented by black open circles, of the reaction of $(C_7H_7N_2)I$ and $(C_7H_7N_2)PbI_3$ which were ground for 5 days in a vibratory ball mill. The Rietveld profile fit (red solid line) indicates that the resulting powder contains a 10:1 ratio of $(C_7H_7N_2)_2PbI_4$ (blue ticks) and $(C_7H_7N_2)PbI_3$ (orange ticks). The difference profile is displayed in grey.

BzImPbI_{4/3}radiation: Cu $K_{\alpha 1}$ $R_{exp} = 2.46 \%$, $R_{wp} = 4.40 \%$, $R_p = 3.48 \%$, $Goof = 1.79$ **Phase 1: $(C_7H_7N_2)_2PbI_4$** space group: $C2/c$ monoclinic, $a = 29.7994(10) \text{ \AA}$, $b = 6.3250(2) \text{ \AA}$, $c = 12.6433(4) \text{ \AA}$, $\alpha = \gamma = 90^\circ$, $\beta = 109.5371(24)^\circ$

Atom	Wyck.	x	y	z	occ.	$B_{eq} (\text{\AA}^2)$
I1	8f	0.3860(2)	0.0639(9)	0.1629(4)	1	4.58(18)
I2	4e	0	0.0409(12)	$\frac{1}{4}$	1	4.95(22)
Pb	4e	0	0.5422(11)	$\frac{1}{4}$	1	5.71(17)
I3	4b	0	$\frac{1}{2}$	0	1	3.99(23)

 $B_{eq}(C,N) = 9.08(79)$ $R_{Bragg} = 2.04 \%$

Phase 2: $(C_7H_7N_2)PbI_3$

space group: $P2_12_12_1$

orthorhombic, $a = 4.6420(5) \text{ \AA}$, $b = 12.5742(16) \text{ \AA}$, $c = 22.5279(35) \text{ \AA}$, $\alpha = \beta = \gamma = 90^\circ$

$R_{\text{Bragg}} = 2.14 \%$

B.4 Photograph of $BzImPbI_4/3$



Figure S4. Photograph of $(C_7H_7N_2)_2PbI_4$ and $(C_7H_7N_2)PbI_3$ in a ratio of 10 to 1 obtained by grinding $(C_7H_7N_2)I$ and $(C_7H_7N_2)PbI_3$ with a vibratory ball mill for 5 days.

B.5 EDX analysis

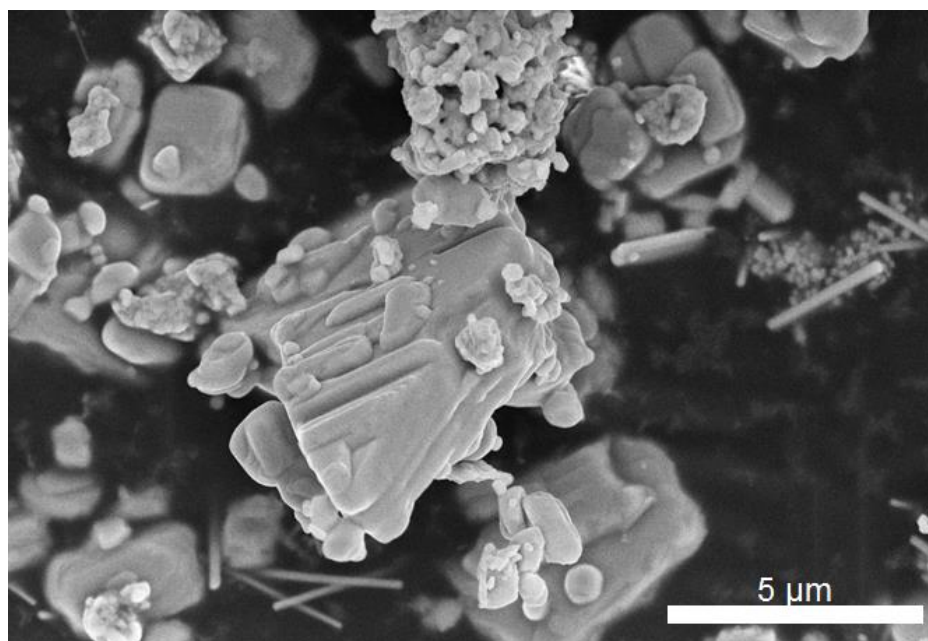


Figure S5. SEM image of $(\text{C}_7\text{H}_7\text{N}_2)_2\text{PbBr}_4$ obtained by a mechanochemical reaction showing Pb-rich needles as a small impurity.

Table XXIII. EDX measurements obtained from the two different morphologies observed for $(\text{C}_7\text{H}_7\text{N}_2)_2\text{PbBr}_4$ which was prepared by a mechanochemical reaction.

	Pb / at%	Br / at%
Needles	28	72
Crystals	23	77

It is not possible to deconvolute the EDX bromine L-line (1.48 keV) and aluminium K-line (1.48 keV). Aluminium shows up in some of the spectra as weak feature due to the sample holder used for the SEM measurements.

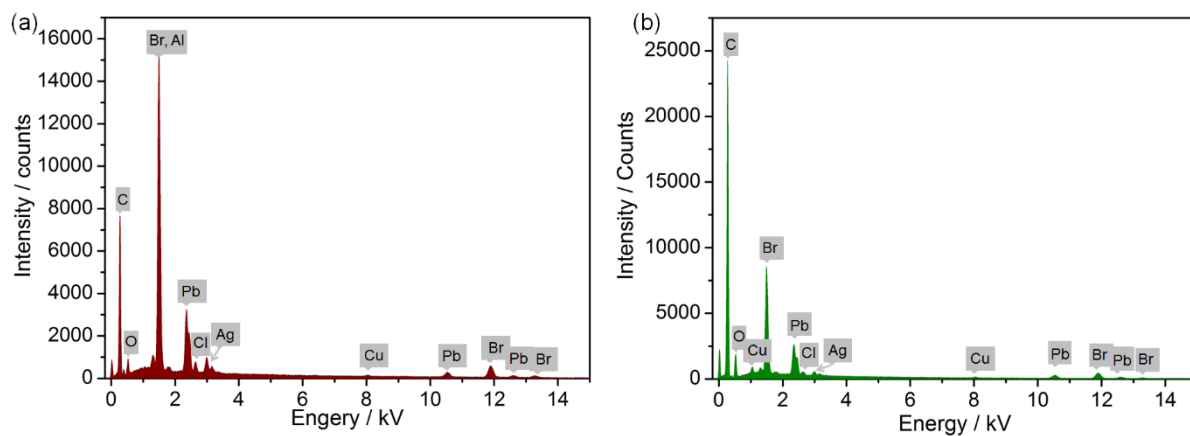


Figure S6. EDX spectra of the different morphologies observed in the $(\text{C}_7\text{H}_7\text{N}_2)_2\text{PbBr}_4$ sample obtained by a mechanochemical reaction: (a) EDX spectrum of the major phase; (b) EDX spectrum of the side phase featuring a needle-like morphology.

B.6 Solid-state NMR spectroscopy – Assignment of chemical shifts

The signals in the ^1H spectra were assigned on the basis of NMR studies on neutral benzimidazole dissolved in DMSO-d_6 , reporting chemical shifts of 12.44 (N-H), 8.20 ($\text{C}_2\text{-H}$), 7.58 ($\text{C}_{4/7}\text{-H}$) and 7.17 ($\text{C}_{5/6}\text{-H}$)¹. The assignment of the signals in the ^{13}C and ^{15}N spectra is indicated in Figure S7.

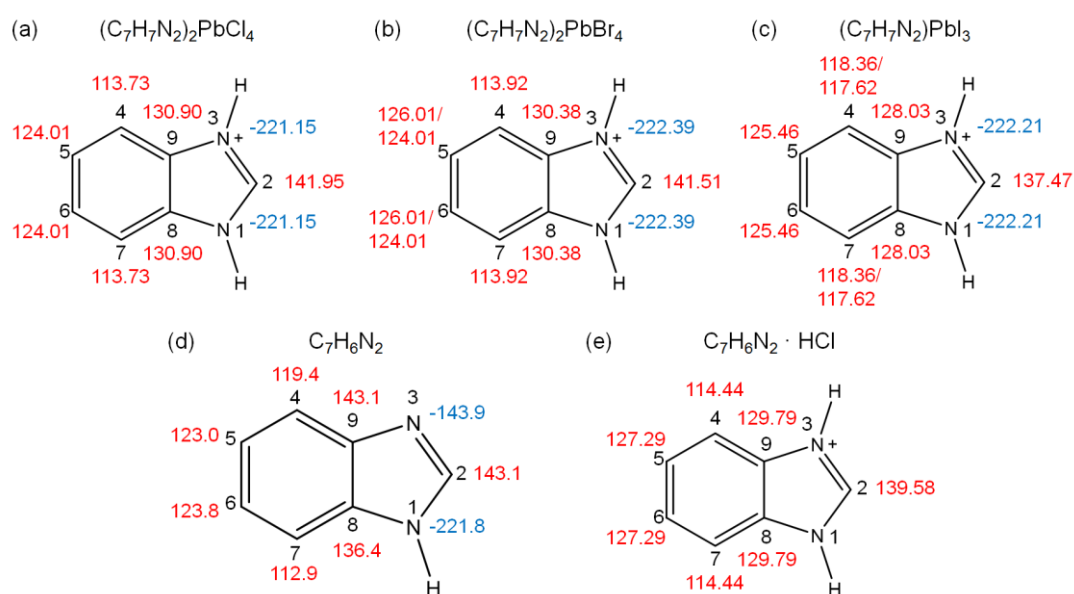


Figure S7. Assignment of the ^{13}C chemical shifts (red) and ^{15}N chemical shifts (blue) obtained from ^{13}C CP MAS and ^{15}N CP MAS solid-state NMR spectroscopy measurements for $(\text{C}_7\text{H}_7\text{N}_2)_2\text{PbCl}_4$ (a), $(\text{C}_7\text{H}_7\text{N}_2)_2\text{PbBr}_4$ (b) and $(\text{C}_7\text{H}_7\text{N}_2)\text{PbI}_3$ (c) based on ^{13}C CP MAS and ^{15}N CP MAS NMR studies on neutral benzimidazole¹ (d) and solution-state NMR studies on a saturated solution of aqueous benzimidazole hydrochloride² (e).

B.7 Absorption measurements

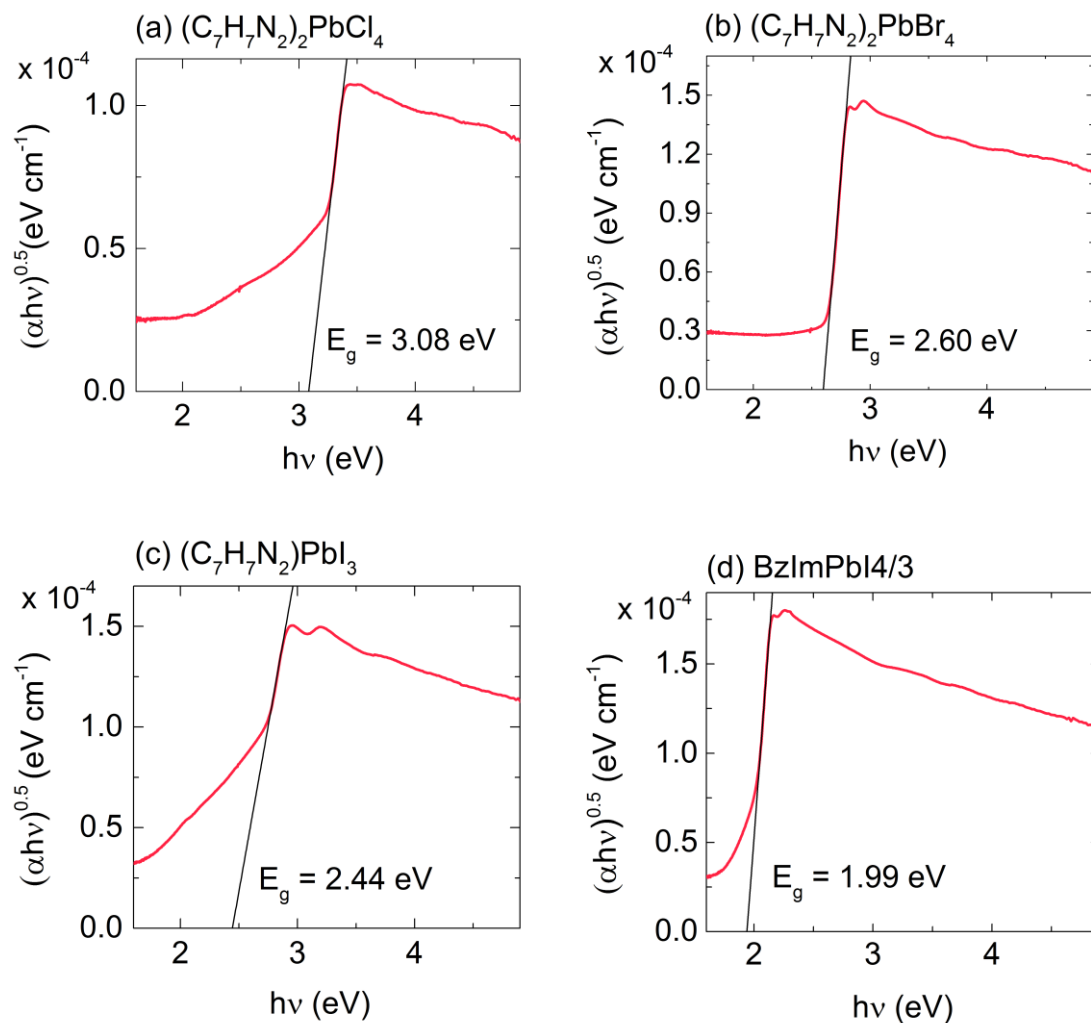


Figure S8. Tauc plots and resulting bandgaps E_g for (a) $(\text{C}_7\text{H}_7\text{N}_2)_2\text{PbCl}_4$, (b) $(\text{C}_7\text{H}_7\text{N}_2)_2\text{PbBr}_4$, (c) $(\text{C}_7\text{H}_7\text{N}_2)_2\text{PbI}_3$ and (d) $(\text{BzImPbI}_4/3)$. Tauc plots were analyzed for an indirect bandgap.

B.8 Thermal analysis

Thermogravimetric analysis suggests a 1-step thermal degradation mechanism for $(C_7H_7N_2)_2PbCl_4$, $(C_7H_7N_2)_2PbBr_4$ and $(C_7H_7N_2)_2PbI_3$. Gravimetric analysis suggests that the respective benzimidazolium halide is completely released between 245 – 410 °C for $(C_7H_7N_2)_2PbCl_4$ (mass loss (2 $(C_7H_7N_2)Cl$) *observed*: 50.22%, *calculated*: 52.65%), in the range of 240 °C – 480 °C for $(C_7H_7N_2)_2PbBr_4$ (mass loss (2 $(C_7H_7N_2)Br$) *observed*: 50.35%, *calculated*: 52.03%) and between 300 °C and 510 °C for $(C_7H_7N_2)_2PbI_3$ (mass loss $((C_7H_7N_2)I)$ *observed*: 34.74%, *calculated*: 34.80%), thus revealing similar thermal stabilities for the chloride and bromide and slightly higher ones for the iodide. The evaporation of the corresponding lead halide happens in a subsequent step. The endothermic signals in the thermal analysis trace which coincide with the beginning of each mass loss are most likely attributed to the release of $(C_7H_7N_2)X$ and PbX_2 ($X = Cl, Br, I$), respectively (Figure S9).

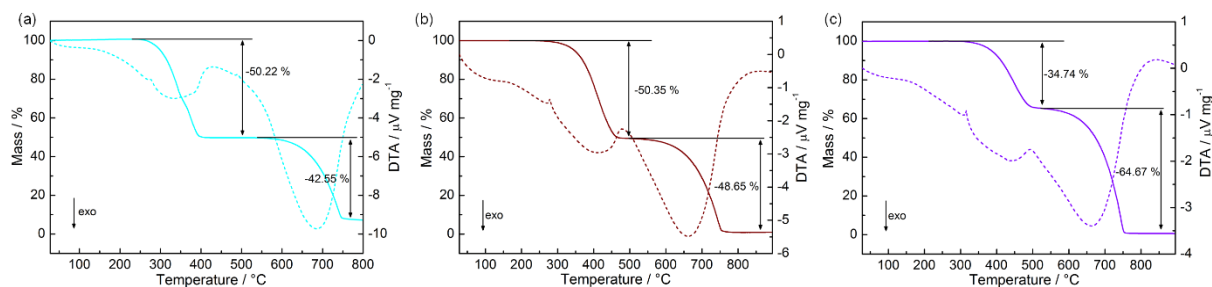


Figure S9. TG (solid lines) and DTA (dashed lines) data $(C_7H_7N_2)_2PbCl_4$ (a), $(C_7H_7N_2)_2PbBr_4$ (b) and $(C_7H_7N_2)_2PbI_3$ (c).

B.9 References

1. Nieto, C. I.; Cabildo, P.; García, M. Á.; Claramunt, R. M.; Alkorta, I.; Elguero, J., An experimental and theoretical NMR study of NH-benzimidazoles in solution and in the solid state: proton transfer and tautomerism. *Beilstein J. Org. Chem.* **2014**, *10*, 1620-1629.
2. Pugmire, R. J.; Grant, D. M., Carbon-13 magnetic resonance. XIX. Benzimidazole, purine, and their anionic and cationic species. *J. Am. Chem. Soc.* **1971**, *93*, (8), 1880-1887.

C Supporting Information for Chapter 4

C.1 Crystallographic data for $(C_6H_{10}N_2)_6IPb_5I_{21} \cdot 3 H_2O$ at 296 K and 100 K

Table SI. Crystallographic data and details of the structure refinement for $(C_6H_{10}N_2)_6IPb_5I_{21} \cdot 3 H_2O$ at 296 K and 100 K (CCDC 1838614 and CCDC 1838610).

Formula		$(C_6H_{10}N_2)_6IPb_5I_{21} \cdot 3 H_2O$	
Molar mass (g mol ⁻¹)		4542.75	
Crystal system		Orthorhombic	
Space group		<i>Pnma</i> (no. 62)	
T (K)	296		100
Radiation, λ (Å)		Mo K α , 0.71073	
<i>a</i> (Å)	26.5785(9)		26.3268(8)
<i>b</i> (Å)	12.9273(5)		12.8308(4)
<i>c</i> (Å)	26.2839(9)		26.0929(8)
<i>V</i> (Å ³)	9030.8(6)		8814.0(5)
<i>Z</i>		4	
Calculated density (g cm ⁻³)	3.337		3.424
Crystal size (mm ³)	0.01 x 0.03 x 0.03		0.02 x 0.06 x 0.10
Absorption coefficient (mm ⁻¹)	16.847		17.261
F(000)	7840		7864
Absorption correction		multi-scan	
θ range	3.2° to 29.6°		3.1° to 26.4°
Index range	-36 ≤ <i>h</i> ≤ 33, -17 ≤ <i>k</i> ≤ 17, -36 ≤ <i>l</i> ≤ 36		-32 ≤ <i>h</i> ≤ 32, -16 ≤ <i>k</i> ≤ 16, -32 ≤ <i>l</i> ≤ 32
Parameters/restraints	391 / 36		398 / 4
Total No. of reflections	127102		155411
No. of independent reflections	13127 [R _{int} = 0.0470]		9446 [R _{int} = 0.0481]
No. of observed reflections	10894		8272
Min./max. residual electron density (e Å ⁻³)	-1.75 / 1.88		-1.26 / 1.20
GooF	1.07		1.05
wR2	0.0579 ^a		0.0353 ^b
R1 (for observed reflections)	0.0274		0.0181

^a $w = [\sigma^2(F_0^2) + (0.0131P)^2 + 40.9896P]^{-1}$, with $P = (F_0^2 + 2F_c^2)/3$

^b $w = [\sigma^2(F_0^2) + (0.0145P)^2 + 18.7051P]^{-1}$, with $P = (F_0^2 + 2F_c^2)/3$

Table SII. Atomic coordinates and equivalent isotropic displacement parameters for $(C_6H_{10}N_2)_6IPb_5I_{21} \cdot 3 H_2O$ at 296 K with standard deviations in parentheses. $U(eq)$ is defined as one third of the trace of the orthogonalized U tensor.

Atom	Wyck.	x	y	z	$U(eq) / \text{\AA}^2$
Pb1	4c	0.42970(2)	$\frac{3}{4}$	0.17050(2)	0.0300(1)
Pb2	4c	0.44579(2)	$\frac{1}{4}$	0.17386(2)	0.0323(1)
Pb3	4c	0.62899(2)	$\frac{1}{4}$	0.21411(2)	0.0330(1)
Pb4	4c	0.34966(2)	$\frac{1}{4}$	0.39701(2)	0.0302(1)
Pb5	4c	0.33546(2)	$\frac{3}{4}$	0.39968(2)	0.0313(1)
I1	4c	0.31873(2)	$\frac{3}{4}$	0.13554(2)	0.0453(2)
I2	4c	0.40625(2)	$\frac{3}{4}$	0.28780(2)	0.0507(2)
I3	4c	0.47132(2)	$\frac{3}{4}$	0.05221(2)	0.0388(2)
I4	4c	0.54705(2)	$\frac{3}{4}$	0.19656(2)	0.0353(1)
I5	8d	0.43765(2)	0.49918(3)	0.17675(2)	0.0441(1)
I6	4c	0.38337(2)	$\frac{1}{4}$	0.06901(2)	0.0512(2)
I7	4c	0.35736(2)	$\frac{1}{4}$	0.25791(2)	0.0453(2)
I8	4c	0.55230(2)	$\frac{1}{4}$	0.11034(2)	0.0431(2)
I9	4c	0.51969(2)	$\frac{1}{4}$	0.26946(2)	0.0410(1)
I10	4c	0.68651(2)	$\frac{1}{4}$	0.31413(2)	0.0542(2)
I11	4c	0.72575(2)	$\frac{1}{4}$	0.14252(2)	0.0482(2)
I12	8d	0.63222(2)	0.49623(3)	0.21932(2)	0.0463(1)
I13	4c	0.46010(2)	$\frac{1}{4}$	0.42046(2)	0.0421(2)
I14	4c	0.32277(2)	$\frac{1}{4}$	0.50820(2)	0.0470(2)
I15	8d	0.34430(2)	0.50071(3)	0.38918(2)	0.0481(1)
I16	4c	0.22452(3)	$\frac{3}{4}$	0.35038(3)	0.0625(2)
I17	4c	0.28649(2)	$\frac{3}{4}$	0.50279(2)	0.0529(2)
I18	4c	0.44317(2)	$\frac{3}{4}$	0.45253(2)	0.0411(2)
I19	4c	0.41495(2)	$\frac{1}{4}$	0.64711(2)	0.0431(2)
O1	4c	0.3132(2)	$\frac{1}{4}$	0.7253(2)	0.0447(17)
O2	8d	0.47973(19)	0.4409(4)	0.03987(19)	0.0643(17)
N1	8d	0.5149(2)	0.5501(4)	0.29373(19)	0.0517(17)
N2	8d	0.5267(2)	0.5507(4)	0.4246(2)	0.0503(17)
C1	8d	0.4925(2)	0.5099(5)	0.3407(2)	0.050(2)
C2	8d	0.5307(2)	0.4939(4)	0.3822(2)	0.0400(17)
C3	8d	0.5696(2)	0.4239(4)	0.3793(2)	0.0433(17)
C4	8d	0.6020(2)	0.4138(5)	0.4200(3)	0.050(2)
C5	8d	0.5962(3)	0.4735(6)	0.4624(2)	0.057(2)
C6	8d	0.5585(3)	0.5436(6)	0.4636(2)	0.060(3)
N3	8d	0.2326(2)	0.5423(5)	0.7779(2)	0.0540(19)
N4	8d	0.27463(17)	0.4285(4)	0.67425(18)	0.0387(14)

Table SII. Continuation.

C7	<i>8d</i>	0.2136(3)	0.4636(5)	0.7419(2)	0.0513(19)
C8	<i>8d</i>	0.2342(2)	0.4832(4)	0.6897(2)	0.0383(17)
C9	<i>8d</i>	0.2127(2)	0.5505(4)	0.6559(2)	0.0417(17)
C10	<i>8d</i>	0.2329(2)	0.5616(5)	0.6074(2)	0.0487(19)
C11	<i>8d</i>	0.2739(2)	0.5036(5)	0.5940(2)	0.0457(19)
C12	<i>8d</i>	0.2942(2)	0.4362(5)	0.6276(2)	0.0450(17)
N5	<i>8d</i>	0.0555(2)	0.5438(4)	0.3928(2)	0.0520(17)
N6	<i>8d</i>	0.1141(2)	0.4829(5)	0.4912(2)	0.0687(19)
C13	<i>8d</i>	0.0958(2)	0.5990(5)	0.4203(2)	0.049(2)
C14	<i>8d</i>	0.1299(2)	0.5273(4)	0.4485(2)	0.0400(16)
C15	<i>8d</i>	0.1782(3)	0.5129(7)	0.4343(3)	0.072(3)
C16	<i>8d</i>	0.2083(3)	0.4442(8)	0.4627(3)	0.078(3)
C17	<i>8d</i>	0.1906(3)	0.3994(6)	0.5050(3)	0.074(2)
C18	<i>8d</i>	0.1435(3)	0.4196(7)	0.5198(3)	0.082(3)
H1A	<i>8d</i>	0.5298(17)	0.616(3)	0.3003(5)	0.0780
H1B	<i>8d</i>	0.4894(10)	0.557(4)	0.2683(12)	0.0780
H1C	<i>8d</i>	0.5402(16)	0.503(3)	0.2820(11)	0.0780
H1D	<i>8d</i>	0.47600	0.44460	0.33340	0.0600
H1E	<i>8d</i>	0.46700	0.55800	0.35250	0.0600
H2	<i>8d</i>	0.50230	0.59410	0.42680	0.0600
H3	<i>8d</i>	0.57400	0.38390	0.35030	0.0520
H4A	<i>8d</i>	0.62810	0.36590	0.41850	0.0610
H5	<i>8d</i>	0.61770	0.46600	0.49010	0.0680
H6A	<i>8d</i>	0.55480	0.58690	0.49160	0.0730
H3A	<i>8d</i>	0.2691(15)	0.535(2)	0.7818(14)	0.0810
H3B	<i>8d</i>	0.2162(15)	0.533(2)	0.8110(14)	0.0810
H3C	<i>8d</i>	0.2250(16)	0.612(3)	0.7647(10)	0.0810
H4	<i>8d</i>	0.28850	0.38670	0.69550	0.0470
H7A	<i>8d</i>	0.17720	0.46590	0.74100	0.0610
H7B	<i>8d</i>	0.22370	0.39530	0.75330	0.0610
H9	<i>8d</i>	0.18460	0.58880	0.66530	0.0500
H10	<i>8d</i>	0.21880	0.60790	0.58440	0.0580
H11	<i>8d</i>	0.28770	0.51050	0.56170	0.0540
H12	<i>8d</i>	0.32160	0.39560	0.61840	0.0540
H5A	<i>8d</i>	0.0701(6)	0.489(3)	0.3723(16)	0.0780
H5B	<i>8d</i>	0.0378(13)	0.592(2)	0.3708(16)	0.0780
H5C	<i>8d</i>	0.0320(13)	0.514(3)	0.4172(9)	0.0780
H6	<i>8d</i>	0.08390	0.49480	0.50120	0.0820
H13A	<i>8d</i>	0.08080	0.64710	0.44420	0.0580
H13B	<i>8d</i>	0.11550	0.63880	0.39610	0.0580
H15	<i>8d</i>	0.19130	0.54760	0.40630	0.0860
H16	<i>8d</i>	0.24080	0.42980	0.45190	0.0940
H17	<i>8d</i>	0.21080	0.35480	0.52380	0.0890
H18	<i>8d</i>	0.13100	0.39040	0.54960	0.0990

Table SIII. (An)isotropic displacement parameters for $(C_6H_{10}N_2)_6IPb_5I_{21} \cdot 3 H_2O$ at 296 K with standard deviations in parentheses.

Atom	U ₁₁	U ₂₂	U ₃₃	U ₂₃	U ₁₃	U ₁₂
Pb1	0.0329(1)	0.0261(1)	0.0309(1)	0	0.0022(1)	0
Pb2	0.0332(1)	0.0259(1)	0.0378(1)	0	-0.0005(1)	0
Pb3	0.0284(1)	0.0318(1)	0.0389(1)	0	0.0001(1)	0
Pb4	0.0327(1)	0.0255(1)	0.0324(1)	0	-0.0037(1)	0
Pb5	0.0387(2)	0.0252(1)	0.0301(1)	0	-0.0004(1)	0
I1	0.0321(3)	0.0430(3)	0.0607(3)	0	0.0016(2)	0
I2	0.0639(4)	0.0587(3)	0.0296(2)	0	0.0126(2)	0
I3	0.0423(3)	0.0429(3)	0.0312(2)	0	0.0004(2)	0
I4	0.0366(3)	0.0335(2)	0.0358(2)	0	-0.0038(2)	0
I5	0.0500(2)	0.0219(2)	0.0604(2)	-0.0011(2)	0.0022(2)	-0.0024(1)
I6	0.0435(3)	0.0537(3)	0.0563(3)	0	-0.0136(3)	0
I7	0.0403(3)	0.0482(3)	0.0473(3)	0	0.0117(2)	0
I8	0.0421(3)	0.0524(3)	0.0348(3)	0	-0.0009(2)	0
I9	0.0331(2)	0.0585(3)	0.0313(2)	0	-0.0011(2)	0
I10	0.0603(4)	0.0521(3)	0.0501(3)	0	-0.0227(3)	0
I11	0.0365(3)	0.0567(3)	0.0514(3)	0	0.0111(2)	0
I12	0.0449(2)	0.0308(2)	0.0631(2)	0.0011(2)	-0.0055(2)	0.0048(2)
I13	0.0299(2)	0.0527(3)	0.0436(3)	0	0.0012(2)	0
I14	0.0487(3)	0.0571(3)	0.0352(3)	0	0.0048(2)	0
I15	0.0657(3)	0.0231(2)	0.0554(2)	0.0002(2)	-0.0091(2)	-0.0006(2)
I16	0.0489(3)	0.0844(5)	0.0541(4)	0	-0.0208(3)	0
I17	0.0571(4)	0.0673(4)	0.0342(3)	0	0.0118(2)	0
I18	0.0320(3)	0.0414(3)	0.0499(3)	0	-0.0040(2)	0
I19	0.0425(3)	0.0425(3)	0.0443(3)	0	0.0020(2)	0
O1	0.047(3)	0.046(3)	0.041(3)	0	0.002(3)	0
O2	0.067(3)	0.061(3)	0.065(3)	0.011(2)	0.000(2)	0.003(3)
N1	0.052(3)	0.057(3)	0.046(3)	0.002(3)	-0.014(2)	-0.001(3)
N2	0.061(3)	0.040(3)	0.050(3)	0.000(2)	0.018(3)	0.007(2)
C1	0.036(3)	0.055(4)	0.059(4)	0.011(3)	-0.001(3)	0.002(3)
C2	0.037(3)	0.036(3)	0.047(3)	0.004(2)	0.002(2)	-0.002(2)
C3	0.044(3)	0.038(3)	0.048(3)	-0.007(3)	-0.004(3)	0.003(2)
C4	0.047(4)	0.043(3)	0.061(4)	0.002(3)	-0.012(3)	0.001(3)
C5	0.073(5)	0.059(4)	0.038(3)	0.007(3)	-0.007(3)	-0.010(4)
C6	0.091(6)	0.057(4)	0.033(3)	-0.005(3)	0.012(3)	-0.014(4)
N3	0.048(3)	0.068(4)	0.046(3)	-0.006(3)	0.004(2)	0.002(3)
N4	0.035(2)	0.038(2)	0.043(3)	0.001(2)	-0.004(2)	0.0032(19)
C7	0.058(4)	0.049(3)	0.047(3)	-0.002(3)	0.006(3)	-0.009(3)
C8	0.038(3)	0.034(3)	0.043(3)	-0.001(2)	-0.002(2)	-0.003(2)
C9	0.040(3)	0.039(3)	0.046(3)	-0.001(2)	-0.001(2)	0.008(2)
C10	0.050(4)	0.046(3)	0.050(3)	0.009(3)	-0.009(3)	0.000(3)
C11	0.047(3)	0.055(4)	0.035(3)	0.000(3)	0.006(2)	-0.004(3)

Table III. Continuation.

C12	0.035(3)	0.052(3)	0.048(3)	-0.010(3)	0.002(2)	0.005(3)
N5	0.052(3)	0.051(3)	0.053(3)	0.010(3)	-0.008(2)	0.009(3)
N6	0.046(3)	0.091(4)	0.069(3)	0.033(3)	0.005(2)	-0.002(3)
C13	0.051(4)	0.042(3)	0.053(4)	0.005(3)	-0.002(3)	0.007(3)
C14	0.041(2)	0.036(3)	0.043(3)	-0.0015(19)	0.001(2)	0.003(2)
C15	0.046(3)	0.120(7)	0.049(4)	0.006(3)	0.009(2)	0.016(4)
C16	0.050(3)	0.112(6)	0.073(4)	-0.018(3)	-0.007(3)	0.032(3)
C17	0.078(3)	0.061(4)	0.084(4)	-0.003(3)	-0.031(3)	0.014(3)
C18	0.063(3)	0.094(5)	0.089(5)	0.051(4)	-0.017(3)	-0.021(3)

Table SIV. Bond distances for $(C_6H_{10}N_2)_6IPb_5I_{21} \cdot 3 H_2O$ at 296 K with standard deviations in parentheses.

Bond	Distance / Å	Bond	Distance / Å
Pb1-I1	3.0892(8)	Pb5-I18	3.1820(8)
Pb1-I2	3.1455(8)	Pb5-I15^f	3.2430(4)
Pb1-I3	3.3001(8)	N1-C1	1.466(7)
Pb1-I4	3.1933(8)	N2-C2	1.339(7)
Pb1-I5	3.2535(4)	N2-C6	1.332(8)
Pb1-I5^f	3.2535(4)	N1-H1C	0.96(4)
Pb2-I5	3.2294(4)	N1-H1A	0.96(4)
Pb2-I6	3.2167(8)	N1-H1B	0.96(3)
Pb2-I7	3.2256(8)	N2-H2	0.8600
Pb2-I8	3.2865(8)	N3-C7	1.478(9)
Pb2-I9	3.1893(8)	N4-C12	1.336(7)
Pb2-I5^e	3.2294(4)	N4-C8	1.349(7)
Pb3-I8	3.4050(8)	N3-H3C	0.99(4)
Pb3-I9	3.2490(8)	N3-H3A	0.98(4)
Pb3-I10	3.0411(8)	N3-H3B	0.98(4)
Pb3-I11	3.1866(8)	N4-H4	0.8600
Pb3-I12	3.1872(4)	N5-C13	1.476(8)
Pb3-I12^e	3.1872(4)	N6-C18	1.358(10)
Pb4-I7	3.6618(8)	N6-C14	1.329(8)
Pb4-I13	2.9993(8)	N5-H5C	0.98(3)
Pb4-I14	3.0086(8)	N5-H5A	0.97(4)
Pb4-I15	3.2507(4)	N5-H5B	0.97(3)
Pb4-I11^a	3.4534(8)	N6-H6	0.8600
Pb4-I15^e	3.2507(4)	C1-C2	1.505(7)
Pb5-I2	3.4910(8)	C2-C3	1.376(7)
Pb5-I15	3.2430(4)	C3-C4	1.380(9)
Pb5-I16	3.2208(10)	C4-C5	1.364(10)
Pb5-I17	3.0065(8)	C5-C6	1.351(11)

Table SIV. Continuation.

C1-H1D	0.9700	C10-H10	0.9300
C1-H1E	0.9700	C11-H11	0.9300
C3-H3	0.9300	C12-H12	0.9300
C4-H4A	0.9300	C13-C14	1.493(8)
C5-H5	0.9300	C14-C15	1.350(10)
C6-H6A	0.9300	C15-C16	1.409(12)
C7-C8	1.499(8)	C16-C17	1.339(12)
C8-C9	1.369(7)	C17-C18	1.337(11)
C9-C10	1.391(7)	C13-H13A	0.9700
C10-C11	1.369(8)	C13-H13B	0.9700
C11-C12	1.353(8)	C15-H15	0.9300
C7-H7B	0.9700	C16-H16	0.9300
C7-H7A	0.9700	C17-H17	0.9300
C9-H9	0.9300	C18-H18	0.9300

$$a = -\frac{1}{2}x, \frac{1}{2}y, \frac{1}{2}z; e = x, \frac{1}{2}y, z; f = x, \frac{3}{2}y, z$$

Table SV. Bond angles for $(C_6H_{10}N_2)_6IPb_5I_{21} \cdot 3 H_2O$ at 296 K with standard deviations in parentheses.

Bond	Angle / °	Bond	Angle / °
I1-Pb1-I2	95.88(2)	I5^e-Pb2-I8	93.99(1)
I1-Pb1-I3	92.28(2)	I5^e-Pb2-I9	91.30(1)
I1-Pb1-I4	175.08(2)	I8-Pb3-I9	79.83(2)
I1-Pb1-I5	94.42(1)	I8-Pb3-I10	173.41(2)
I1-Pb1-I5^f	94.42(1)	I8-Pb3-I11	90.58(2)
I2-Pb1-I3	171.84(2)	I8-Pb3-I12	92.90(1)
I2-Pb1-I4	89.04(2)	I8-Pb3-I12^e	92.90(1)
I2-Pb1-I5	87.90(1)	I9-Pb3-I10	93.58(2)
I2-Pb1-I5^f	87.90(1)	I9-Pb3-I11	170.41(2)
I3-Pb1-I4	82.80(2)	I9-Pb3-I12	90.28(1)
I3-Pb1-I5	91.48(1)	I9-Pb3-I12^e	90.28(1)
I3-Pb1-I5^f	91.48(1)	I10-Pb3-I11	96.01(2)
I4-Pb1-I5	85.74(1)	I10-Pb3-I12	87.10(1)
I4-Pb1-I5^f	85.74(1)	I10-Pb3-I12^e	87.10(1)
I5-Pb1-I5^f	170.56(2)	I11-Pb3-I12	90.21(1)
I5-Pb2-I6	89.18(1)	I11-Pb3-I12^e	90.21(1)
I5-Pb2-I7	86.28(1)	I12-Pb3-I12^e	174.19(2)
I5-Pb2-I8	93.99(1)	I7-Pb4-I13	98.66(2)
I5-Pb2-I9	91.30(1)	I7-Pb4-I14	169.46(2)
I5-Pb2-I5^e	171.86(2)	I7-Pb4-I15	86.52(1)
I6-Pb2-I7	102.18(2)	I7-Pb4-I11^a	75.69(2)
I6-Pb2-I8	90.52(2)	I7-Pb4-I15^e	86.52(1)

Table SV. Continuation

I6-Pb2-I9	173.03(2)	I13-Pb4-I14	91.88(2)
I5^e-Pb2-I6	89.18(1)	I13-Pb4-I15	93.21(1)
I7-Pb2-I8	167.30(2)	I11^a-Pb4-I13	174.35(2)
I7-Pb2-I9	84.79(2)	I13-Pb4-I15^e	93.21(1)
I5^e-Pb2-I7	86.28(1)	I14-Pb4-I15	92.93(1)
I8-Pb2-I9	82.52(2)	I11^a-Pb4-I14	93.77(2)
I14-Pb4-I15^e	92.93(1)	C1-N1-H1A	109.4(12)
I11^a-Pb4-I15	86.51(1)	C1-N1-H1B	110(2)
I15-Pb4-I15^e	171.17(2)	H1B-N1-H1C	109(3)
I11^a-Pb4-I15^e	86.51(1)	H1A-N1-H1B	110(4)
I2-Pb5-I15	83.64(1)	H1A-N1-H1C	110(4)
I2-Pb5-I16	98.89(2)	C6-N2-H2	118.00
I2-Pb5-I17	173.04(2)	C2-N2-H2	118.00
I2-Pb5-I18	83.27(2)	C8-N4-C12	123.2(5)
I2-Pb5-I15^f	83.64(1)	H3A-N3-H3B	110(3)
I15-Pb5-I16	91.84(1)	C7-N3-H3B	109.4(19)
I15-Pb5-I17	96.21(1)	C7-N3-H3C	109.5(19)
I15-Pb5-I18	88.39(1)	H3B-N3-H3C	110(3)
I15-Pb5-I15^f	167.17(2)	H3A-N3-H3C	109(3)
I16-Pb5-I17	88.07(2)	C7-N3-H3A	109.8(19)
I16-Pb5-I18	177.84(3)	C8-N4-H4	118.00
I15^f-Pb5-I16	91.84(1)	C12-N4-H4	118.00
I17-Pb5-I18	89.77(2)	C14-N6-C18	123.1(6)
I15^f-Pb5-I17	96.21(1)	C13-N5-H5B	109.4(19)
I15^f-Pb5-I18	88.39(1)	C13-N5-H5C	109.5(18)
Pb1-I2-Pb5	158.82(2)	H5B-N5-H5C	110(3)
Pb1-I5-Pb2	175.76(2)	H5A-N5-H5B	109(3)
Pb2-I7-Pb4	136.43(2)	C13-N5-H5A	109.5(14)
Pb2-I8-Pb3	96.24(2)	H5A-N5-H5C	109(3)
Pb2-I9-Pb3	101.41(2)	C14-N6-H6	118.00
Pb3-I11-Pb4^b	161.32(2)	C18-N6-H6	118.00
Pb4-I15-Pb5	171.33(2)	N1-C1-C2	112.7(4)
C2-N2-C6	123.5(6)	N2-C2-C1	118.3(5)
C1-N1-H1C	109(2)	C1-C2-C3	123.9(5)
N2-C2-C3	117.8(5)	N3-C7-H7B	110.00
C2-C3-C4	119.2(5)	N3-C7-H7A	110.00
C3-C4-C5	120.6(6)	H7A-C7-H7B	108.00
C4-C5-C6	118.8(6)	C10-C9-H9	120.00
N2-C6-C5	119.9(6)	C8-C9-H9	120.00
C2-C1-H1D	109.00	C11-C10-H10	120.00
N1-C1-H1E	109.00	C9-C10-H10	120.00
C2-C1-H1E	109.00	C10-C11-H11	120.00
H1D-C1-H1E	108.00	C12-C11-H11	120.00
N1-C1-H1D	109.00	N4-C12-H12	120.00

Table SV. Continuation

C4-C3-H3	120.00	C11-C12-H12	120.00
C2-C3-H3	120.00	N5-C13-C14	112.5(5)
C5-C4-H4A	120.00	N6-C14-C15	118.3(6)
C3-C4-H4A	120.00	C13-C14-C15	121.7(6)
C4-C5-H5	121.00	N6-C14-C13	119.7(5)
C6-C5-H5	120.00	C14-C15-C16	118.7(7)
N2-C6-H6A	120.00	C15-C16-C17	120.9(7)
C5-C6-H6A	120.00	C16-C17-C18	119.1(8)
N3-C7-C8	110.2(5)	N6-C18-C17	119.7(7)
C7-C8-C9	123.3(5)	N5-C13-H13A	109.00
N4-C8-C7	118.6(5)	N5-C13-H13B	109.00
N4-C8-C9	118.1(5)	C14-C13-H13A	109.00
C8-C9-C10	120.0(5)	C14-C13-H13B	109.00
C9-C10-C11	119.1(5)	H13A-C13-H13B	108.00
C10-C11-C12	120.2(5)	C14-C15-H15	121.00
N4-C12-C11	119.5(5)	C16-C15-H15	121.00
C8-C7-H7A	110.00	C15-C16-H16	120.00
C8-C7-H7B	110.00	C17-C16-H16	120.00
C16-C17-H17	120.00	N6-C18-H18	120.00
C18-C17-H17	120.00	C17-C18-H18	120.00

$$a = -\frac{1}{2}x, \frac{1}{2}y, \frac{1}{2}z; b = \frac{1}{2}x, \frac{1}{2}y, \frac{1}{2}z; e = x, \frac{1}{2}y, z; f = x, \frac{3}{2}y, z$$

Table SVI. Hydrogen bond distances (in Å) and angles (in °) for $(C_6H_{10}N_2)_6IPb_5I_{21} \cdot 3 H_2O$ at 296 K with standard deviations in parentheses.

D-H...A	H...A	D...A	∠D-H...A
N1-H1A...I4	3.26	3.732(5)	112.4
N1-H1A...I19^u	2.66	3.545(5)	154.5
N1-H1B...I5	2.87	3.756(5)	154.2
N1-H1C...I12	2.95	3.745(6)	141.5
N2-H2...I18	2.64	3.479(5)	164.4
N3-H3A...I12^u	2.65	3.629(5)	172.8
N3-H3B...I15ⁱⁱ	2.65	3.612(5)	168.3
N3-H3C...I7ⁱⁱ	2.83	3.633(6)	139.2
N4-H4...O1	2.04	2.860(6)	158.6
N5-H5A...I8^c	3.16	3.800(6)	125.1
N5-H5A...I12^c	2.92	3.636(6)	131.1
N5-H5B...I4^c	2.71	3.560(5)	145.7
N5-H5B...I5^c	3.18	3.672(5)	113.5
N5-H5C...O2^c	2.03	2.993(8)	172.3
N6-H6...O2ⁱⁱ	2.14	2.971(8)	162.4

$$c = -\frac{1}{2}x, y, \frac{1}{2}z; u = 1-x, 1-y, 1-z; ii = \frac{1}{2}-x, 1-y, \frac{1}{2}+z$$

Table SVII. Atomic coordinates and equivalent isotropic displacement parameters for $(C_6H_{10}N_2)_6IPb_5I_{21} \cdot 3 H_2O$ at 100 K with standard deviations in parentheses. $U(eq)$ is defined as one third of the trace of the orthogonalized U tensor.

Atom	Wyck.	x	y	z	$U(eq) / \text{\AA}^2$
Pb1	4c	0.42908(2)	$\frac{3}{4}$	0.17118(2)	0.0101(1)
Pb2	4c	0.44601(2)	1/4	0.17466(2)	0.0110(1)
Pb3	4c	0.62883(2)	1/4	0.21410(2)	0.0112(1)
Pb4	4c	0.35015(2)	1/4	0.39697(2)	0.0099(1)
Pb5	4c	0.33484(2)	$\frac{3}{4}$	0.39960(2)	0.0107(1)
I1	4c	0.40727(2)	$\frac{3}{4}$	0.28796(2)	0.0170(1)
I2	4c	0.54750(2)	$\frac{3}{4}$	0.19549(2)	0.0119(1)
I3	4c	0.47170(2)	$\frac{3}{4}$	0.05057(2)	0.0125(1)
I4	4c	0.31749(2)	$\frac{3}{4}$	0.13588(2)	0.0145(1)
I5	8d	0.43696(2)	0.49920(2)	0.17608(2)	0.0142(1)
I6	4c	0.55230(2)	$\frac{1}{4}$	0.11089(2)	0.0141(1)
I7	4c	0.38333(2)	$\frac{1}{4}$	0.06817(2)	0.0174(1)
I8	4c	0.35599(2)	$\frac{1}{4}$	0.25833(2)	0.0148(1)
I9	4c	0.51901(2)	$\frac{1}{4}$	0.27033(2)	0.0141(1)
I10	8d	0.63169(2)	0.49701(2)	0.21855(2)	0.0150(1)
I11	4c	0.72512(2)	$\frac{1}{4}$	0.14114(2)	0.0167(1)
I12	4c	0.68708(2)	$\frac{1}{4}$	0.31478(2)	0.0180(1)
I13	4c	0.46146(2)	$\frac{1}{4}$	0.42031(2)	0.0137(1)
I14	4c	0.32376(2)	$\frac{1}{4}$	0.50921(2)	0.0166(1)
I15	8d	0.34434(2)	0.50069(2)	0.38934(2)	0.0163(1)
I16	4c	0.44287(2)	$\frac{3}{4}$	0.45339(2)	0.0135(1)
I17	4c	0.28576(2)	$\frac{3}{4}$	0.50336(2)	0.0179(1)
I18	4c	0.22320(2)	$\frac{3}{4}$	0.35056(2)	0.0235(1)
I19	4c	0.58325(2)	$\frac{3}{4}$	0.35269(2)	0.0142(1)
O1	8d	0.47911(12)	0.4406(2)	0.03933(11)	0.0202(10)
O2	4c	0.31320(16)	$\frac{1}{4}$	0.72450(15)	0.0151(11)
N1	8d	0.23333(13)	0.5425(3)	0.77884(13)	0.0183(11)
N2	8d	0.27527(12)	0.4280(2)	0.67429(12)	0.0125(10)
C1	8d	0.21391(16)	0.4628(3)	0.74241(15)	0.0173(12)
C2	8d	0.23390(15)	0.4822(3)	0.68922(15)	0.0130(11)
C3	8d	0.21186(16)	0.5507(3)	0.65575(14)	0.0142(11)
C4	8d	0.23225(16)	0.5622(3)	0.60685(15)	0.0153(12)
C5	8d	0.27418(15)	0.5037(3)	0.59257(15)	0.0153(12)
C6	8d	0.29543(16)	0.4357(3)	0.62742(15)	0.0143(12)
N3	8d	0.05406(13)	0.5421(3)	0.39367(12)	0.0160(10)
N4	8d	0.11409(15)	0.4827(3)	0.49298(15)	0.0317(14)

Table SVII. Continuation.

C7	<i>8d</i>	0.09624(15)	0.5991(3)	0.42049(15)	0.0147(12)
C8	<i>8d</i>	0.13075(15)	0.5264(3)	0.44897(15)	0.0136(11)
C9	<i>8d</i>	0.17880(17)	0.5095(4)	0.43392(15)	0.0259(14)
C10	<i>8d</i>	0.20982(18)	0.4414(4)	0.46334(18)	0.0363(18)
C11	<i>8d</i>	0.19162(19)	0.3977(3)	0.50662(19)	0.0310(16)
C12	<i>8d</i>	0.14309(18)	0.4194(4)	0.5217(2)	0.0383(17)
N5	<i>8d</i>	0.51498(13)	0.5487(3)	0.29223(12)	0.0175(10)
N6	<i>8d</i>	0.52637(13)	0.5497(3)	0.42461(13)	0.0170(11)
C13	<i>8d</i>	0.49188(16)	0.5093(3)	0.34070(16)	0.0183(12)
C14	<i>8d</i>	0.53149(16)	0.4932(3)	0.38186(15)	0.0143(12)
C15	<i>8d</i>	0.57072(15)	0.4235(3)	0.37867(15)	0.0137(12)
C16	<i>8d</i>	0.55820(17)	0.5429(3)	0.46485(15)	0.0209(14)
C17	<i>8d</i>	0.59740(16)	0.4731(3)	0.46307(16)	0.0197(12)
C18	<i>8d</i>	0.60383(16)	0.4128(3)	0.41937(15)	0.0170(12)
H1A	<i>8d</i>	0.17630	0.46490	0.74190	0.0210
H1B	<i>8d</i>	0.22450	0.39260	0.75400	0.0210
H1C	<i>8d</i>	0.26780	0.53760	0.78090	0.0280
H1D	<i>8d</i>	0.21950	0.53150	0.81030	0.0280
H1E	<i>8d</i>	0.22460	0.60720	0.76750	0.0280
H2	<i>8d</i>	0.28970	0.38560	0.69650	0.0150
H3	<i>8d</i>	0.18290	0.59000	0.66580	0.0170
H4	<i>8d</i>	0.21750	0.60990	0.58340	0.0180
H5	<i>8d</i>	0.28810	0.51050	0.55920	0.0190
H6	<i>8d</i>	0.32410	0.39480	0.61820	0.0170
H3A	<i>8d</i>	0.06750	0.49170	0.37320	0.0240
H3B	<i>8d</i>	0.03590	0.58780	0.37420	0.0240
H3C	<i>8d</i>	0.03330	0.51220	0.41730	0.0240
H4A	<i>8d</i>	0.08290	0.49620	0.50320	0.0380
H7A	<i>8d</i>	0.11630	0.63850	0.39490	0.0180
H7B	<i>8d</i>	0.08140	0.64980	0.44490	0.0180
H9	<i>8d</i>	0.19180	0.54250	0.40410	0.0310
H10	<i>8d</i>	0.24350	0.42670	0.45250	0.0440
H11	<i>8d</i>	0.21230	0.35220	0.52640	0.0370
H12	<i>8d</i>	0.12990	0.39010	0.55240	0.0460
H5A	<i>8d</i>	0.53220	0.60880	0.29870	0.0260
H5B	<i>8d</i>	0.49000	0.56120	0.26890	0.0260
H5C	<i>8d</i>	0.53680	0.50010	0.27960	0.0260
H6A	<i>8d</i>	0.50080	0.59370	0.42660	0.0200
H13A	<i>8d</i>	0.47440	0.44250	0.33390	0.0220
H13B	<i>8d</i>	0.46620	0.55990	0.35300	0.0220
H15	<i>8d</i>	0.57520	0.38270	0.34860	0.0160
H16	<i>8d</i>	0.55350	0.58610	0.49410	0.0250
H17	<i>8d</i>	0.61990	0.46600	0.49130	0.0240
H18	<i>8d</i>	0.63100	0.36410	0.41750	0.0200

Table SVII. Continuation.

H911	8 <i>d</i>	0.4619(16)	0.403(3)	0.0574(16)	0.0300
H912	8 <i>d</i>	0.4958(16)	0.397(3)	0.0235(16)	0.0300
H921	4 <i>c</i>	0.314(2)	$\frac{1}{4}$	0.7561(8)	0.0230
H922	4 <i>c</i>	0.3422(11)	$\frac{1}{4}$	0.714(2)	0.0230

Table SVIII. (An)isotropic displacement parameters for (C₆H₁₀N₂)₆IPb₅I₂₁ · 3 H₂O at 100 K with standard deviations in parentheses.

Atom	U₁₁	U₂₂	U₃₃	U₂₃	U₁₃	U₁₂
Pb1	0.0121(1)	0.0086(1)	0.0097(1)	0	0.0010(1)	0
Pb2	0.0123(1)	0.0089(1)	0.0120(1)	0	-0.0005(1)	0
Pb3	0.0103(1)	0.0108(1)	0.0125(1)	0	0.0001(1)	0
Pb4	0.0116(1)	0.0082(1)	0.0100(1)	0	-0.0012(1)	0
Pb5	0.0153(1)	0.0078(1)	0.0091(1)	0	-0.0004(1)	0
I1	0.0223(2)	0.0198(2)	0.0090(2)	0	0.0044(2)	0
I2	0.0135(2)	0.0112(2)	0.0110(2)	0	-0.0008(1)	0
I3	0.0147(2)	0.0132(2)	0.0095(2)	0	0.0006(1)	0
I4	0.0121(2)	0.0134(2)	0.0182(2)	0	0.0012(2)	0
I5	0.0169(1)	0.0073(1)	0.0186(1)	-0.0004(1)	0.0006(1)	-0.0009(1)
I6	0.0158(2)	0.0161(2)	0.0104(2)	0	-0.0009(1)	0
I7	0.0138(2)	0.0185(2)	0.0198(2)	0	-0.0039(2)	0
I8	0.0135(2)	0.0164(2)	0.0144(2)	0	0.0040(2)	0
I9	0.0122(2)	0.0208(2)	0.0093(2)	0	-0.0007(1)	0
I10	0.0145(1)	0.0112(1)	0.0194(1)	0.0003(1)	-0.0012(1)	0.0016(1)
I11	0.0129(2)	0.0204(2)	0.0168(2)	0	0.0031(2)	0
I12	0.0204(2)	0.0175(2)	0.0162(2)	0	-0.0071(2)	0
I13	0.0110(2)	0.0166(2)	0.0135(2)	0	0.0006(1)	0
I14	0.0197(2)	0.0191(2)	0.0111(2)	0	0.0021(2)	0
I15	0.0244(2)	0.0071(1)	0.0174(1)	0.0000(1)	-0.0041(1)	-0.0004(1)
I16	0.0110(2)	0.0134(2)	0.0162(2)	0	-0.0009(2)	0
I17	0.0196(2)	0.0241(2)	0.0101(2)	0	0.0035(2)	0
I18	0.0171(2)	0.0358(2)	0.0177(2)	0	-0.0072(2)	0
I19	0.0145(2)	0.0140(2)	0.0140(2)	0	0.0010(2)	0
O1	0.0230(18)	0.0182(17)	0.0195(16)	0.0038(12)	0.0056(13)	0.0022(13)
O2	0.017(2)	0.017(2)	0.0114(19)	0	0.0018(18)	0
N1	0.0136(18)	0.024(2)	0.0173(18)	-0.0036(15)	0.0025(15)	0.0024(15)
N2	0.0125(17)	0.0119(17)	0.0130(16)	0.0017(13)	-0.0039(14)	0.0019(14)
C1	0.021(2)	0.015(2)	0.016(2)	-0.0026(17)	0.0049(18)	-0.0020(18)
C2	0.013(2)	0.012(2)	0.0139(19)	-0.0012(16)	0.0025(16)	-0.0057(16)
C3	0.017(2)	0.0117(19)	0.0139(19)	-0.0034(16)	-0.0015(17)	0.0010(17)
C4	0.018(2)	0.013(2)	0.015(2)	-0.0010(16)	-0.0056(17)	-0.0020(17)
C5	0.014(2)	0.018(2)	0.014(2)	0.0002(17)	-0.0006(17)	-0.0055(17)

Table SVIII. Continuation.

C6	0.013(2)	0.011(2)	0.019(2)	-0.0043(16)	-0.0007(17)	-0.0022(17)
N3	0.0175(19)	0.0156(18)	0.0149(17)	0.0019(14)	-0.0021(14)	0.0037(15)
N4	0.018(2)	0.045(3)	0.032(2)	0.019(2)	0.0018(18)	-0.0024(19)
C7	0.014(2)	0.012(2)	0.018(2)	0.0017(16)	0.0022(17)	0.0022(16)
C8	0.014(2)	0.013(2)	0.0137(19)	-0.0017(16)	-0.0019(16)	0.0014(16)
C9	0.015(2)	0.056(3)	0.0066(19)	0.009(2)	0.0024(17)	0.005(2)
C10	0.016(2)	0.064(4)	0.029(3)	-0.020(3)	-0.008(2)	0.020(2)
C11	0.035(3)	0.019(2)	0.039(3)	-0.004(2)	-0.024(2)	0.007(2)
C12	0.025(3)	0.045(3)	0.045(3)	0.033(3)	-0.016(2)	-0.018(2)
N5	0.0199(19)	0.0178(18)	0.0147(17)	0.0017(14)	-0.0042(15)	0.0029(15)
N6	0.020(2)	0.0124(17)	0.0187(18)	0.0013(14)	0.0093(15)	-0.0002(15)
C13	0.012(2)	0.020(2)	0.023(2)	0.0035(18)	0.0002(18)	-0.0016(17)
C14	0.014(2)	0.012(2)	0.017(2)	0.0025(16)	0.0005(17)	-0.0035(17)
C15	0.013(2)	0.013(2)	0.015(2)	-0.0016(16)	-0.0001(16)	0.0000(17)
C16	0.032(3)	0.022(2)	0.0086(19)	-0.0007(17)	0.0066(18)	-0.009(2)
C17	0.021(2)	0.024(2)	0.014(2)	0.0038(18)	-0.0026(18)	-0.0071(19)
C18	0.017(2)	0.012(2)	0.022(2)	0.0012(17)	-0.0011(18)	-0.0011(17)

Table SIX. Bond distances for $(C_6H_{10}N_2)_6IPb_5I_{21} \cdot 3 H_2O$ at 100 K with standard deviations in parentheses.

Bond	Distance / Å	Bond	Distance / Å
Pb1-I1	3.1008(7)	Pb5-I18	3.2056(8)
Pb1-I2	3.1815(8)	Pb5-I15^f	3.2198(3)
Pb1-I3	3.3411(7)	O1-H911	0.81(4)
Pb1-I4	3.0788(7)	O1-H912	0.82(4)
Pb1-I5	3.2272(3)	N1-C1	1.487(5)
Pb1-I5^f	3.2272(3)	N2-C6	1.337(5)
Pb2-I5	3.2065(3)	N2-C2	1.350(5)
Pb2-I6	3.2556(7)	N1-H1D	0.9100
Pb2-I7	3.2317(7)	N1-H1E	0.9100
Pb2-I8	3.2223(7)	N1-H1C	0.9100
Pb2-I9	3.1504(7)	O2-H922	0.81(3)
Pb2-I5^e	3.2065(3)	N2-H2	0.8800
Pb3-I6	3.3633(7)	O2-H921	0.83(2)
Pb3-I9	3.2422(7)	N3-C7	1.503(5)
Pb3-I10	3.1724(3)	N4-C12	1.343(6)
Pb3-I11	3.1703(7)	N4-C8	1.351(6)
Pb3-I12	3.0419(7)	N3-H3A	0.9100
Pb3-I10^e	3.1724(3)	N3-H3C	0.9100
Pb4-I8	3.6208(7)	N3-H3B	0.9100
Pb4-I13	2.9931(8)	N4-H4A	0.8800

Table SIX. Continuation.

Pb4-I14	3.0100(7)	N5-C13	1.492(5)
Pb4-I15	3.2263(3)	N6-C14	1.337(5)
Pb4-I11^a	3.4386(8)	N6-C16	1.346(5)
Pb4-I15^e	3.2263(3)	N5-H5C	0.9100
Pb5-I1	3.4816(7)	N5-H5B	0.9100
Pb5-I15	3.2198(3)	N5-H5A	0.9100
Pb5-I16	3.1716(7)	N6-H6A	0.8800
Pb5-I17	2.9999(7)	C1-C2	1.505(6)
C2-C3	1.368(5)	C7-H7A	0.9900
C3-C4	1.392(5)	C9-H9	0.9500
C4-C5	1.386(6)	C10-H10	0.9500
C5-C6	1.379(6)	C11-H11	0.9500
C1-H1B	0.9900	C12-H12	0.9500
C1-H1A	0.9900	C13-C14	1.511(6)
C3-H3	0.9500	C14-C15	1.369(6)
C4-H4	0.9500	C15-C18	1.381(6)
C5-H5	0.9500	C16-C17	1.367(6)
C6-H6	0.9500	C17-C18	1.388(6)
C7-C8	1.499(6)	C13-H13A	0.9900
C8-C9	1.342(6)	C13-H13B	0.9900
C9-C10	1.421(7)	C15-H15	0.9500
C10-C11	1.349(7)	C16-H16	0.9500
C11-C12	1.366(7)	C17-H17	0.9500
C7-H7B	0.9900	C18-H18	0.9500

$$a = \frac{1}{2}+x, \frac{1}{2}-y, \frac{1}{2}-z; e = x, \frac{1}{2}-y, z; f = x, \frac{3}{2}-y, z$$

Table SX. Bond angles for $(C_6H_{10}N_2)_6IPb_5I_{21} \cdot 3 H_2O$ at 100 K with standard deviations in parentheses.

Bond	Angle / °	Bond	Angle / °
I1-Pb1-I2	89.17(2)	I5^e-Pb2-I8	86.42(1)
I1-Pb1-I3	171.05(2)	I5^e-Pb2-I9	92.07(1)
I1-Pb1-I4	96.74(2)	I6-Pb3-I9	80.11(2)
I1-Pb1-I5	88.45(1)	I6-Pb3-I10	92.50(1)
I1-Pb1-I5^f	88.45(1)	I6-Pb3-I11	89.90(2)
I2-Pb1-I3	81.88(2)	I6-Pb3-I12	173.47(2)
I2-Pb1-I4	174.09(2)	I6-Pb3-I10^e	92.50(1)
I2-Pb1-I5	85.94(1)	I9-Pb3-I10	90.26(1)
I2-Pb1-I5^f	85.94(1)	I9-Pb3-I11	170.00(2)
I3-Pb1-I4	92.22(2)	I9-Pb3-I12	93.37(2)
I3-Pb1-I5	90.90(1)	I9-Pb3-I10^e	90.26(1)
I3-Pb1-I5^f	90.90(1)	I10-Pb3-I11	90.17(1)

Table SX. Continuation.

I5-Pb2-I5^e	171.38(2)	I8-Pb4-I15	86.58(1)
I4-Pb1-I5	94.20(1)	I10-Pb3-I12	87.50(1)
I4-Pb1-I5^f	94.20(1)	I10-Pb3-I10^e	175.00(2)
I5-Pb1-I5^f	171.34(2)	I11-Pb3-I12	96.63(2)
I5-Pb2-I6	94.00(1)	I10^e-Pb3-I11	90.17(1)
I5-Pb2-I7	88.40(1)	I10^e-Pb3-I12	87.50(1)
I5-Pb2-I8	86.42(1)	I8-Pb4-I13	99.31(2)
I5-Pb2-I9	92.07(1)	I8-Pb4-I14	169.09(2)
I6-Pb2-I7	89.97(2)	I8-Pb4-I11^a	75.62(2)
I6-Pb2-I8	168.09(2)	I8-Pb4-I15^e	86.58(1)
I6-Pb2-I9	83.15(2)	I13-Pb4-I14	91.61(2)
I5^e-Pb2-I6	94.00(1)	I13-Pb4-I15	93.38(1)
I7-Pb2-I8	101.95(2)	I11^a-Pb4-I13	174.93(2)
I7-Pb2-I9	173.11(2)	I13-Pb4-I15^e	93.38(1)
I5^e-Pb2-I7	88.40(1)	I14-Pb4-I15	92.81(1)
I8-Pb2-I9	84.94(2)	I11^a-Pb4-I14	93.46(2)
I14-Pb4-I15^e	92.81(1)	C1-N1-H1E	109.00
I11^a-Pb4-I15	86.38(1)	C1-N1-H1D	109.00
I15-Pb4-I15^e	171.07(2)	H1D-N1-H1E	110.00
I11^a-Pb4-I15^e	86.38(1)	C1-N1-H1C	109.00
I1-Pb5-I15	83.56(1)	H1C-N1-H1E	109.00
I1-Pb5-I16	83.06(2)	H1C-N1-H1D	110.00
I1-Pb5-I17	172.30(2)	C2-N2-H2	118.00
I1-Pb5-I18	99.68(2)	C6-N2-H2	118.00
I1-Pb5-I15^f	83.56(1)	H921-O2-H922	108(5)
I15-Pb5-I16	88.12(1)	C8-N4-C12	122.7(4)
I15-Pb5-I17	96.23(1)	C7-N3-H3C	110.00
I15-Pb5-I18	92.18(1)	H3B-N3-H3C	110.00
I15-Pb5-I15^f	166.93(2)	C7-N3-H3B	110.00
I16-Pb5-I17	89.25(2)	C7-N3-H3A	109.00
I16-Pb5-I18	177.26(2)	H3A-N3-H3C	109.00
I15^f-Pb5-I16	88.12(1)	H3A-N3-H3B	110.00
I17-Pb5-I18	88.01(2)	C8-N4-H4A	119.00
I15^f-Pb5-I17	96.23(1)	C12-N4-H4A	119.00
I15^f-Pb5-I18	92.18(1)	C14-N6-C16	123.6(4)
Pb1-I1-Pb5	157.46(2)	H5B-N5-H5C	110.00
Pb1-I5-Pb2	177.01(2)	C13-N5-H5B	109.00
Pb2-I6-Pb3	96.07(2)	C13-N5-H5C	109.00
Pb2-I8-Pb4	135.09(2)	H5A-N5-H5C	109.00
Pb2-I9-Pb3	100.69(2)	C13-N5-H5A	109.00
Pb3-I11-Pb4^b	159.90(2)	H5A-N5-H5B	110.00
Pb4-I15-Pb5	171.51(2)	C16-N6-H6A	118.00
H911-O1-H912	101(4)	C14-N6-H6A	118.00
C2-N2-C6	123.1(3)	N1-C1-C2	110.8(3)

Table SX. Continuation.

C2-C1-H1A	109.00	C11-C10-H10	120.00
C1-C2-C3	123.1(4)	C8-C7-H7A	109.00
N2-C2-C1	117.6(3)	N3-C7-H7B	109.00
N2-C2-C3	119.3(4)	C8-C7-H7B	109.00
C2-C3-C4	119.3(4)	H7A-C7-H7B	108.00
C3-C4-C5	119.8(4)	N3-C7-H7A	109.00
C4-C5-C6	119.3(4)	C10-C9-H9	121.00
N2-C6-C5	119.3(4)	C8-C9-H9	120.00
C2-C1-H1B	109.00	C9-C10-H10	120.00
N1-C1-H1B	109.00	C10-C11-H11	120.00
H1A-C1-H1B	108.00	C12-C11-H11	120.00
N1-C1-H1A	109.00	N4-C12-H12	120.00
C2-C3-H3	120.00	C11-C12-H12	120.00
C4-C3-H3	120.00	N5-C13-C14	111.6(3)
C5-C4-H4	120.00	C13-C14-C15	124.5(4)
C3-C4-H4	120.00	N6-C14-C15	118.8(4)
C4-C5-H5	120.00	N6-C14-C13	116.7(4)
C6-C5-H5	120.00	C14-C15-C18	119.6(4)
N2-C6-H6	120.00	N6-C16-C17	119.1(4)
C5-C6-H6	120.00	C16-C17-C18	119.0(4)
N3-C7-C8	112.1(3)	C15-C18-C17	120.0(4)
N4-C8-C9	119.2(4)	N5-C13-H13B	109.00
C7-C8-C9	121.8(4)	C14-C13-H13A	109.00
N4-C8-C7	118.9(4)	H13A-C13-H13B	108.00
C8-C9-C10	118.9(4)	C14-C13-H13B	109.00
C9-C10-C11	120.3(4)	N5-C13-H13A	109.00
C10-C11-C12	119.3(4)	C14-C15-H15	120.00
N4-C12-C11	119.6(5)	C18-C15-H15	120.00
C17-C16-H16	120.00	C18-C17-H17	121.00
N6-C16-H16	120.00	C17-C18-H18	120.00
C16-C17-H17	120.00	C15-C18-H18	120.00

$$a = -\frac{1}{2}x, \frac{1}{2}y, \frac{1}{2}z; b = \frac{1}{2}x, \frac{1}{2}y, \frac{1}{2}z; e = x, \frac{1}{2}y, z; f = x, \frac{3}{2}y, z$$

Table SXI. Hydrogen bond distances (in Å) and angles (in °) for $(C_6H_{10}N_2)_6IPb_5I_{21} \cdot 3 H_2O$ at 100 K with standard deviations in parentheses.

D-H...A	H...A	D...A	∠D-H...A
N1-H1C...I10^x	2.68	3.590(3)	173.6
N1-H1D...I15ⁱⁱ	2.69	3.578(3)	164.9
N1-H1E...I8ⁱⁱ	2.81	3.592(3)	144.2
N2-H2...O2	1.99	2.816(4)	156.6
N3-H3A...I6^c	3.15	3.750(3)	124.9
N3-H3A...I10^c	2.93	3.617(3)	133.4
N3-H3B...I2^c	2.78	3.544(3)	142.1
N3-H3B...I5^c	3.13	3.622(3)	115.9
N3-H3C...O1^c	2.04	2.940(5)	170.8
N4-H4A...O1ⁱⁱ	2.05	2.907(5)	163.5
N5-H5A...I2	3.27	3.712(3)	112.3
N5-H5A...I19	2.66	3.520(3)	157.9
N5-H5B...I1	3.30	3.837(3)	120.4
N5-H5B...I5	2.91	3.716(3)	148.9
N5-H5C...I9	3.25	3.876(3)	127.8
N5-H5C...I10	2.96	3.685(3)	137.4
N6-H6A...I16	2.62	3.465(3)	162.4
O1-H911...I7	2.87(3)	3.592(3)	150(4)
O1-H912...I3^l	2.84(2)	3.628(3)	163(4)
O2-H921...I18ⁱⁱ	2.66(3)	3.426(4)	156(6)
O2-H922...I19^x	2.62(3)	3.389(4)	158(6)

$c = -\frac{1}{2}+x, y, \frac{1}{2}-z; l = 1-x, 1-y, -z; x = 1-x, 1-y, 1-z; ii = \frac{1}{2}-x, 1-y, \frac{1}{2}+z;$

7. Appendix

C.2 Crystallographic data for (C₆H₁₀N₂)PbCl₄, (C₆H₁₀N₂)PbBr₄ and (C₆H₁₀N₂)PbI₄ at 296 K**Table SXII.** Crystallographic data and details of the structure refinement for (C₆H₁₀N₂)PbCl₄, (C₆H₁₀N₂)PbBr₄ and (C₆H₁₀N₂)PbI₄ at 296 K (CCDC 1838616, CCDC 1838617 and CCDC 1838615).

Formula	(C ₆ H ₁₀ N ₂)PbCl ₄	(C ₆ H ₁₀ N ₂)PbBr ₄	(C ₆ H ₁₀ N ₂)PbI ₄
Molar mass (g mol ⁻¹)	459.15	636.99	824.95
Crystal system	Orthorhombic	Orthorhombic	Orthorhombic
Space group	<i>Pbca</i> (no. 61)	<i>Pbca</i> (no. 61)	<i>Pbca</i> (no. 61)
T (K)	296	296	296
Radiation, λ (Å)	Mo K _α , 0.71073	Mo K _α , 0.71073	Mo K _α , 0.71073
<i>a</i> (Å)	16.7592(13)	17.3765(3)	18.3568(4)
<i>b</i> (Å)	7.8750(5)	8.2397(1)	8.7037(2)
<i>c</i> (Å)	18.4791(15)	18.7056(4)	19.6480(4)
<i>V</i> (Å ³)	2438.9(3)	2678.22(8)	3139.20(12)
<i>Z</i>	8	8	8
Calculated density (g cm ⁻³)	2.501	3.159	3.491
Crystal size (mm ³)	0.01 x 0.02 x 0.07	0.02 x 0.02 x 0.04	0.01 x 0.03 x 0.04
Absorption coefficient (mm ⁻¹)	14.671	24.498	18.587
F(000)	1680	2256	2832
Absorption correction	multi-scan	multi-scan	multi-scan
θ range	3.3° to 26.9°	3.2° to 30.5°	3.2° to 29.6°
Index range	-18 ≤ <i>h</i> ≤ 21, -9 ≤ <i>k</i> ≤ 10, -23 ≤ <i>l</i> ≤ 23	-24 ≤ <i>h</i> ≤ 24, -11 ≤ <i>k</i> ≤ 11, -26 ≤ <i>l</i> ≤ 26	-25 ≤ <i>h</i> ≤ 25, -11 ≤ <i>k</i> ≤ 12, -27 ≤ <i>l</i> ≤ 27
Parameters/restraints	121 / 1	119 / 0	119 / 10
Total No. of reflections	25803	47304	35718
No. of independent reflections	2623 [R _{int} = 0.0706]	4084 [R _{int} = 0.0488]	4396 [R _{int} = 0.0647]
No. of observed reflections	1967	3103	3553
Min./max. residual electron density (e Å ⁻³)	-0.78 / 1.81	-1.59 / 1.74	-2.45 / 1.58
Goof	1.05	1.04	1.03
wR2	0.0576 ^a	0.0626 ^b	0.0739 ^c
R1 (for observed reflections)	0.0288	0.0288	0.0315

^a $w = [\sigma^2(F_0^2) + (0.0129P)^2 + 8.5526P]^{-1}$, with $P = (F_0^2 + 2F_c^2)/3$

^b $w = [\sigma^2(F_0^2) + (0.0166P)^2 + 14.0185P]^{-1}$, with $P = (F_0^2 + 2F_c^2)/3$

^c $w = [\sigma^2(F_0^2) + (0.0223P)^2 + 17.7232P]^{-1}$, with $P = (F_0^2 + 2F_c^2)/3$

Table SXIII. Atomic coordinates and equivalent isotropic displacement parameters for $(C_6H_{10}N_2)PbCl_4$ at 296 K with standard deviations in parentheses. $U(eq)$ is defined as one third of the trace of the orthogonalized U tensor.

Atom	Wyck.	x	y	z	$U(eq) / \text{\AA}^2$
Pb1	8c	0.62175(2)	0.38458(2)	0.26878(2)	0.0285(1)
Cl1	8c	0.73658(10)	0.1200(2)	0.26975(11)	0.0457(5)
Cl2	8c	0.59548(12)	0.3565(3)	0.42349(11)	0.0595(7)
Cl3	8c	0.50535(13)	0.1377(3)	0.24465(12)	0.0694(8)
Cl4	8c	0.65040(11)	0.4184(3)	0.11901(10)	0.0539(7)
N1	8c	0.3498(5)	0.3479(9)	0.3425(4)	0.082(3)
N2	8c	0.4406(3)	0.2540(7)	0.4974(3)	0.044(2)
C1	8c	0.3685(5)	0.4305(11)	0.4083(4)	0.066(3)
C2	8c	0.3691(4)	0.3077(9)	0.4731(4)	0.045(2)
C3	8c	0.3021(4)	0.2571(9)	0.5089(4)	0.045(3)
C4	8c	0.3097(4)	0.1565(10)	0.5703(4)	0.052(3)
C5	8c	0.3839(5)	0.1094(9)	0.5947(4)	0.052(3)
C6	8c	0.4493(4)	0.1593(9)	0.5575(4)	0.051(3)
H1A	8c	0.396(3)	0.268(7)	0.328(2)	0.1240
H1B	8c	0.342(4)	0.437(4)	0.302(2)	0.1240
H1C	8c	0.298(3)	0.279(7)	0.3488(11)	0.1240
H1D	8c	0.32970	0.51950	0.41710	0.0790
H1E	8c	0.42060	0.48350	0.40400	0.0790
H2	8c	0.484(4)	0.283(3)	0.472(2)	0.0520
H3	8c	0.25190	0.28960	0.49250	0.0550
H4	8c	0.26430	0.12080	0.59500	0.0630
H5	8c	0.38910	0.04400	0.63630	0.0620
H6	8c	$\frac{1}{2}$	0.12830	0.57330	0.0610

Table SXIV. (An)isotropic displacement parameters for (C₆H₁₀N₂)PbCl₄ at 296 K with standard deviations in parentheses.

Atom	U ₁₁	U ₂₂	U ₃₃	U ₂₃	U ₁₃	U ₁₂
Pb1	0.0224(1)	0.0235(1)	0.0396(1)	0.0008(1)	-0.0013(1)	-0.0004(1)
Cl1	0.0446(9)	0.0373(9)	0.0553(10)	0.0015(10)	0.0063(9)	0.0146(8)
Cl2	0.0545(11)	0.0698(13)	0.0543(12)	-0.0029(10)	0.0171(9)	-0.0077(10)
Cl3	0.0602(12)	0.0541(13)	0.0939(18)	0.0021(10)	-0.0155(11)	-0.0306(10)
Cl4	0.0448(10)	0.0758(14)	0.0412(11)	-0.0018(9)	-0.0018(8)	-0.0051(9)
N1	0.125(7)	0.066(5)	0.056(4)	-0.001(3)	-0.016(5)	0.002(5)
N2	0.033(3)	0.055(4)	0.043(4)	0.002(3)	0.002(3)	-0.003(3)
C1	0.077(6)	0.076(6)	0.044(4)	0.004(4)	0.003(4)	-0.012(5)
C2	0.042(4)	0.053(4)	0.040(4)	0.001(3)	-0.008(3)	-0.005(3)
C3	0.034(4)	0.059(5)	0.043(5)	0.000(4)	0.002(3)	-0.002(3)
C4	0.045(4)	0.064(5)	0.048(5)	-0.004(4)	0.008(4)	-0.008(4)
C5	0.061(5)	0.049(4)	0.045(4)	0.010(4)	-0.004(4)	-0.003(4)
C6	0.034(4)	0.052(5)	0.066(6)	0.003(4)	-0.015(4)	0.008(3)

Table SXV. Bond distances for (C₆H₁₀N₂)PbCl₄ at 296 K with standard deviations in parentheses.

Bond	Distance / Å	Bond	Distance / Å
Pb1-Cl1	2.8364(17)	N2-H2	0.90(6)
Pb1-Cl2	2.901(2)	C1-C2	1.539(11)
Pb1-Cl3	2.790(2)	C2-C3	1.363(10)
Pb1-Cl4	2.8216(19)	C3-C4	1.390(10)
Pb1-Cl3^b	2.928(2)	C4-C5	1.374(11)
Pb1-Cl1^e	3.0124(17)	C5-C6	1.352(11)
N1-C1	1.414(11)	C1-H1D	0.9700
N2-C2	1.348(9)	C1-H1E	0.9700
N2-C6	1.346(9)	C3-H3	0.9300
N1-H1C	1.03(5)	C4-H4	0.9300
N1-H1A	1.03(5)	C5-H5	0.9300
N1-H1B	1.03(4)	C6-H6	0.9300

$$b = 1-x, \frac{1}{2}+y, \frac{1}{2}-z; e = \frac{3}{2}-x, \frac{1}{2}+y, z$$

Table SXVI. Bond angles for (C₆H₁₀N₂)PbCl₄ at 296 K with standard deviations in parentheses.

Bond	Angle / °	Bond	Angle / °
Cl1-Pb1-Cl2	92.34(6)	C6-N2-H2	119(3)
Cl1-Pb1-Cl3	87.91(6)	C2-N2-H2	118(3)
Cl1-Pb1-Cl4	87.71(6)	N1-C1-C2	112.4(7)
Cl1-Pb1-Cl3 ^b	173.87(6)	N2-C2-C3	118.6(7)
Cl1-Pb1-Cl1 ^e	85.26(5)	C1-C2-C3	123.8(6)
Cl2-Pb1-Cl3	89.90(6)	N2-C2-C1	117.5(6)
Cl2-Pb1-Cl4	178.50(6)	C2-C3-C4	119.2(6)
Cl2-Pb1-Cl3 ^b	91.43(6)	C3-C4-C5	120.3(7)
Cl1 ^e -Pb1-Cl2	99.25(6)	C4-C5-C6	119.2(7)
Cl3-Pb1-Cl4	91.60(6)	N2-C6-C5	119.5(6)
Cl3-Pb1-Cl3 ^b	87.26(7)	N1-C1-H1D	109.00
Cl1 ^e -Pb1-Cl3	168.78(6)	N1-C1-H1E	109.00
Cl3 ^b -Pb1-Cl4	88.65(6)	C2-C1-H1D	109.00
Cl1 ^e -Pb1-Cl4	79.26(6)	C2-C1-H1E	109.00
Cl1 ^e -Pb1-Cl3 ^b	98.91(5)	H1D-C1-H1E	108.00
Pb1-Cl1-Pb1 ^d	170.68(6)	C2-C3-H3	120.00
Pb1-Cl3-Pb1 ^a	175.31(9)	C4-C3-H3	120.00
C2-N2-C6	123.0(6)	C3-C4-H4	120.00
C1-N1-H1C	109.4(16)	C5-C4-H4	120.00
C1-N1-H1A	110(2)	C4-C5-H5	120.00
C1-N1-H1B	110(2)	C6-C5-H5	120.00
H1B-N1-H1C	109(4)	N2-C6-H6	120.00
H1A-N1-H1B	109(4)	C5-C6-H6	120.00
H1A-N1-H1C	110(4)		

$$a = 1-x, \frac{1}{2}+y, \frac{1}{2}-z; b = 1-x, \frac{1}{2}+y, \frac{1}{2}-z; d = \frac{3}{2}-x, \frac{1}{2}+y, z; e = \frac{3}{2}-x, \frac{1}{2}+y, z$$

Table SXVII. Hydrogen bond distances (in Å) and angles (in °) for (C₆H₁₀N₂)PbCl₄ at 296 K with standard deviations in parentheses.

D-H...A	H...A	D...A	∠D-H...A
N1-H1A...Cl3	2.61	3.578(9)	156.6
N1-H1B...Cl1 ^b	2.36	3.316(8)	153.6
N1-H1C...Cl1 ^m	2.73	3.335(8)	118.1
N1-H1C...Cl4 ^m	2.78	3.462(9)	124.3
N2-H2...Cl2	2.15	3.042(6)	173.9
C6-H6...Cl4 ^p	2.68	3.609(7)	173.0

$$b = 1-x, \frac{1}{2}+y, \frac{1}{2}-z; m = \frac{1}{2}+x, y, \frac{1}{2}-z; p = x, \frac{1}{2}-y, \frac{1}{2}+z$$

Table SXVIII. Atomic coordinates and equivalent isotropic displacement parameters for $(C_6H_{10}N_2)PbBr_4$ at 296 K with standard deviations in parentheses. $U(eq)$ is defined as one third of the trace of the orthogonalized U tensor.

Atom	Wyck.	x	y	z	$U(eq) / \text{\AA}^2$
Pb1	8 <i>c</i>	0.37761(2)	0.62138(2)	0.26894(2)	0.0278(1)
Br1	8 <i>c</i>	0.40030(4)	0.64097(9)	0.42796(3)	0.0562(2)
Br2	8 <i>c</i>	0.49695(4)	0.86953(8)	0.24497(5)	0.0714(3)
Br3	8 <i>c</i>	0.34880(4)	0.59468(9)	0.11379(3)	0.0543(2)
Br4	8 <i>c</i>	0.26021(3)	0.88599(7)	0.27321(3)	0.0453(2)
N1	8 <i>c</i>	0.3489(5)	0.3406(9)	0.6547(4)	0.090(3)
N2	8 <i>c</i>	0.4392(3)	0.2465(7)	0.5038(3)	0.0487(16)
C1	8 <i>c</i>	0.3686(5)	0.4237(11)	0.5931(4)	0.082(4)
C2	8 <i>c</i>	0.3711(3)	0.2986(9)	0.5280(3)	0.0507(19)
C3	8 <i>c</i>	0.3070(3)	0.2495(8)	0.4924(3)	0.051(2)
C4	8 <i>c</i>	0.3134(4)	0.1542(8)	0.4317(3)	0.0517(19)
C5	8 <i>c</i>	0.3848(4)	0.1101(8)	0.4077(4)	0.054(2)
C6	8 <i>c</i>	0.4471(3)	0.1580(8)	0.4442(4)	0.054(2)
H1A	8 <i>c</i>	0.41850	0.47450	0.59890	0.0990
H1B	8 <i>c</i>	0.33100	0.50790	0.58350	0.0990
H2	8 <i>c</i>	0.47990	0.27100	0.52770	0.0580
H3	8 <i>c</i>	0.25860	0.28010	0.50880	0.0610
H4	8 <i>c</i>	0.26960	0.12030	0.40740	0.0620
H5	8 <i>c</i>	0.39000	0.04770	0.36650	0.0640
H6	8 <i>c</i>	0.49590	0.12980	0.42810	0.0650
H11	8 <i>c</i>	0.31030	0.27260	0.64540	0.1350
H12	8 <i>c</i>	0.33420	0.41100	0.68810	0.1350
H13	8 <i>c</i>	0.38940	0.28470	0.67030	0.1350

Table SXIX. (An)isotropic displacement parameters for (C₆H₁₀N₂)PbBr₄ at 296 K with standard deviations in parentheses.

Atom	U ₁₁	U ₂₂	U ₃₃	U ₂₃	U ₁₃	U ₁₂
Pb1	0.0228(1)	0.0238(1)	0.0367(1)	-0.0007(1)	0.0006(1)	-0.0001(1)
Br1	0.0474(3)	0.0741(4)	0.0472(3)	-0.0035(3)	-0.0116(3)	-0.0058(3)
Br2	0.0594(4)	0.0551(4)	0.0998(6)	-0.0015(4)	0.0144(4)	-0.0345(3)
Br3	0.0422(3)	0.0847(5)	0.0359(3)	0.0046(3)	0.0005(2)	-0.0004(3)
Br4	0.0423(3)	0.0371(3)	0.0565(3)	-0.0025(3)	-0.0065(2)	0.0166(2)
N1	0.119(6)	0.075(5)	0.076(5)	0.006(4)	0.003(4)	0.003(4)
N2	0.031(2)	0.065(3)	0.050(3)	0.000(3)	-0.004(2)	-0.004(2)
C1	0.098(7)	0.103(7)	0.046(4)	0.007(4)	-0.009(4)	-0.046(5)
C2	0.040(3)	0.069(4)	0.043(3)	-0.006(3)	0.001(3)	0.001(3)
C3	0.034(3)	0.076(5)	0.043(3)	-0.005(3)	0.005(2)	0.006(3)
C4	0.048(3)	0.062(4)	0.045(3)	-0.005(3)	-0.006(3)	-0.008(3)
C5	0.055(4)	0.059(4)	0.047(4)	-0.013(3)	0.010(3)	-0.002(3)
C6	0.037(3)	0.060(4)	0.065(4)	-0.006(3)	0.014(3)	0.004(3)

Table SXX. Bond distances for (C₆H₁₀N₂)PbBr₄ at 296 K with standard deviations in parentheses.

Bond	Distance / Å	Bond	Distance / Å
Pb1-Br1	3.0049(7)	N2-H2	0.8600
Pb1-Br2	2.9465(7)	C1-C2	1.596(10)
Pb1-Br3	2.9532(7)	C2-C3	1.359(8)
Pb1-Br4	2.9869(6)	C3-C4	1.385(8)
Pb1-Br2^a	3.0208(7)	C4-C5	1.369(10)
Pb1-Br4^d	3.0828(6)	C5-C6	1.339(9)
N1-C1	1.383(11)	C1-H1A	0.9700
N2-C2	1.338(8)	C1-H1B	0.9700
N2-C6	1.339(9)	C3-H3	0.9300
N1-H13	0.8900	C4-H4	0.9300
N1-H11	0.8900	C5-H5	0.9300
N1-H12	0.8900	C6-H6	0.9300

$$a = 1-x, \frac{1}{2}+y, \frac{1}{2}-z; d = \frac{1}{2}-x, \frac{1}{2}+y, z$$

Table SXXI. Bond angles for (C₆H₁₀N₂)PbBr₄ at 296 K with standard deviations in parentheses.

Bond	Angle / °	Bond	Angle / °
Br1-Pb1-Br2	91.20(2)	C6-N2-H2	118.00
Br1-Pb1-Br3	177.47(2)	C2-N2-H2	118.00
Br1-Pb1-Br4	91.37(2)	N1-C1-C2	108.8(7)
Br1-Pb1-Br2 ^a	91.58(2)	N2-C2-C3	117.6(6)
Br1-Pb1-Br4 ^d	96.32(2)	C1-C2-C3	122.9(6)
Br2-Pb1-Br3	91.23(2)	N2-C2-C1	119.3(5)
Br2-Pb1-Br4	88.75(2)	C2-C3-C4	120.3(5)
Br2-Pb1-Br2 ^a	87.47(2)	C3-C4-C5	119.5(6)
Br2-Pb1-Br4 ^d	170.85(2)	C4-C5-C6	119.2(6)
Br3-Pb1-Br4	87.99(2)	N2-C6-C5	120.1(6)
Br2 ^a -Pb1-Br3	89.23(2)	N1-C1-H1A	110.00
Br3-Pb1-Br4 ^d	81.19(2)	N1-C1-H1B	110.00
Br2 ^a -Pb1-Br4	175.25(2)	C2-C1-H1A	110.00
Br4-Pb1-Br4 ^d	85.87(2)	C2-C1-H1B	110.00
Br2 ^a -Pb1-Br4 ^d	97.50(2)	H1A-C1-H1B	108.00
Pb1-Br2-Pb1 ^b	176.06(4)	C2-C3-H3	120.00
Pb1-Br4-Pb1 ^e	171.54(2)	C4-C3-H3	120.00
C2-N2-C6	123.2(5)	C3-C4-H4	120.00
C1-N1-H13	109.00	C5-C4-H4	120.00
C1-N1-H11	110.00	C4-C5-H5	120.00
C1-N1-H12	109.00	C6-C5-H5	120.00
H12-N1-H13	110.00	N2-C6-H6	120.00
H11-N1-H12	109.00	C5-C6-H6	120.00
H11-N1-H13	109.00		

$$a = 1-x, \frac{1}{2}+y, \frac{1}{2}-z; b = 1-x, \frac{1}{2}+y, \frac{1}{2}-z; d = \frac{1}{2}-x, \frac{1}{2}+y, z; e = \frac{1}{2}-x, \frac{1}{2}+y, z$$

Table SXXII. Hydrogen bond distances (in Å) and angles (in °) for (C₆H₁₀N₂)PbBr₄ at 296 K with standard deviations in parentheses.

D-H...A	H...A	D...A	∠D-H...A
N1-H11...Br3 ^m	3.03	3.559(8)	119.8
N1-H11...Br4 ^m	2.99	3.463(7)	115.2
N1-H12...Br4 ⁿ	2.64	3.516(7)	167.1
N1-H13...Br2 ^f	2.83	3.701(8)	165.1
N2-H2...Br1 ^f	2.36	3.204(5)	168.9
C3-H3...Br3 ^m	2.90	3.760(6)	154.0
C6-H6...Br3 ^a	2.82	3.745(6)	171.0

$$a = 1-x, \frac{1}{2}+y, \frac{1}{2}-z; f = 1-x, 1-y, 1-z; m = \frac{1}{2}-x, 1-y, \frac{1}{2}+z; n = x, \frac{3}{2}-y, \frac{1}{2}+z$$

Table SXXIII. Atomic coordinates and equivalent isotropic displacement parameters for $(C_6H_{10}N_2)PbI_4$ at 296 K with standard deviations in parentheses. $U(eq)$ is defined as one third of the trace of the orthogonalized U tensor.

Atom	Wyck.	x	y	z	$U(eq) / \text{\AA}^2$
Pb1	8 <i>c</i>	0.37798(2)	0.87257(2)	0.26853(2)	0.0299(1)
I1	8 <i>c</i>	0.26443(3)	0.59417(5)	0.27571(2)	0.0462(1)
I2	8 <i>c</i>	0.35068(3)	0.89700(6)	0.10842(2)	0.0498(1)
I3	8 <i>c</i>	0.39733(3)	0.85678(6)	0.42829(2)	0.0520(1)
I4	8 <i>c</i>	0.50929(4)	0.64679(8)	0.24425(4)	0.0834(3)
N1	8 <i>c</i>	0.3393(5)	0.1774(9)	0.6506(4)	0.073(3)
N2	8 <i>c</i>	0.4366(3)	0.2510(7)	0.5068(3)	0.051(2)
C1	8 <i>c</i>	0.3705(5)	0.1016(10)	0.5914(4)	0.065(3)
C2	8 <i>c</i>	0.3716(3)	0.2030(9)	0.5295(4)	0.044(2)
C3	8 <i>c</i>	0.3115(4)	0.2455(9)	0.4933(4)	0.052(2)
C4	8 <i>c</i>	0.3190(4)	0.3332(10)	0.4345(4)	0.057(3)
C5	8 <i>c</i>	0.3859(4)	0.3778(9)	0.4133(5)	0.059(3)
C6	8 <i>c</i>	0.4449(4)	0.3360(10)	0.4508(5)	0.064(3)
H1A	8 <i>c</i>	0.37220	0.24010	0.66890	0.1100
H1B	8 <i>c</i>	0.32620	0.10710	0.68120	0.1100
H1C	8 <i>c</i>	0.30040	0.23140	0.63800	0.1100
H1D	8 <i>c</i>	0.34250	0.00980	0.58140	0.0780
H1E	8 <i>c</i>	0.42000	0.07000	0.60200	0.0780
H2	8 <i>c</i>	0.47490	0.22580	0.52940	0.0610
H3	8 <i>c</i>	0.26550	0.21580	0.50800	0.0620
H4	8 <i>c</i>	0.27790	0.36120	0.40970	0.0680
H5	8 <i>c</i>	0.39130	0.43580	0.37380	0.0710
H6	8 <i>c</i>	0.49130	0.36680	0.43740	0.0760

Table SXXIV. (An)isotropic displacement parameters for (C₆H₁₀N₂)PbI₄ at 296 K with standard deviations in parentheses.

Atom	U ₁₁	U ₂₂	U ₃₃	U ₂₃	U ₁₃	U ₁₂
Pb1	0.0259(1)	0.0270(1)	0.0369(1)	0.0009(1)	-0.0001(1)	0.0002(1)
I1	0.0448(2)	0.0382(2)	0.0555(3)	0.0034(2)	-0.0083(2)	-0.0187(2)
I2	0.0417(2)	0.0743(3)	0.0333(2)	-0.0042(2)	0.0011(2)	-0.0012(2)
I3	0.0470(2)	0.0711(3)	0.0380(2)	0.0012(2)	-0.0082(2)	0.0065(2)
I4	0.0688(4)	0.0727(4)	0.1087(5)	-0.0081(4)	0.0032(3)	0.0488(3)
N1	0.095(6)	0.080(5)	0.045(4)	-0.003(4)	0.009(4)	-0.010(4)
N2	0.034(3)	0.065(4)	0.054(4)	0.001(3)	-0.003(3)	0.005(3)
C1	0.073(6)	0.068(5)	0.054(5)	0.008(4)	0.007(4)	0.015(4)
C2	0.037(3)	0.056(4)	0.040(4)	0.003(3)	0.004(3)	0.003(3)
C3	0.031(3)	0.071(5)	0.053(4)	0.006(4)	0.003(3)	-0.004(3)
C4	0.044(4)	0.073(5)	0.053(4)	0.004(4)	-0.007(3)	0.006(4)
C5	0.058(5)	0.066(5)	0.053(5)	0.016(4)	0.008(4)	0.004(4)
C6	0.041(4)	0.074(5)	0.076(6)	0.005(5)	0.015(4)	-0.008(4)

Table SXXV. Bond distances for (C₆H₁₀N₂)PbI₄ at 296 K with standard deviations in parentheses.

Bond	Distance / Å	Bond	Distance / Å
Pb1-I1	3.1994(6)	N2-H2	0.8600
Pb1-I2	3.1926(6)	C1-C2	1.503(11)
Pb1-I3	3.1620(6)	C2-C3	1.364(10)
Pb1-I4	3.1463(8)	C3-C4	1.392(11)
Pb1-I4^b	3.1689(8)	C4-C5	1.354(11)
Pb1-I1^e	3.2518(6)	C5-C6	1.360(12)
N1-C1	1.455(12)	C1-H1D	0.9700
N2-C2	1.341(8)	C1-H1E	0.9700
N2-C6	1.335(11)	C3-H3	0.9300
N1-H1C	0.8900	C4-H4	0.9300
N1-H1A	0.8900	C5-H5	0.9300
N1-H1B	0.8900	C6-H6	0.9300

$$b = 1-x, \frac{1}{2}+y, \frac{1}{2}-z; e = \frac{1}{2}-x, \frac{1}{2}+y, z$$

Table SXXVI. Bond angles for (C₆H₁₀N₂)PbI₄ at 296 K with standard deviations in parentheses.

Bond	Angle / °	Bond	Angle / °
I1-Pb1-I2	89.52(1)	C6-N2-H2	118.00
I1-Pb1-I3	89.80(1)	C2-N2-H2	118.00
I1-Pb1-I4	91.88(2)	N1-C1-C2	112.7(7)
I1-Pb1-I4 ^b	177.97(2)	N2-C2-C3	117.5(7)
I1-Pb1-I1 ^e	85.62(2)	C1-C2-C3	124.8(6)
I2-Pb1-I3	177.09(2)	N2-C2-C1	117.7(6)
I2-Pb1-I4	90.71(2)	C2-C3-C4	120.1(7)
I2-Pb1-I4 ^b	88.53(2)	C3-C4-C5	120.2(7)
I1 ^e -Pb1-I2	82.94(1)	C4-C5-C6	118.6(8)
I3-Pb1-I4	92.14(2)	N2-C6-C5	120.3(7)
I3-Pb1-I4 ^b	92.18(2)	N1-C1-H1D	109.00
I1 ^e -Pb1-I3	94.19(2)	N1-C1-H1E	109.00
I4-Pb1-I4 ^b	87.60(2)	C2-C1-H1D	109.00
I1 ^e -Pb1-I4	173.18(2)	C2-C1-H1E	109.00
I1 ^e -Pb1-I4 ^b	94.69(2)	H1D-C1-H1E	108.00
Pb1-I1-Pb1 ^d	166.19(2)	C2-C3-H3	120.00
Pb1-I4-Pb1 ^a	169.33(3)	C4-C3-H3	120.00
C2-N2-C6	123.3(6)	C3-C4-H4	120.00
C1-N1-H1C	109.00	C5-C4-H4	120.00
C1-N1-H1A	110.00	C4-C5-H5	121.00
C1-N1-H1B	110.00	C6-C5-H5	121.00
H1B-N1-H1C	110.00	N2-C6-H6	120.00
H1A-N1-H1B	109.00	C5-C6-H6	120.00
H1A-N1-H1C	109.00		

$$a = 1-x, \frac{1}{2}+y, \frac{1}{2}-z; b = 1-x, \frac{1}{2}+y, \frac{1}{2}-z; d = \frac{1}{2}-x, \frac{1}{2}+y, z; e = \frac{1}{2}-x, \frac{1}{2}+y, z$$

Table SXXVII. Hydrogen bond distances (in Å) and angles (in °) for (C₆H₁₀N₂)PbI₄ at 296 K with standard deviations in parentheses.

D-H...A	H...A	D...A	∠D-H...A
N1-H1A...I4 ^o	2.93	3.786(9)	160.7
N1-H1B...I1 ⁿ	2.79	3.676(7)	171.5
N1-H1C...I2 ^m	3.05	3.643(9)	126.2
N2-H2...I3 ^o	2.59	3.435(6)	167.5
C6-H6...I2 ^a	3.05	3.965(8)	168.0

$$a = 1-x, \frac{1}{2}+y, \frac{1}{2}-z; m = \frac{1}{2}-x, 1-y, \frac{1}{2}+z; n = x, \frac{1}{2}-y, \frac{1}{2}+z; o = 1-x, 1-y, 1-z$$

C.3 Crystallographic data for $(C_6H_{10}N_2)PbCl_4$, $(C_6H_{10}N_2)PbBr_4$ and $(C_6H_{10}N_2)PbI_4$ at 100 K and 153 K, respectively

Table SXXVIII. Crystallographic data and details of the structure refinement for $(C_6H_{10}N_2)_4Pb_4Cl_{16}^*$, $(C_6H_{10}N_2)PbBr_4^{**}$ and $(C_6H_{10}N_2)PbI_4$ at 100 K and 153 K, respectively (CCDC 1838611, CCDC 1838612 and CCDC 1838613).

Formula	$(C_6H_{10}N_2)_4Pb_4Cl_{16}$	$(C_6H_{10}N_2)PbBr_4$	$(C_6H_{10}N_2)PbI_4$
Molar mass (g mol ⁻¹)	1836.60	636.99	824.95
Crystal system	Orthorhombic	Orthorhombic	Orthorhombic
Space group	<i>Pna</i> 2 ₁ (no. 33)	<i>Pbca</i> (no. 61)	<i>Pbca</i> (no. 61)
T (K)	100	100	153
Radiation, λ (Å)	Mo K _α , 0.71073	Mo K _α , 0.71073	Mo K _α , 0.71073
<i>a</i> (Å)	18.1050(8)	17.3155(6)	18.3561(10)
<i>b</i> (Å)	15.7555(6)	8.2244(3)	8.5392(5)
<i>c</i> (Å)	16.6214(6)	18.4056(6)	19.8563(11)
<i>V</i> (Å ³)	4741.3(3)	2621.13(16)	3112.4(3)
<i>Z</i>	4	8	8
Calculated density (g cm ⁻³)	2.573	3.228	3.521
Crystal size (mm ³)	0.05 x 0.08 x 0.10	0.02 x 0.04 x 0.07	0.01 x 0.03 x 0.03
Absorption coefficient (mm ⁻¹)	15.093	25.032	18.747
F(000)	3360	2256	2832
Absorption correction	multi-scan	multi-scan	multi-scan
θ range	3.0° to 26.4°	3.2° to 27.5°	3.3° to 33.1°
Index range	-22 ≤ <i>h</i> ≤ 18, -19 ≤ <i>k</i> ≤ 19, -20 ≤ <i>l</i> ≤ 20	-22 ≤ <i>h</i> ≤ 22, -10 ≤ <i>k</i> ≤ 10, -23 ≤ <i>l</i> ≤ 23	-28 ≤ <i>h</i> ≤ 28, -13 ≤ <i>k</i> ≤ 13, -30 ≤ <i>l</i> ≤ 30
Parameters/restraints	474 / 1	122 / 0	121 / 0
Total No. of reflections	45933	46772	63128
No. of independent reflections	9700 [R _{int} = 0.0322]	3013 [R _{int} = 0.0403]	5935 [R _{int} = 0.0736]
No. of observed reflections	8927	2633	4865
Min./max. residual electron density (e Å ⁻³)	-0.71 / 2.08	-2.27 / 1.74	-2.02 / 2.8
Goof	1.02	1.06	1.08
wR2	0.0402 ^a	0.0589 ^b	0.0618 ^c
R1 (for observed reflections)	0.0196	0.0267	0.0332

$$^a w = [\sigma^2(F_0^2) + (0.0145P)^2]^{-1}, \text{with } P = (F_0^2 + 2F_c^2)/3$$

$$^b w = [\sigma^2(F_0^2) + (0.0226P)^2 + 24.8386P]^{-1}, \text{with } P = (F_0^2 + 2F_c^2)/3$$

$$^c w = [\sigma^2(F_0^2) + (0.0001P)^2 + 28.6616P]^{-1}, \text{with } P = (F_0^2 + 2F_c^2)/3$$

* This structure has been refined as a 2-component twin (BASF 0.534(4)).

** A split model was used for the refinement because of the disordered 2-(aminomethyl)pyridinium cations (site occupation factor ratio 0.68:0.32).

Table SXXIX. Atomic coordinates and equivalent isotropic displacement parameters for $(\text{C}_6\text{H}_{10}\text{N}_2)_4\text{Pb}_4\text{Cl}_{16}$ at 100 K with standard deviations in parentheses. $U(\text{eq})$ is defined as one third of the trace of the orthogonalized U tensor.

Atom	Wyck.	x	y	z	$U(\text{eq}) / \text{\AA}^2$
Pb1	4a	0.24335(2)	0.17982(2)	-0.03616(2)	0.0072(1)
Pb2	4a	0.26310(2)	0.43009(2)	0.21057(2)	0.0076(1)
Pb3	4a	0.27542(2)	0.17751(2)	0.46456(2)	0.0073(1)
Pb4	4a	0.22886(2)	0.42327(2)	0.70767(2)	0.0075(1)
Cl1	4a	0.39669(11)	0.16455(11)	-0.06640(11)	0.0152(5)
Cl2	4a	0.08658(11)	0.18679(11)	-0.01161(10)	0.0172(5)
Cl3	4a	0.26854(14)	0.04818(14)	0.08658(12)	0.0181(6)
Cl4	4a	0.24193(13)	0.31994(12)	-0.14155(13)	0.0140(6)
Cl5	4a	0.24727(15)	0.30187(14)	0.09220(13)	0.0228(6)
Cl6	4a	0.11534(10)	0.41532(11)	0.24519(11)	0.0129(5)
Cl7	4a	0.41532(11)	0.44268(11)	0.15037(11)	0.0213(6)
Cl8	4a	0.22524(13)	0.55585(13)	0.10187(12)	0.0185(6)
Cl9	4a	0.26112(11)	0.56257(13)	0.33096(14)	0.0122(5)
Cl10	4a	0.26867(12)	0.30392(14)	0.34591(13)	0.0122(6)
Cl11	4a	0.12325(10)	0.15280(11)	0.43054(10)	0.0139(5)
Cl12	4a	0.42805(10)	0.21248(10)	0.48932(10)	0.0151(5)
Cl13	4a	0.27806(11)	0.05691(14)	0.31681(12)	0.0128(5)
Cl14	4a	0.23822(13)	0.30431(13)	0.56731(12)	0.0168(6)
Cl15	4a	0.37650(9)	0.43291(9)	0.71505(11)	0.0138(5)
Cl16	4a	0.05955(10)	0.42967(10)	0.68931(10)	0.0137(5)
N1	4a	0.6554(3)	0.0623(3)	0.4402(3)	0.0127(17)
N2	4a	0.4985(4)	0.0078(4)	0.5298(4)	0.0113(17)
C1	4a	0.5812(4)	0.1023(4)	0.4559(4)	0.014(2)
C2	4a	0.5207(4)	0.0369(4)	0.4574(4)	0.0110(19)
C3	4a	0.4841(4)	0.0069(5)	0.3904(5)	0.012(2)
C4	4a	0.4287(5)	-0.0526(5)	0.3989(5)	0.013(2)
C5	4a	0.4063(5)	-0.0799(4)	0.4753(5)	0.015(2)
C6	4a	0.4439(5)	-0.0464(5)	0.5403(4)	0.018(3)
N3	4a	0.6651(3)	0.3114(3)	0.2325(3)	0.0173(19)
N4	4a	0.5102(4)	0.2546(4)	0.1427(4)	0.0127(19)
C7	4a	0.5923(4)	0.3503(4)	0.2151(5)	0.016(2)
C8	4a	0.5304(4)	0.2857(4)	0.2149(5)	0.0110(19)
C9	4a	0.4941(5)	0.2606(5)	0.2824(4)	0.012(3)
C10	4a	0.4354(5)	0.2027(5)	0.2749(4)	0.016(3)
C11	4a	0.4151(5)	0.1727(4)	0.2009(6)	0.017(3)
C12	4a	0.4527(4)	0.1996(5)	0.1335(4)	0.013(2)
N5	4a	0.3986(3)	0.1278(3)	0.7471(3)	0.0153(17)
N6	4a	0.5003(4)	0.2733(4)	0.6447(4)	0.0143(19)
C13	4a	0.3941(4)	0.2183(4)	0.7179(4)	0.0140(19)
C14	4a	0.4711(4)	0.2553(4)	0.7168(4)	0.0093(17)

Table SXXIX. Continuation.

C15	4a	0.5123(4)	0.2722(4)	0.7846(4)	0.012(2)
C16	4a	0.5833(5)	0.3067(5)	0.7763(4)	0.014(2)
C17	4a	0.6123(5)	0.3239(4)	0.7012(6)	0.021(3)
C18	4a	0.5677(5)	0.3064(5)	0.6344(4)	0.015(3)
N7	4a	0.6561(3)	0.5467(3)	0.4602(4)	0.0207(17)
N8	4a	0.4970(4)	0.5043(4)	0.5038(4)	0.0137(19)
C19	4a	0.5879(5)	0.5880(4)	0.4296(5)	0.019(2)
C20	4a	0.5230(4)	0.5296(4)	0.4314(4)	0.012(2)
C21	4a	0.4855(4)	0.5025(4)	0.3636(4)	0.016(2)
C22	4a	0.4249(5)	0.4502(5)	0.3718(4)	0.018(2)
C23	4a	0.3987(5)	0.4279(4)	0.4480(5)	0.019(3)
C24	4a	0.4365(5)	0.4555(5)	0.5133(5)	0.018(3)
H1A	4a	0.58250	0.13240	0.50820	0.0170
H1B	4a	0.57050	0.14450	0.41340	0.0170
H1C	4a	0.66750	0.02750	0.48190	0.0190
H1D	4a	0.69020	0.10370	0.43530	0.0190
H1E	4a	0.65340	0.03160	0.39390	0.0190
H2	4a	0.52190	0.02620	0.57280	0.0140
H3	4a	0.49710	0.02710	0.33840	0.0140
H4	4a	0.40540	-0.07520	0.35240	0.0150
H5	4a	0.36730	-0.11960	0.48200	0.0170
H6	4a	0.43010	-0.06270	0.59320	0.0210
H3A	4a	0.66150	0.27800	0.27700	0.0260
H3B	4a	0.69900	0.35310	0.24140	0.0260
H3C	4a	0.67960	0.27940	0.18980	0.0260
H4A	4a	0.53500	0.27050	0.09980	0.0150
H7A	4a	0.59420	0.37860	0.16200	0.0200
H7B	4a	0.58160	0.39420	0.25610	0.0200
H9	4a	0.50810	0.28170	0.33370	0.0150
H10	4a	0.40960	0.18420	0.32150	0.0190
H11	4a	0.37530	0.13370	0.19600	0.0210
H12	4a	0.43890	0.18020	0.08150	0.0160
H5A	4a	0.43940	0.10250	0.72590	0.0230
H5B	4a	0.35750	0.09910	0.73140	0.0230
H5C	4a	0.40180	0.12730	0.80180	0.0230
H6A	4a	0.47360	0.26260	0.60160	0.0170
H13A	4a	0.36210	0.25200	0.75410	0.0170
H13B	4a	0.37270	0.21990	0.66310	0.0170
H15	4a	0.49280	0.26050	0.83660	0.0150
H16	4a	0.61180	0.31840	0.82300	0.0160
H17	4a	0.66050	0.34670	0.69510	0.0250
H18	4a	0.58530	0.31810	0.58170	0.0180
H7C	4a	0.65680	0.54950	0.51490	0.0310
H7D	4a	0.69640	0.57400	0.44010	0.0310

Table SXXIX. Continuation.

H7E	4a	0.65690	0.49140	0.44450	0.0310
H8	4a	0.52100	0.52070	0.54710	0.0160
H19A	4a	0.59630	0.60720	0.37370	0.0240
H19B	4a	0.57700	0.63860	0.46280	0.0240
H21	4a	0.50140	0.51970	0.31160	0.0190
H22	4a	0.40070	0.42910	0.32520	0.0210
H23	4a	0.35550	0.39430	0.45390	0.0230
H24	4a	0.42040	0.44040	0.56580	0.0220

Table SXXX. (An)isotropic displacement parameters for $(C_6H_{10}N_2)_4Pb_4Cl_{16}$ at 100 K with standard deviations in parentheses.

Atom	U₁₁	U₂₂	U₃₃	U₂₃	U₁₃	U₁₂
Pb1	0.0096(1)	0.0064(1)	0.0055(1)	-0.0005(1)	-0.0004(2)	0.0005(1)
Pb2	0.0110(2)	0.0063(1)	0.0055(1)	-0.0003(1)	-0.0001(1)	0.0005(1)
Pb3	0.0089(1)	0.0066(1)	0.0063(1)	0.0000(1)	-0.0004(2)	-0.0001(1)
Pb4	0.0093(1)	0.0069(1)	0.0064(1)	0.0001(1)	0.0003(1)	0.0002(1)
Cl1	0.0087(9)	0.0238(9)	0.0131(8)	0.0008(7)	-0.0004(7)	0.0010(7)
Cl2	0.0126(10)	0.0205(9)	0.0184(9)	-0.0040(7)	0.0052(7)	-0.0033(7)
Cl3	0.0293(14)	0.0136(9)	0.0113(9)	0.0045(7)	-0.0011(8)	-0.0013(9)
Cl4	0.0150(11)	0.0130(9)	0.0140(10)	0.0068(7)	-0.0001(8)	0.0009(8)
Cl5	0.0366(14)	0.0153(9)	0.0164(10)	-0.0070(8)	-0.0054(9)	-0.0015(9)
Cl6	0.0083(9)	0.0181(8)	0.0122(8)	0.0010(7)	0.0007(7)	-0.0023(7)
Cl7	0.0126(10)	0.0261(9)	0.0252(10)	0.0065(8)	0.0079(8)	0.0021(8)
Cl8	0.0242(14)	0.0149(9)	0.0163(10)	0.0076(7)	-0.0045(8)	-0.0003(9)
Cl9	0.0119(10)	0.0126(8)	0.0122(9)	-0.0046(7)	0.0018(8)	-0.0008(8)
Cl10	0.0162(12)	0.0101(8)	0.0103(9)	0.0037(7)	-0.0028(7)	0.0004(8)
Cl11	0.0101(9)	0.0182(8)	0.0133(8)	-0.0007(7)	-0.0002(7)	-0.0010(7)
Cl12	0.0121(9)	0.0196(8)	0.0137(8)	-0.0021(7)	-0.0023(7)	0.0000(7)
Cl13	0.0136(10)	0.0111(8)	0.0137(10)	-0.0041(7)	-0.0007(7)	0.0017(8)
Cl14	0.0233(13)	0.0141(9)	0.0130(10)	-0.0053(7)	0.0004(8)	0.0014(9)
Cl15	0.0079(8)	0.0139(8)	0.0196(9)	0.0016(7)	-0.0006(8)	-0.0007(6)
Cl16	0.0103(9)	0.0188(9)	0.0119(8)	0.0021(6)	-0.0031(7)	-0.0009(7)
N1	0.009(3)	0.017(3)	0.012(3)	0.001(2)	-0.001(2)	0.000(2)
N2	0.013(3)	0.014(3)	0.007(3)	-0.006(2)	-0.003(2)	0.000(3)
C1	0.008(4)	0.016(3)	0.017(4)	-0.006(3)	-0.001(3)	-0.001(3)
C2	0.010(4)	0.011(3)	0.012(3)	0.004(3)	0.006(3)	0.003(3)
C3	0.008(4)	0.021(4)	0.007(4)	0.000(3)	0.000(3)	0.007(3)
C4	0.011(4)	0.014(4)	0.014(4)	0.000(3)	-0.005(3)	0.000(3)
C5	0.012(4)	0.015(4)	0.017(4)	0.001(3)	0.006(3)	-0.002(3)
C6	0.023(5)	0.018(4)	0.013(4)	0.003(3)	0.005(3)	0.002(4)
N3	0.009(3)	0.016(3)	0.027(4)	0.002(2)	0.002(3)	0.000(3)

Table SXXX. Continuation.

N4	0.014(4)	0.013(3)	0.011(3)	0.002(2)	0.001(3)	0.003(3)
C7	0.011(4)	0.012(3)	0.026(4)	-0.002(3)	0.000(4)	-0.001(3)
C8	0.011(4)	0.010(3)	0.012(3)	0.003(3)	-0.004(3)	0.002(3)
C9	0.017(5)	0.011(4)	0.009(4)	-0.005(3)	-0.001(3)	0.003(3)
C10	0.021(5)	0.017(4)	0.010(4)	0.004(3)	0.003(3)	0.004(4)
C11	0.011(4)	0.016(4)	0.025(5)	-0.002(3)	-0.002(4)	-0.005(3)
C12	0.014(4)	0.013(4)	0.013(4)	-0.004(3)	-0.001(3)	0.001(3)
N5	0.010(3)	0.014(3)	0.022(3)	-0.003(2)	0.004(3)	-0.002(2)
N6	0.014(4)	0.017(3)	0.012(3)	0.002(2)	0.001(3)	0.002(3)
C13	0.015(4)	0.011(3)	0.016(3)	0.002(3)	-0.005(3)	0.002(3)
C14	0.009(3)	0.009(3)	0.010(3)	0.002(3)	0.002(3)	0.002(3)
C15	0.013(4)	0.014(4)	0.009(4)	0.001(3)	-0.001(3)	0.005(3)
C16	0.014(4)	0.012(4)	0.015(4)	-0.002(3)	-0.003(3)	0.003(3)
C17	0.022(5)	0.015(4)	0.025(5)	0.001(3)	0.000(4)	-0.003(3)
C18	0.020(5)	0.012(4)	0.012(4)	-0.001(3)	0.001(3)	-0.001(3)
N7	0.011(3)	0.019(3)	0.032(3)	0.003(3)	-0.005(3)	-0.004(3)
N8	0.014(4)	0.011(3)	0.016(3)	-0.004(2)	-0.005(3)	0.000(3)
C19	0.018(5)	0.012(3)	0.028(4)	0.002(3)	0.001(3)	-0.002(3)
C20	0.012(4)	0.006(3)	0.018(4)	0.004(3)	0.005(3)	0.004(3)
C21	0.017(4)	0.017(4)	0.013(4)	0.000(3)	0.002(3)	0.006(3)
C22	0.019(4)	0.016(4)	0.018(4)	-0.003(3)	-0.002(3)	0.000(3)
C23	0.009(4)	0.014(4)	0.033(6)	-0.007(3)	0.005(4)	-0.005(3)
C24	0.021(5)	0.012(4)	0.021(4)	0.008(3)	0.004(3)	0.005(3)

Table SXXXI. Bond distances for $(\text{C}_6\text{H}_{10}\text{N}_2)_4\text{Pb}_4\text{Cl}_{16}$ at 100 K with standard deviations in parentheses.

Bond	Distance / Å	Bond	Distance / Å
Pb1-Cl1	2.832(2)	N1-H1C	0.9100
Pb1-Cl2	2.870(2)	N1-H1D	0.9100
Pb1-Cl3	2.945(2)	N2-H2	0.8800
Pb1-Cl4	2.818(2)	N3-C7	1.482(9)
Pb1-Cl5	2.873(2)	N4-C12	1.363(10)
Pb1-Cl9^c	2.881(2)	N4-C8	1.347(10)
Pb2-Cl5	2.835(2)	N3-H3C	0.9100
Pb2-Cl6	2.7463(19)	N3-H3A	0.9100
Pb2-Cl7	2.939(2)	N3-H3B	0.9100
Pb2-Cl8	2.768(2)	N4-H4A	0.8800
Pb2-Cl9	2.892(2)	N5-C13	1.508(8)
Pb2-Cl10	3.004(2)	N6-C18	1.338(11)
Pb3-Cl10	2.806(2)	N6-C14	1.340(10)
Pb3-Cl11	2.8393(18)	N5-H5C	0.9100

Table SXXXI. Continuation.

Pb4-Cl15	2.6801(17)	N8-C20	1.352(9)
Pb3-Cl12	2.8477(18)	N5-H5A	0.9100
Pb3-Cl13	3.105(2)	N5-H5B	0.9100
Pb3-Cl14	2.713(2)	N6-H6A	0.8800
Pb3-Cl18^d	2.981(2)	N7-C19	1.486(10)
Pb4-Cl14	2.997(2)	N8-C24	1.348(11)
Pb4-Cl16	3.0822(18)	N7-H7D	0.9100
Pb4-Cl4^b	2.998(2)	N7-H7E	0.9100
Pb4-Cl3^f	2.815(2)	N7-H7C	0.9100
Pb4-Cl13^f	2.782(2)	N8-H8	0.8800
N1-C1	1.507(9)	C1-C2	1.504(10)
N2-C2	1.349(9)	C2-C3	1.379(10)
N2-C6	1.318(11)	C3-C4	1.380(11)
N1-H1E	0.9100	C4-C5	1.401(12)
C5-C6	1.382(11)	C15-C16	1.403(11)
C1-H1B	0.9900	C16-C17	1.381(12)
C1-H1A	0.9900	C17-C18	1.400(12)
C3-H3	0.9500	C13-H13B	0.9900
C4-H4	0.9500	C13-H13A	0.9900
C5-H5	0.9500	C15-H15	0.9500
C6-H6	0.9500	C16-H16	0.9500
C7-C8	1.514(10)	C17-H17	0.9500
C8-C9	1.359(11)	C18-H18	0.9500
C9-C10	1.406(12)	C19-C20	1.493(11)
C10-C11	1.368(12)	C20-C21	1.383(10)
C11-C12	1.378(12)	C21-C22	1.379(11)
C7-H7A	0.9900	C22-C23	1.397(11)
C7-H7B	0.9900	C23-C24	1.355(12)
C9-H9	0.9500	C19-H19A	0.9900
C10-H10	0.9500	C19-H19B	0.9900
C11-H11	0.9500	C21-H21	0.9500
C12-H12	0.9500	C22-H22	0.9500
C13-C14	1.511(10)	C23-H23	0.9500
C14-C15	1.377(10)	C24-H24	0.9500

$$b = x, y, 1+z; c = \frac{1}{2}x, \frac{1}{2}y, \frac{1}{2}+z; d = \frac{1}{2}x, \frac{1}{2}y, \frac{1}{2}+z; f = \frac{1}{2}x, \frac{1}{2}y, \frac{1}{2}+z$$

Table SXXXII. Bond angles for (C₆H₁₀N₂)PbCl₄ at 100 K with standard deviations in parentheses.

Bond	Angle / °	Bond	Angle / °
Cl1-Pb1-Cl2	176.61(5)	Cl8-Pb2-Cl10	166.17(6)
Cl1-Pb1-Cl3	84.91(6)	Cl9-Pb2-Cl10	87.70(6)
Cl1-Pb1-Cl4	88.00(6)	Cl10-Pb3-Cl11	85.13(6)
Cl1-Pb1-Cl5	99.47(7)	Cl10-Pb3-Cl12	90.37(6)
Cl1-Pb1-Cl9 ^c	80.62(5)	Cl10-Pb3-Cl13	83.06(6)
Cl2-Pb1-Cl3	94.68(6)	Cl10-Pb3-Cl14	84.78(6)
Cl2-Pb1-Cl4	92.83(6)	Cl8 ^d -Pb3-Cl10	174.08(6)
Cl2-Pb1-Cl5	83.87(6)	Cl11-Pb3-Cl12	175.50(5)
Cl2-Pb1-Cl9 ^c	96.07(5)	Cl11-Pb3-Cl13	76.91(5)
Cl3-Pb1-Cl4	169.65(7)	Cl11-Pb3-Cl14	89.17(6)
Cl3-Pb1-Cl5	87.31(6)	Cl8 ^d -Pb3-Cl11	93.46(6)
Cl3-Pb1-Cl9 ^c	94.81(6)	Cl12-Pb3-Cl13	102.58(5)
Cl4-Pb1-Cl5	86.42(6)	Cl12-Pb3-Cl14	90.43(6)
Cl4-Pb1-Cl9 ^c	91.46(6)	Cl8 ^d -Pb3-Cl12	91.01(6)
Cl5-Pb1-Cl9 ^c	177.87(6)	Cl13-Pb3-Cl14	162.20(6)
Cl5-Pb2-Cl6	89.23(7)	Cl8 ^d -Pb3-Cl13	102.25(6)
Cl5-Pb2-Cl7	84.64(6)	Cl8 ^d -Pb3-Cl14	89.46(6)
Cl5-Pb2-Cl8	91.84(6)	Cl14-Pb4-Cl15	90.84(6)
Cl5-Pb2-Cl9	173.47(7)	Cl14-Pb4-Cl16	89.98(5)
Cl5-Pb2-Cl10	92.96(6)	Cl4 ^b -Pb4-Cl14	107.86(6)
Cl6-Pb2-Cl7	172.15(5)	Cl3 ^f -Pb4-Cl14	83.09(6)
Cl6-Pb2-Cl8	87.49(6)	Cl13 ^f -Pb4-Cl14	169.52(6)
Cl6-Pb2-Cl9	84.50(6)	Cl15-Pb4-Cl16	174.03(5)
Cl6-Pb2-Cl10	79.61(6)	Cl4 ^b -Pb4-Cl15	85.05(6)
Cl7-Pb2-Cl8	87.80(6)	Cl3 ^f -Pb4-Cl15	88.65(6)
Cl7-Pb2-Cl9	101.45(5)	Cl13 ^f -Pb4-Cl15	88.41(5)
Cl7-Pb2-Cl10	105.56(6)	Cl4 ^b -Pb4-Cl16	100.31(6)
Cl8-Pb2-Cl9	86.10(6)	Cl3 ^f -Pb4-Cl16	85.58(6)
Cl13 ^f -Pb4-Cl16	89.71(5)	C8-N4-H4A	119.00
Cl3 ^f -Pb4-Cl4 ^b	167.40(6)	C12-N4-H4A	119.00
Cl4 ^b -Pb4-Cl13 ^f	82.50(6)	C14-N6-C18	123.8(7)
Cl3 ^f -Pb4-Cl13 ^f	86.44(6)	C13-N5-H5B	109.00
Pb1-Cl3-Pb4 ^c	171.97(10)	C13-N5-H5C	109.00
Pb1-Cl4-Pb4 ^a	161.03(8)	H5B-N5-H5C	110.00
Pb1-Cl5-Pb2	174.25(10)	H5A-N5-H5B	110.00
Pb2-Cl8-Pb3 ^e	164.01(9)	C13-N5-H5A	109.00
Pb1 ^f -Cl9-Pb2	173.64(9)	H5A-N5-H5C	109.00
Pb2-Cl10-Pb3	176.14(9)	C14-N6-H6A	118.00
Pb3-Cl13-Pb4 ^c	167.97(8)	C18-N6-H6A	118.00
Pb3-Cl14-Pb4	164.66(9)	C20-N8-C24	123.7(7)
C2-N2-C6	124.2(7)	C19-N7-H7C	109.00
C1-N1-H1E	109.00	H7C-N7-H7D	109.00
C1-N1-H1C	110.00	H7D-N7-H7E	110.00

Table SXXXII. Continuation.

C1-N1-H1D	109.00	C19-N7-H7E	110.00
H1D-N1-H1E	109.00	H7C-N7-H7E	109.00
H1C-N1-H1D	109.00	C19-N7-H7D	109.00
H1C-N1-H1E	109.00	C20-N8-H8	118.00
C6-N2-H2	118.00	C24-N8-H8	118.00
C2-N2-H2	118.00	N1-C1-C2	111.5(5)
C8-N4-C12	122.6(7)	N2-C2-C3	117.4(7)
H3A-N3-H3B	109.00	N2-C2-C1	117.7(6)
C7-N3-H3B	109.00	C1-C2-C3	124.8(6)
C7-N3-H3C	109.00	C2-C3-C4	120.0(7)
H3B-N3-H3C	109.00	C3-C4-C5	120.8(8)
H3A-N3-H3C	110.00	C4-C5-C6	116.7(7)
C7-N3-H3A	110.00	N2-C6-C5	120.9(7)
C2-C1-H1A	109.00	C11-C10-H10	120.00
N1-C1-H1A	109.00	C9-C10-H10	120.00
C2-C1-H1B	109.00	C10-C11-H11	120.00
H1A-C1-H1B	108.00	C12-C11-H11	120.00
N1-C1-H1B	109.00	N4-C12-H12	120.00
C4-C3-H3	120.00	C11-C12-H12	121.00
C2-C3-H3	120.00	N5-C13-C14	108.6(5)
C3-C4-H4	120.00	C13-C14-C15	124.4(6)
C5-C4-H4	120.00	N6-C14-C13	117.2(6)
C4-C5-H5	122.00	N6-C14-C15	118.5(7)
C6-C5-H5	122.00	C14-C15-C16	119.4(6)
C5-C6-H6	119.00	C15-C16-C17	120.9(7)
N2-C6-H6	120.00	C16-C17-C18	117.3(8)
N3-C7-C8	112.4(5)	N6-C18-C17	120.1(7)
N4-C8-C7	116.6(7)	C14-C13-H13A	110.00
C7-C8-C9	123.5(7)	C14-C13-H13B	110.00
N4-C8-C9	119.9(7)	N5-C13-H13B	110.00
C8-C9-C10	118.8(6)	N5-C13-H13A	110.00
C9-C10-C11	120.5(7)	H13A-C13-H13B	108.00
C10-C11-C12	119.5(7)	C16-C15-H15	120.00
N4-C12-C11	118.8(7)	C14-C15-H15	120.00
C8-C7-H7A	109.00	C17-C16-H16	120.00
N3-C7-H7B	109.00	C15-C16-H16	120.00
C8-C7-H7B	109.00	C16-C17-H17	121.00
H7A-C7-H7B	108.00	C18-C17-H17	121.00
N3-C7-H7A	109.00	N6-C18-H18	120.00
C10-C9-H9	121.00	C17-C18-H18	120.00
C8-C9-H9	121.00	N7-C19-C20	112.2(5)
N8-C20-C21	117.6(6)	C20-C19-H19B	109.00
C19-C20-C21	124.1(6)	H19A-C19-H19B	108.00
N8-C20-C19	118.3(6)	C20-C21-H21	120.00

Table SXXXII. Continuation.

C20-C21-C22	119.6(6)	C22-C21-H21	120.00
C21-C22-C23	120.7(7)	C21-C22-H22	120.00
C22-C23-C24	118.3(8)	C23-C22-H22	120.00
N8-C24-C23	120.0(8)	C22-C23-H23	121.00
N7-C19-H19A	109.00	C24-C23-H23	121.00
N7-C19-H19B	109.00	N8-C24-H24	120.00
C20-C19-H19A	109.00	C23-C24-H24	120.00

$$a = x, y, -1+z; b = x, y, 1+z; c = \frac{1}{2}x, \frac{1}{2}y, \frac{1}{2}+z; d = \frac{1}{2}x, \frac{1}{2}y, \frac{1}{2}+z; e = \frac{1}{2}x, \frac{1}{2}y, \frac{1}{2}+z; f = \frac{1}{2}x, \frac{1}{2}y, \frac{1}{2}+z$$

Table SXXXIII. Hydrogen bond distances (in Å) and angles (in °) for $(C_6H_{10}N_2)_4Pb_4Cl_{16}$ at 100 K with standard deviations in parentheses.

D-H...A	H...A	D...A	$\angle D-H...A$
N1-H1C...Cl3 ^v	2.41	3.294(6)	164.7
N1-H1D...Cl10 ^w	2.52	3.332(6)	148.9
N1-H1D...Cl14 ^w	2.77	3.336(6)	121.5
N1-H1E...Cl6 ^w	2.70	3.340(5)	128.3
N1-H1E...Cl9 ^w	2.66	3.291(6)	126.8
N2-H2...Cl16 ^w	2.17	3.036(6)	169.3
N3-H3A...Cl10 ^w	2.60	3.220(6)	126.3
N3-H3A...Cl11 ^w	2.86	3.425(6)	121.4
N3-H3B...Cl13 ^w	2.37	3.232(6)	157.4
N3-H3C...Cl5 ^w	2.40	3.292(6)	165.8
N4-H4A...Cl2 ^w	2.18	3.057(7)	174.5
N5-H5A...Cl16 ^w	2.32	3.199(6)	163.6
N5-H5B...Cl8 ^d	2.71	3.485(6)	143.7
N5-H5B...Cl9 ^d	2.77	3.371(6)	124.5
N5-H5C...Cl1 ^b	2.27	3.153(6)	163.4
N6-H6A...Cl12	2.19	3.049(7)	165.9
N7-H7C...Cl7 ^t	2.61	3.419(7)	149.1
N7-H7D...Cl4 ^t	2.43	3.269(6)	154.2
N7-H7E...Cl11 ^w	2.36	3.237(6)	160.9
N8-H8...Cl7 ^t	2.15	3.026(6)	176.9
C3-H3...Cl6 ^w	2.79	3.602(8)	143.0
C4-H4...Cl16 ^c	2.79	3.501(8)	133.0
C6-H6...Cl6 ^d	2.68	3.621(7)	171.0
C9-H9...Cl11 ^w	2.83	3.660(8)	147.0
C12-H12...Cl1	2.59	3.518(7)	167.0
C15-H15...Cl1 ^b	2.81	3.659(7)	149.0
C18-H18...Cl11 ^w	2.64	3.593(7)	175.0
C19-H19A...Cl15 ^m	2.76	3.639(9)	149.0
C23-H23...Cl10	2.78	3.498(8)	133.0
C24-H24...Cl15	2.61	3.543(9)	168.0

$$b = x, y, 1+z; c = \frac{1}{2}-x, \frac{1}{2}+y, \frac{1}{2}+z; d = \frac{1}{2}-x, \frac{1}{2}+y, \frac{1}{2}+z; m = 1-x, 1-y, \frac{1}{2}+z; t = 1-x, 1-y, \frac{1}{2}+z;$$

$$v = 1-x, -y, \frac{1}{2}+z; w = \frac{1}{2}+x, \frac{1}{2}-y, z;$$

The organic cation in $(\text{C}_6\text{H}_{10}\text{N}_2)\text{PbBr}_4$ is disordered over two sets of sites at 100 K and was refined using a split model (site occupation factor ratio 0.68:0.32). In the following, the sites of the organic cation which is present in 32% of the cases is marked with an additional B.

Table SXXXIV. Atomic coordinates and equivalent isotropic displacement parameters for $(\text{C}_6\text{H}_{10}\text{N}_2)\text{PbBr}_4$ at 100 K with standard deviations in parentheses. $U(\text{eq})$ is defined as one third of the trace of the orthogonalized U tensor.

Atom	Wyck.	x	y	z	$U(\text{eq}) / \text{\AA}^2$
Pb1	8c	0.37694(2)	0.11473(2)	0.26958(2)	0.0095(1)
Br1	8c	0.26053(3)	0.37937(6)	0.27478(3)	0.0173(2)
Br2	8c	0.34582(3)	0.09573(8)	0.11365(3)	0.0279(2)
Br3	8c	0.39838(3)	0.13655(9)	0.43150(4)	0.0301(2)
Br4	8c	0.50482(4)	-0.13410(7)	0.25463(4)	0.0335(2)
N1	8c	0.3510(4)	0.8488(9)	0.6612(4)	0.022(2)
N2	8c	0.4435(3)	0.7562(9)	0.5080(4)	0.021(3)
C1	8c	0.3695(5)	0.9284(11)	0.5910(5)	0.019(3)
C2	8c	0.3705(4)	0.8090(8)	0.5285(3)	0.014(2)
C3	8c	0.3057(3)	0.7556(8)	0.4908(4)	0.013(2)
C4	8c	0.3139(4)	0.6493(8)	0.4327(4)	0.016(3)
C5	8c	0.3870(5)	0.5964(8)	0.4121(3)	0.016(3)
C6	8c	0.4518(4)	0.6498(9)	0.4498(4)	0.019(3)
N1B	8c	0.3403(9)	0.9903(18)	0.6074(8)	0.013(2)
N2B	8c	0.4413(7)	0.726(2)	0.5038(9)	0.013(2)
C1B	8c	0.3713(9)	0.821(2)	0.6084(9)	0.013(2)
C2B	8c	0.3686(9)	0.7470(19)	0.5345(7)	0.013(2)
C3B	8c	0.3029(7)	0.7045(19)	0.4954(9)	0.013(2)
C4B	8c	0.3099(10)	0.6413(19)	0.4257(9)	0.013(2)
C5B	8c	0.3826(12)	0.621(2)	0.3950(7)	0.013(2)
C6B	8c	0.4483(9)	0.663(3)	0.4341(9)	0.013(2)
H1A	8c	0.42070	0.98130	0.59470	0.0220
H1B	8c	0.33070	1.01400	0.58110	0.0220
H1C	8c	0.30720	0.78870	0.65630	0.0330
H1D	8c	0.34370	0.92610	0.69590	0.0330
H1E	8c	0.39080	0.78290	0.67450	0.0330
H2	8c	0.48450	0.79000	0.53180	0.0250
H3	8c	0.25580	0.79170	0.50490	0.0160
H4	8c	0.26970	0.61270	0.40690	0.0190
H5	8c	0.39270	0.52370	0.37230	0.0190
H6	8c	0.50170	0.61370	0.43570	0.0230
H1BA	8c	0.42530	0.82210	0.62590	0.0160
H1BB	8c	0.34040	0.75380	0.64230	0.0160
H2B	8c	0.48290	0.75320	0.52860	0.0160
H1B1	8c	0.36120	1.04570	0.56940	0.0190

Table SXXXIV. Continuation.

H3B	8c	0.25320	0.71860	0.51640	0.0160
H1B2	8c	0.35290	1.04120	0.64970	0.0190
H4B	8c	0.26510	0.61230	0.39900	0.0160
H1B3	8c	0.28810	0.98740	0.60260	0.0190
H5B	8c	0.38740	0.57750	0.34740	0.0160
H6B	8c	0.49800	0.64900	0.41310	0.0160

Table SXXXV. (An)isotropic displacement parameters for (C₆H₁₀N₂)PbBr₄ at 100 K with standard deviations in parentheses.

Atom	U₁₁	U₂₂	U₃₃	U₂₃	U₁₃	U₁₂
Pb1	0.0064(1)	0.0075(1)	0.0147(1)	0.0005(1)	0.0001(1)	-0.0003(1)
Br1	0.0146(3)	0.0119(3)	0.0253(3)	-0.0006(2)	0.0001(2)	0.0069(2)
Br2	0.0160(3)	0.0467(4)	0.0210(3)	0.0144(3)	0.0010(2)	0.0071(3)
Br3	0.0144(3)	0.0454(4)	0.0305(3)	-0.0077(3)	-0.0076(2)	0.0020(3)
Br4	0.0282(3)	0.0196(3)	0.0528(4)	0.0045(3)	0.0123(3)	0.0165(3)
N1	0.023(4)	0.019(4)	0.024(4)	-0.004(3)	0.000(3)	0.001(3)
N2	0.016(4)	0.027(6)	0.020(4)	0.007(4)	-0.005(3)	0.002(3)
C1	0.021(5)	0.015(5)	0.020(4)	-0.001(3)	-0.007(3)	0.002(4)
C2	0.008(4)	0.014(4)	0.019(4)	0.007(3)	-0.004(3)	-0.001(3)
C3	0.013(4)	0.009(4)	0.017(4)	0.005(3)	0.004(3)	0.000(3)
C4	0.013(4)	0.014(4)	0.020(5)	0.003(3)	-0.006(3)	0.000(3)
C5	0.023(5)	0.008(4)	0.017(4)	-0.001(3)	0.003(4)	0.003(3)
C6	0.009(4)	0.016(4)	0.031(6)	0.005(4)	0.003(4)	0.003(3)

Table SXXXVI. Bond distances for (C₆H₁₀N₂)PbBr₄ at 100 K with standard deviations in parentheses.

Bond	Distance / Å	Bond	Distance / Å
Pb1-Br1	2.9681(6)	C2-C3	1.391(9)
Pb1-Br2	2.9243(7)	C3-C4	1.389(10)
Pb1-Br3	3.0086(8)	C4-C5	1.391(11)
Pb1-Br4	3.0277(7)	C5-C6	1.391(11)
Pb1-Br4^b	2.9424(7)	C1-H1B	0.9900
Pb1-Br1^d	3.0696(6)	C1-H1A	0.9900
N1-C1	1.484(12)	C3-H3	0.9500
N2-C2	1.389(9)	C4-H4	0.9500
N2-C6	1.391(10)	C5-H5	0.9500
N1-H1E	0.9100	C6-H6	0.9500
N1-H1C	0.9100	C1B-C2B	1.49(2)
N1-H1D	0.9100	C2B-C3B	1.39(2)
N2-H2	0.8800	C3B-C4B	1.39(2)
N1B-C1B	1.49(2)	C4B-C5B	1.39(3)
N2B-C6B	1.39(2)	C5B-C6B	1.39(3)
N2B-C2B	1.39(2)	C1B-H1BA	0.9900
N1B-H1B3	0.9100	C1B-H1BB	0.9900
N1B-H1B1	0.9100	C3B-H3B	0.9500
N1B-H1B2	0.9100	C4B-H4B	0.9500
N2B-H2B	0.8800	C5B-H5B	0.9500
C1-C2	1.513(11)	C6B-H6B	0.9500

$$b = 1-x, \frac{1}{2}+y, \frac{1}{2}-z; d = \frac{1}{2}-x, \frac{1}{2}+y, z$$

Table SXXXVII. Bond angles for (C₆H₁₀N₂)PbBr₄ at 100 K with standard deviations in parentheses.

Bond	Angle / °	Bond	Angle / °
Br1-Pb1-Br2	86.89(2)	C1B-N1B-H1B2	109.00
Br1-Pb1-Br3	90.47(2)	C1B-N1B-H1B3	110.00
Br1-Pb1-Br4	174.43(2)	H1B2-N1B-H1B3	109.00
Br1-Pb1-Br4 ^b	87.86(2)	H1B1-N1B-H1B3	110.00
Br1-Pb1-Br1 ^d	86.26(2)	C1B-N1B-H1B1	109.00
Br2-Pb1-Br3	176.46(2)	C2B-N2B-H2B	120.00
Br2-Pb1-Br4	90.54(2)	C6B-N2B-H2B	120.00
Br2-Pb1-Br4 ^b	90.98(2)	N1-C1-C2	112.2(7)
Br1 ^d -Pb1-Br2	81.61(2)	C1-C2-C3	125.1(6)
Br3-Pb1-Br4	92.30(2)	N2-C2-C1	114.8(6)
Br3-Pb1-Br4 ^b	91.28(2)	N2-C2-C3	120.0(6)
Br1 ^d -Pb1-Br3	95.88(2)	C2-C3-C4	120.1(6)
Br4-Pb1-Br4 ^b	87.24(2)	C3-C4-C5	120.0(6)
Br1 ^d -Pb1-Br4	98.26(2)	C4-C5-C6	120.0(6)
Br1 ^d -Pb1-Br4 ^b	170.77(2)	N2-C6-C5	120.0(6)
Pb1-Br1-Pb1 ^e	171.14(2)	C2-C1-H1A	109.00
Pb1-Br4-Pb1 ^a	175.71(3)	C2-C1-H1B	109.00
C2-N2-C6	120.0(6)	N1-C1-H1B	109.00
C1-N1-H1E	109.00	N1-C1-H1A	109.00
C1-N1-H1C	109.00	H1A-C1-H1B	108.00
C1-N1-H1D	109.00	C4-C3-H3	120.00
H1D-N1-H1E	109.00	C2-C3-H3	120.00
H1C-N1-H1D	109.00	C5-C4-H4	120.00
H1C-N1-H1E	110.00	C3-C4-H4	120.00
C6-N2-H2	120.00	C4-C5-H5	120.00
C2-N2-H2	120.00	C6-C5-H5	120.00
C2B-N2B-C6B	120.0(13)	N2-C6-H6	120.00
H1B1-N1B-H1B2	109.00	C5-C6-H6	120.00
N1B-C1B-C2B	111.0(13)	C2B-C1B-H1BB	109.00
N2B-C2B-C3B	119.9(13)	H1BA-C1B-H1BB	108.00
C1B-C2B-C3B	126.9(14)	C2B-C3B-H3B	120.00
N2B-C2B-C1B	113.1(13)	C4B-C3B-H3B	120.00
C2B-C3B-C4B	120.0(13)	C3B-C4B-H4B	120.00
C3B-C4B-C5B	120.0(15)	C5B-C4B-H4B	120.00
C4B-C5B-C6B	120.1(14)	C4B-C5B-H5B	120.00
N2B-C6B-C5B	120.0(14)	C6B-C5B-H5B	120.00
N1B-C1B-H1BA	110.00	N2B-C6B-H6B	120.00
N1B-C1B-H1BB	110.00	C5B-C6B-H6B	120.00
C2B-C1B-H1BA	109.00		

$$a = 1-x, \frac{1}{2}+y, \frac{1}{2}-z; b = 1-x, \frac{1}{2}+y, \frac{1}{2}-z; d = \frac{1}{2}-x, \frac{1}{2}+y, z; e = \frac{1}{2}-x, \frac{1}{2}+y, z$$

Table SXXXVIII. Hydrogen bond distances (in Å) and angles (in °) for (C₆H₁₀N₂)PbBr₄ at 100 K with standard deviations in parentheses.

D-H...A	H...A	D...A	∠D-H...A
N1-H1C...Br1 ^t	2.84	3.409(7)	122.2
N1-H1C...Br2 ^t	2.92	3.548(7)	127.3
N1-H1D...Br1 ^u	2.60	3.438(7)	154.2
N1-H1E...Br4 ⁱⁱ	2.75	3.629(8)	162.2
N2-H2...Br3 ^w	2.22	3.084(5)	167.0
C3-H3...Br2 ^t	2.82	3.673(6)	150.0
C6-H6...Br2 ^b	2.80	3.721(7)	165.0
N1B-H1B1...Br3 ^v	2.72	3.597(14)	161.5
N1B-H1B2...Br1 ^u	2.88	3.542(16)	131.0
N1B-H1B2...Br4 ^w	3.12	3.877(14)	141.6
N1B-H1B3...Br2 ^t	2.43	3.302(15)	161.9
N2B-H2B...Br3 ^w	2.36	3.224(13)	165.6

$$b = 1-x, \frac{1}{2}+y, \frac{1}{2}-z; t = \frac{1}{2}-x, 1-y, \frac{1}{2}+z; u = x, \frac{3}{2}-y, \frac{1}{2}+z; v = x, 1+y, z; w = 1-x, 1-y, 1-z; ii = x, \frac{1}{2}-y, \frac{1}{2}+z$$

Table SXXXIX. Atomic coordinates and equivalent isotropic displacement parameters for (C₆H₁₀N₂)PbI₄ at 153 K with standard deviations in parentheses. U(eq) is defined as one third of the trace of the orthogonalized U tensor.

Atom	Wyck.	x	y	z	U(eq) / Å ²
Pb1	8c	0.38108(2)	0.37704(2)	0.27010(2)	0.0154(1)
I1	8c	0.35520(2)	0.39818(4)	0.10894(2)	0.0206(1)
I2	8c	0.39927(2)	0.35354(5)	0.42689(2)	0.0233(1)
I3	8c	0.26881(2)	0.08889(4)	0.27512(2)	0.0204(1)
I4	8c	0.52406(2)	0.18662(5)	0.24313(2)	0.0338(1)
N1	8c	0.3282(3)	0.6841(6)	0.6474(3)	0.0267(14)
N2	8c	0.4335(2)	0.7488(6)	0.5076(3)	0.0245(15)
C1	8c	0.3676(3)	0.6027(7)	0.5936(3)	0.0283(17)
C2	8c	0.3684(3)	0.6992(7)	0.5294(3)	0.0210(12)
C3	8c	0.3074(3)	0.7371(7)	0.4923(3)	0.0257(16)
C4	8c	0.3152(3)	0.8289(7)	0.4347(3)	0.0267(16)
C5	8c	0.3839(3)	0.8792(8)	0.4146(3)	0.0323(19)
C6	8c	0.4428(3)	0.8345(8)	0.4513(3)	0.0317(17)
H1A	8c	0.34400	0.50050	0.58470	0.0340
H1B	8c	0.41830	0.58240	0.60820	0.0340
H2	8c	0.474(3)	0.723(2)	0.5325(19)	0.0290
H3	8c	0.26070	0.70100	0.50580	0.0310
H4	8c	0.27350	0.85730	0.40920	0.0320
H5	8c	0.38960	0.94350	0.37590	0.0390
H6	8c	0.49040	0.86360	0.43740	0.0380

Table SXXXIX. Continuation.

H11	8c	0.3482(18)	0.776(5)	0.6545(17)	0.0400
H12	8c	0.330(2)	0.628(4)	0.6845(18)	0.0400
H13	8c	0.282(2)	0.697(5)	0.6356(11)	0.0400

Table SXL. (An)isotropic displacement parameters for (C₆H₁₀N₂)PbI₄ at 153 K with standard deviations in parentheses.

Atom	U₁₁	U₂₂	U₃₃	U₂₃	U₁₃	U₁₂
Pb1	0.0132(1)	0.0152(1)	0.0176(1)	0.0006(1)	-0.0007(1)	0.0002(1)
I1	0.0178(1)	0.0279(2)	0.0162(2)	-0.0017(1)	0.0004(1)	0.0003(1)
I2	0.0202(2)	0.0325(2)	0.0173(2)	-0.0009(1)	-0.0031(1)	0.0034(1)
I3	0.0205(2)	0.0172(1)	0.0235(2)	0.0012(1)	-0.0037(1)	-0.0067(1)
I4	0.0271(2)	0.0313(2)	0.0428(2)	-0.0045(2)	-0.0025(2)	0.0172(2)
N1	0.023(2)	0.034(3)	0.023(2)	0.003(2)	0.0028(19)	-0.007(2)
N2	0.0155(19)	0.032(3)	0.026(3)	-0.002(2)	-0.0005(18)	0.0020(18)
C1	0.034(3)	0.028(3)	0.023(3)	0.004(2)	-0.003(2)	0.010(2)
C2	0.021(2)	0.022(2)	0.020(2)	-0.0023(19)	0.003(2)	0.0045(19)
C3	0.016(2)	0.036(3)	0.025(3)	0.000(2)	0.005(2)	0.002(2)
C4	0.020(2)	0.038(3)	0.022(3)	0.001(2)	-0.002(2)	0.005(2)
C5	0.029(3)	0.044(4)	0.024(3)	0.011(3)	0.011(2)	0.008(3)
C6	0.021(3)	0.037(3)	0.037(3)	0.003(3)	0.006(2)	-0.001(2)

Table SXLI. Bond distances for (C₆H₁₀N₂)PbI₄ at 153 K with standard deviations in parentheses.

Bond	Distance / Å	Bond	Distance / Å
Pb1-I1	3.2401(6)	N2-H2	0.92(5)
Pb1-I2	3.1376(6)	C1-C2	1.518(8)
Pb1-I3	3.2111(5)	C2-C3	1.379(8)
Pb1-I4	3.1335(5)	C3-C4	1.394(8)
Pb1-I4^b	3.1764(5)	C4-C5	1.391(8)
Pb1-I3^e	3.2943(5)	C5-C6	1.359(8)
N1-C1	1.465(8)	C1-H1A	0.9900
N2-C2	1.340(7)	C1-H1B	0.9900
N2-C6	1.347(8)	C3-H3	0.9500
N1-H13	0.89(4)	C4-H4	0.9500
N1-H11	0.88(4)	C5-H5	0.9500
N1-H12	0.88(4)	C6-H6	0.9500

$$b = 1-x, \frac{1}{2}+y, \frac{1}{2}-z; e = \frac{1}{2}-x, \frac{1}{2}+y, z$$

Table SXLII. Bond angles for (C₆H₁₀N₂)PbI₄ at 153 K with standard deviations in parentheses.

Bond	Angle / °	Bond	Angle / °
I1-Pb1-I2	177.63(2)	C6-N2-H2	118(3)
I1-Pb1-I3	88.81(1)	C2-N2-H2	118(3)
I1-Pb1-I4	89.02(1)	N1-C1-C2	111.1(5)
I1-Pb1-I4 ^b	87.27(1)	N2-C2-C3	118.5(5)
I1-Pb1-I3 ^e	82.93(1)	C1-C2-C3	124.6(5)
I2-Pb1-I3	89.34(1)	N2-C2-C1	116.9(5)
I2-Pb1-I4	92.71(1)	C2-C3-C4	119.1(5)
I2-Pb1-I4 ^b	94.41(1)	C3-C4-C5	120.2(5)
I2-Pb1-I3 ^e	95.39(1)	C4-C5-C6	118.8(6)
I3-Pb1-I4	98.35(1)	N2-C6-C5	119.8(5)
I3-Pb1-I4 ^b	172.80(2)	N1-C1-H1A	109.00
I3-Pb1-I3 ^e	83.33(1)	N1-C1-H1B	109.00
I4-Pb1-I4 ^b	87.63(1)	C2-C1-H1A	109.00
I3_e-Pb1-I4	171.75(2)	C2-C1-H1B	109.00
I3_e-Pb1-I4 ^b	90.19(1)	H1A-C1-H1B	108.00
Pb1-I3-Pb1 ^d	162.91(1)	C2-C3-H3	120.00
Pb1-I4-Pb1 ^a	154.84(2)	C4-C3-H3	120.00
C2-N2-C6	123.6(5)	C3-C4-H4	120.00
C1-N1-H13	109.8(19)	C5-C4-H4	120.00
C1-N1-H11	110(2)	C4-C5-H5	121.00
C1-N1-H12	110(2)	C6-C5-H5	121.00
H12-N1-H13	109(3)	N2-C6-H6	120.00
H11-N1-H12	110(3)	C5-C6-H6	120.00
H11-N1-H13	109(4)		

$$a = 1-x, \frac{1}{2}+y, \frac{1}{2}-z; b = 1-x, \frac{1}{2}+y, \frac{1}{2}-z; d = \frac{1}{2}-x, \frac{1}{2}+y, z; e = \frac{1}{2}-x, \frac{1}{2}+y, z$$

Table SXLIII. Hydrogen bond distances (in Å) and angles (in °) for (C₆H₁₀N₂)PbI₄ at 153 K with standard deviations in parentheses.

D-H...A	H...A	D...A	∠D-H...A
N1-H11...I1 ^o	2.93	3.682(5)	144.9
N1-H11...I4 ⁱ	3.12	3.646(5)	120.7
N1-H12...I3 ^p	2.82	3.612(5)	151.1
N1-H13...I1 ^m	2.71	3.523(5)	155.2
N2-H2...I2 ⁱ	2.54	3.446(5)	166.1
C6-H6...I1 ^b	2.99	3.934(6)	170.0

$$b = 1-x, \frac{1}{2}+y, \frac{1}{2}-z; i = 1-x, 1-y, 1-z; m = \frac{1}{2}-x, 1-y, \frac{1}{2}+z; o = x, \frac{3}{2}-y, \frac{1}{2}+z; p = x, \frac{1}{2}-y, \frac{1}{2}+z$$

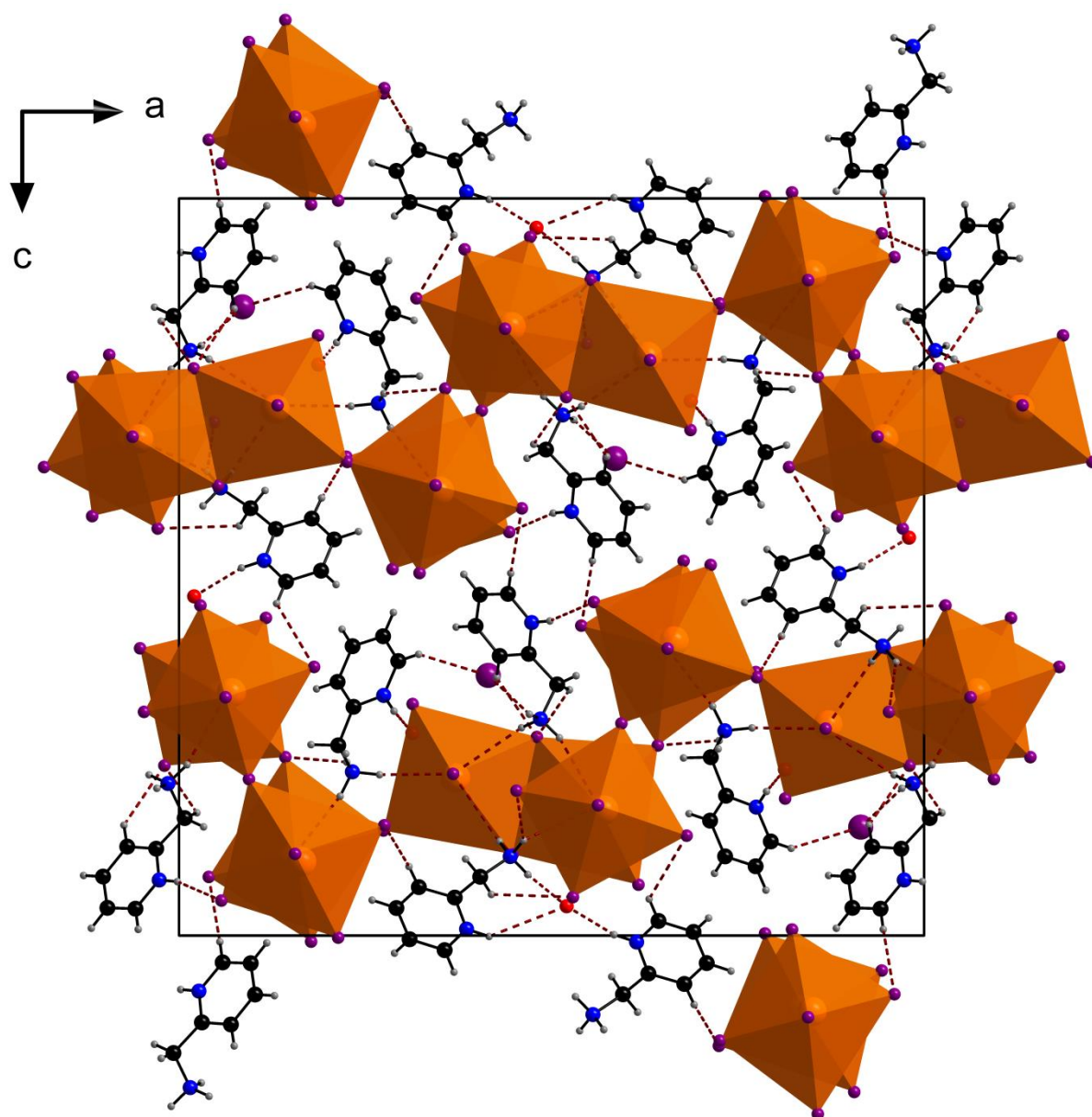
C.4 Hydrogen bonds in $(\text{C}_6\text{H}_{10}\text{N}_2)_6\text{IPb}_5\text{I}_{21} \cdot 3 \text{H}_2\text{O}$ and $(\text{C}_6\text{H}_{10}\text{N}_2)\text{PbI}_4$ at 296 K

Figure S1. Crystal structure of $(\text{C}_6\text{H}_{10}\text{N}_2)_6\text{IPb}_5\text{I}_{21} \cdot 3 \text{H}_2\text{O}$ at 296 K projected down the b axis. Hydrogen bonds are highlighted with red dashed lines. For clarity the hydrogen atoms of the water molecules are omitted. Pb is displayed in orange, I is purple, N is blue, C is black, O is red, and H is grey.

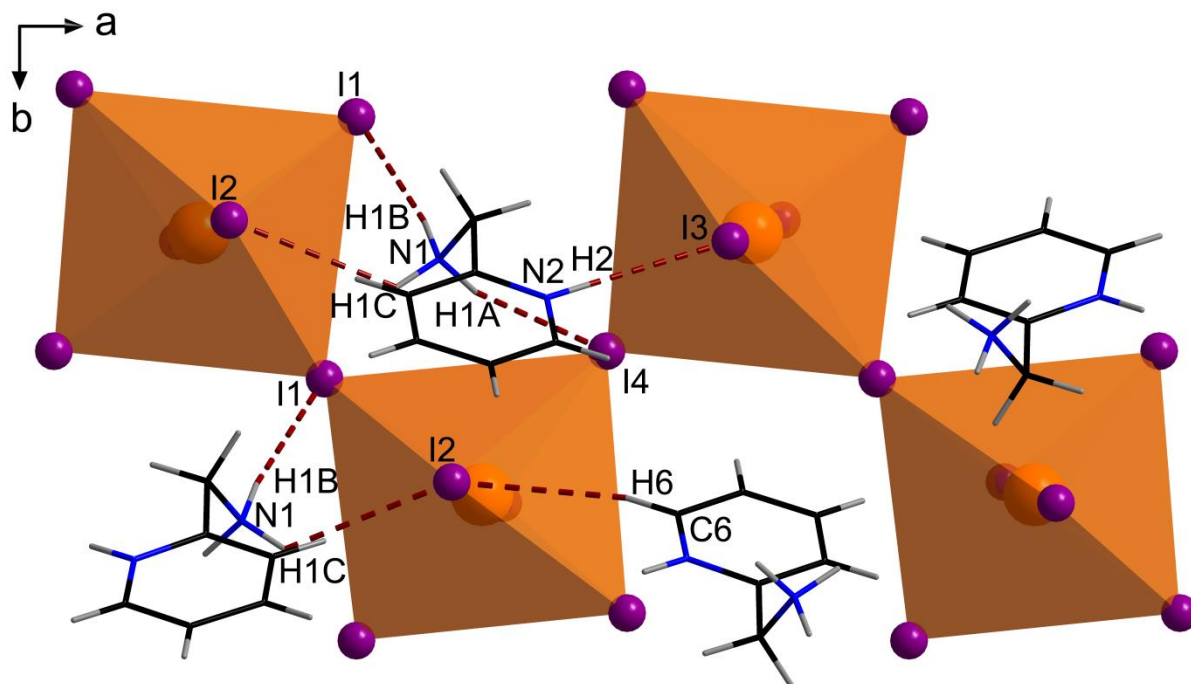


Figure S2. Section of the crystal structure of $(C_6H_{10}N_2)PbI_4$ at 296 K projected down the c axis. Hydrogen bonds are indicated with red dashed lines. Pb is displayed in orange, I is purple, N is blue, C is black, and H is grey.

C.5 Disorder in $(C_6H_{10}N_2)PbBr_4$ at 100 K

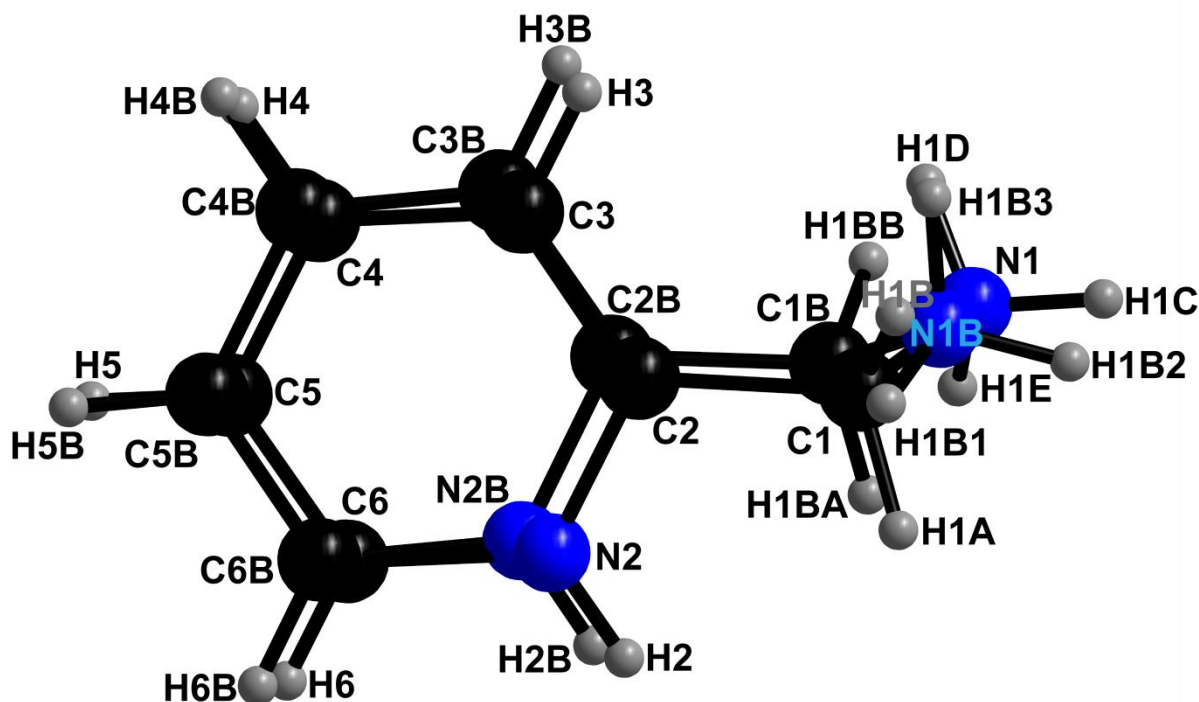


Figure S3. Representation of the disordered 2-(aminomethyl)pyridinium cations in $(C_6H_{10}N_2)PbBr_4$ at 100 K with labeling of atoms. N is displayed in blue, C is black, and H is grey.

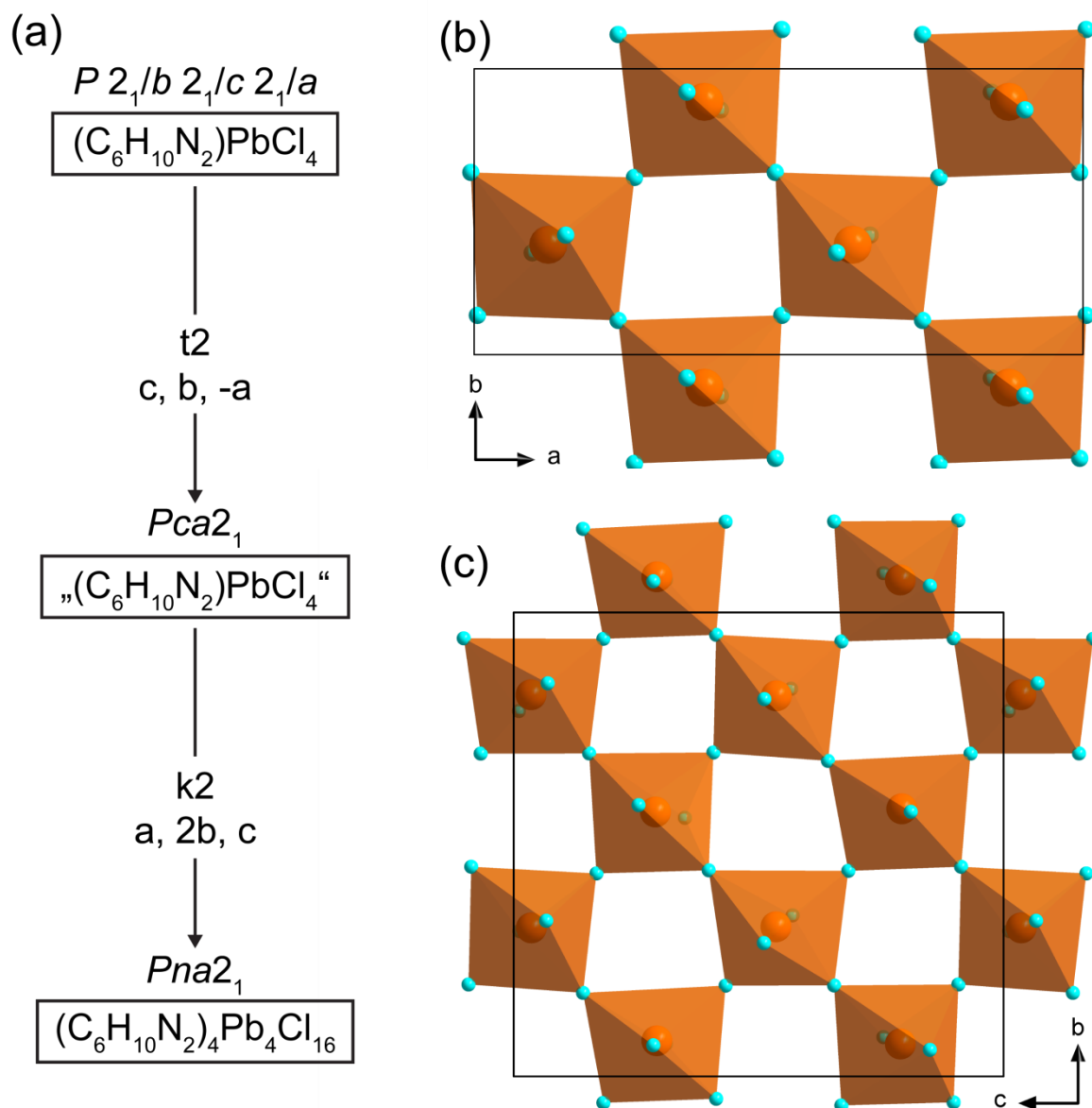
C.6 Temperature-dependent phase transition in $(\text{C}_6\text{H}_{10}\text{N}_2)\text{PbCl}_4$ 

Figure S4. (a) Bärnighausen tree illustrating the group-subgroup relations between the space group of $(\text{C}_6\text{H}_{10}\text{N}_2)\text{PbCl}_4$ at 296 K and the space group of $(\text{C}_6\text{H}_{10}\text{N}_2)_4\text{Pb}_4\text{Cl}_{16}$ at 100 K. (b, c) Comparison of the octahedral tilting patterns in (b) $(\text{C}_6\text{H}_{10}\text{N}_2)\text{PbCl}_4$ at 296 K and (c) $(\text{C}_6\text{H}_{10}\text{N}_2)_4\text{Pb}_4\text{Cl}_{16}$ at 100 K. Pb is displayed in orange, and Cl is turquoise.

C.7 Octahedral distortion in $(C_6H_{10}N_2)PbX_4$ ($X = Cl, Br$ and I) and $(C_6H_{10}N_2)_6IPb_5I_{21} \cdot 3 H_2O$

Table SXLIV. Overview of the magnitude of the distortions found for the individual octahedra in $(C_6H_{10}N_2)PbCl_4$, $(C_6H_{10}N_2)PbBr_4$, $(C_6H_{10}N_2)PbI_4$, and $(C_6H_{10}N_2)_6IPb_5I_{21} \cdot 3 H_2O$.

compound	Δd_{Pb1} ($\times 10^{-4}$)	Δd_{Pb2} ($\times 10^{-4}$)	Δd_{Pb3} ($\times 10^{-4}$)	Δd_{Pb4} ($\times 10^{-4}$)	Δd_{Pb5} ($\times 10^{-4}$)	Δd_{avg} ($\times 10^{-4}$)
$(C_6H_{10}N_2)PbCl_4$	6.8					6.8
$(C_6H_{10}N_2)PbBr_4$	2.3					2.3
$(C_6H_{10}N_2)PbI_4$	1.1					1.1
$(C_6H_{10}N_2)_6IPb_5I_{21} \cdot 3 H_2O$	5.0	0.8	11.3	51.3	19.3	17.5

$$\Delta d = \frac{1}{6} \sum \left[\frac{d_n - d}{d} \right]^2 \quad (1)$$

d_n individual Pb- X ($X = Cl, Br, I$) distances

d arithmetic mean of the individual Pb- X ($X = Cl, Br, I$) distances

The equation was introduced by Alonso et al. to determine the relative distortion of octahedra quantitatively.¹

C.8 Rietveld refinement results

The Rietveld refinement results of $(C_6H_{10}N_2)_6IPb_5I_{21} \cdot 3 H_2O$ and $(C_6H_{10}N_2)PbX_4$ ($X = Cl, Br, I$) are listed in the following. The lattice parameters and atom positions of the heavy atoms Pb, Cl, Br and I were freely refined. The peak profile was determined using the fundamental parameter approach. Additionally, the microstructure using a Lorentzian component for microstrain broadening and a Gaussian component for the crystallite size in the case of $(C_6H_{10}N_2)PbCl_4$ and $(C_6H_{10}N_2)PbBr_4$ and a Lorentzian component for the crystallite size in the case of $(C_6H_{10}N_2)_6IPb_5I_{21} \cdot 3 H_2O$ was subject of refinement.

7. Appendix

(C₆H₁₀N₂)₆IPb**₅I₂₁ · 3 H₂O**radiation: Cu K_{α1}space group: *Pnma*orthorhombic, $a = 26.5427(5)$ Å, $b = 12.9247(2)$ Å, $c = 26.2812(5)$ Å, $\alpha = \beta = \gamma = 90^\circ$

Atom	Wyck.	x	y	z	occ.	B _{eq} (Å ²)
Pb1	4c	0.4297(3)	$\frac{3}{4}$	0.1704(3)	1	1
Pb2	4c	0.4456(3)	$\frac{1}{4}$	0.1748(3)	1	1
Pb3	4c	0.6281(3)	$\frac{1}{4}$	0.2145(3)	1	1
Pb4	4c	0.3509(3)	$\frac{1}{4}$	0.3957(3)	1	1
Pb5	4c	0.3335(3)	$\frac{3}{4}$	0.4007(3)	1	1
I1	4c	0.3222(5)	$\frac{3}{4}$	0.1362(4)	1	1
I2	4c	0.4042(4)	$\frac{3}{4}$	0.2885(5)	1	1
I3	4c	0.4715(5)	$\frac{3}{4}$	0.0555(4)	1	1
I4	4c	0.5469(4)	$\frac{3}{4}$	0.1983(5)	1	1
I5	8d	0.4382(3)	0.4942(7)	0.1770(3)	1	1
I6	4c	0.3847(4)	$\frac{1}{4}$	0.0716(4)	1	1
I7	4c	0.3562(4)	$\frac{1}{4}$	0.2564(5)	1	1
I8	4c	0.5536(4)	$\frac{1}{4}$	0.1110(5)	1	1
I9	4c	0.5194(4)	$\frac{1}{4}$	0.2719(4)	1	1
I10	4c	0.6886(4)	$\frac{1}{4}$	0.3125(5)	1	1
I11	4c	0.7251(4)	$\frac{1}{4}$	0.1450(4)	1	1
I12	8d	0.6322(3)	0.4923(7)	0.2203(3)	1	1
I13	4c	0.4595(5)	$\frac{1}{4}$	0.4201(5)	1	1
I14	4c	0.3222(5)	$\frac{1}{4}$	0.5070(4)	1	1
I15	8d	0.3435(3)	0.4978(8)	0.3879(3)	1	1
I16	4c	0.2291(4)	$\frac{3}{4}$	0.3504(4)	1	1
I17	4c	0.2865(4)	$\frac{3}{4}$	0.5025(5)	1	1
I18	4c	0.4421(4)	$\frac{3}{4}$	0.4525(4)	1	1
I19	4c	0.4133(4)	$\frac{1}{4}$	0.6464(5)	1	1

R_{exp} = 2.38 %, R_{wp} = 4.97 %, R_p = 3.90 %, R_{Bragg} = 2.12 %, GooF = 2.09

(C₆H₁₀N₂)₆IPb**₅I₂₁ · 3 H₂O, 9 months after synthesis**radiation: Cu K_{α1}space group: *Pnma*orthorhombic, $a = 26.5582(3)$ Å, $b = 12.9221(1)$ Å, $c = 26.2863(3)$ Å, $\alpha = \beta = \gamma = 90^\circ$

Atom	Wyck.	x	y	z	occ.	B _{eq} (Å ²)
Pb1	4c	0.4294(3)	$\frac{3}{4}$	0.1700(3)	1	1
Pb2	4c	0.4462(3)	$\frac{1}{4}$	0.1745(3)	1	1
Pb3	4c	0.6283(3)	$\frac{1}{4}$	0.2150(3)	1	1
Pb4	4c	0.3500(3)	$\frac{1}{4}$	0.3958(3)	1	1
Pb5	4c	0.3344(3)	$\frac{3}{4}$	0.4003(3)	1	1
I1	4c	0.3205(4)	$\frac{3}{4}$	0.1361(4)	1	1
I2	4c	0.4065(4)	$\frac{3}{4}$	0.2864(5)	1	1
I3	4c	0.4716(4)	$\frac{3}{4}$	0.0530(4)	1	1
I4	4c	0.5465(4)	$\frac{3}{4}$	0.1975(4)	1	1
I5	8d	0.4383(3)	0.4940(7)	0.1783(3)	1	1
I6	4c	0.3839(4)	$\frac{1}{4}$	0.0704(4)	1	1
I7	4c	0.3570(4)	$\frac{1}{4}$	0.2569(5)	1	1
I8	4c	0.5532(4)	$\frac{1}{4}$	0.1111(5)	1	1
I9	4c	0.5202(4)	$\frac{1}{4}$	0.2701(5)	1	1
I10	4c	0.6867(4)	$\frac{1}{4}$	0.3151(5)	1	1
I11	4c	0.7250(4)	$\frac{1}{4}$	0.1445(4)	1	1
I12	8d	0.6321(3)	0.4930(7)	0.2196(3)	1	1
I13	4c	0.4592(4)	$\frac{1}{4}$	0.4188(5)	1	1
I14	4c	0.3231(5)	$\frac{1}{4}$	0.5076(4)	1	1
I15	8d	0.3443(3)	0.4961(7)	0.3884(3)	1	1
I16	4c	0.2262(4)	$\frac{3}{4}$	0.3504(4)	1	1
I17	4c	0.2863(4)	$\frac{3}{4}$	0.5017(4)	1	1
I18	4c	0.4435(4)	$\frac{3}{4}$	0.4532(4)	1	1
I19	4c	0.4156(4)	$\frac{1}{4}$	0.6468(5)	1	1

R_{exp} = 3.21 %, R_{wp} = 5.90 %, R_p = 4.24 %, R_{Bragg} = 2.43 %, GooF = 1.84

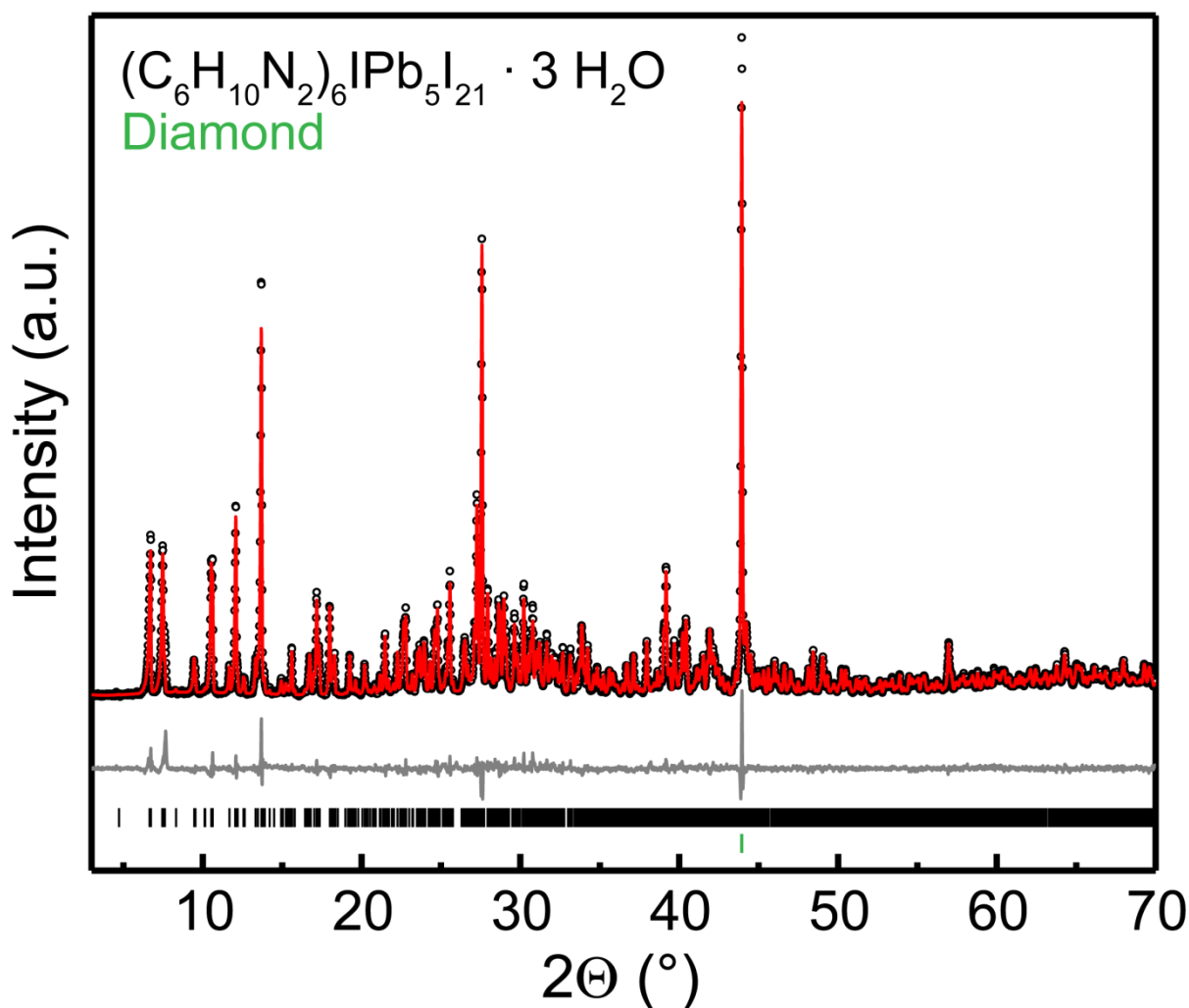


Figure S5. X-ray powder diffraction data ($\lambda = \text{Cu K}\alpha_1$) of $(\text{C}_6\text{H}_{10}\text{N}_2)_6\text{IPb}_5\text{I}_{21} \cdot 3 \text{H}_2\text{O}$ represented by black open circles recorded 9 months after synthesis. The Rietveld profile fit is displayed in red and the difference profile in grey. $(\text{C}_6\text{H}_{10}\text{N}_2)_6\text{IPb}_5\text{I}_{21} \cdot 3 \text{H}_2\text{O}$ (black ticks) was diluted with diamond (green tick) to increase signal intensity.

$(\text{C}_6\text{H}_{10}\text{N}_2)\text{PbCl}_4$

radiation: Ag $\text{K}\alpha_1$

space group: *Pbca*

orthorhombic, $a = 16.7133(11) \text{ \AA}$, $b = 7.8551(5) \text{ \AA}$, $c = 18.4129(12) \text{ \AA}$, $\alpha = \beta = \gamma = 90^\circ$

Atom	Wyck.	x	y	z	occ.	$B_{\text{eq}} (\text{\AA}^2)$
Pb1	8c	0.6230(5)	0.3835(5)	0.2681(3)	1	1
Cl1	8c	0.732(2)	0.117(7)	0.268(2)	1	1
Cl2	8c	0.594(2)	0.352(4)	0.425(2)	1	1
Cl3	8c	0.498(2)	0.154(5)	0.244(2)	1	1
Cl4	8c	0.652(2)	0.425(4)	0.120(2)	1	1

$R_{\text{exp}} = 1.55 \%$, $R_{\text{wp}} = 3.81 \%$, $R_p = 2.58 \%$, $R_{\text{Bragg}} = 2.12 \%$, $\text{Goof} = 2.46$

(C₆H₁₀N₂)PbBr₄radiation: Ag K_{α1}space group: *Pbca*orthorhombic, $a = 17.3844(10)$ Å, $b = 8.2415(5)$ Å, $c = 18.7176(10)$ Å, $\alpha = \beta = \gamma = 90^\circ$

Atom	Wyck.	x	y	z	occ.	B _{eq} (Å ²)
Pb1	8c	0.3769(4)	0.6209(6)	0.2696(3)	1	1
Br1	8c	0.3996(6)	0.651(2)	0.4286(5)	1	1
Br2	8c	0.4962(8)	0.866(3)	0.2451(6)	1	1
Br3	8c	0.3508(7)	0.598(2)	0.1157(5)	1	1
Br4	8c	0.2593(8)	0.895(3)	0.2749(6)	1	1

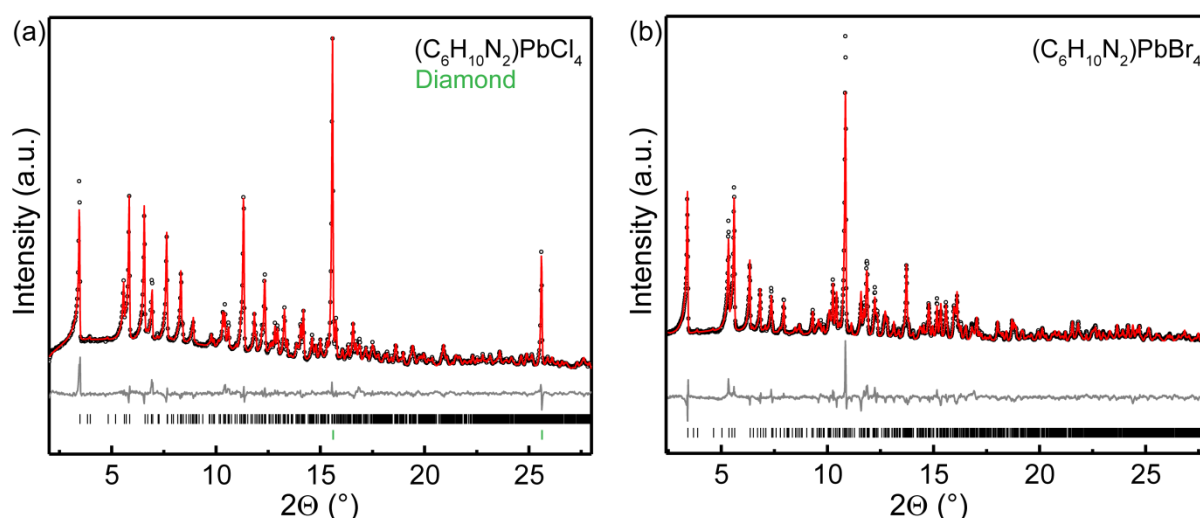
 $R_{\text{exp}} = 1.04$ %, $R_{\text{wp}} = 3.91$ %, $R_p = 2.76$ %, $R_{\text{Bragg}} = 3.09$ %, $\text{Goof} = 3.77$ 

Figure S6. X-ray powder diffraction data ($\lambda = \text{Ag K}\alpha_1$) of (C₆H₁₀N₂)PbCl₄ (a) and (C₆H₁₀N₂)PbBr₄ (b) represented by black open circles. The Rietveld profile fit is displayed in red and the difference profile in grey. (C₆H₁₀N₂)PbCl₄ (black ticks) was diluted with diamond (green ticks) to increase signal intensity.

(C₆H₁₀N₂)PbI₄radiation: Mo K_{α1}space group: *Pbca*orthorhombic, $a = 18.3652(6)$ Å, $b = 8.7090(3)$ Å, $c = 19.6585(6)$ Å, $\alpha = \beta = \gamma = 90^\circ$

Atom	Wyck.	x	y	z	occ.	B _{eq} (Å ²)
Pb1	8c	0.3774(3)	0.8748(5)	0.2685(2)	1	1
I1	8c	0.2652(3)	0.5960(9)	0.2764(3)	1	1
I2	8c	0.3506(3)	0.8931(9)	0.1106(3)	1	1
I3	8c	0.3961(4)	0.8497(8)	0.4288(3)	1	1
I4	8c	0.5077(3)	0.649(2)	0.2440(3)	1	1

 $R_{\text{exp}} = 1.86$ %, $R_{\text{wp}} = 4.88$ %, $R_p = 3.62$ %, $R_{\text{Bragg}} = 2.63$ %, $\text{Goof} = 2.63$

The conversion of $(\text{C}_6\text{H}_{10}\text{N}_2)_6\text{IPb}_5\text{I}_{21} \cdot 3 \text{H}_2\text{O}$ to $(\text{C}_6\text{H}_{10}\text{N}_2)\text{PbI}_4$ induced by heating the sample to 160°C was monitored by powder X-ray diffraction. A Rietveld refinement of the final product's powder pattern recorded at 30°C was performed to ensure complete transformation. The background was modelled by Chebychev polynomials of 13th order with an additional peak phase for modelling the amorphous hump around $10^\circ 2\theta$. The lattice parameters, peak profile, microstructure using a Gaussian component for the crystallite size and a Lorentzian component for microstrain broadening were freely refined. The results are shown in the following.

$(\text{C}_6\text{H}_{10}\text{N}_2)\text{PbI}_4$

radiation: Mo $K_{\alpha 1}$

space group: *Pbca*

orthorhombic, $a = 18.3644(10) \text{ \AA}$, $b = 8.7262(4) \text{ \AA}$, $c = 19.6313(9) \text{ \AA}$, $\alpha = \beta = \gamma = 90^\circ$

$R_{\text{exp}} = 1.88 \%$, $R_{\text{wp}} = 3.39 \%$, $R_p = 2.56 \%$, $R_{\text{Bragg}} = 1.68 \%$, $\text{GooF} = 1.80$

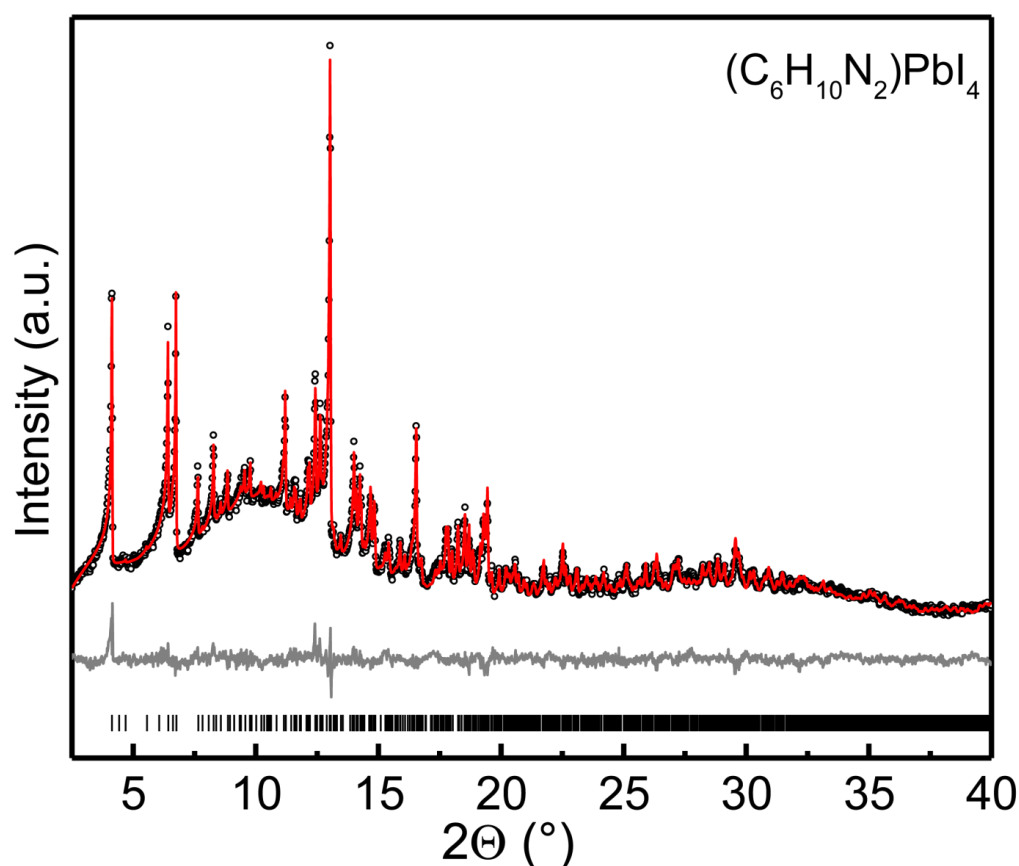


Figure S7. X-ray powder diffraction data ($\lambda = \text{Mo } K_{\alpha 1}$) of $(\text{C}_6\text{H}_{10}\text{N}_2)\text{PbI}_4$ at 30°C represented by black open circles. The Rietveld profile fit is displayed in red and the difference profile in grey. $(\text{C}_6\text{H}_{10}\text{N}_2)\text{PbI}_4$ was obtained as the final product of the temperature-dependent PXRD measurement of $(\text{C}_6\text{H}_{10}\text{N}_2)_6\text{IPb}_5\text{I}_{21} \cdot 3 \text{H}_2\text{O}$. $(\text{C}_6\text{H}_{10}\text{N}_2)_6\text{IPb}_5\text{I}_{21} \cdot 3 \text{H}_2\text{O}$ was heated in an open capillary to 160°C and subsequently cooled down to 30°C .

C.9 Thermal analysis

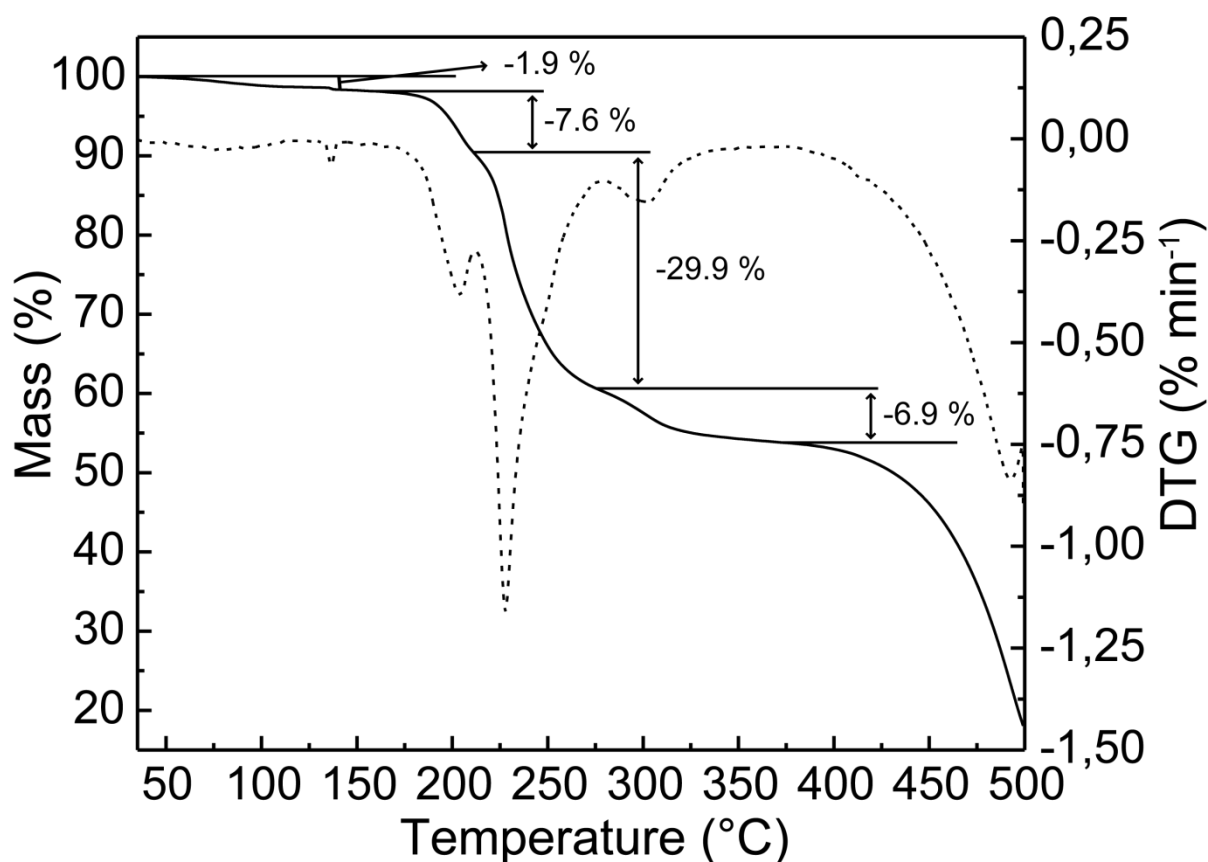


Figure S8. TG (solid line) and DTG (dashed line) data of $(\text{C}_6\text{H}_{10}\text{N}_2)_6\text{IPb}_5\text{I}_{21} \cdot 3 \text{H}_2\text{O}$ recorded with a heating rate of 1 K min^{-1} .

C.10 Solid-state NMR spectroscopy

^1H , ^{13}C and ^{15}N solid-state NMR spectroscopy measurements on $(\text{C}_6\text{H}_{10}\text{N}_2)_6\text{IPb}_5\text{I}_{21} \cdot 3 \text{H}_2\text{O}$ and $(\text{C}_6\text{H}_{10}\text{N}_2)\text{PbI}_4$ were performed to confirm phase-purity. The results and the assignment of the signals are discussed below.

The compound $(\text{C}_6\text{H}_{10}\text{N}_2)_6\text{IPb}_5\text{I}_{21} \cdot 3 \text{H}_2\text{O}$ contains three crystallographically distinct 2-(aminomethyl)pyridinium cations with six inequivalent carbon atoms each. Two out of these three organic molecules exhibit a very similar conformation as illustrated in Figure S9. The recorded ^{13}C NMR spectrum only shows 12 instead of 18 signals, since two out of the three crystallographically distinct organic molecules feature nearly the same chemical environments and, hence, shifts, and the signals are not resolved (Figure S10b). Five signals can be observed in the ^{15}N NMR spectrum: The signals at 172.7 and 175.4 ppm can be assigned to the aromatic NH^+ -group and the signals at 331.5, 333.2 and 335.5 ppm can be assigned to the exocyclic NH_3^+ -group. The three crystallographically distinct organic cations vary most widely in the position of the

NH_3^+ -group which is a possible explanation for the resolution of all three signals (Figure S10c). The ^1H spectrum shows very broad and overlapping signals. The assignment is displayed in Figure S10a showing the deconvoluted signals.²

$(\text{C}_6\text{H}_{10}\text{N}_2)\text{PbI}_4$ contains one crystallographically distinct 2-(aminomethyl)pyridinium cation. The ^{13}C and ^{15}N spectra show the expected number of signals (Figure S13). No impurities were detected. The protonation of both amino groups could be verified with a ^{15}N , ^1H HETCOR MAS solid-state NMR spectrum of $(\text{C}_6\text{H}_{10}\text{N}_2)\text{PbI}_4$ at 298 K. The spectrum assigns both signals in the ^{15}N spectrum to signals in the ^1H spectrum. Due to the lower pK_a value of the aromatic amino group (2.73) and its evident protonation, the exocyclic amino group must also be protonated ($\text{pK}_a = 8.99$) (Figure S15).³ CASTEP calculations to assign the chemical shifts have been carried out for $(\text{C}_6\text{H}_{10}\text{N}_2)\text{PbI}_4$.⁴⁻⁵ The results are in good agreement with the experimental data as demonstrated in Figure S13b.

^1H and ^{13}C NMR spectra of $(\text{C}_6\text{H}_{10}\text{N}_2)_6\text{IPb}_5\text{I}_{21} \cdot 3 \text{H}_2\text{O}$ and $(\text{C}_6\text{H}_{10}\text{N}_2)\text{PbI}_4$ were recorded at 343 K to confirm that the crystal structure is maintained at the temperature where the impedance spectroscopy measurements were performed (Figures 11 and 14).

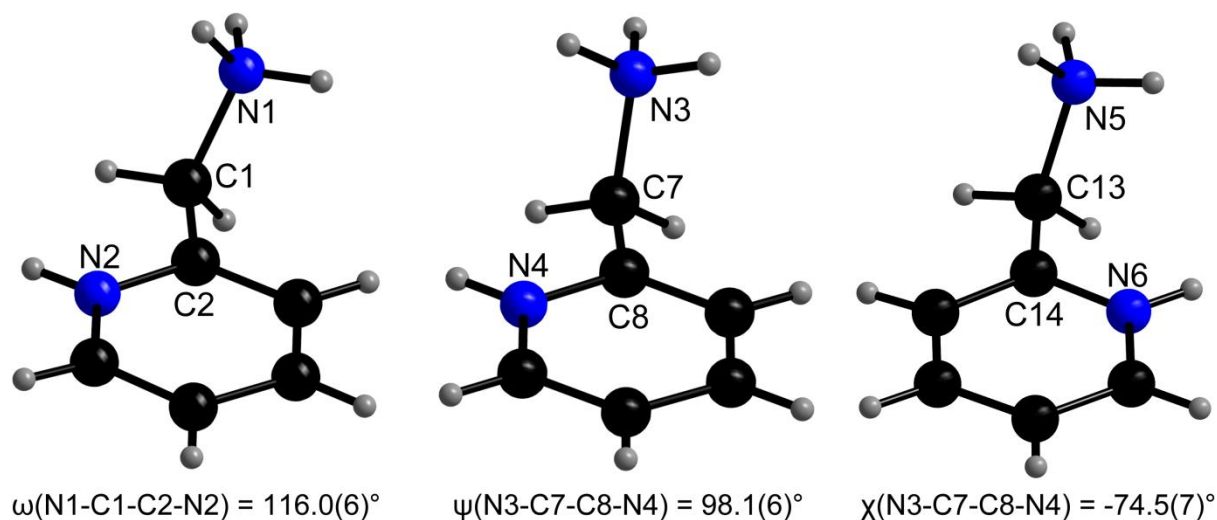


Figure S9. Conformation of the 2-(aminomethyl)pyridinium cations in $(\text{C}_6\text{H}_{10}\text{N}_2)_6\text{IPb}_5\text{I}_{21} \cdot 3 \text{H}_2\text{O}$ at 298 K and torsion angles illustrating the positioning of the amino groups to each other.

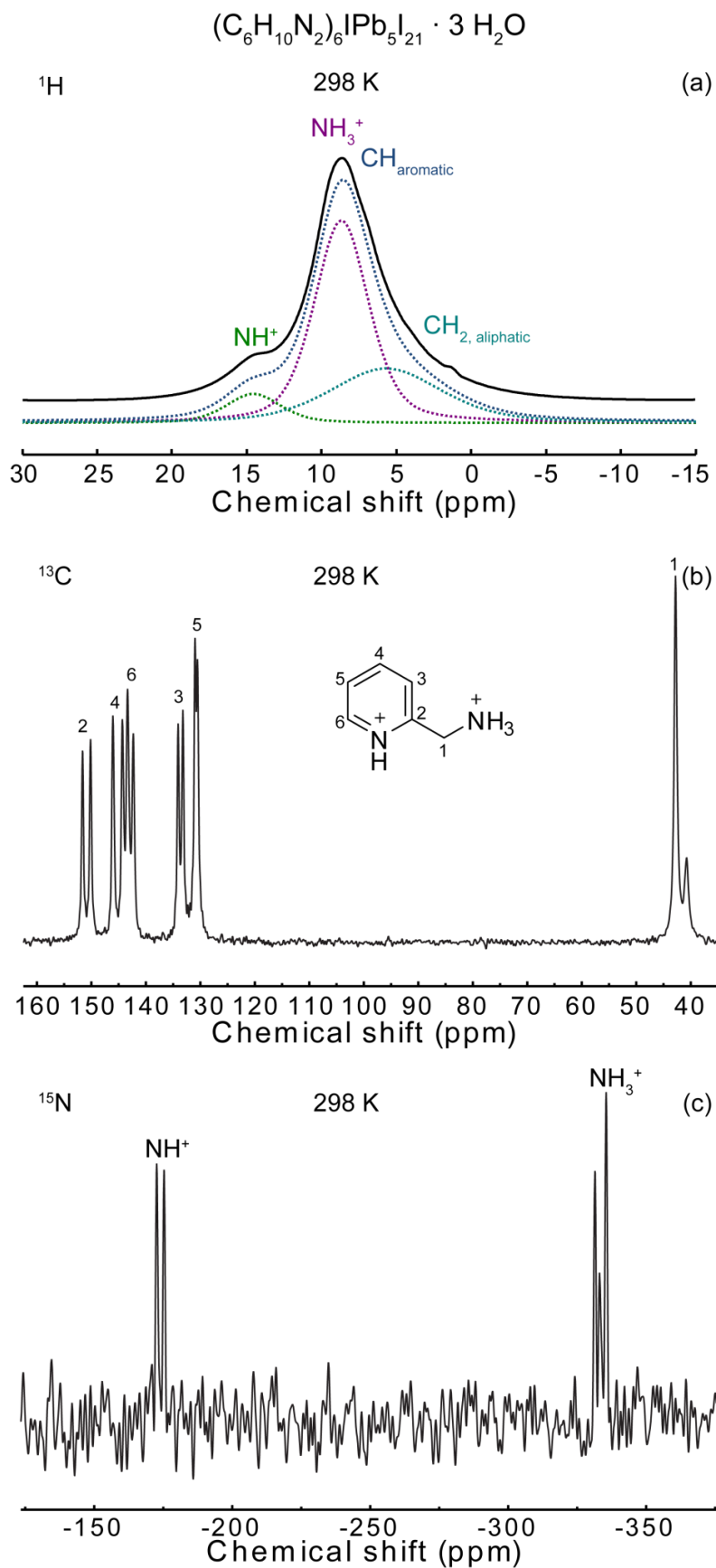


Figure S10. (a) 1H MAS (black solid line), (b) ^{13}C CP MAS and (c) ^{15}N CP MAS solid-state NMR spectra of $(C_6H_{10}N_2)_6IPb_5I_{21} \cdot 3 H_2O$ at 298 K. (a) A combination of a Lorentzian and a Gaussian line was used to fit the deconvoluted signals marked with colored dashed lines.

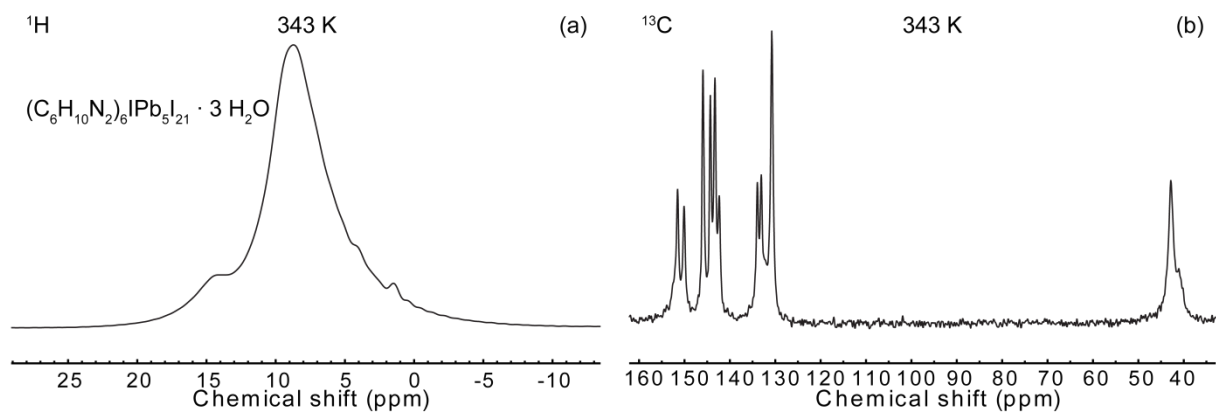


Figure S11. (a) ^1H MAS and (b) ^{13}C CP MAS solid-state NMR spectra of $(\text{C}_6\text{H}_{10}\text{N}_2)_6\text{IPb}_5\text{I}_{21} \cdot 3 \text{H}_2\text{O}$ at 343 K.

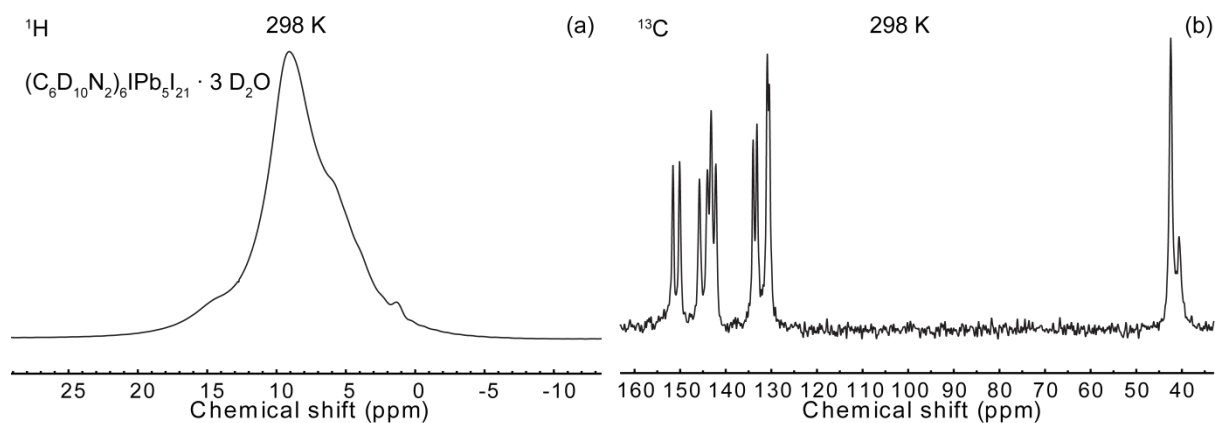


Figure S12. (a) ^1H MAS and (b) ^{13}C CP MAS solid-state NMR spectra of $(\text{C}_6\text{D}_{10}\text{N}_2)_6\text{IPb}_5\text{I}_{21} \cdot 3 \text{D}_2\text{O}$ at 298 K.

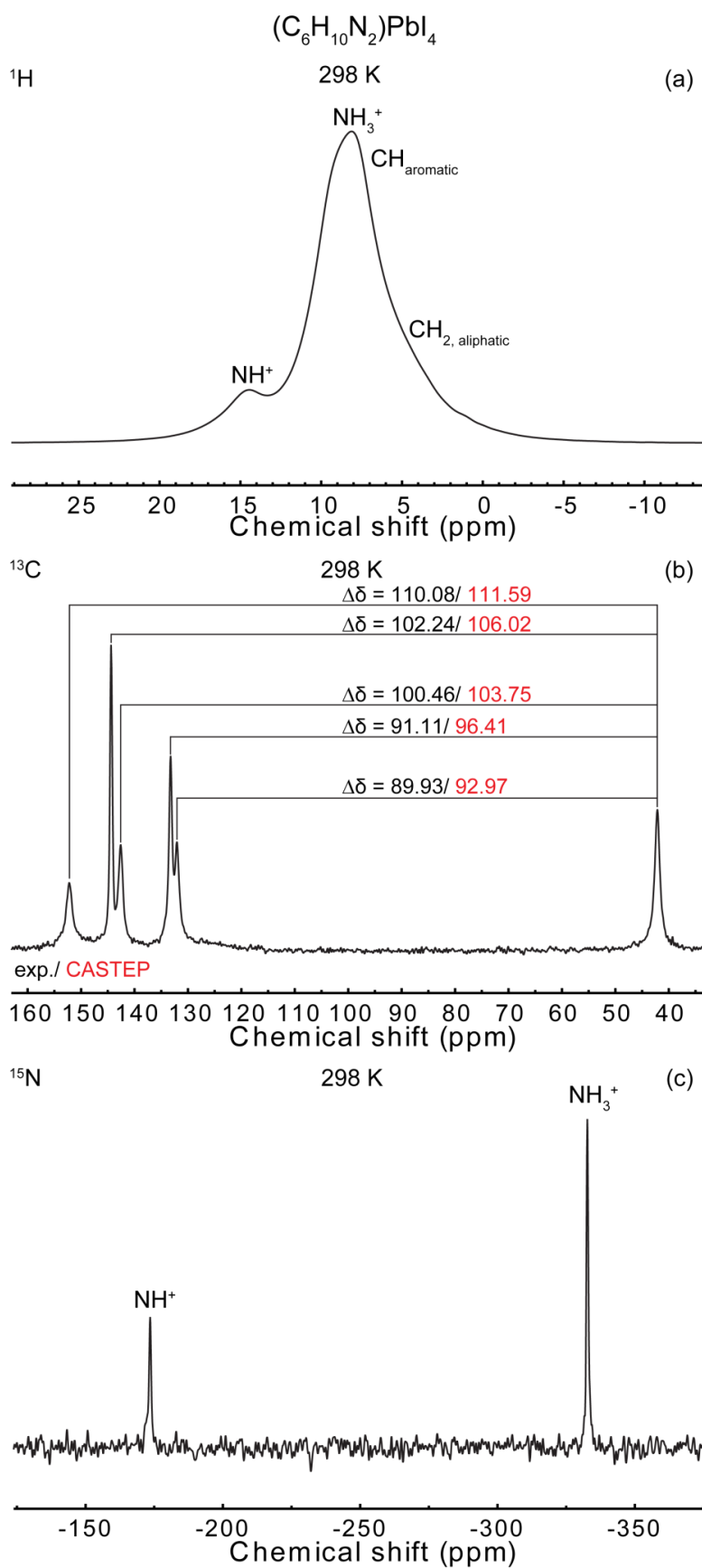


Figure S13. (a) 1H MAS, (b) ^{13}C CP MAS and (c) ^{15}N CP MAS solid-state NMR spectra of $(C_6H_{10}N_2)PbI_4$ at 298 K. (b) Comparison of the CASTEP/ Zora predictions for $\Delta\delta$ with the experimental values for $\Delta\delta$.

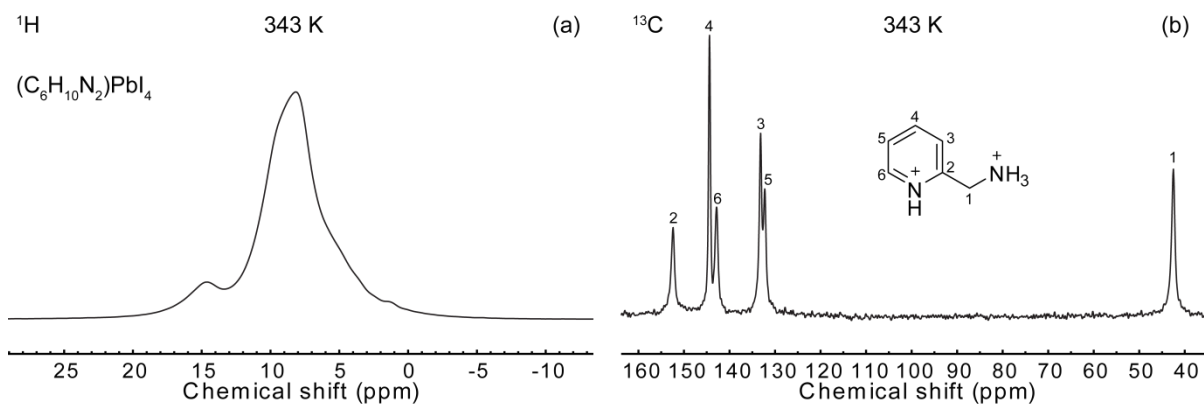


Figure S14. (a) ^1H MAS and (b) ^{13}C CP MAS solid-state NMR spectra of $(\text{C}_6\text{H}_{10}\text{N}_2)\text{PbI}_4$ at 343 K.

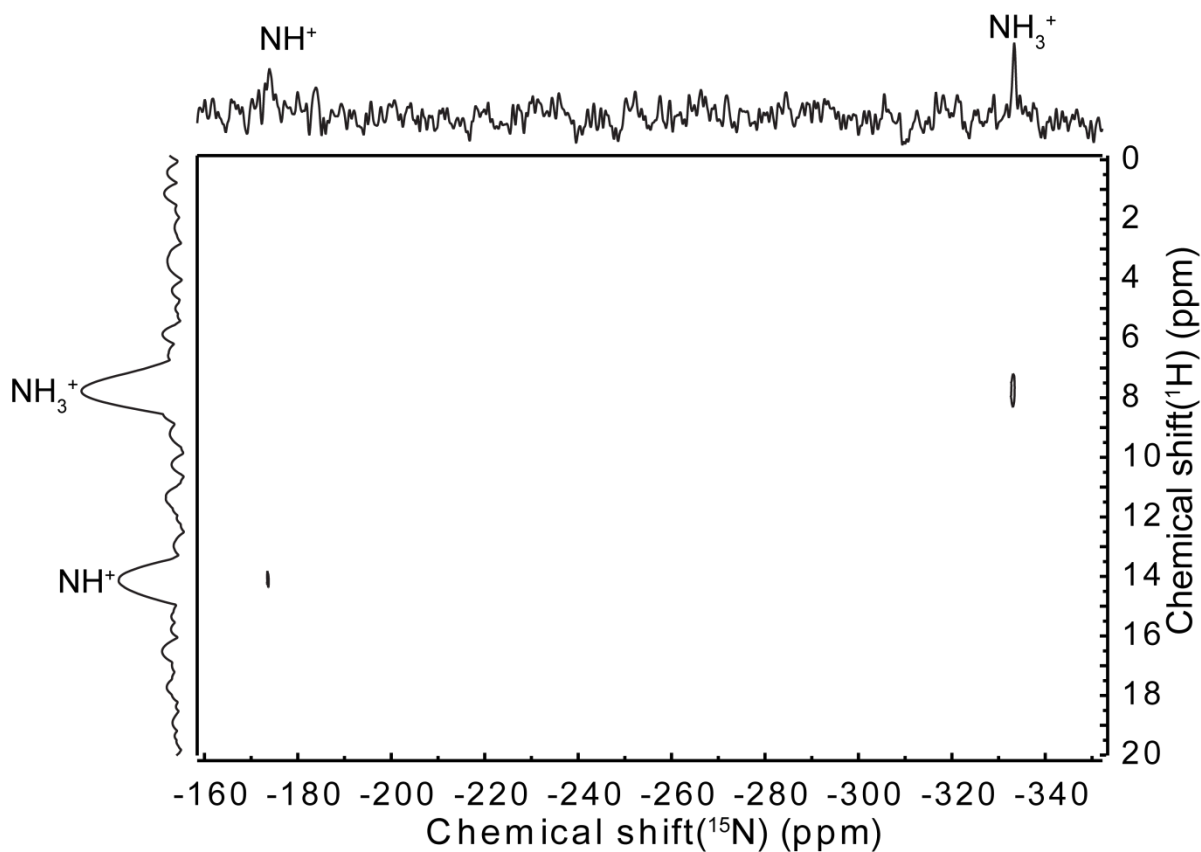


Figure S15. ^{15}N , ^1H HETCOR MAS solid-state NMR spectrum of $(\text{C}_6\text{H}_{10}\text{N}_2)\text{PbI}_4$ at 298 K.

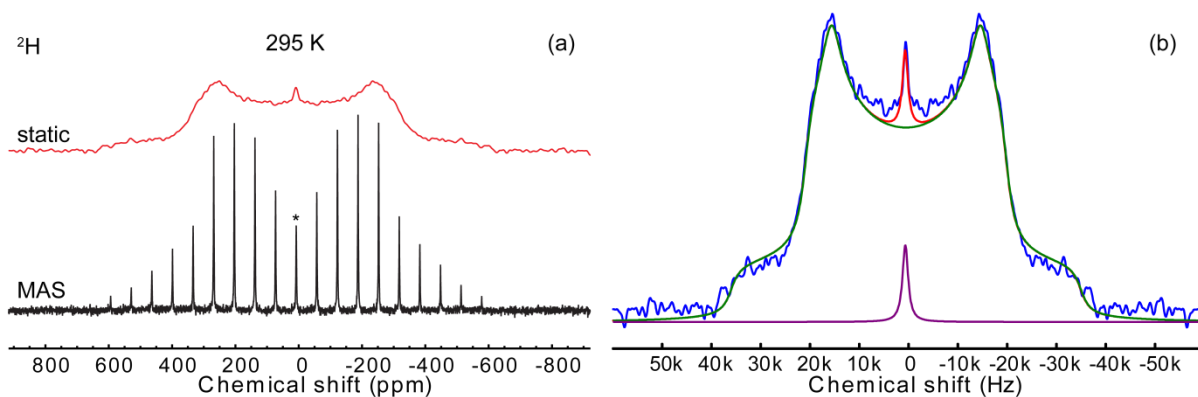


Figure S16. (a) ^2H static and MAS solid-state NMR spectra of $(\text{C}_6\text{H}_{10}\text{N}_2)_6\text{IPb}_5\text{I}_{21} \cdot 3 \text{H}_2\text{O}$ at 295 K. The signal in the MAS NMR spectrum is marked with an asterisk. The remaining signals are spinning side bands. (b) Fit (purple) of the ^2H static solid-state NMR spectrum (blue) of $(\text{C}_6\text{D}_{10}\text{N}_2)_6\text{IPb}_5\text{I}_{21} \cdot 3 \text{D}_2\text{O}$ at 295 K. A quadrupolar (Cq) line shape was used for the broad component of the signal (green) and a combination of a Lorentzian and a Gaussian line was applied for the narrow component of the signal (red). The relative populations of the sites were obtained from the integrals of the simulated lines.

C.11 Optical measurements

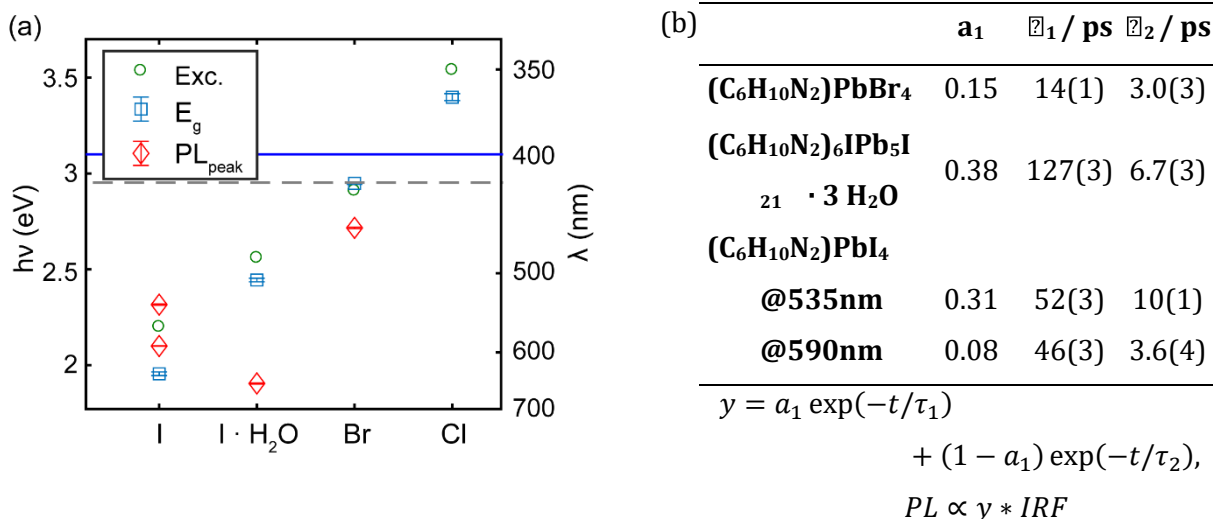


Figure S17. (a) Extracted energetic positions of bandgaps (blue squares), exciton peaks (green circles), and PL peaks (red diamonds) for $(\text{C}_6\text{H}_{10}\text{N}_2)\text{PbI}_4$, $(\text{C}_6\text{H}_{10}\text{N}_2)_6\text{IPb}_5\text{I}_{21} \cdot 3 \text{H}_2\text{O}$, $(\text{C}_6\text{H}_{10}\text{N}_2)\text{PbBr}_4$, and $(\text{C}_6\text{H}_{10}\text{N}_2)\text{PbCl}_4$. Excitation wavelength (blue solid line, $\lambda_{\text{excitation}} = 400 \text{ nm}$) and longpass filter cut-off (gray dashed line) are indicated. (b) Resulting parameters and formula used to fit the PL decays. Parentheses specify 95% confidence intervals of the last given digit.

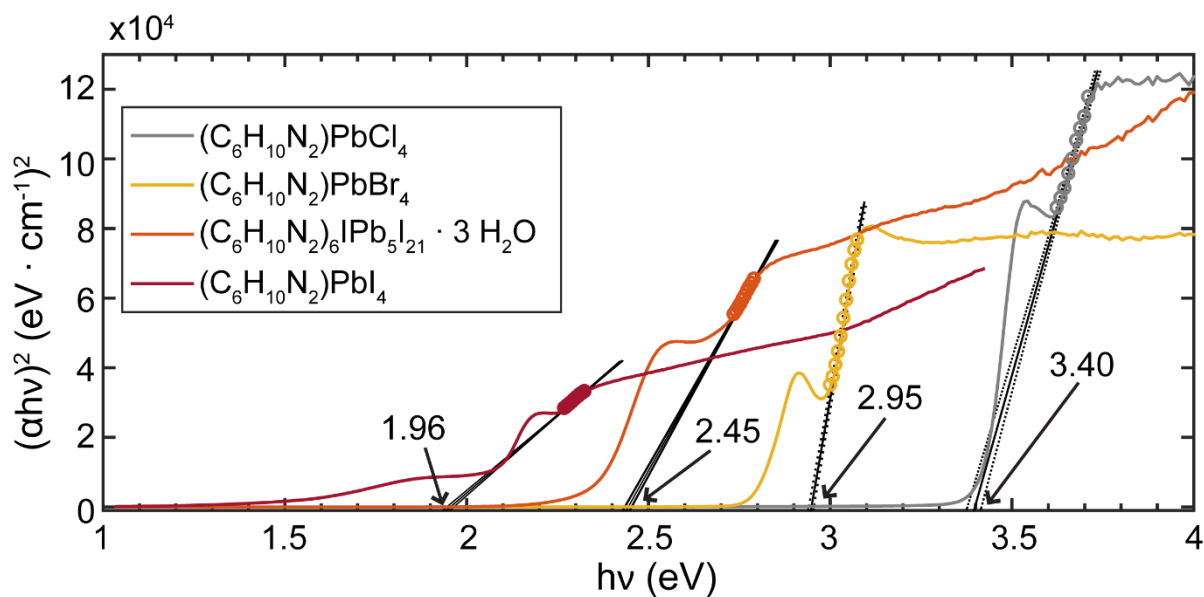


Figure S18. Bandgaps were determined by Tauc Plots fitted to the band edge, whereby excitonic distributions were neglected. The x -axis intercept is used as value for E_g . Fitted data points (circles), linear fits (black solid lines) and their 95% confidence intervals (black dotted lines) are indicated.

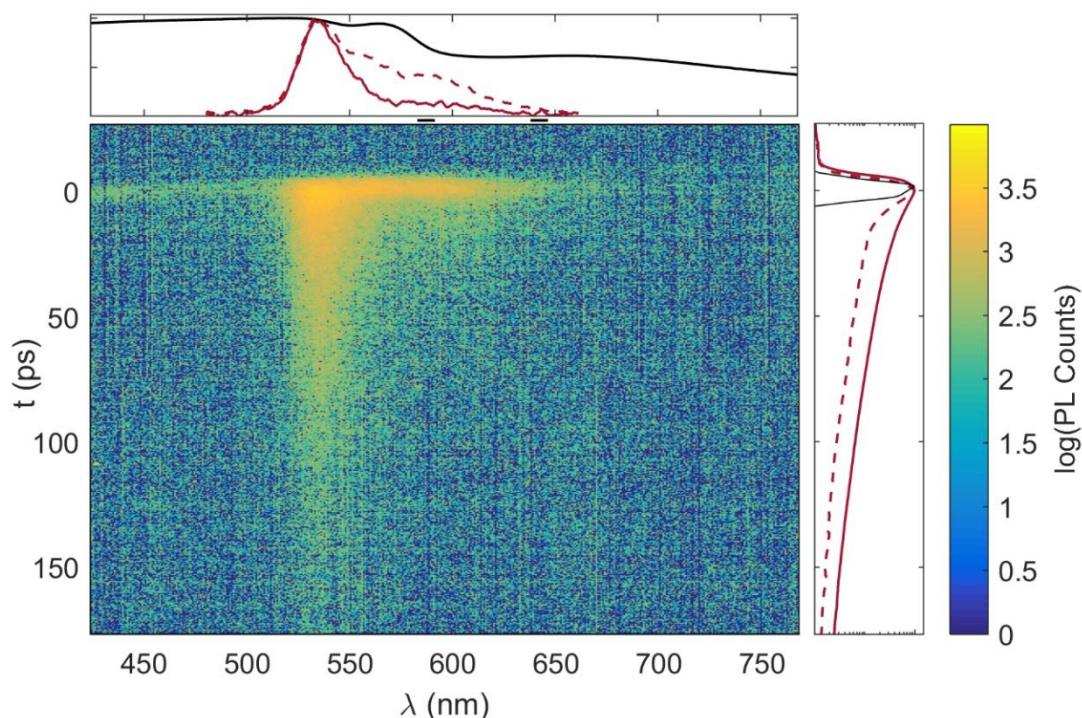


Figure S19. Time-resolved PL map of $(\text{C}_6\text{H}_{10}\text{N}_2)\text{PbI}_4$. The graph on top shows normalized PL spectra recorded immediately upon excitation (red dotted line) and at several tens of ps after excitation (red solid line). The absorbance spectrum is indicated in black. Fitted normalized PL decays at ~ 535 nm (red solid line) and at ~ 590 nm (red dashed line), as well as the IRF (black line) are displayed in the graph on the right. Note the logarithmical scaling for main and side axes and the linear scaling for the top axes.

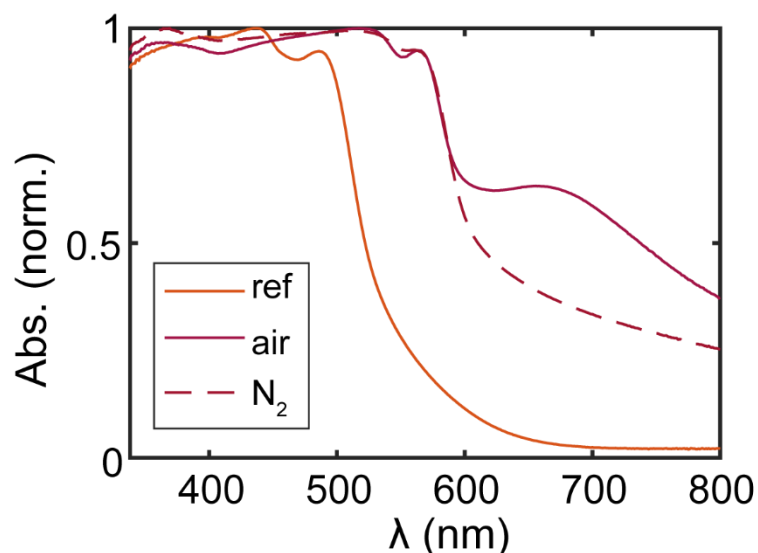


Figure S20. Near-band edge absorbance spectra of $(\text{C}_6\text{H}_{10}\text{N}_2)\text{PbI}_4$ synthesized by heating $(\text{C}_6\text{H}_{10}\text{N}_2)_6\text{IPb}_5\text{I}_{21} \cdot 3 \text{H}_2\text{O}$ (orange line) to 160°C in air (red solid line) and in nitrogen atmosphere (red dashed line), respectively.

C.12 Band structure calculations

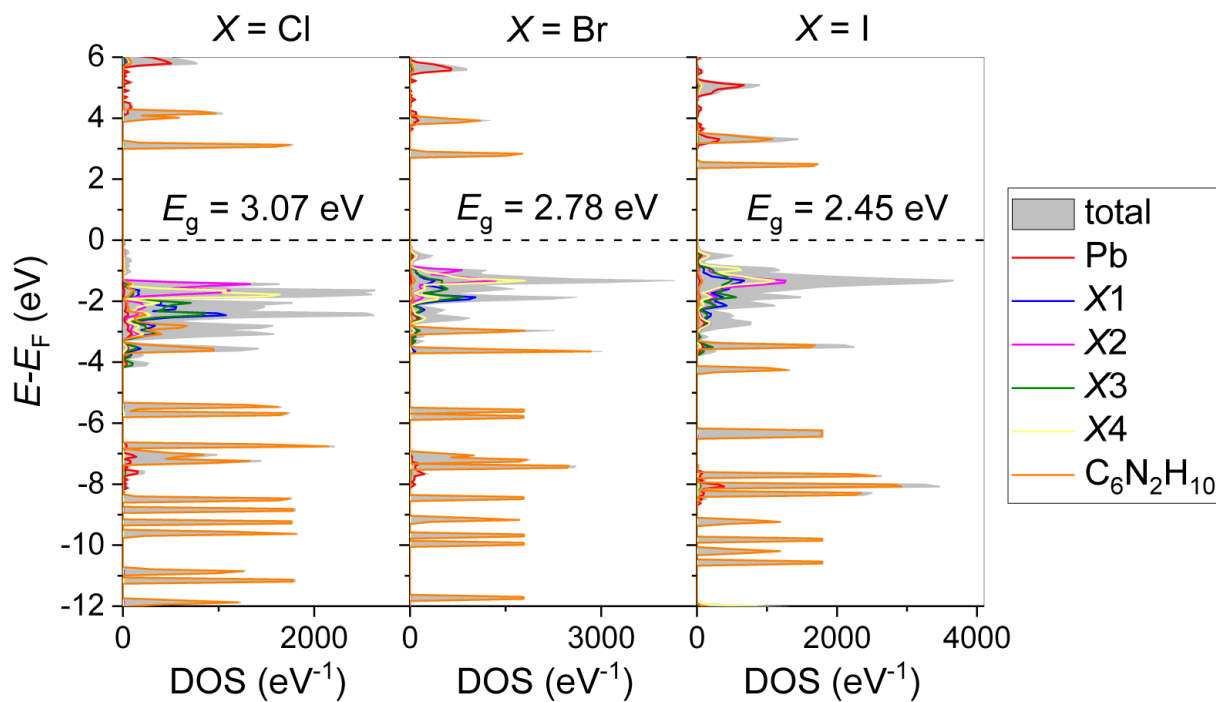


Figure S21. Calculated densities of states for $(\text{C}_6\text{H}_{10}\text{N}_2)\text{PbX}_4$ ($X = \text{Cl}, \text{Br}, \text{I}$) with band gap energies E_g .

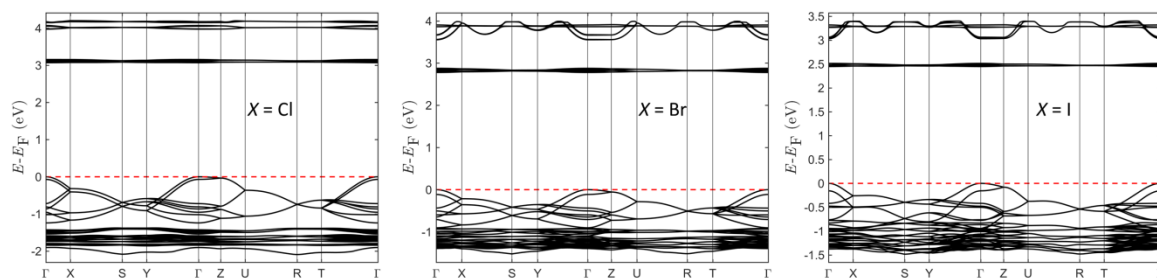


Figure S22. Calculated band structures for $(\text{C}_6\text{H}_{10}\text{N}_2)\text{PbX}_4$ ($X = \text{Cl}, \text{Br}, \text{I}$).

C.13 References

1. Alonso, J. A.; Martínez-Lope, M. J.; Casais, M. T.; Fernández-Díaz, M. T., Evolution of the Jahn–Teller Distortion of MnO_6 Octahedra in RMnO_3 Perovskites ($R = \text{Pr}, \text{Nd}, \text{Dy}, \text{Tb}, \text{Ho}, \text{Er}, \text{Y}$): A Neutron Diffraction Study. *Inorg. Chem.* **2000**, *39* (5), 917-923.
2. Massiot, D.; Fayon, F.; Capron, M.; King, I.; Le Calvé, S.; Alonso, B.; Durand, J.-O.; Bujoli, B.; Gan, Z.; Hoatson, G., Modelling one- and two-dimensional solid-state NMR spectra. *Magn. Reson. Chem.* **2002**, *40* (1), 70-76.
3. Kita, E.; Lisiak, R., Potential biochromium sources; kinetic studies on acid- and base-catalyzed aquation of $[\text{Cr}(\text{ox})_2(2\text{-}[\text{aminomethyl}]\text{pyridine})^-]$. *Transition Met. Chem.* **2010**, *35* (4), 441-450.
4. Segall, M. D.; Philip, J. D. L.; Probert, M. J.; Pickard, C. J.; Hasnip, P. J.; Clark, S. J.; Payne, M. C., First-principles simulation: ideas, illustrations and the CASTEP code. *J. Phys.: Condens. Matter* **2002**, *14* (11), 2717.
5. Yates, J. R.; Pickard, C. J.; Mauri, F., Calculation of NMR chemical shifts for extended systems using ultrasoft pseudopotentials. *Phys. Rev. B* **2007**, *76* (2), 024401.

D List of publications within this thesis and author contributions

This thesis comprises the following papers published in and submitted to scientific journals, respectively. Author contributions are itemized for every publication.

1. **Completing the picture of 2-(aminomethylpyridinium) lead hybrid perovskites– Insights into structure, conductivity behavior and optical properties.**

Claudia Lermer, Alessandro Senocrate, Igor L. Moudrakovski, Tobias Seewald, Anna-Katharina Hatz, Peter Mayer, Florian Pielhofer, Julian A. Jaser, Lukas Schmidt-Mende, Joachim Maier, Bettina V. Lotsch

Chem. Mater., to be submitted.

Claudia Lermer wrote the main part of the manuscript, did the literature research, created the figures (unless otherwise noted), conceived and performed the syntheses, recorded the majority of the PXRD data and carried out the Rietveld refinements. Alessandro Senocrate and Anna-Katharina Hatz performed the a.c. impedance spectroscopy and d.c. galvanostatic polarization measurements, evaluated the results and provided the respective figures. Igor L. Moudrakovski carried out solid-state NMR measurements, conducted theoretical calculations and was involved in designing figures presenting the NMR data. Peter Mayer carried out the single-crystal X-ray diffraction measurements and also solved and refined the crystal structures published within this paper. Florian Pielhofer did band structure calculations and provided the respective figures. Julian A. Jaser was involved in developing the syntheses. Alessandro Senocrate, Igor L. Moudrakovski, Tobias Seewald and Anna-Katharina Hatz contributed to writing the manuscript. Bettina V. Lotsch, Lukas Schmidt-Mende and Joachim Maier directed and supervised the work. All authors revised the manuscript.

2. **Benzimidazolium Lead Halide Perovskites: Effects of Anion Substitution and Dimensionality on the Bandgap.**

Claudia Lermer, Sascha P. Harm, Susanne T. Birkhold, Julian A. Jaser, Christopher M. Kutz, Peter Mayer, Lukas Schmidt-Mende, Bettina V. Lotsch

Z. Anorg. Allg. Chem. **2016**, 642 (23), 1369-1376.

Claudia Lermer wrote the main part of the manuscript, did the literature research, created the figures (unless otherwise noted), conceived the syntheses and evaluated the NMR and PXRD data. Claudia Lermer and Julian A. Jaser performed the syntheses of the benzimidazolium lead halides. Sascha P. Harm carried out the Rietveld refinements and was involved in designing the figures. Susanne T.

Birkhold performed the absorption and PL measurements, provided the respective figures and contributed to writing the manuscript. Peter Mayer carried out the single-crystal X-ray diffraction measurements and also solved and refined the crystal structures. Julian A. Jaser took the photographs of the benzimidazolium lead halide powders. Bettina V. Lotsch and Lukas Schmidt-Mende directed and supervised the work. All authors revised the manuscript.

3. **Toward Fluorinated Spacers for MAPI-Derived Hybrid Perovskites: Synthesis, Characterization, and Phase Transitions of $(\text{FC}_2\text{H}_4\text{NH}_3)_2\text{PbCl}_4$.**

Claudia Lerner, Susanne T. Birkhold, Igor L. Moudrakovski, Peter Mayer, Leslie M. Schoop, Lukas Schmidt-Mende, Bettina V. Lotsch
Chem. Mater. **2016**, *28* (18), 6560-6566.

Claudia Lerner wrote the main part of the manuscript, did the literature research, created the figures (unless otherwise noted), developed and carried out the syntheses, evaluated the PXRD data and performed the Rietveld refinements. Susanne T. Birkhold carried out the photoluminescence and absorption measurements, provided the respective figures and contributed to writing the manuscript. Igor L. Moudrakovski performed the solid-state NMR measurements and provided the interpretation of the results. Peter Mayer carried out the single-crystal X-ray diffraction measurements and solved and refined the crystal structures published within this paper. Leslie M. Schoop performed band structure calculations. Bettina V. Lotsch and Lukas Schmidt-Mende directed and supervised the work. All authors discussed the results and revised the manuscript.

E CCDC deposition numbers

Crystallographic data for the compounds synthesized as part of this work were deposited with the Cambridge Crystallographic Data Centre (CCDC) and are available on quoting the respective CCDC numbers listed in the following table.

Table I. CCDC Numbers of the compounds synthesized as part of this work.

Compound	Temperature	CCDC Number
$(\text{FC}_2\text{H}_4\text{NH}_3)_2\text{PbCl}_4$	173 K	1479690
$(\text{FC}_2\text{H}_4\text{NH}_3)\text{PbBr}_3 \cdot \text{C}_3\text{H}_7\text{NO}$	173 K	1479691
$(\text{C}_7\text{H}_7\text{N}_2)_2\text{PbCl}_4$	100 K	1507155
$(\text{C}_7\text{H}_7\text{N}_2)_2\text{PbBr}_4$	173 K	1507157
$(\text{C}_7\text{H}_7\text{N}_2)_2\text{PbI}_4$	100 K	1507154
$(\text{C}_7\text{H}_7\text{N}_2)\text{PbI}_3$	173 K	1507156
$(\text{C}_6\text{H}_{10}\text{N}_2)_6\text{IPb}_5\text{I}_{21} \cdot 3 \text{H}_2\text{O}$	296 K	1838614
$(\text{C}_6\text{H}_{10}\text{N}_2)_6\text{IPb}_5\text{I}_{21} \cdot 3 \text{H}_2\text{O}$	100 K	1838610
$(\text{C}_6\text{H}_{10}\text{N}_2)\text{PbCl}_4$	296 K	1838616
$(\text{C}_6\text{H}_{10}\text{N}_2)_4\text{Pb}_4\text{Cl}_{16}$	100 K	1838611
$(\text{C}_6\text{H}_{10}\text{N}_2)\text{PbBr}_4$	296 K	1838617
$(\text{C}_6\text{H}_{10}\text{N}_2)\text{PbBr}_4$	100 K	1838612
$(\text{C}_6\text{H}_{10}\text{N}_2)\text{PbI}_4$	296 K	1838615
$(\text{C}_6\text{H}_{10}\text{N}_2)\text{PbI}_4$	153 K	1838613

F List of presentations

Oral presentations

1. **New 2D hybrid perovskite systems for optoelectronic applications**

Claudia Lermer, Susanne T. Birkhold, Sascha P. Harm, Igor L. Moudrakovski, Leslie M. Schoop, Peter Mayer, Lukas Schmidt-Mende, Bettina V. Lotsch
253. ACS National Meeting, San Francisco, 04/04/2017.

Poster presentations

1. **Towards Low-Dimensional Hybrid Perovskites with Fluorinated Spacers**

Claudia Lermer, Susanne T. Birkhold, Igor L. Moudrakovski, Lukas Schmidt-Mende, Bettina V. Lotsch
"International Conference on Hybrid and Organic Photovoltaics" (HOPV16), Swansea, June 2016

2. **Towards Low-Dimensional Hybrid Perovskites with Fluorinated Spacers**

Claudia Lermer, Susanne T. Birkhold, Igor L. Moudrakovski, Lukas Schmidt-Mende, Bettina V. Lotsch
"International Conference on Perovskite Thin Film Photovoltaics" (ABXPV), Barcelona, March 2016

3. **Revealing the Crystal Structure of Acetamidinium Copper Chloride**

Claudia Lermer, Jannik Schwab, Bettina V. Lotsch
CeNS Workshop "Channels and Bridges to the Nanoworld", Venedig, September 2015

4. **Revealing the Crystal Structure of Acetamidinium Copper Chloride**

Claudia Lermer, Jannik Schwab, Bettina V. Lotsch
NIM Summer Retreat, Fall (Lenggries), July 2015

G Abbreviations

0D	zero-dimensional
1D	one-dimensional
2D	two-dimensional
3D	three-dimensional
Å	Ångström
a.c.	alternating current
AEA	3-(2-ammonioethyl)anilinium
API	<i>N</i> -(3-aminopropyl)imidazolium
AVA	5-ammoniumvaleric acid
BA	butylammonium
BFGS	Broyden-Fletcher-Goldfarb-Shanno
C	capacitance
CA	cyclopropylammonium
calcd	calculated
CB	conduction band
CFMPIB	Cs _{0.1} FA _{0.74} MA _{0.13} PbI _{2.48} Br _{0.39}
CIE	International Commission on Illumination (Fr., Commission Internationale de l'Éclairage)
CIGS	copper indium gallium selenide
CP	cross-polarization
CPE	constant phase element
CRI	color rendering index
CyA	cyclohexylammonium
CyBMA	1,3-cyclohexanebis(methylammonium)
Δd	magnitude of distortion
d.c.	direct current
DFT	density functional theory
DMABA	<i>N</i> ¹ , <i>N</i> ¹ -dimethylbutane-1,4-diaminium
DMAPA	<i>N</i> ¹ , <i>N</i> ¹ -dimethylpropane-1,3-diaminium
DMEN	<i>N</i> ¹ , <i>N</i> ¹ -dimethylethane-1,2-diammonium

DMF	dimethylformamide
DMSO	dimethyl sulfoxide
DOS	density of states
DSC	differential scanning calorimetry
DSSC	dye-sensitized solar cells
DTA	differential thermal analysis
DTG	differential thermogravimetry
EA	ethylammonium
E_b	exciton binding energy
EDBE	2,2'-(ethylenedioxy)bis(ethylammonium)
EDX	energy-dispersive X-ray spectroscopy
ETM	electron transporting material
FA	formamidinium
FE	free-exciton state
FF	fill factor
FPEA	4-fluorophenethylammonium
FT	Fourier transform
FTO	fluorine doped tin oxide
fs	femtosecond
FWHM	full width at half maximum
GGA	generalized approximation
GooF	Goodness of fit
GS	ground state
HTM	hole transporting material
h	hour
Hz	hertz
IR	infrared
IRF	instrument response function
J_{sc}	short-circuit current density
LCA	life cycle assessment
LED	light-emitting diode

MA	methylammonium
MAS	magic-angle spinning
MAPI	methylammonium lead iodide
mg	milligram
min	minute
mL	milliliter
mmol	millimole
<i>N</i> -MEDA	<i>N</i> ¹ -methylethane-1,2-diammonium
NMR	nuclear magnetic resonance
PBE	Perdew–Burke–Ernzerhof
PCBM	[6,6]-phenyl-C ₆₁ -butyric acid methyl ester
PCE, η	power conversion efficiency
pc-LED	phosphor-converted light-emitting diode
PEDOT:PSS	poly(3,4-ethylenedioxythiophene) polystyrene sulfonate
PLQE	photoluminescence quantum efficiency
S	Huang-Rhys parameter
SEM	scanning electron microscope
spiro-OMeTAD	<i>N</i> ² , <i>N</i> ² , <i>N</i> ^{2'} , <i>N</i> ^{2'} , <i>N</i> ⁷ , <i>N</i> ⁷ , <i>N</i> ^{7'} , <i>N</i> ^{7'} -octakis(4-methoxyphenyl)-9,9'-spirobi[9H-fluorene]-2,2',7,7'-tetramine
STE	self-trapped exciton state
<i>t</i>	Goldschmidt's tolerance factor
TG	thermogravimetry
TMS	tetramethylsilane
UV	ultraviolet
pc-LED	phosphor-converted LED
PDOS	partial density of states
PEA	phenethylammonium
PEI	polyethylenimine
PL	photoluminescence
PLQE	photoluminescence quantum efficiency
ppm	parts per million
PXRD	powder X-ray diffraction

RGB	red-green-blue
VB	valence band
vis	visible
V_{oc}	open-circuit voltage
wt	weight
WLED	white light-emitting diode
ZORA	zeroth-order regular approximation